



**University of
Nottingham**

UK | CHINA | MALAYSIA

Metal Oxides Inside
Carbon Nanoreactors for
Environmental Remediation

Maxwell A. Astle, MSci.

Thesis submitted to the University of Nottingham for the degree of doctor of
Philosophy

2019

Abstract

The work presented in this thesis demonstrates the key principles of 'catalytic nanoreactors' and 'nanosponges', whereby the unique effects of spatial confinement inside carbon nanotubes can be harnessed to drive important decontamination reactions. The versatile gas and liquid phase filling strategies developed, allow control over the structure and functionality of the encapsulated metal oxide by varying the synthesis conditions or by post-synthesis thermal treatment. Using a holistic approach, a diverse range of bulk and local probe characterisation techniques were applied and a strategy for the characterisation of these challenging nanomaterials established. Group IV (Ti, Zr and Hf) nanomaterials are found to coat the interior channel of hollow graphitised carbon nanofibres (GNF). This amorphous structure with a thickness of 6-10 nm provides maximised catalytic surface area and minimal transport resistance for reactants. Discrete group VI (Cr, Mo and W) metal oxide nanomaterials are embedded within GNF and effectively catalyse the combustion of the GNF due to the interactions between the guest and host species. As a result of spatial confinement, a catalytic carbon nanoreactor containing hydroxylated zirconia thin films ($\text{ZrO}_x(\text{OH})_y@GNF$) promoted a four-fold enhancement in the rate of hydrolysis of organophosphorus compounds relative to the GNF and hydroxylated zirconia in isolation. Confined molybdenum dioxide nanoparticles inside carbon nanoreactors also showed superior abilities towards oxidative desulphurisation affording over 98 % fuel desulphurisation at low catalyst loading. The roles of the carbon nanoreactors were found to improve the activity and stability of catalytic centres in these reactions as well as enhancing the local concentration of reagents to catalysts. Surprisingly, the nanotube cavity was found to sequester the undesirable species

out of the reaction media allowing them to act as a nanosponge. This effect provided further enrichment of the molecules within the nanoreactor and also an effective adsorption mechanism increasing the removal of the toxic species. This synergistic dual functionality has led to the improved catalytic performance and demonstrated amplified nanoremediation applicable to nerve agent destruction and the production of ultra-low sulphur fuel.

Publications

- (1) **Maxwell A. Astle**, Graham A. Rance, Michael W. Fay, Stuart Notman, Mark R. Sambrook and Andrei N. Khlobystov, "Synthesis of hydroxylated group IV metal oxides inside hollow graphitised carbon nanofibers: nanosponges and nanoreactors for enhanced decontamination of organophosphates", *J. Mater. Chem. A*, 2018, **6**, 20444-20453.
- (2) **Maxwell A. Astle**, Graham A. Rance, Hannah J. Loughlin, Thomas D. Peters, and Andrei N. Khlobystov, "Molybdenum dioxide in carbon nanoreactors as a catalytic nanosponge for the efficient desulphurisation of liquid fuels", *Adv. Funct. Mater.*, 2019, **29**, 1808092.
- (3) Nityananda Agasti, **Maxwell A. Astle**, Graham A. Rance, Jairton Dupont, Andrei N. Khlobystov, "Ceria nanoparticles inside hollow carbon nanofibres in catalysis of selective allylic oxidation of cyclohexene", *Manuscript in preparation*.

Acknowledgements

Firstly, I would like to express my thanks to my Supervisor Andrei Khlobystov. His infectious enthusiasm and passion for science is unwavering and I am especially grateful to him for allowing me to flourish during this PhD.

I also wouldn't be the scientist I am today without the guidance of Dr Graham Rance. His endless help and assistance in every aspect of my PhD studies have been essential and for that, I am truly thankful.

I would also like to thank the Nottingham Nanoscale and Microscale Research Centre for providing me with access to their instruments and particularly, Dr Mike Fay for his training and guidance on the microscopes. Dr Mick Cooper was also important in providing training and assistance for many of the analytical techniques used in this work.

Thanks also to our collaborators within the DSTL, Mark Sambrook and Stuart Notman, who have provided crucial advice during my research towards the decontamination of toxic agents. I have also been fortunate to supervise some excellent MSci research students, Hannah Loughlin, Tom Peters and Nityananda Agasti who built some of the foundations of my research.

I would like to extend my sincere thanks to all current and past members of the Nottingham Nanocarbon group who have been a pleasure to work with. In particular, Rob, Scott, Rhys, Kate, Bradley, Julie, Kayleigh, Luke, Ruth and Will who have directed and supported me throughout this experience. Two members of the group, Craig Stoppiello and Jack Jordan, deserve a special mention as without their never-ending "moral support" and amusement this

PhD wouldn't have been the same. Katie, Pritesh, Alison, Glen and Ellen are just a few other people from the department who also deserve thanks as they have not only been great colleagues but also amazing friends.

Finally, I would like to thank my parents, Shona and Darren, as even though I have been a "bundle of joy" when writing this thesis, their continuing love and support throughout my PhD has kept me going.

List of acronyms, abbreviations and symbols

<u>Acronym, abbreviation or symbol</u>	<u>Definition</u>
@	[...] encapsulated within [...]
acac	Acetylacetonate, $((\text{CH}_3\text{CO})_2\text{CH})-$
ADS	Adsorptive desulphurisation
BDS	Biodesulphurisation
BET	Brunauer-Emmett-Teller analysis
BT	Benzothiophene
BTO	Benzothiophene sulfoxide
BTO ₂	Benzothiophene sulfone
CNT	Carbon nanotube(s)
CWA	Chemical warfare agent(s)
DBT	Dibenzothiophene
DBTO	Dibenzothiophene sulfoxide
DBTO ₂	Dibenzothiophene sulfone
DMDBT	4,6-Dimethyldibenzothiophene
DMDBTO	4,6-Dimethyldibenzothiophene sulfoxide
DMDBTO ₂	4,6-Dimethyldibenzothiophene sulfone
DMMP	Dimethyl methylphosphate
DMNP	Dimethyl 4-nitrophenyl phosphate
DWNT	Double walled carbon nanotube(s)
^e d	External diameter
EDX	Energy dispersive X-ray spectroscopy
EELS	Electron energy loss spectroscopy
FWHM	Full width half maximum
GB	Sarin
GC-MS	Gas chromatography-mass spectrometry
GD	Soman
GNF	Graphitised nanofibre(s)
GO	Reduced graphene oxide
HDS	Hydrodesulphurisation
HP	Hydrogen peroxide
HRTEM	High resolution transmission electron microscopy
ⁱ d	Internal diameter
MOF	Metal-organic framework
MO _x	Metal oxide
MO _x (OH) _y	Metal oxyhydroxide
MS	Mass spectrometry

MWNT	Multi-walled nanotube(s)
NMR	Nuclear magnetic resonance
NP	Nanoparticle(s)
ODS	Oxidative desulphurisation
OP	Organophosphorus
OS	Organosulphur
POM	Polyoxometalate
PXRD	Powder X-ray diffraction
RT	Room temperature
SEM	Scanning electron microscopy
STEM	Scanning transmission electron microscopy
SWNT	Single walled carbon nanotube(s)
T	Thiophene
TBHP	Tert-butyl hydroperoxide
TEM	Transmission electron microscopy
TGA	Thermogravimetric analysis
TMP	Trimethyl phosphate
TOF	Turnover frequency
T _{ox}	Temperature of oxidation
ULSD	Ultra-low sulphur diesel
UV-Vis	Ultraviolet–visible spectroscopy
w	width
Z	Atomic number

1. Nanoremediation of environmental contaminants	1
1.1. Nanoscale materials	3
1.2. Metal oxide nanomaterials for nanoremediation	13
1.2.1. Size modification	17
1.2.2. Morphology modification	19
1.2.3. Composition and surface structure	22
1.3. Metal oxides and carbon composite nanomaterials	25
1.4. Scope for further investigation	39
1.5. References	41
2. Synthesis of hydroxylated group IV metal oxide compounds in hollow graphitised nanofibres	47
2.1. Background	47
2.2. Aim and Objectives	54
2.3. Results and discussion	55
2.3.1. Synthesis of $MO_x(OH)_y@GNF$	55
2.3.2. Transmission Electron Microscopy of $MO_x(OH)_y@GNF$	64
2.3.3. Localised elemental analysis of $MO_x(OH)_y@GNF$	71
2.3.4. Thermally activated inorganic transformations of $MO_x(OH)_y@GNF$	74
2.3.4.1. Thermal treatment of $MO_x(OH)_y@GNF$ in air	75
2.3.4.2. Thermal treatment of $MO_x(OH)_y@GNF$ in inert atmosphere	82
2.4. Conclusions	87
2.5. Experimental	88
2.5.1. General	88
2.5.2. Carbon nanomaterials sources and pre-treatment	89
2.5.3. Preparation of hydroxylated metal oxides inside graphitised nanofibres	90
2.5.4. Manipulation of hydroxylated metal oxides inside graphitised nanofibres	91
2.6. References	91

3. Nanoreactors and nanosponges for enhanced decontamination of organophosphates	95
3.1. Background	95
3.2. Aim and Objectives	101
3.3. Results and discussion	102
3.3.1. Hydrolysis procedure of organophosphorus species	102
3.3.2. Hydrolysis of DMNP using nanoreactors	107
3.3.2.1. Hydrolysis of DMNP - Control reactions	107
3.3.2.2. Effect of encapsulated metal oxide species on hydrolysis of DMNP	108
3.3.2.3. Effect of the catalyst composition on hydrolysis of DMNP	118
3.3.2.4. Effect of catalyst loading on hydrolysis of DMNP	119
3.3.2.5. Effect of buffer system on hydrolysis of DMNP with $ZrO(OH)_2@GNF$	121
3.4. Conclusions	123
3.5. Experimental	124
3.5.1. General	124
3.5.2. Preparation of bulk hydroxylated zirconia	126
3.5.3. Hydrolysis procedure of DMNP in KOH buffer	126
3.5.4. Hydrolysis procedure of DMNP in organic buffer	128
3.6. References	129
4. Synthesis of group VI metal oxides in hollow graphitised nanofibres	131
4.1. Background	131
4.2. Aim and objectives	140
4.3. Results and discussion	141
4.3.1. Synthesis of tungsten oxide inside graphitised nanofibres	143
4.3.1.1. Tungsten hexacarbonyl as a precursor	143
4.3.1.2. Effect of thermal treatment on $WO_x@GNF$	147
4.3.1.3. Effect of precursor loading on the $WO_x@GNF$ formation	149

4.3.1.4. <i>Effect of the decomposition rate of the precursor on $WO_x@GNF$ formation</i>	151
4.3.2. Synthesis of molybdenum oxide inside graphitised nanofibres	155
4.3.2.1. <i>Molybdenum hexacarbonyl as a precursor</i>	155
4.3.2.2. <i>Molybdenum dioxide bisacetylacetonate as a precursor</i>	158
4.3.2.2.1. <i>Effect of precursor loading on $MoO_x@GNF$ formation</i>	163
4.3.2.2.2. <i>Effect of thermal treatment on $MoO_x@GNF$</i>	165
4.3.3. Synthesis of chromium oxide inside graphitised nanofibres	169
4.3.3.1. <i>Chromium hexacarbonyl as a precursor</i>	169
4.3.3.2. <i>Chromium acetylacetonate as a precursor</i>	169
4.3.3.2.1. <i>Effect of thermal treatment on $CrO_x@GNF$</i>	173
4.3.4. Nanoreactor guest-host interactions	177
4.4. Conclusions	180
4.5. Experimental	181
4.5.1. General	181
4.5.2. Preparation of metal oxides inside graphitised nanofibres using gas phase deposition procedure	183
4.6. References	185

5. Carbon nanoreactors as a catalytic nanosponge for the efficient desulphurisation of liquid fuels

5.1. Background	188
5.2. Aim and objectives	194
5.3. Results and discussion	196
5.3.1. Investigation of oxidative desulphurisation reactions	196
5.3.2. Evaluation of group VI metal oxide-carbon nanoreactors for the ODS of a model fuel	203
5.3.3. Investigating $MoO_2@GNF$ towards the ODS of fuel	205
5.3.3.1. <i>Catalytic nanosponge for ODS</i>	215
5.3.4. ODS of more representative model fuel systems with $MoO_2@GNF$	220
5.3.4.1. <i>Individual component model fuels</i>	220
5.3.5.2. <i>Multi-component model fuels</i>	224

5.4. Conclusions	228
5.5. Experimental	229
5.5.1. General	229
5.5.2. Oxidative desulphurisation procedure with extraction procedure	232
5.5.3. Oxidative desulphurisation procedure without extraction procedure	233
5.5.4. Preparation of MoO ₂ @Graphite	233
5.6. References	234
<i>6. Concluding remarks</i>	237

Nanoremediation of environmental contaminants

Harmful species released into the environment due to anthropogenic activity represent a major concern (Table 1.1). Nanoremediation is a diverse field of research dedicated to the decontamination of these undesirable compounds using nanoscale materials and can neutralise environmental contaminants by employing direct or in-direct decontamination strategies.^{1, 2}

Table 1.1. Current anthropogenic environmental issues.

Resource	Contamination	Source	Risks
Air	Release of SO ₂ and NO _x	Transport and energy industry	Acid rain and corrosion
	Release of CO ₂ and particulates	Transport and energy industry	Environmental depreciation and damaging to human health
Water	Heavy metals in water streams	Industrial process and mining	Harmful to human health
	Oil leakages	Oil industry	Harmful to aquatic life
	Biological contamination	Human, animal and hospital waste	Harmful to human health directly and through food chain
	Organophosphorus pesticides contamination	Agriculture	These agents are inhibiting/lethal to living organisms directly and can be passed down the food chain
Land	Release of chemical warfare agents	Chemical warfare	Very toxic and inhibiting to living organisms
	Radioactive contamination	Nuclear industry or warfare	Damaging to living organisms and long term pollution renders land unusable

When toxic species have polluted natural resources and require removal or destruction to prevent harmful effects on the environment or human health, a direct decontamination approach is required (Figure 1.1).³

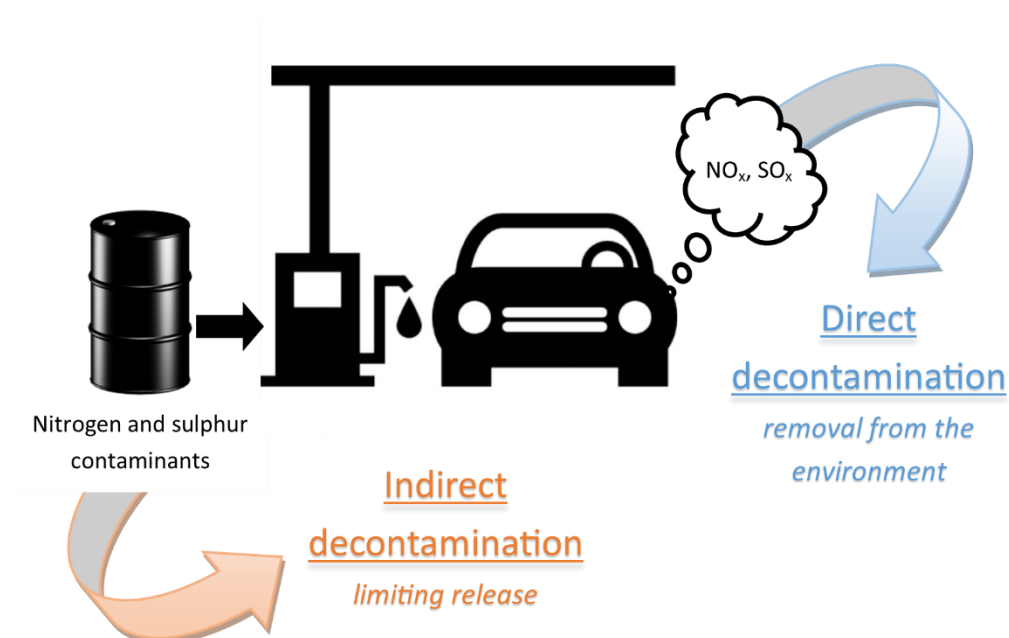


Figure 1.1. Schematic diagram highlighting direct and indirect decontamination approaches. The indirect route involves the desulphurisation and denitrogenation of fuel which prevents the release of toxic gases when combusted. If released, these toxic gases require a direct decontamination strategy from the environment.

A direct strategy can be applied to the treatment of polluted water to remove heavy metals, biological agents or organic species like organophosphorus (OP) agents.⁴⁻⁶ Although critical work has been performed on developing new materials for onsite decontamination, minimising their initial release is preferential where possible, as it reduces the risk to the environment. This can be achieved by employing an indirect decontamination strategy, which destroys or removes the environmental contaminants before the toxic species are released into natural resources. This approach can be employed for treating stockpiles of chemical warfare agents (CWA) or the removal of organic species

from fuel which can result in the release of toxic gases such as SO₂, CO and NO_x during combustion.^{7, 8} Both strategies provide crucial abatement of environmental contamination and several mechanisms, materials and methods have been exploited. More specifically, there has been a steady growth in the application of nanomaterials towards enhancing environmental nanoremediation (Figure 1.2).

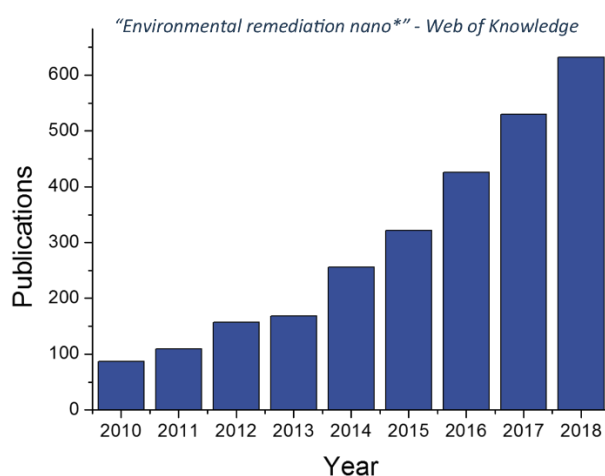


Figure 1.2. Growth of nanoremediation in the literature.

1.1. Nanoscale materials

The advancement of local probe characterisation techniques, such as electron microscopy, which can achieve near-atomic resolution, has propelled this area of research, providing key rationalisation of the impact of size, structure and different reactive surfaces on the activity of materials at the nanoscale.^{9, 10} Nanomaterials are defined as materials with a single unit size between 1-100 nm and have revolutionised numerous applied fields, including semiconductors, medicine, sensors and catalysis. Their small dimensions give nanomaterials higher total surface areas, interesting morphologies and unique chemical properties when compared with the bulk macroscale analogues.

Nanoscale materials are often easy to disperse and possess high mobility in solvents allowing large volumes of contaminated solutions to be quickly remedied with minimal amounts of materials.¹¹ The surfaces of nanomaterials are of particular interest due to the high density of low coordinated atoms at the surfaces and edges that grow exponentially with decreasing size of the nanoparticles (Figure 1.3).¹² The increased number of surface atoms, reactive edges and defect sites have a significant impact on their catalytic, photocatalytic and electronic abilities.¹³⁻¹⁶

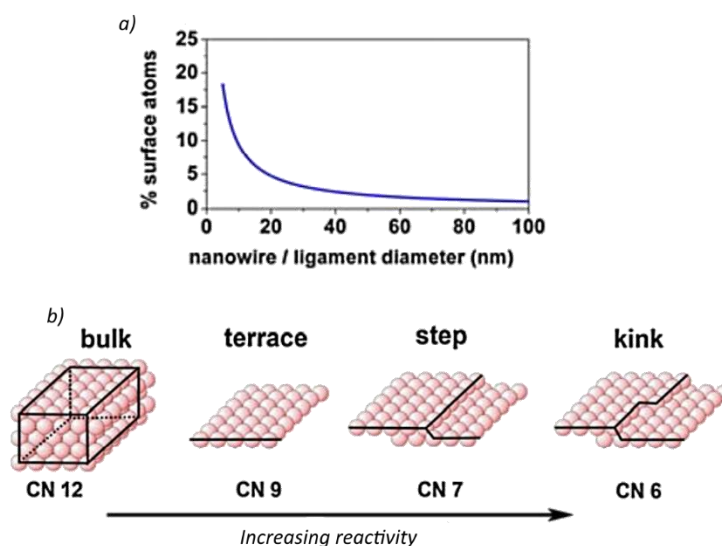


Figure 1.3. Nanomaterials with high surface-to-volume ratios lead to (a) increased surface atoms and (b) increased and more reactive surface edges. Adapted from Biener *et al*, copyright Molecular Diversity Preservation International.¹²

Interactions of the substrate to a nanomaterial surface can result in physical adsorption (due to non-covalent interactions with the surface) or chemical adsorption when bonds are formed or modified.¹⁷ Decontamination can be achieved by the adsorbed species undergoing a chemical reaction with other species or by the effective adhesion at the heterogeneous surface. These can

result in the chemical transformation of the contaminant to reduce the toxicity or can allow for entrapment of the toxic species which removes it from the natural resource respectively (Figure 1.4).

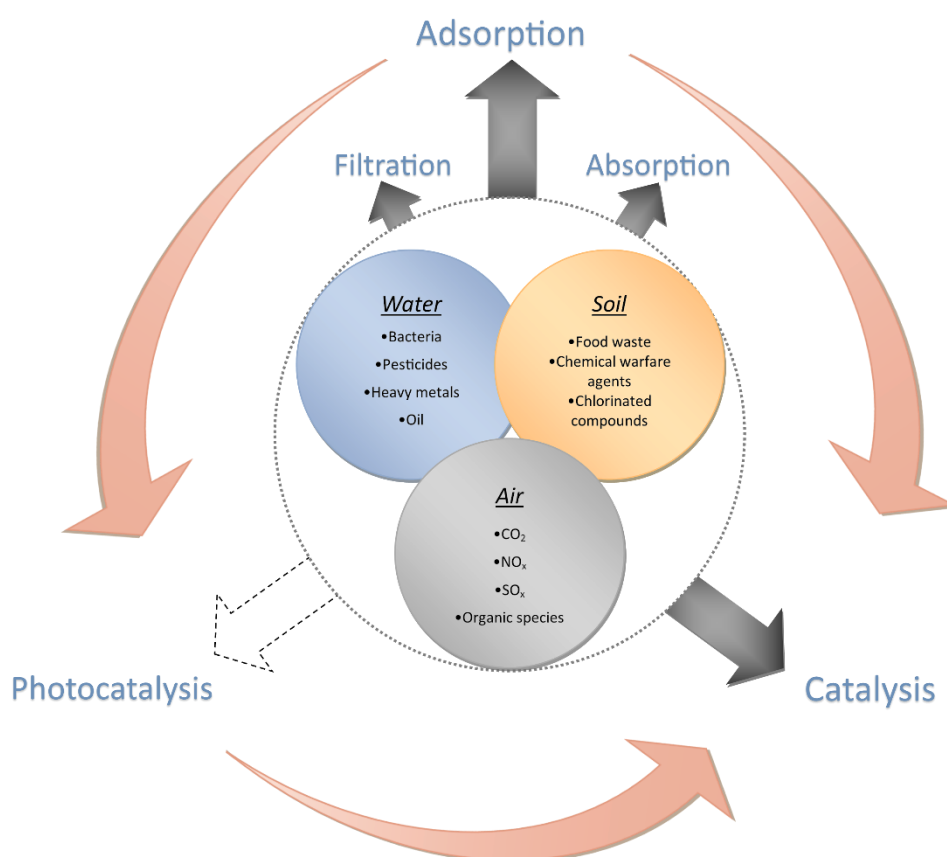
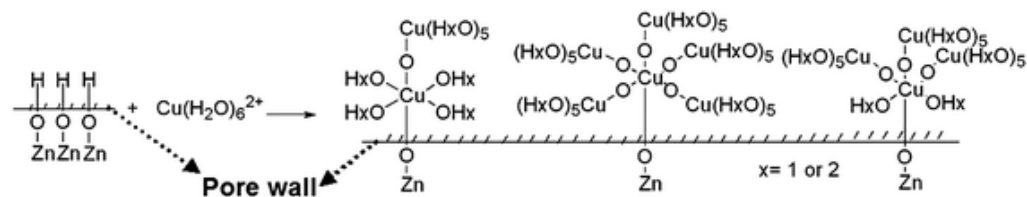


Figure 1.4. Environmental nanoremediation strategies.¹⁸

By exploiting only the adsorption interactions involving the adhesion of molecules (gases, liquids or dissolved solids) to a surface, contaminants can be removed from environmental media very effectively.¹⁹ This has shown promise towards gas filtering, water treatment, desulphurisation of fuel and chemical warfare agent adsorption (Scheme 1.1).^{20 21-23}



Scheme 1.1. The adsorption of toxic Cu(II) ions onto porous ZnO nanoplates. The hydrated Cu(II) reacts with the hydroxyl groups and form Cu–O weak bonds through a Lewis interaction. Adapted from Wang et al, copyright The Royal Society of Chemistry.

24

Although activated carbons are widely implemented for several environmental remediation challenges harnessing adsorption, carbon nanotubes have shown much higher efficiency than activated carbons for sequestration of various organic compounds and heavy metals.^{25, 26} Both activated carbon and multi-walled carbon nanotubes with oxidised functional groups were applied to their abilities to remove heavy metals from water. Despite the activated carbon possessing a higher surface area, the curved nature of the nanotubes promoted active surface groups which could effectively remove over double the Ni²⁺ quantity from the solution compared to the activated carbon equivalent.²⁷ This work identifies that whilst maximising surface area is important, adsorption can depend on a number of surface features such as surface groups present. Other porous nanoscale materials, principally metal oxides such as MgO, CaO and TiO₂, have also been shown to readily adsorb polar organic compounds, including aldehydes and ketones, outperforming the activated carbon systems that are currently utilised.¹⁷

Once adsorbed to the surface of nanomaterials toxic species can be decontaminated by separation or can be chemically destroyed using catalysis and reactive species which are present or generated at the nanomaterial

surface.¹⁸ Nanomaterials have been broadly applied in catalysis and a significant foundation has been established for the size dependence of nanoparticles on their catalytic properties.²⁸ Catalysts can be generally divided into heterogeneous, where the phase of the reactants is different from the phase of the catalyst, or homogeneous where the reactants and catalyst are in the same phase. The lower effective concentration of the catalyst in heterogeneous catalysis is the result of the reaction only occurring at the exposed active surface and generally leads to lower catalytic activity.²⁹ However, nanoparticles which offer increased surface areas and possess maximised unsaturated surface atoms can readily interact with chemical species and overcome this issue, therefore, nanomaterials have been described as “semi-heterogeneous”.^{30, 31} The phase of the catalyst clearly has significant implications on the targeted reaction and therefore, there are several factors to consider when employing materials for catalysis (Table 1.2).^{32, 33}

Table 1.2. The characteristic properties of homogeneous, heterogeneous and nanoparticle catalysis.

	Homogeneous catalysis	Heterogeneous catalysis	Nanoparticle catalysis
Activity (rel. to metal content)	High	Variable	High
Selectivity to substrate/product formation	High	Variable	Variable
Reaction conditions	Mild	Harsh	Mild
Service life of catalyst	Variable	Long	Variable
Sensitivity to catalyst poisoning	Low	High	High
Diffusion problems (reactants reaching sites/products leaving)	None	Important	Important
Catalyst recovery	Hard	Easy	Relatively Easy

Deactivation of heterogeneous and nanoparticle catalysts represents a significant problem as it causes loss of catalytic activity over time. Catalyst decay varies dramatically as cracking catalyst deactivation can occur in seconds, whereas, ammonia synthesis iron catalysts can last for up to 10 years.³⁴ There are several mechanisms for catalyst decay and despite significant and ongoing research into this area to minimise deactivation, this issue will always remain inevitable (Table 1.3).³⁵

Table 1.3. Catalyst deactivation mechanisms

Mechanism	Type	Brief definition/description
Poisoning	Chemical	Strong chemisorption of species on catalytic sites which block sites for catalytic reactions
Fouling	Mechanical	Physical deposition of species from fluid phase onto the catalytic surface and in catalyst pores
Thermal degradation and sintering	Thermal Thermal/chemical	Thermally induced loss of catalytic surface area, support area, and active phase-support reactions
Vapor formation	Chemical	Reaction of gas with catalyst phase to produce volatile compound
Vapor–solid and solid–solid reactions	Chemical	Reaction of vapor, support, or promoter with catalytic phase to produce inactive phase
Attrition/crushing	Mechanical	Loss of catalytic material due to abrasion; loss of internal surface area due to mechanical-induced crushing of the catalyst particle

The prevention of catalyst deactivation can be achieved by insertion of traps or “getters” (which act as sacrificial reactants that preferentially adsorb the poison over the active metal) or by controlling the reaction conditions to decrease the effect of thermal degradation or sintering.^{36, 37} Catalyst regeneration is also feasible in some cases and can extend the lifetime of the catalysts but is often difficult when considering strongly adsorbed poisons or sintered catalysts and prevention is often recommended.³⁸

Catalyst recovery is also an important factor and with nanoparticles being a heterogeneous catalyst the ease of separation of the catalysts after the reaction and their long catalytic lifetimes make them more economical for industrial processes when compared to homogeneous catalysts.^{39, 40} Nanomaterials appear to bridge the two traditional classes of catalysis and drives materials which possess the activity and selectivity of homogeneous catalysts but recoverability and lifetimes of heterogeneous catalysts. These features are crucial for environmental remediation as removing the toxic species and catalyst from the environment effectively and efficiently is desirable from a safety and economical aspect.

Chemical destruction by catalysis represents one of the most widely employed decontamination pathways as it promotes the formation of species that can neutralise the toxic components by nucleophilic substitution, oxidation or reduction.⁴¹ Chemical destruction methods using nanomaterials have included H₂O₂ oxidation, photocatalytic degradation, supercritical water oxidation, electrochemical methods and enzymatic treatment methods.⁴²⁻⁴⁴

Reactive species that facilitate chemical destruction can be generated in multiple ways. The first route requires an initiator which interacts with the metal oxide at the surface to form a reactive species which can readily attack the contaminant species. Using peroxides, ozone and peroxymonosulfates generate oxygen, hydroxide or sulfate radicals, which act as very powerful oxidants for harmful species (Figure 1.5).^{4, 45-49} This method has shown effectiveness in oxidative desulphurisation of fuel or ozonolysis of organic dyes

and bacterial disinfection. However, it does require the presence of excess quantities of reagents and often harsh conditions to facilitate the degradation which is not suitable for large-scale decontamination.⁴¹

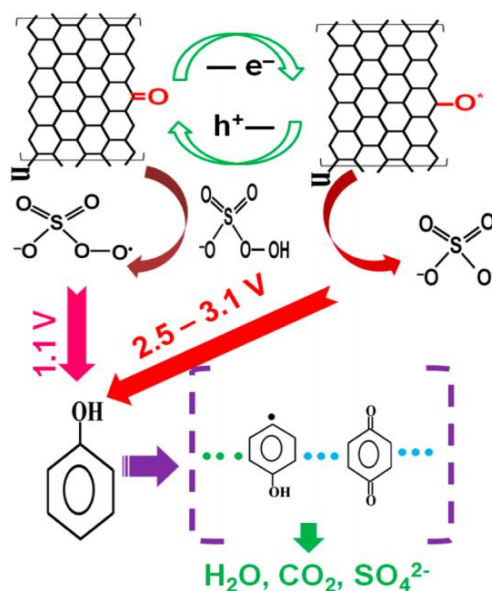
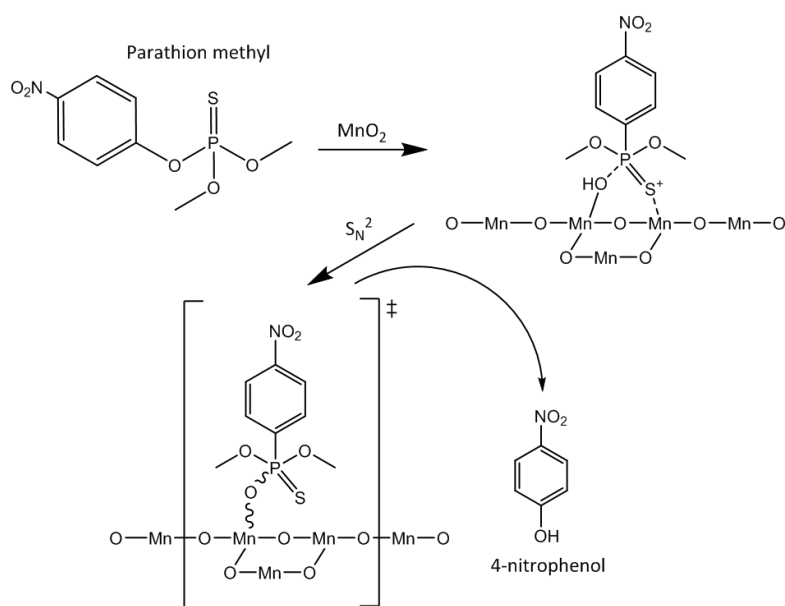


Figure 1.5. Schematic diagram for the catalytic oxidation of organic pollutants. Reduced graphene oxide was found to effectively activate peroxydisulfate to produce sulfate radicals ideal for the oxidation of phenol, 2,4-dichlorophenol and other dyes. Reproduced from Sun et al, copyright Elsevier B.V.⁴⁹

Surface groups such as hydroxides or alcohol groups provide destruction due to an attack via an SN_2 mechanism which neutralises the toxic component (Scheme 1.2).^{5, 50}



Scheme 1.2. Proposed reaction mechanism for the hydrolysis degradation of organophosphorus species involving the adsorption and corresponding destruction as a result of the hydroxyl groups on the surface of manganese oxide. Adapted from St'astny et al, copyright Springer.⁵⁰

This mechanism is often employed in the hydrolysis of organosulphur and organophosphorus agents used in chemical warfare agents and agriculture.⁵¹ In theory, this route requires only the nanomaterials during decontamination making it very applicable to real-world situations, however, loss of the surface groups results in a decrease in catalytic ability, therefore, maximising or regeneration of the surface groups is required.

Finally, reactive species can be generated by a photocatalytic mechanism. The absorption of photons enables the generation of radical species which can very effectively destroy the adsorbed organic species (Figure 1.6).⁵² One issue with photocatalysis is the use of dopants and precious metals are often required to allow absorption of a photon in the visible region.⁵³ These dopants can block

the active adsorption sites which decrease the adsorptive and catalytic ability of the surface.

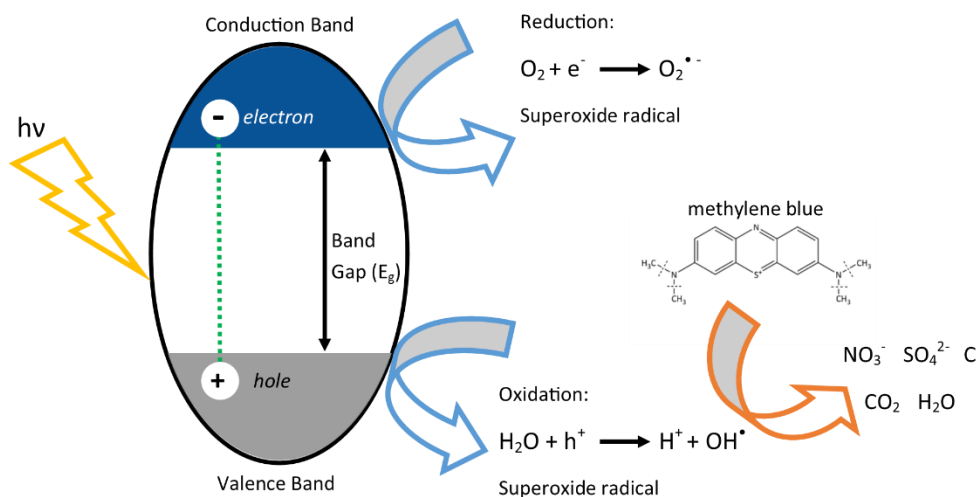


Figure 1.6. Schematic diagram of the photocatalytic mechanism and corresponding generation of reactive species. The $\bullet\text{OH}$ radical attacks methylene blue to degrade the dye.^{54, 55}

By first adsorbing the toxic species to a catalytic surface the rate of decontamination is less dependent on the rate of a chemical reaction and relies more on the contaminant-surface combination.¹⁷ This often results in enhanced catalysis as, once adsorbed, the reaction with active surface groups or radical species is rapid and leads to effective neutralisation of the toxic species.⁵⁶ This mechanism has shown effectiveness for the decontamination of organic contaminants, common air pollutants, chemical warfare agents, pesticides or solvents from industry.^{57, 58}

One class of nanoscale materials which has shown significant promise towards decontamination using these approaches is nanoscale metal oxides. Their stability, cost, low toxicity and versatility have resulted in them being employed to address many environmental challenges.^{59, 60}

1.2. Metal oxide nanomaterials for nanoremediation

Metal oxides have become an essential component for several applications due to their large range of properties, and therefore, many catalysts utilised in the chemical and petrochemical industries employ metal oxides as an active catalyst, promotor or support.^{39, 61}

Their catalytic properties are governed by the surface imperfections, and as these materials approach the nanoscale their properties can change significantly.²⁸ The increased surface area and surface atoms present on nanomaterials results in more reactive edges, corners and vacancies which are responsible for the reactivity of the surface.⁶² Nanoscale metal oxides thus represent an ideal candidate for targeting environmental remediation challenges due to them possessing adsorptive and reactive properties towards contaminants.⁶³⁻⁶⁵

Although alkali earth and main group metal oxide nanomaterials, such as Al_2O_3 , CaO , MgO , have shown significant promise for the adsorption of harmful chemicals, including chemical warfare agents, nanoscale transition metal oxides offer additional advantages, specifically tuneable photocatalytic and redox properties which prove critical for the generation of reactive species during chemical destruction.⁶⁵⁻⁶⁹

Significant work has been performed on nanoscale metal oxides and their catalytic abilities, an overview of these materials and their effects towards environmental remediation is shown below (Table 1.4).

Table 1.4. Overview of transition metal oxide nanomaterials and their properties towards environmental remediation.

Metal oxide	Structure and composition	Decontamination mechanism	Application - Targeted contaminant	Comments	Ref
TiO ₂	Nanotube (d = 5 nm)	Hydrolysis	CWA decontamination – Mustard and nerve agents	Unique morphologies resulted in the nanotubular TiO ₂ hydrolysing organophosphorus agents an order of magnitude faster than bulk anatase TiO ₂ .	70
	Nanoparticles (8.3 nm)	Adsorption	Heavy metal removal – Pb, Cd, Cu, Zn and Ni	Nanoparticles had large adsorption capacities due to their increased surface area, the nanoparticle adsorption rates were 5 times greater than the bulk. They were able to outperform Fe ₃ O ₄ NP and activated carbon.	71
	Cu-doped TiO ₂ NP (26 nm)	Photocatalytic oxidation	Biological disinfection – Escherichia coli	Doping shifts optical absorption edge into the visible region to generate reactive oxygen species that could destroy bacteria in sunlight.	72
MnO ₂	TiO ₂ nanofibres (d = 200 nm)	Photocatalytic oxidation	Air purification – NOx and toluene decomposition	Fibrous and porous structures led to large surface areas for adsorption and decomposition. Minimal agglomeration when compared to nanoparticles also maximised effectiveness.	46
	Cobalt oxide doped nanoparticles (50-100 nm)	Oxidation	Desulphurisation of fuel – organosulphur compounds	Co dopants sharply increased catalysis due to increased defects in the surface structure, significant amounts of Co led to blocked active sites and resulted in the reduction of activity.	73
	hierarchical hollow nanoparticles (300 nm)	Adsorption	Organic pollutants in water – Azo dye	90% of the organic dye could be removed which was shown to be 9 times higher than commercial MnO ₂ due to the hierarchical structure.	74
	Nanobelts (w = 15-25 nm)	Hydrolysis	CWA decontamination – Mustard and nerve agents	Nanobelts provide increased surface area and enhanced chemical reactivity for adsorption and hydrolysis of CWA agents.	75

Table 1.4. (Continued).

Metal oxide	Structure and composition	Decontamination mechanism	Application - Targeted contaminant	Comments	Ref
Fe ₂ O ₃	Nanoparticles (50 nm)	Adsorption	Heavy metal removal - Mo	Increased hydroxyl groups on the surface led to effective adsorption capabilities (33.4mg/g) and magnetic separation provided simple removal.	76
Co ₃ O ₄	Nanorods (w= 5-15 nm)	Hydrogenation	Desulphurisation of fuel – carbonyl sulphide	Rod morphologies led to the exposure of specific crystal planes of the metal oxide which played an important role in presulfurisation and consequent catalytic performance.	77
ZnFe ₂ O ₄	Nanorods (°d= 60 nm)	Photocatalytic oxidation	Organic pollutants in water – Brilliant Red M5B (dye)	Nanorods exhibited enhanced catalytic efficiency ascribed to high surface area, a relatively larger band gap and better delocalization of the charged species when compared with nanoparticles or nanoflowers.	78
	Nanosheets	Adsorption	Heavy metal removal – Pb	Shown good sorption capacities for Pb ²⁺ (6.7mg/g) due to increased surface hydroxyl groups.	79
ZnO	Nanorods (°d = 100-500 nm)	Hydrolysis	CWA decontamination – Mustard agents	The increased surface area of the nanorods facilitates the adsorption, followed by surface hydroxyl groups which decontaminated the toxic agents. These results are comparable with nanosized MgO and Al ₂ O ₃ .	80
	Nanoparticles (100-800 nm)	Oxidation	Biological disinfection – Staphylococcus aureus and Escherichia coli	Antibacterial activity increases with decreasing particle size due to enhanced H ₂ O ₂ formation from the surface.	81
	Nanoparticles (27 nm)	Oxidation	Organic pollutants in water – Trichlorophenol	Rate of oxidation was enhanced three-fold by employing nanosized, compared to micro-sized catalysts. The increase was attributed to increased surface area and surface charge.	82

Table 1.4. (Continued).

Metal oxide	Structure and composition	Decontamination mechanism	Application - Targeted contaminant	Comments	Ref
ZrO ₂	Nanoparticles (70 nm)	Photocatalytic oxidation	Organic pollutants in water – Methylene blue	Although the monoclinic crystal structure was effective, the tetragonal structure showed poor photocatalytic activity towards decontamination due to oxygen vacancies and defect sites which led to a high recombination rate.	⁸³
CeO ₂	Ce _{1-x} Zr _x O ₂ (>20 nm)	Adsorption	Air purification – NO ₂ absorption	Mixed oxides show a better NO ₂ adsorption capacity than the parent materials. This effect is linked to the presence of reduced cerium and oxygen vacancies induced by the addition of Zr ⁴⁺ cations to the structure.	⁸⁴
	Nanoparticles supported on Alumina (<6 nm)	Hydrolysis	CWA decontamination – nerve agent	775 µmol/g of OP to the catalyst could be decontaminated at ambient temperature due to highly dispersed active domains capable of adsorbing increased contaminants.	⁸⁵
	Nanorods (°d = 10 nm)	Oxidation	Desulphurisation of fuel – Organosulphur	Deep desulphurisation could be achieved due to amphiphilic properties and oxygen defects of the nanocatalyst.	⁸⁶
WO ₃	Nanoparticles (9-47 nm)	Hydrolysis	CWA decontamination – Mustard and nerve agents	Both agent types reacted with isolated hydroxyl and Lewis acid sites to form bound species which were hydrolysed by surface groups. Smaller as-prepared NP performed better than larger annealed NP.	⁸⁷
	Nanowires (°d = 10 nm)	Photocatalytic oxidation	Organic pollutants in water – Methyl orange	Monoclinic crystal structures showed more photo-efficiency than hexagonal crystal structures. Nanowires outperform nanoparticles regarding photocatalytic activity due to their better charge carrier abilities and higher surface area.	⁸⁸

°d) external diameter, ⁱd) Internal diameter w) width.

From the literature, there appear to be distinctive attributes of nanoscale metal oxides that provide enhancement towards decontamination reactions (Figure 1.7). As a result, these factors should be considered when developing new materials for environmental remediation.

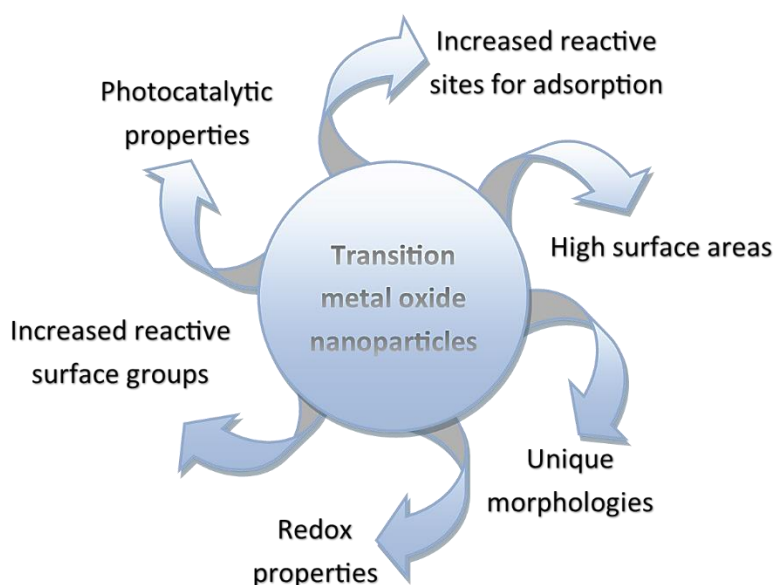


Figure 1.7. Intrinsic properties of transition nanoscale metal oxides for decontaminating environmental contaminants.⁸⁹⁻⁹¹

These properties appear to be controllable by changing the physical and chemical properties of the nanomaterials and result in dramatic effects on the catalytic abilities. Therefore, modifications in size, morphology, surface structure and composition of nanoscale metal oxides will be explored in more detail.

1.2.1. Size modification

The size-function relationship of metal oxides is crucial for the design of new nanomaterials as catalytic performance has been shown to increase dramatically with decreasing nanoparticle diameter. When comparing micro

(27.6 μm), submicron (0.46 μm) and nanosized (31 nm) nanoparticles towards the oxidation of trichlorophenol (TCP) there was a clear relationship on size and rate of catalysis (Table 1.5).⁸² The area, low coordination sites and charge of the surface were maximised at the nanoscale and were attributed to the far superior performance of the nanoscale ZnO.

*Table 1.5. Physical properties for different sized ZnO particles and their respective rate constants for the total removal of TCP during catalytic oxidation.*⁸²

	Size (nm)	External surface area (m^2/g)	Rate constant (min^{-1})
Micro-ZnO	27600	23.6	0.09
Submicro-ZnO	460	40.1	0.13
Nano-ZnO	31	52.7	0.24

Similar effects were seen for TiO_2 nanoparticles (8.3 nm) in the adsorption of heavy metals.⁷¹ For all the contaminant metals tested, the nanoparticles adsorbed more metal at the same sorbent concentration than the bulk particles (329 nm), with the Cd requiring a 5-fold increase of the bulk loading to achieve what the nanoparticles could remove (97.8%). Although impressive, the difference in removal is not particularly reflective of the significant decrease in the particle size and the expected increase in the surface area. This was also shown for Co_3O_4 nanoparticles which catalysed the ozonation of phenol for wastewater treatment. Decreasing nanoparticle size from 70nm to 19nm showed a slight improvement of catalysis due to the higher surface areas and improved dispersibility, which could achieve 84% to 90% degradation of phenol respectively (Figure 1.8).⁹² Despite this dramatic decrease in diameter

by a factor of 3.7, the catalyst activity doesn't reflect this significant change. This could suggest that although surface area does have an impact on reactivity, more focus should be dedicated to changing other attributes of the metal oxide which may induce more of a catalytic effect at the nanoscale.

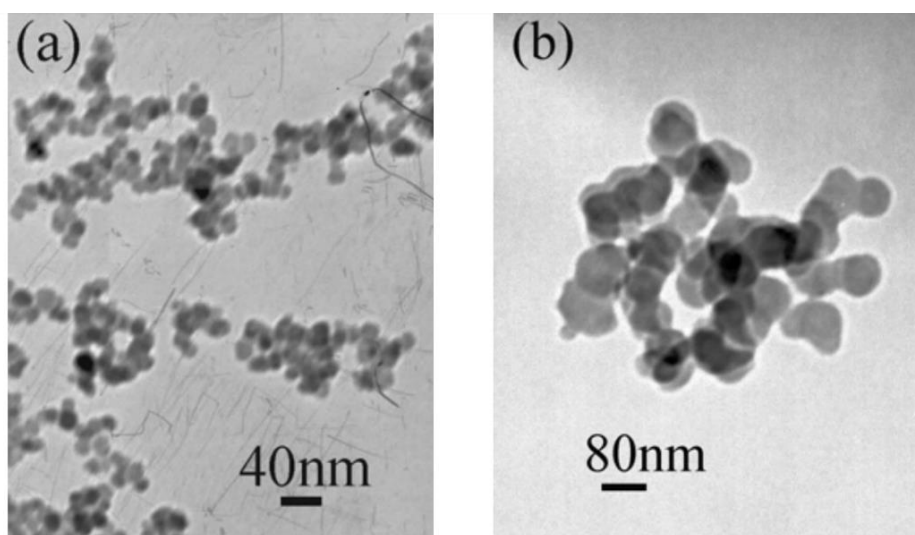


Figure 1.8. TEM images of Co₃O₄ nanoparticles with diameter (a) 19nm and (b) 70nm, which were applied for the catalytic ozonation degradation of phenol. Reproduced from Dong et al, copyright IOP publishing.⁹²

1.2.2. Morphology modification

Previous work has supported that there is a dependency between the surface reactivity and morphology of the metal oxide species. Unique and interesting morphologies of nanoscale metal oxides are continuously emerging and their enhanced surface properties towards catalytic reactions have been investigated. ZnFe₂O₄ nanoflowers which are composed of flaky morphologies assembled in a floriated manner introduces numerous pores and high surface areas (Figure 1.9).⁹³ As a result, the Fe³⁺ sites are more exposed which maximised adsorption of heavy metal ions.⁷⁸

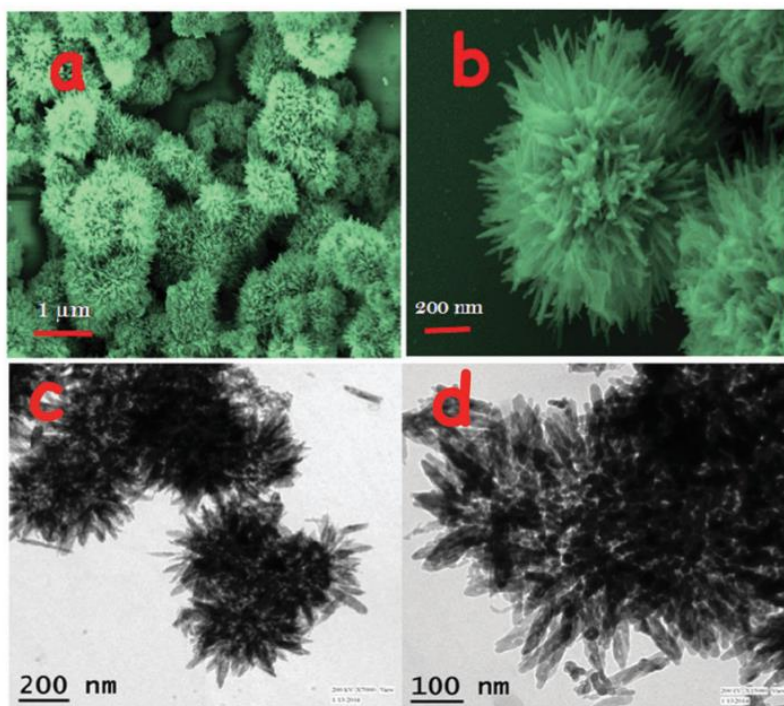


Figure 1.9. SEM and TEM of ZnFe_2O_4 nanoflowers which show promise in catalysis and sensing applications. Reproduced from Sahoo et al, copyright The Royal Society of Chemistry.⁹⁴

Co_3O_4 nanocrystals with different morphologies were applied to the hydrodesulphurisation of carbonyl sulphide.⁷⁷ It was shown that the catalytic activity of the nanorods was much higher than the nanopolyhedra structure. This was attributed to the more exposed (110) crystal plane which possessed a higher concentration of Co^{3+} which could facilitate the increase hydrodesulfurization at lower temperatures when compared to the nanopolyhedra surface (Figure 1.10). The ability to maximise active planes and increased reactive sites as a result of unique morphologies at the nanoscale can clearly have a significant impact on catalytic ability.⁹⁵

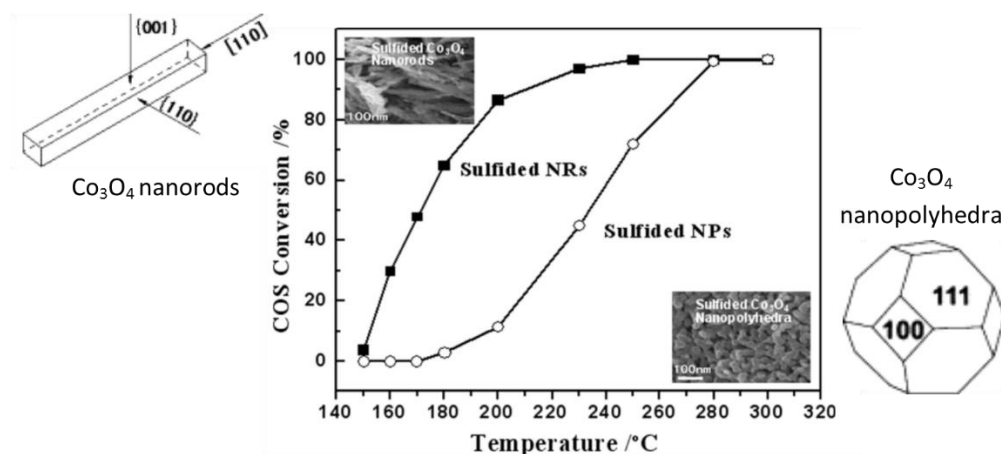


Figure 1.10. Carbonyl sulphide conversion during hydrodesulphurisation using different morphologies of Co_3O_4 nanocatalysts and schematic representations of their corresponding exposed crystal planes. Adapted from Wang et al, copyright Elsevier B.V.⁷⁷

The morphology and phase of the nanoscale WO_3 were also shown to be important as the hexagonal WO_3 nanowires could outperform hexagonal WO_3 nanoparticles by almost a factor of 3 for the decontamination of methyl orange. Despite the monoclinic phase being known as a better photocatalyst, the hexagonal phased nanowires outperformed the monoclinic phase due to their high aspect ratio which could promote more enhanced carrier transport and suppress recombination.⁸⁸

Nanobelt morphologies of MnO_2 promoted the hydrolysis of toxic organophosphorus and organosulphur agents. Although this nanomaterial was on par or outperformed by other metal oxide species, it was the interesting morphology of the sheet-like structure that provided enough surface area to maximise intercalated water, isolated surface hydroxyl groups and Lewis acidic sites that facilitated effective adsorption and decontamination.⁷⁵ Similar observations were made for TiO_2 and V_2O_5 nanotubular structures as they

proved very effective towards the decontamination of chemical warfare agents. This was attributed to the increased Lewis acid sites and large surface area formed as a result of the curved nanotube structure which showed an 8-fold enhancement when compared with the TiO₂ nanocrystals. Despite having identical mechanisms of decontamination the half-lives of the organophosphorus agents with these nanotubes were measured at 5.99 and 6.30 h⁻¹ for TiO₂NT and V₂O₅NT, respectively.^{96, 97} The TiO₂NT had an external diameter of around 10 nm compared to the larger 50 nm diameters for the V₂O₅NT, therefore, the decrease in total surface area may be a factor in the reduced hydrolysis. This increase in size also results in a decrease in curvature of the tubular metal oxide surface which could also reduce the reactivity of the surface sites or groups. The availability and activity of the surface active groups (such as hydroxyl groups) were shown to be crucial for the efficient hydrolysis of both organophosphorus and organosulphur agents, therefore, the change in curvature also plays a key role in the enhanced hydrolysis.⁹⁶ It is clear from many studies that by forming unique morphologies, defects and edges can be introduced which provide effective sites for adsorption. There also seems to be a strong influence of the composition and structure of these surfaces which can promote destruction.

1.2.3. Composition and surface structure

The increased concentrations of oxygen vacancies, reactive Lewis acidic and basic sites has been shown to be essential to the catalytic reactivity of metal oxide surfaces. This was further shown by introducing copper into ceria

nanoparticles (0-20mol%) which provided optimum oxygen vacancies and reactive defects sites into the nanostructure. As a result, activity toward methanol and ethylene incineration was strongly dependant on the composition and crystallite size. The importance of the composition was confirmed by doping ceria with zirconium cations towards toxic gas adsorption. Despite structural changes, no correlation was found between increasing pore volume with gas adsorption, and it was the chemical modifications which corresponded to a significant impact. The insertion of Zr^{4+} cations was found to promote the partial reduction of Ce^{4+} into Ce^{3+} and the formation of oxygen vacancies. The vacancies act as reactive sites which upon exposure to the NO_2 , lead to an electron transfer from the reduced ceria to the NO_2 molecule which leads to nitrites on the surface (Figure 1.11).⁸⁴

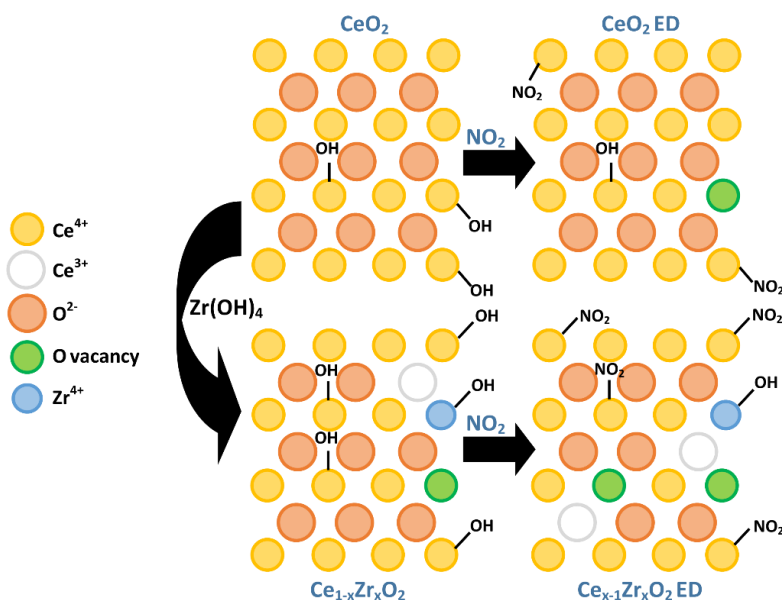


Figure 1.11. Increased oxygen vacancies and defects sites generated in a metal oxide structure due to insertion of dopant, highlighting the importance of defect sites on the adsorption of toxic species. Adapted from Levasseur et al, copyright American Chemical Society.⁸⁴

An increase in the OH groups on the ceria surface was also caused by the addition of the $Zr(OH)_4$ and reactions between these groups and NO_x species also lead to surface nitrite and nitrate species. Although it is not clear whether the reaction is carried out on the cerium or zirconium, the increased density of Ce^{3+} and OH groups on the surface were identified as responsible for the best performance in NO_2 adsorption. This work highlights that by changing the composition of the surface, interesting redox properties can be introduced in the metal oxides. At the nanoscale, the ease in reducibility and formation of oxygen vacancies of the metal oxides can be significantly increased which could provide enhanced decontamination abilities.⁹⁸

Iron (III) oxide has been shown to absorb organophosphorus agents at specific binding sites and the addition of the dopants was shown to disrupt the stoichiometry, causing disorder in the crystal lattice, which results in increased active sites present for decontamination.^{99, 100} Although individual metal oxides provided minimal hydrolysis, the doped-iron mixed oxides showed degradation efficiency approaching 70% for hydrolysis of OP contaminants.

A positive relationship between the surface hydroxyl group concentration on nanoscale TiO_2 and the rate of Mustard Gas hydrolysis has been reported.¹⁰¹

An increase in the concentration of the surface hydroxides corresponded to the half-life of the agent being decreased by a factor of 5 when employing nanocrystalline TiO_2 compared to the anatase bulk. Although the size of the nanoparticles could play a key role in this example, the decontamination abilities were attributed to the increased reactive surface groups present. The

importance of reactive sites on the surface for adsorption and consecutive destruction of contaminants has been identified, therefore, maximising these must be considered when developing new materials for this field.

Although dopants have been used to change surface properties, they are unable to control the size and morphology of the nanoparticles very effectively. Therefore, investigating a strategy in which all three can be simultaneously controlled is of great interest. Employing additional nanomaterials as supports allows unique nanomaterials to be templated on the surface and can result in electronic interactions which can enhance the catalytic surface. Therefore, metal oxide composites have emerged and more specifically, carbon nanomaterials have shown significant promise towards enhancing the abilities of nanoscale metal oxides.

1.3. Metal oxides and carbon composite nanomaterials

Carbon nanomaterials such as graphene, reduced graphene oxide (GO) and carbon nanotubes (CNT) possess small dimensions, high mechanical strength and exceptional electrical and thermal conductivity properties which makes them independently applicable to several applications (Figure 1.12).¹⁰²⁻¹⁰⁷ Exploiting their features for the formation of novel nanocomposites allows a new class of materials with synergistic properties.

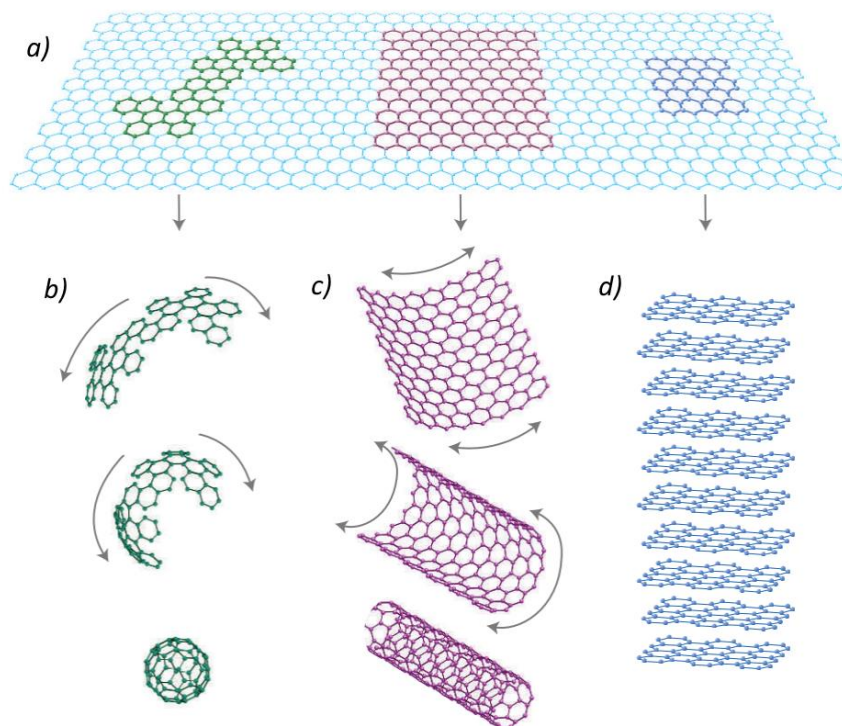


Figure 1.12. A schematic diagram showing the relationships between (a) graphene (b) fullerenes (c) CNTs and (d) graphene sheets. Adapted from Kong et al, copyright Elsevier B.V.¹⁰⁸

Graphene oxide (GO) is a two-dimensional crystal monolayer formed by the exfoliation of graphite which can be transformed into chemically reduced graphene oxide by various reduction techniques (Figure 1.13a).¹⁰⁹ This results in surface functionalisation with oxygen-containing groups which can be manipulated to change the electronic or optical properties such that they can be semiconductors or insulators depending on the degree of oxidation.¹¹⁰

Carbon nanotubes (CNT) consist of a layer or layers of sp^2 -hybridised carbon atoms in a sheet that are rolled into a cylinder. The simplest single walled carbon nanotube (SWNT) are narrow structures (with internal diameters of 0.7-2nm) which are only susceptible to functionalisation by some reagents, therefore, they remain unreactive towards most reaction conditions making

them suitable host materials.^{111, 112} Multi-walled nanotubes which consist of several concentric carbon nanotubes offer increased robustness and a diverse range of diameters (4-30 nm) which allows more control over the dimensions of the host/support compared to GO, which could result in the development of more precise nanoscale composites (Figure 1.13b).^{28, 113, 114}

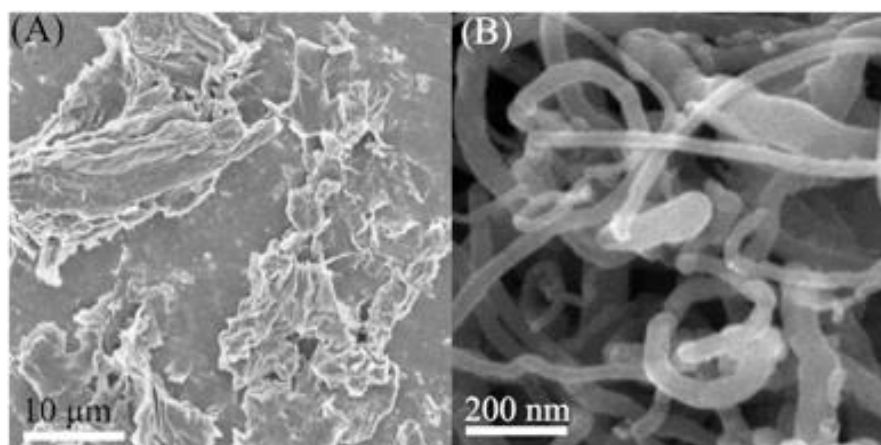


Figure 1.13. Scanning electron microscopy of (a) GO and (b) MWNT (outer diameter 10-30 nm). Reproduced from Ren et al, copyright The Royal Society of Chemistry.¹¹⁵

Graphene oxide and CNT has been widely employed for composite materials and the synthesis and fundamental interactions of metal oxide-carbon nanostructures have been the focus of significant work. Some successes of forming metal oxide-carbon nanocomposites towards environmental remediation are summarised below (Table 1.6).

Table 1.6. Overview of metal oxide-carbon composite nanomaterials and their properties towards environmental remediation.

Metal oxide	Carbon Support	Structure and composition	Decontamination mechanism	Application - Targeted contaminant	Comments	Ref
TiO ₂	GO	Nanorods (w < 5 nm)	Photocatalytic oxidation	Organic pollutants – dyes Antimicrobial	Composite achieved >95% degradation of acid orange dye compared to 70% of just the nanorods after 30 minutes. The composite effectively prevents the charge recombination during the photocatalytic process.	116
TiO ₂	MWNT	Nanoparticles (15 nm)	Photocatalytic oxidation	Organic pollutants	CNTs/TiO ₂ were able to enhance the degradation of methylene blue by 10 % compared to nanoparticles. Increased activities attributed to higher surface areas of nanoparticles formed, reduced recombination rates and shifts in Fermi level.	117
TiO ₂	MWNT	Nanoparticles (4-6 nm)	Photocatalytic oxidation	Organic pollutants – dyes	Confined nanoparticles inside the MWNT modified the physical and electronic structure of TiO ₂ which achieved a 24% enhancement compared to nanoparticles on the exterior.	118
MnO ₂	GO	Nanoflowers (50 nm in diameter with 2 nm pores)	Hydrolysis	CWA decontamination – Organophosphorus compounds	Near complete destruction was observed for the GO/MnO ₂ nanocomposite systems due to the increase of highly reactive sites at the edges or on the surfaces of carbon-based nanosheets.	119
FeOOH	GO	Nanorods (w = 15-30 nm)	Photocatalytic oxidation	Organic pollutants – dyes	Photocatalysis could be enhanced by 2.4-fold due to radicals increasing the presence of Fe ²⁺ compared to pristine FeOOH. Composites possessed excellent durability over 6 runs.	120

Table 1.6. (Continued)

Metal oxide	Carbon Support	Structure and composition	Decontamination mechanism	Application - Targeted contaminant	Comments	Ref
Fe ₂ O ₃	MWNT	Nanoparticles (50-100 nm)	Adsorption	Heavy metal – As	Composite increased high specific surface area and dispersibility and possesses good magnetic properties, allowing arsenic removal capacities of up to 47.41 mg/g and magnetic separation.	121
Co ₃ O ₄	GO	Nanoparticles (3-5 nm)	Hydrolysis	CWA decontamination – Organophosphorus compounds	A 5-fold enhancement could be achieved due to synergic effects of Co ₃ O ₄ and GO which improved the binding capacity of OP and water molecules and facilitated electron transfer in the hydrolysis process.	122
ZrO ₂	GO	Nanorods (w = 20-30 nm)	Adsorption	CWA decontamination – Organophosphorus compounds	Graphene sheets acted as a growth directing template for creating zirconia nanopatterns which were effective for the selective capture and efficient removal of nerve agents.	123

GO – reduced graphene oxide, MWNT – multi-walled carbon nanotube, w – width.

The exploitation of carbon hosts to control the size and morphology of the metal oxide can have promising effects toward catalysis. This was highlighted by the formation of iron hydroxide nanorods that were anchored on graphene oxide (GO).¹²⁰ By exploiting the oxygen groups on the graphene oxide surface and electrostatic interactions, small nanorods with diameters of 15–30 nm could be achieved. The carbon support was found to act as a template to induce exclusive physical properties. GO also modified the redox properties of the Fe centre allowing efficient reduction and generation of reactive species during decontamination of organic compounds.

The combination of TiO₂ on GO sheets were also shown to possess enhanced guest-host interactions as these composites resulted in significant photoluminescence quenching of the TiO₂ which indicates a strong charge transfer between these components. This led to the improved photocatalytic abilities due to the effective prevention of electron-hole charge recombination in the metal oxide which can maximise the radical species generated. As a result, increased photocatalytic degradation of dyes and antibacterial activity of the composite compared to bare TiO₂ nanorods was observed.¹¹⁶

MnO₂ nanoflowers on GO were also applied for OP agent hydrolysis, where the nanocomposites exhibited enhanced adsorptive degradation abilities compared to pure manganese oxide (MnO₂) and GO.¹¹⁹ The synergistic effects of the composite material improved degradation efficiency as GO allowed for effective adsorption followed by degradation by hydrolysis provided by the manganese oxide component. (Figure 1.14a,b). Interestingly, significant

amounts of the GO in the nanocomposites decreased their degradation activity substantially as a result of the metal oxide active sites becoming inaccessible (Figure 1.14c,d).

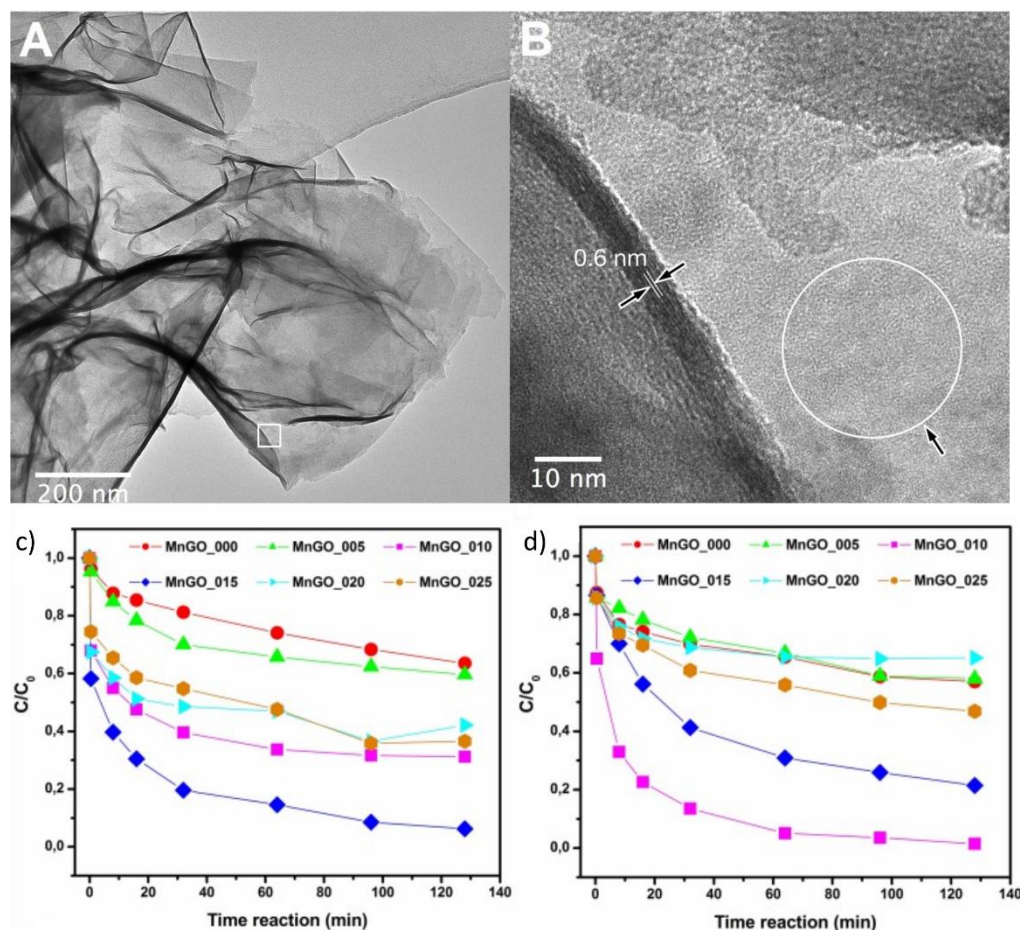


Figure 1.14. (a) and (b) TEM of MoO₂ nanoflower-graphene oxide nanocomposite (MnGO_10). Kinetic profiles for decontamination of different GO loading composites against the hydrolysis of OP simulants (c) dimethyl methyl phosphonate and (d) triethyl phosphate. Reproduced from St'astny et al, copyright Elsevier B.V. ¹¹⁹

This highlights that although these composites can enhance the catalytic abilities of the metal oxide, there appears to be a fine balance between active component and support that must be considered when engineering new materials. Despite the significant number of metal oxides which have shown promise towards environmental remediation titanium, iron and zinc oxides are

prominently used to form metal oxide composites with carbon nanotubes.¹²⁴⁻¹²⁷ In these cases, their photocatalytic abilities, magnetic properties and sensing applications are exploited respectively with little investigation of how the unique sizes, morphologies and compositions of the guest metal oxide might affect other decontamination pathways. Increasing surface area, dispersibility and enhancing reactivity was observed when forming composite nanomaterials with carbon nanotubes.^{117, 121, 128} For this carbon support, further improvements of the decontamination abilities could be achieved by manipulating the location of the nanoparticles, as TiO₂ nanoparticles on the inside of the nanotubes were found to have impressive photocatalytic abilities due to the confinement of the catalysts compared to external (non-confined) species (Figure 1.15).¹¹⁸

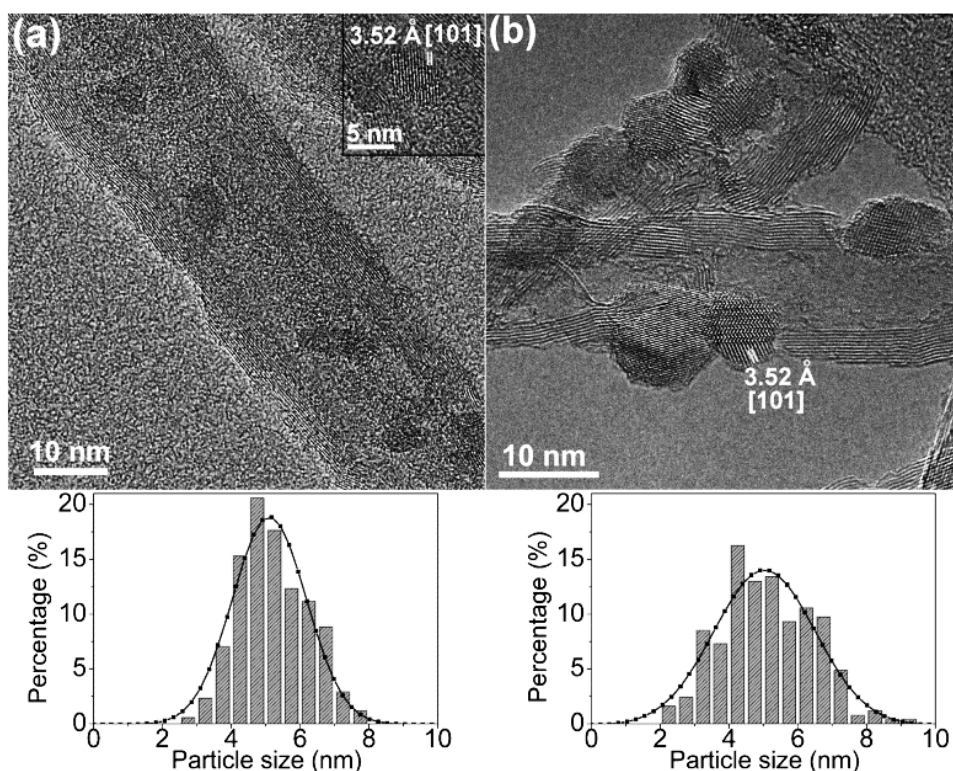


Figure 1.15. TEM and particle sizing distributions for TiO_2 nanoparticles (a) inside and (b) outside carbon nanotubes. Encapsulation is shown to influence the nanoparticle size and was also shown to enhance the degradation of methylene blue by 24%. Reproduced from Chen et al, copyright American Chemical Society. ¹¹⁸

Despite this interesting work, carbon nanotube-metal oxide composites for environmental remediation have been limited to externally located nanomaterials and have focused on the photocatalytic enhancement of the composites. The confined internal channel represents an underexplored catalytic surface for depositing metal oxide catalysts and may induce smaller sizes, interesting morphologies and surface compositions of these metal oxide nanomaterials compared to GO and could promote improved adsorption and chemical destruction effects.

There appears to be significant scope for investigating the synergistic effects of confining metal oxide catalysts in restricted space and exploiting the effects of

spatial confinement inside carbon nanotubes to template the formation of novel nanostructures has drawn a lot of attention.^{128 129-132} For example, SWNT have been shown to template the formation of strictly linear oligomers of C₆₀ fullerene epoxides due to the restricted space available.¹³³ The formation of this product would not be possible by any other approach and demonstrated the control that spatial confinement can offer for the selectivity of product formation. This concept was further demonstrated by the fabrication of sulphur-terminated graphene nanoribbons (S-GNR) within the internal channel of SWNT. Synthesis of graphene nanoribbons, which are expected to offer promising electronic properties, has proved problematic; however, confinement of a tetrathiafulvalene precursor inside SWNT, followed by the application of a stimulus (electron beam or heat) provided an elegant way to form S-GNR@SWNT (Figure 1.16).¹³⁴

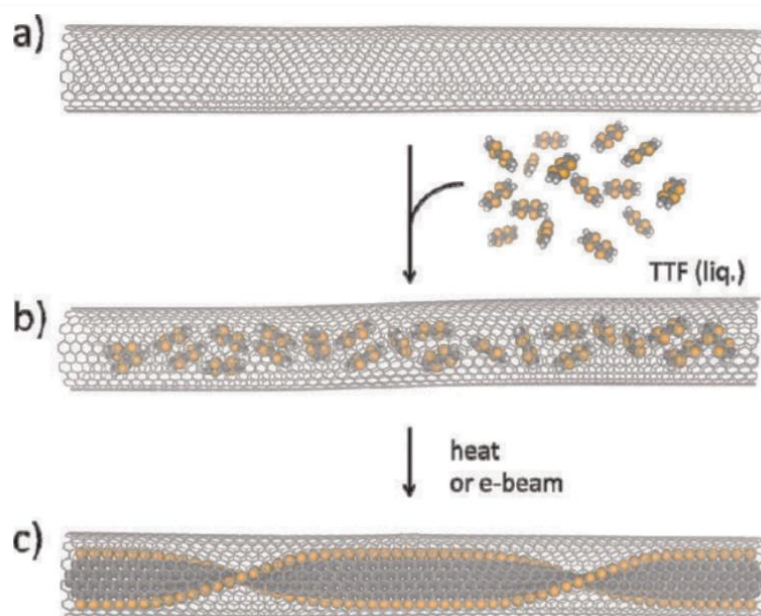


Figure 1.16. A schematic diagram detailing the synthesis of S-GNRs@SWNT (a) molten filling of tetrathiafulvalene (TTF) followed by (b) condensation of molecules inside the nanotube to afford the composite structure TTF@SWNT. (c) Upon thermal treatment under argon or e-beam irradiation in vacuum, the TTF molecules transform into sulphur-terminated graphene nanoribbons due to spatial confinement within the SWNT. Reproduced from Chamberlain et al, copyright American Chemical Society.¹³⁴

Increased surface energies may result in poor stability of the formed nanostructure, however, the nanocontainer may provide stabilisation of these reactive species.¹⁹ As well as hosts for nanomaterials, carbon nanotubes can also act as nanoreactors. This is the result of several favourable interactions in the confined system between the guest and host which can promote enhanced reactivity (Table 1.7).¹³²

Table 1.7. Effects of carbon nanoreactors on chemical reactions.¹³²

Interactions between nanoreactor and catalysts	Interactions between nanoreactor and reactants	Interactions between nanoreactor and products
Enhanced stability of the catalyst inside the porous cavity	Attractive interaction between internal cavity and reactant molecules leading to higher local concentrations and effective pressures	Restriction of reactive space inside the host favouring formation of one product over another
Electron transfer between the catalyst and interior surface of host altering the catalytic activity	Physical or chemical interactions between nanoreactor and reactants initiates reactions	Efficient transport of the product molecules from the nanoreactor to the bulk phase
	Alignment of the reactant molecules within the confined space facilitating reaction	

Favourable hydrophobic interactions with benzene have been previously shown to increase the reactant concentration within the nanotube cavity.^{135,}
¹³⁶ This leads to a high local concentration of reagents to catalyst which enhances catalysis rate and allows carbon nanotubes to act as nanoreactors. Interestingly, the unfavourable interactions with the products of this reaction (phenol) with the nanoreactor resulted in expulsion from the surface of the catalyst and further promoted catalysis (Figure 1.17).

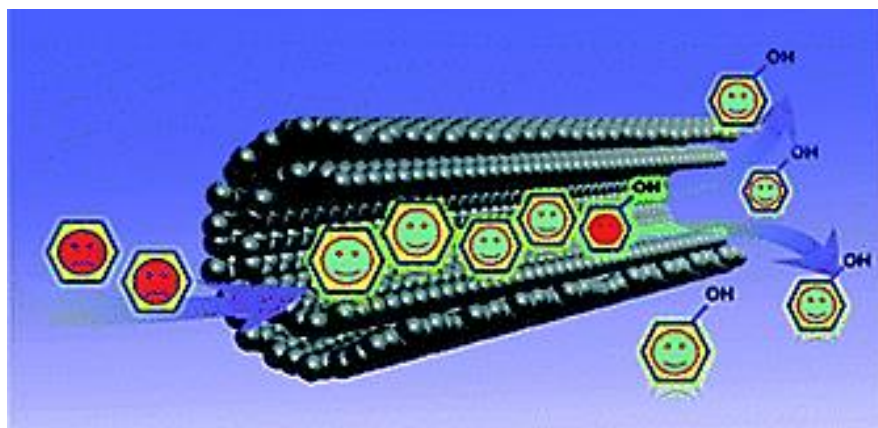


Figure 1.17. Schematic diagram demonstrating the hydrophobic enrichment effects of a carbon nanoreactor where the benzene reactant is drawn into the internal cavity to enhance local concentrations around the confined catalyst. Reproduced from Zhang et al, copyright Royal Society of Chemistry.¹³⁶

One issue with carbon nanoreactors originates from their small internal diameters which restricts the movement of reagent molecules and hinders diffusion due to extreme spatial confinement.¹³¹ To overcome this issue significant research has been completed supporting that carbon nanotubes with increased diameters (multi-walled carbon nanotubes or graphitised nanofibres) still promote the formation of unique confined catalysts but are also able to overcome transport resistance of reactants. Local concentration effects were shown to be a balance between the energy of encapsulation (E_e) and the mass transfer rate (k_c) of the reactants (Figure 1.18).¹³⁷ The interesting confinement effects of a graphitised nanofibre (GNF)(which possess internally corrugated surfaces), provided similar constraint environments to double walled carbon nanotubes (DWNT) but wider diameters which can facilitate rapid diffusion of the reagents into the internal cavity.

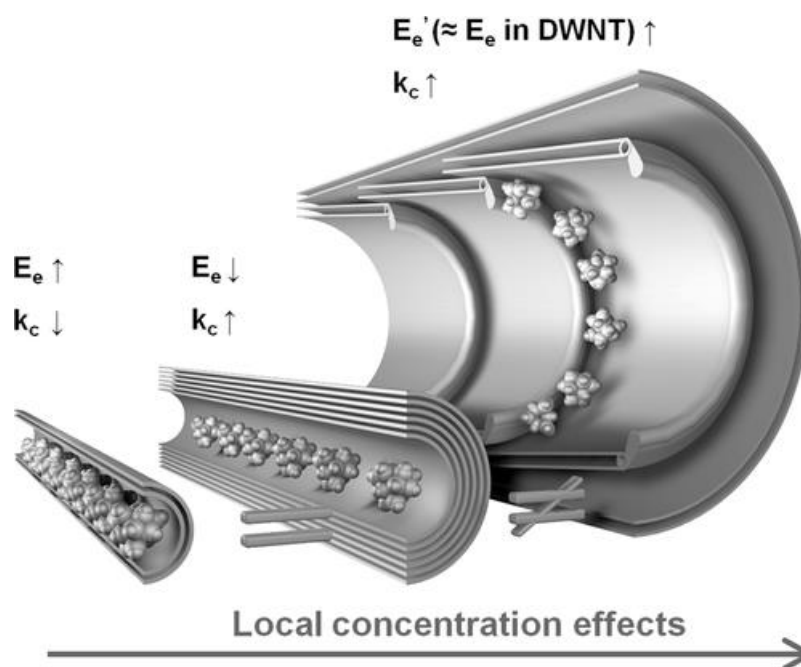


Figure 1.18. Schematic representation of the contrasting relative local concentration effects induced inside several carbon nanoreactors. The observed effects are the result of a balance between the energy of encapsulation in CNT (E_e) and encapsulation in GNF (E_e') with the mass transfer rate (k_c) of reactants. Reproduced from Solomansz et al, copyright Wiley-VCH.¹³⁷

This new breed of nanoreactors which exploit the valuable properties of the GNF have shown significant promise in the literature and improved rates and selectivity of reactions such as the Suzuki-Miyaura and hydrosilylation reactions.^{138, 139} For the Suzuki-Miyaura reaction Pd nanoparticles have been previously encapsulated in zeolites and multi-walled carbon nanofibres and have both shown selectivity towards certain cross-coupled products and negligible loss of catalytic activity even after 5 cycles.^{139, 140} Confinement is an effective way to protect and stabilise the catalytic nanoparticles and is useful for real-world applications as it adds a defensive layer to potentially toxic nanoparticles and minimises catalyst leaching into the environment.

Although the benefits for confining catalytic species inside carbon nanotubes has been established there is still a variety of guest and host species which can be investigated. Exploiting confinement effects with catalysts which have shown potential towards environmental remediation could offer new superior materials which can effectively and efficiently target contaminants.

1.4. Scope for further investigation

Nanoscale metal oxides have shown significant potential for several environmental remediation challenges. Their decontamination abilities can be controlled due to a structure-function relationship whereby changing the physical properties of the materials can enhance their reactivity. The ability to manipulate the size, morphology and surface composition can provide increased surface areas and reactive sites, new surface chemistry and novel electronic properties. These new features have led to impressive chemical reactivities that can maximise adsorption or destruction of harmful compounds. It would appear, therefore, that further enhancing the abilities of these nanomaterials is of significant interest and is motivating for the application of environmental remediation.

Forming metal oxide composite materials with carbon nanostructures offers another strategy for tuning the properties of the metal oxide as these support materials can template unique structures and can facilitate electron transfer between the guest and host species. Although nanoscale metal oxide-carbon

composites have shown promise towards the enhancement of the metal oxide surfaces, probing their abilities in confined space can offer other benefits.

Carbon nanotubes represent an attractive class of nanoscale reaction vessels that require only ubiquitous van der Waals interactions to drive the encapsulation of a broad range of molecules and nanoscale materials. Carbon nanotubes have been previously shown to be effective at controlling properties of guest species as they can template the formation of unique nanomaterials which cannot be formed by any other means. Encapsulation of catalysts has also led to a range of confinement effects which can help promote the enrichment of reactants inside the nanotube cavity and increase non-covalent interactions between the guest and host molecules.¹⁴¹ These effects result in carbon nanotubes being able to act as a nanoreactor which has led to impressive enhancement of the activity, selectivity and stability of catalysts towards reactions. Employing larger diameter multi-walled nanotubes provides the benefits of using carbon nanoreactors as well as reducing the potential problem of transport resistance.¹³⁹

The encapsulation of metal oxide nanoparticles inside carbon nanotubular structures offers an innovative approach to forming new architectures within confined space with modified functionality. Exploiting the confinement effects and non-covalent interactions with the nanotube host could allow the reactivity of these metal oxide catalysts to be further enhanced.¹⁴² The synthesis, modification and application of metal oxide-carbon nanotube composite materials, therefore, represents a motivating research challenge

which may offer the potential to improve destruction of toxic environmental contaminants.

1.5. References

1. P. Bardos, C. Merly, P. Kvapil and H. P. Koschitzky, *Remediation*, 2018, **28**, 43-56.
2. W. Gao and J. Wang, *ACS nano*, 2014, **8**, 3170-3180.
3. H. Maleki and N. Hüsing, *Appl. Catal., B.*, 2018, **221**, 530-555.
4. D. Shahidi, R. Roy and A. Azzouz, *Appl. Catal. B-Environ.*, 2015, **174**, 277-292.
5. Y. C. Yang, J. A. Baker and J. R. Ward, *Chem. Rev.*, 1992, **92**, 1729-1743.
6. L. Giovanni, M. Diego, L. Giusy, G. Marco, C. Maurizio, A. Francesco, C. Barbara and N. Michele, *Sci. Total Environ.*, 2018, **621**, 85-94.
7. V. C. Srivastava, *RSC Adv.*, 2012, **2**, 759-783.
8. G. S. Pearson and R. S. Magee, *Pure Appl. Chem.*, 2002, **74**, 187-316.
9. G. A. Somorjal and J. Carrazza, *Ind. Eng. Chem. Fundam.*, 1986, **25**, 63-69.
10. M. Che and C. O. Bennett, *Adv. Catal.*, 1989, **36**, 55-172.
11. A. Hatamie, H. Parham, B. Zargar and Z. Heidari, *J. Mol. Liq.*, 2016, **219**, 694-702.
12. J. Biener, A. Wittstock, T. F. Baumann, J. Weissmuller, M. Baumer and A. V. Hamza, *Materials*, 2009, **2**, 2404-2428.
13. O. Ola and M. M. Maroto-Valer, *J. Photochem. Photobiol. C-Photochem. Rev.*, 2015, **24**, 16-42.
14. R. Narayanan and M. A. El-Sayed, *J. Am. Chem. Soc.*, 2003, **125**, 8340-8347.
15. W. L. Zhu, R. Michalsky, O. Metin, H. F. Lv, S. J. Guo, C. J. Wright, X. L. Sun, A. A. Peterson and S. H. Sun, *J. Am. Chem. Soc.*, 2013, **135**, 16833-16836.
16. S. Navalon and H. Garcia, *Nanomaterials*, 2016, **6**, 3.
17. G. E. Fryxell and G. Cao, *Environmental applications of nanomaterials: synthesis, sorbents and sensors*, World Scientific, 2012.
18. F. D. Guerra, M. F. Attia, D. C. Whitehead and F. Alexis, *Molecules*, 2018, **23**, 23.
19. C. Santhosh, V. Velmurugan, G. Jacob, S. K. Jeong, A. N. Grace and A. Bhatnagar, *Chem. Eng. J.*, 2016, **306**, 1116-1137.
20. Y. C. Sharma, V. Srivastava, V. K. Singh, S. N. Kaul and C. H. Weng, *Environ. Technol.*, 2009, **30**, 583-609.
21. J. Bu, G. Loh, C. G. Gwie, S. Dewiyanti, M. Tasrif and A. Borgna, *Chem. Eng. J.*, 2011, **166**, 207-217.
22. S. B. Wang, H. Q. Sun, H. M. Ang and M. O. Tade, *Chem. Eng. J.*, 2013, **226**, 336-347.
23. W. C. Hung, J. C. Wang and K. H. Wu, *Appl. Surf. Sci.*, 2018, **444**, 330-335.
24. X. B. Wang, W. P. Cai, Y. X. Lin, G. Z. Wang and C. H. Liang, *J. Mater. Chem.*, 2010, **20**, 8582-8590.

25. T. J. Bandosz, *Activated carbon surfaces in environmental remediation*, Elsevier, 2006.
26. Y. T. Ong, A. L. Ahmad, S. H. S. Zein and S. H. Tan, *Braz. J. Chem. Eng.*, 2010, **27**, 227-242.
27. C. Y. Lu, C. Liu and G. P. Rao, *J. Hazard. Mater.*, 2008, **151**, 239-246.
28. G. A. Somorjai and B. Chaudret, *Nanomaterials in catalysis*, John Wiley & Sons, 2012.
29. S. Shylesh, V. Schunemann and W. R. Thiel, *Angew. Chem.-Int. Edit.*, 2010, **49**, 3428-3459.
30. S. Schauer mann, N. Nilius, S. Shaikhutdinov and H. J. Freund, *Acc. Chem. Res.*, 2013, **46**, 1673-1681.
31. D. Astruc, F. Lu and J. R. Aranzaes, *Angew. Chem.-Int. Edit.*, 2005, **44**, 7852-7872.
32. G. Rothenberg, *Catalysis: concepts and green applications*, John Wiley & Sons, 2017.
33. S. B. Singh and P. K. Tandon, *J. Energy. Chem. Eng*, 2014, **2**, 106-115.
34. M. D. Argyle and C. H. Bartholomew, *Catalysts*, 2015, **5**, 145-269.
35. C. H. Bartholomew, *Applied Catalysis a-General*, 2001, **212**, 17-60.
36. G. Jacobs, F. Ghadiali, A. Pisanu, C. L. Padro, A. Borgna, W. E. Alvarez and D. E. Resasco, *J. Catal.*, 2000, **191**, 116-127.
37. S. Jongpatiwut, P. Sackamduang, T. Rirksomboon, S. Osuwan, W. E. Alvarez and D. E. Resasco, *Applied Catalysis a-General*, 2002, **230**, 177-193.
38. D. L. Trimm, *Applied Catalysis a-General*, 2001, **212**, 153-160.
39. G. Ertl, H. Knözinger and J. Weitkamp, *Handbook of heterogeneous catalysis*, Wiley-VCH, Weinheim, 1997.
40. Q. Zhang and Y. D. Yin, *Pure Appl. Chem.*, 2014, **86**, 53-69.
41. M. M. Khin, A. S. Nair, V. J. Babu, R. Murugan and S. Ramakrishna, *Energy Environ. Sci.*, 2012, **5**, 8075-8109.
42. M. A. Tarr, *Chemical degradation methods for wastes and pollutants: environmental and industrial applications*, CRC Press, 2003.
43. D. Gandini, E. Mahe, P. A. Michaud, W. Haenni, A. Perret and C. Comninellis, *J. Appl. Electrochem.*, 2000, **30**, 1345-1350.
44. A. M. Klibanov, T. M. Tu and K. P. Scott, *Science*, 1983, **221**, 259-260.
45. D. E. Giammar, C. J. Maus and L. Y. Xie, *Environ. Eng. Sci.*, 2007, **24**, 85-95.
46. C. Srisitthiratkul, V. Pongsorarith and N. Intasanta, *Appl. Surf. Sci.*, 2011, **257**, 8850-8856.
47. S. Rengaraj and X. Z. Li, *J. Mol. Catal. A: Chem.*, 2006, **243**, 60-67.
48. D. H. Wang, E. W. H. Qian, H. Amano, K. Okata, A. Ishihara and T. Kabe, *Appl. Catal., A*, 2003, **253**, 91-99.
49. H. Q. Sun, S. Z. Liu, G. L. Zhou, H. M. Ang, M. O. Tade and S. B. Wang, *ACS Appl. Mater. Interfaces*, 2012, **4**, 5466-5471.
50. M. St'astny, V. Stengl, J. Henych, J. Tolasz, P. Vomacka and J. Ederer, *J. Mater. Sci.*, 2016, **51**, 2634-2642.

51. Y. J. Jang, K. Kim, O. G. Tsay, D. A. Atwood and D. G. Churchill, *Chem. Rev.*, 2015, **115**, PR1-76.
52. J. G. Yu and X. X. Yu, *Environ. Sci. Technol.*, 2008, **42**, 4902-4907.
53. S. Neatu, B. Cojocar, V. I. Parvulescu, V. Somoghi, M. Alvaro and H. Garcia, *J. Mater. Chem.*, 2010, **20**, 4050-4054.
54. M. Pelaez, N. T. Nolan, S. C. Pillai, M. K. Seery, P. Falaras, A. G. Kontos, P. S. M. Dunlop, J. W. J. Hamilton, J. A. Byrne, K. O'Shea, M. H. Entezari and D. D. Dionysiou, *Appl. Catal. B-Environ.*, 2012, **125**, 331-349.
55. B. Ahmed, S. Kumar, S. Kumar and A. K. Ojha, *J. Alloys Compd.*, 2016, **679**, 324-334.
56. K. Klabunde, D. Park, J. Stark, O. Koper, S. Decker, Y. Jiang and I. Lagadic, *Nanoscale Metal Oxides as Destructive Adsorbents. New Surface Chemistry and Environmental Applications*, Springer, Dordrecht, 1996.
57. S. P. Decker, J. S. Klabunde, A. Khaleel and K. J. Klabunde, *Environ. Sci. Technol.*, 2002, **36**, 762-768.
58. D. A. Reddy, R. Ma and T. K. Kim, *Ceram. Int.*, 2015, **41**, 6999-7009.
59. M. B. Gawande, R. K. Pandey and R. V. Jayaram, *Catal. Sci. Technol.*, 2012, **2**, 1113-1125.
60. J. Theerthagiri, S. Chandrasekaran, S. Salla, V. Elakkiya, R. A. Senthil, P. Nithyadharseni, T. Maiyalagan, K. Micheal, A. Ayeshamariam, M. V. Arasu, N. A. Al-Dhabi and H.-S. Kim, *J. Solid State Chem.*, 2018, **267**, 35-52.
61. S. D. Jackson and J. S. Hargreaves, *Metal Oxide Catalysis, 2 Volume Set*, John Wiley & Sons, 2009.
62. S. Utamapanya, K. J. Klabunde and J. R. Schlup, *Chem. Mater.*, 1991, **3**, 175-181.
63. N. Sharma and R. Kakkar, *Adv. Mat. Lett.*, 2013, **4**, 508-521.
64. T. H. Mahato, B. Singh, A. K. Srivastava, G. K. Prasad, A. R. Srivastava, K. Ganesan and R. Vijayaraghavan, *J. Hazard. Mater.*, 2011, **192**, 1890-1895.
65. G. K. Prasad, P. Ramacharyulu, B. Singh, K. Batra, A. R. Srivastava, K. Ganesan and R. Vijayaraghavan, *J. Mol. Catal. A: Chem.*, 2011, **349**, 55-62.
66. A. W. Khan, S. Kotta, S. H. Ansari, J. Ali and R. K. Sharma, *Def. Sci. J.*, 2013, **63**, 487-496.
67. G. W. Wagner, P. W. Bartram, O. Koper and K. J. Klabunde, *J. Phys. Chem. B*, 1999, **103**, 3225-3228.
68. G. W. Wagner, O. B. Koper, E. Lucas, S. Decker and K. J. Klabunde, *J. Phys. Chem. B*, 2000, **104**, 5118-5123.
69. G. W. Wagner, L. R. Procell, R. J. O'Connor, S. Munavalli, C. L. Carnes, P. N. Kapoor and K. J. Klabunde, *J. Am. Chem. Soc.*, 2001, **123**, 1636-1644.
70. G. W. Wagner, Q. Chen and Y. Wu, *J Phys Chem C*, 2008, **112**, 11901-11906.
71. K. E. Engates and H. J. Shipley, *Environ. Sci. Pollut. Res. Int.*, 2011, **18**, 386-395.
72. C. Karunakaran, G. Abiramasundari, P. Gomathisankar, G. Manikandan and V. Anandi, *J. Colloid Interface Sci.*, 2010, **352**, 68-74.
73. W. Mokhtar, W. A. W. Abu Bakar, R. Ali and A. A. A. Kadir, *Clean Technol. Environ. Policy*, 2015, **17**, 1487-1497.

74. J. B. Fei, Y. Cui, X. H. Yan, W. Qi, Y. Yang, K. W. Wang, Q. He and J. B. Li, *Adv. Mater.*, 2008, **20**, 452-456.
75. T. H. Mahato, G. K. Prasad, B. Singh, K. Batra and K. Ganesan, *Microporous Mesoporous Mater.*, 2010, **132**, 15-21.
76. A. Afkhami and R. Norooz-Asl, *Colloid Surf. A-Physicochem. Eng. Asp.*, 2009, **346**, 52-57.
77. X. Z. Wang, L. Ding, Z. B. Zhao, W. Y. Xu, B. Meng and J. S. Qiu, *Catal. Today*, 2011, **175**, 509-514.
78. M. Dhiman, R. Sharma, V. Kumar and S. Singhal, *Ceram. Int.*, 2016, **42**, 12594-12605.
79. X. Ma, Y. Wang, M. Gao, H. Xu and G. Li, *Catal. Today*, 2010, **158**, 459-463.
80. G. K. Prasad, T. H. Mahato, B. Singh, K. Ganesan, P. Pandey and K. Sekhar, *J. Hazard. Mater.*, 2007, **149**, 460-464.
81. O. Yamamoto, *Int. J. Inorg. Mater.*, 2001, **3**, 643-646.
82. W. J. Huang, G. C. Fang and C. C. Wang, *Colloid Surf. A-Physicochem. Eng. Asp.*, 2005, **260**, 45-51.
83. S. R. Teeparthi, E. W. Awin and R. Kumar, *Sci. Rep.*, 2018, **8**, 11.
84. B. Levasseur, A. M. Ebrahim and T. J. Bandosz, *Langmuir*, 2011, **27**, 9379-9386.
85. M. B. Mitchell, V. N. Sheinker, W. W. Cox, E. N. Gatimu and A. B. Tesfamichael, *J. Phys. Chem. B*, 2004, **108**, 1634-1645.
86. H. Sun, P. Wu, J. He, M. Liu, L. Zhu, F. Zhu, G. Chen, M. He and W. Zhu, *Petrol Sci.*, 2018, **15**, 849-856.
87. M. Verma, R. Chandra and V. K. Gupta, *J. Colloid Interface Sci.*, 2015, **453**, 60-68.
88. D. Nagy, I. M. Szilágyi, T. Firkala and F. Xianfeng, *Eur. Chem. Bull.*, 2016, **5**, 40-42.
89. K. J. K. J. G. Ekerdt, J. R. Shapley, J. M. White, and J. T. Yates Jr., *J Phys Chem C*, 1988, **92**, 6182-6188.
90. T. H. Mahato, G. K. Prasad, B. Singh, J. Acharya, A. R. Srivastava and R. Vijayaraghavan, *J. Hazard. Mater.*, 2009, **165**, 928-932.
91. D. B. Mawhinney, J. A. Rossin, K. Gerhart and J. T. Yates, *Langmuir*, 1999, **15**, 4789-4795.
92. Y. M. Dong, K. He, L. Yin and A. M. Zhang, *Nanotechnology*, 2007, **18**, 6.
93. H. J. Lv, L. Ma, P. Zeng, D. N. Ke and T. Y. Peng, *J. Mater. Chem.*, 2010, **20**, 3665-3672.
94. R. Sahoo, S. Santra, C. Ray, A. Pal, Y. Negishi, S. K. Ray and T. Pal, *New J. Chem.*, 2016, **40**, 1861-1871.
95. R. Menzel, A. Duerrbeck, E. Liberti, H. C. Yau, D. McComb and M. S. P. Shaffer, *Chem. Mater.*, 2013, **25**, 2137-2145.
96. T. H. Mahato, G. K. Prasad, B. Singh, A. R. Srivastava, K. Ganesan, J. Acharya and R. Vijayaraghavan, *J. Hazard. Mater.*, 2009, **166**, 1545-1549.
97. G. K. Prasad, T. H. Mahato, B. Singh, K. Ganesan, A. R. Srivastava, M. P. Kaushik and R. Vijayaraghavan, *AIChE J.*, 2008, **54**, 2957-2963.
98. A. R. Puigdollers, F. Illas and G. Pacchioni, *Rend. Lincei.-Sci. Fis. Nat.*, 2017, **28**, 19-27.

99. A. Dannenberg and S. O. Pehkonen, *J. Agric. Food. Chem.*, 1998, **46**, 325-334.
100. J. Henych, V. Stengl, M. Slusna, T. M. Grygar, P. Janos, P. Kuran and M. Stastny, *Appl. Surf. Sci.*, 2015, **344**, 9-16.
101. G. W. Wagner, G. W. Peterson and J. J. Mahle, *Ind. Eng. Chem. Res*, 2012, **51**, 3598-3603.
102. M. F. Yu, O. Lourie, M. J. Dyer, K. Moloni, T. F. Kelly and R. S. Ruoff, *Science*, 2000, **287**, 637-640.
103. E. Pop, D. Mann, Q. Wang, K. E. Goodson and H. J. Dai, *Nano Lett.*, 2006, **6**, 96-100.
104. P. C. Collins, M. S. Arnold and P. Avouris, *Science*, 2001, **292**, 706-709.
105. X. Mu, X. F. Wu, T. Zhang, D. B. Go and T. F. Luo, *Scientific reports*, 2014, **4**, 9.
106. J. W. Suk, R. D. Piner, J. H. An and R. S. Ruoff, *ACS nano*, 2010, **4**, 6557-6564.
107. R. Menzel, D. Iruretagoyena, Y. F. Wang, S. M. Bawaked, M. Mokhtar, S. A. Al-Thabaiti, S. N. Basahel and M. S. P. Shaffer, *Fuel*, 2016, **181**, 531-536.
108. H. X. Kong, *Curr. Opin. Solid State Mater. Sci.*, 2013, **17**, 31-37.
109. Z.-Y. He, X.-W. Wei and Y.-Q. Wei, in *Antimicrobial Nanoarchitectonics*, ed. A. M. Grumezescu, Elsevier, 2017, pp. 167-194.
110. M. Inagaki and F. Kang, *Materials science and engineering of carbon: fundamentals*, Butterworth-Heinemann, 2014.
111. M. Terrones, *Int. Mater. Rev.*, 2004, **49**, 325-377.
112. N. Karousis, N. Tagmatarchis and D. Tasis, *Chem. Rev.*, 2010, **110**, 5366-5397.
113. P. Serp and B. Machado, in *Nanostructured Carbon Materials for Catalysis*, Royal Soc Chemistry, Cambridge, 2015, pp. 1-555.
114. D. S. Su, S. Perathoner and G. Centi, *Chem. Rev.*, 2013, **113**, 5782-5816.
115. X. M. Ren, J. X. Li, X. L. Tan and X. K. Wang, *Dalton Trans.*, 2013, **42**, 5266-5274.
116. J. C. Liu, L. Liu, H. W. Bai, Y. J. Wang and D. D. Sun, *Appl. Catal. B-Environ.*, 2011, **106**, 76-82.
117. B. Gao, G. Z. Chen and G. Li Puma, *Appl. Catal., B*, 2009, **89**, 503-509.
118. W. Chen, Z. L. Fan, B. Zhang, G. J. Ma, K. Takanebe, X. X. Zhang and Z. P. Lai, *J. Am. Chem. Soc.*, 2011, **133**, 14896-14899.
119. M. St'astny, J. Tolasz, V. Stengl, J. Henych and D. Zizka, *Appl. Surf. Sci.*, 2017, **412**, 19-28.
120. Y. Y. Liu, X. M. Liu, Y. P. Zhao and D. D. Dionysiou, *Appl. Catal. B-Environ.*, 2017, **213**, 74-86.
121. B. Chen, Z. Zhu, J. Ma, M. Yang, J. Hong, X. Hu, Y. Qiu and J. Chen, *J. Colloid Interface Sci.*, 2014, **434**, 9-17.
122. T. Wang, J. N. Wang, Y. Yang, P. Su and Y. Yang, *Ind. Eng. Chem. Res*, 2017, **56**, 9762-9769.
123. V. V. Singh, A. Martin, K. Kaufmann, S. D. S. de Oliveira and J. Wang, *Chem. Mater.*, 2015, **27**, 8162-8169.
124. W. Al Sekhaneh and H. Dahmani, *Mediterr. Archaeol. Archaeom.*, 2014, **14**, 25-35.
125. J. H. Im, S. J. Yang, C. H. Yun and C. R. Park, *Nanotechnology*, 2012, **23**, 10.

126. M. Daranyi, T. Csesznok, A. Kukovecz, Z. Konya, I. Kiricsi, P. M. Ajayan and R. Vajtai, *Nanotechnology*, 2011, **22**, 9.
127. Y. N. Jiao, S. L. Fu, L. Ding, Q. Gong, S. H. Zhu, L. B. Wang and H. Li, *Anal. Methods*, 2012, **4**, 2729-2734.
128. S. Mallakpour and E. Khadem, *Chem. Eng. J.*, 2016, **302**, 344-367.
129. P. Serp and E. Castillejos, *ChemCatChem*, 2010, **2**, 41-47.
130. X. L. Pan and X. H. Bao, *Acc. Chem. Res.*, 2011, **44**, 553-562.
131. S. A. Miners, G. A. Rance and A. N. Khlobystov, *Chem. Soc. Rev.*, 2016, **45**, 4727-4746.
132. A. N. Khlobystov, *ACS nano*, 2011, **5**, 9306-9312.
133. D. A. Britz, A. N. Khlobystov, K. Porfyrakis, A. Ardavan and G. A. D. Briggs, *Chem. Commun.*, 2005, 37-39.
134. T. W. Chamberlain, J. Biskupek, G. A. Rance, A. Chuvilin, T. J. Alexander, E. Bichoutskaia, U. Kaiser and A. N. Khlobystov, *ACS nano*, 2012, **6**, 3943-3953.
135. R. Breslow, *Acc. Chem. Res.*, 1991, **24**, 159-164.
136. H. Zhang, X. Pan, X. Han, X. Liu, X. Wang, W. Shen and X. Bao, *Chem. Sci.*, 2013, **4**, 1075-1078.
137. W. A. Solomonsz, G. A. Rance and A. N. Khlobystov, *Small*, 2014, **10**, 1866-1872.
138. W. A. Solomonsz, G. A. Rance, B. J. Harris and A. N. Khlobystov, *Nanoscale*, 2013, **5**, 12200-12205.
139. B. Cornelio, A. R. Saunders, W. A. Solomonsz, M. Laronze-Cochard, A. Fontana, J. Sapi, A. N. Khlobystov and G. A. Rance, *J. Mater. Chem.*, 2015, **3**, 3918-3927.
140. C. Y. Dai, X. M. Li, A. F. Zhang, C. Liu, C. S. Song and X. W. Guo, *RSC Adv.*, 2015, **5**, 40297-40302.
141. X. L. Pan and X. H. Bao, *Chem. Commun.*, 2008, 6271-6281.
142. W. Chen, Z. Fan, B. Zhang, G. Ma, K. Takanabe, X. Zhang and Z. Lai, *J. Am. Chem. Soc.*, 2011, **133**, 14896-14899.

Synthesis of hydroxylated group IV metal oxide compounds in hollow graphitised nanofibres

2.1. Background

Transition-metal oxides are widely used in important industrial processes, both as catalysts and as catalytic supports. The challenge for the formation of these nanoscale metal oxides is particularly topical because early transition metal oxides have low toxicity, high availability and chemical robustness.¹⁻⁴ Moreover, they possess low coordination numbers, high Lewis acidity of metal sites, and different types of hydroxide groups on their surface, and thus exhibit remarkable catalytic performance in the oxidation, reduction and hydrolysis of organic molecules.⁵⁻¹⁰

Nanoscale oxides and hydroxides of the group IV metals (titanium, zirconium and hafnium) have attracted significant attention in recent years due to their wide range of applications.^{11, 12} The relationship between the structure and function of these nanomaterials has resulted in a focus on producing small and unique structures of these metal oxides as to promote higher active surface areas, increased reactive sites and tunable surface compositions.¹³ The enhancement of these features has shown to be directly responsible for the impressive rates of decontamination of chemical warfare agents (CWA), due to increased Lewis acid sites (M^{4+}) and surface-bound hydroxyl groups which are

able to affect both the adsorption and hydrolysis of these toxic compounds.^{8,}

14-17

For nanomaterials with desired functions, the synthesis route selected is critical, therefore, several strategies have been implemented for producing novel metal oxide nanoparticles which apply solid, liquid or gas-phase methods (Table 2.1).¹⁸⁻²²

Table 2.1. Nanoscale metal oxide synthesis approaches.

Synthesis method		Advantages	Disadvantages
Solid-state methods	Milling	<ul style="list-style-type: none"> •Fast synthesis •Inexpensive equipment •Easily scalable 	<ul style="list-style-type: none"> •Less control of particle size •Particle sizes usually greater than 100nm •Increased strain or impurities in crystal structures
	Sonication		
Solution-phase methods	Co-precipitation	<ul style="list-style-type: none"> •Often easily scalable •Excellent control over size, morphology and dispersability 	<ul style="list-style-type: none"> •Often inorganic impurities •Required capping agents which can restrict access to the metal oxide surface •Surfactant free methods result in larger size distributions and agglomeration of nanoparticles
	Sol-gel		
	Micro-emulsion		
	Solvothermal/hydrothermal		
	Non-aqueous		
Gas-phase methods	Spray pyrolysis	<ul style="list-style-type: none"> •One dimensional nanostructures can be achieved •Uncapped surfaces 	<ul style="list-style-type: none"> •High vacuum or expensive equipment often required •High energy cost to vaporise reagents •Generally applied for metal nanoparticles, post-treatment required
	Inert gas condensation		
	Sublimation		

When considering metal oxides for catalysis controlling size, morphology and surface composition is crucial to driving increased reactivity. As solid-state methods commonly generate nanoparticles with diameters over 100 nm the total surface catalyst areas are reduced which can affect the activity.²⁰ Less control over the sizes in this strategy also make specific morphologies with desired functions unachievable. Conversely, solution-phase methods have shown significant popularity due to their impressive versatility to generate unique and tunable sizes and morphologies of metal oxide structures allowing effective control of their functional properties. Forming these structures often requires capping agents which can act as a barrier between the reagents and the catalytic surface and thus reduces its activity.²³ Gas phase methods have shown great promise in forming thin films, nanowires and nanobelts which have large surface areas and increased reactive edges which are important features when considering catalysis.²⁴ Uniform nucleation sites are often required to produce high-quality thin films and the stability of these species is often decreased due to their one-dimensional structures. As a result, no single technique provides full control over the physical and chemical properties of the metal oxides and finding new strategies to tune and stabilise nanoscale metal oxide catalysts represents an interesting research challenge.

One strategy that may be able to overcome these issues is forming these nanoscale metal oxides in confined space. The internal cavity of carbon nanotubes represents a suitable environment which could allow the formation and stabilisation of unique nanoscale metal oxide catalysts without the need

for capping agents. Utilising the effects of spatial confinement inside carbon nanotubes to template the formation of novel nanostructures has received increasing attention in recent times.²⁵⁻²⁸ The remarkable capability of carbon nanotubes to contain chemical reactions originates from their superior chemical, mechanical and thermal stability relative to more traditional nanoscale containers, including molecular capsules and porous solids.^{29, 30} Moreover, the encapsulation of materials inside carbon nanotubes provides a universal platform, distinct from other nanocontainers, as carbon nanotubes rely predominantly on ubiquitous van der Waals interactions to drive encapsulation.²⁶

Encapsulating metal oxides within carbon nanotubes represents a considerable challenge but has been achieved using capillary filling techniques with liquid solutions or molten materials. This has been thoroughly reported in the literature and relies upon exploiting the adhesive forces between the liquid phase and the hydrophobic and narrow interior carbon nanotubes to aid the uptake of the desired solution into the internal cavity.³¹ Gas phase filling strategies have also been successfully utilised and offer high filling rates, even dispersity of the guest material and is not restricted by surface tension requirements.³² This method involves the sublimation of the desired compounds which diffuse deep within the internal cavity.³³ A significant proportion of the literature has focused on encapsulating metal oxides inside single walled nanotubes as this allows for the stoichiometry, dimensions and electronic properties of the guest to be controlled and probed.³⁴⁻³⁶ However,

the encapsulation of guest species within narrow carbon nanotubes can potentially lead to the filling of the whole internal volume, resulting in the formation of blockages which would be detrimental when employing these materials for catalysis.

To overcome this issue, large diameter multi-walled carbon nanotubes can be employed and although confinement effects are less pronounced, the compromise between maximum confinement and effective diffusion of reactant molecules in and product molecules out is crucial for these materials to act as reaction vessels for chemical reactions. Amongst multi-walled carbon nanotubes, hollow graphitised carbon nanofibres (GNF) are attractive for templating the formation of unique nanomaterials and are particularly suitable for hosting catalytic reactions, due to their large internal diameter, high chemical robustness and unique internal morphology (Figure 2.1).^{37, 38}

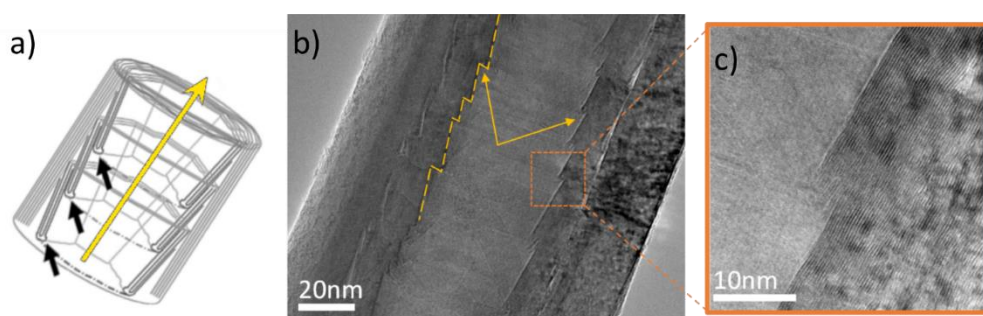


Figure 2.1. (a) Schematic representation of the structure of GNF (corrugated interior are denoted by black arrows; the yellow arrow signifies the direction of the nanofibre growth axis). (b,c) Transmission electron microscopy (TEM) images highlighting the large internal diameter and unique structure of GNF. The interior folds, emphasised in (c), act as anchoring points for atoms, molecules and nanomaterials due to increased van der Waals interactions between the confined guest and the host-nanofibre at these locations.

Whilst the hydrophobic internal channels of carbon nanotubes allow for reactants to be readily drawn into the lumen from solution, GNF, being significantly wider than typical carbon nanotubes (internal diameters of 30-60 nm compared to 1-5 nm respectively), additionally permit the efficient diffusion of products from the internal channel. This makes them particularly effective as reaction vessels for catalytic reactions and yields a new class of materials which can act as nanoreactors. Furthermore, the 3-4 nm high folds on the interior surfaces of GNF are understood to provide exemplary anchoring points for guest-materials, with previous studies demonstrating that small uncapped metallic nanoparticle catalysts can be effectively formed at these sites (Figure 2.2).³⁹⁻⁴¹

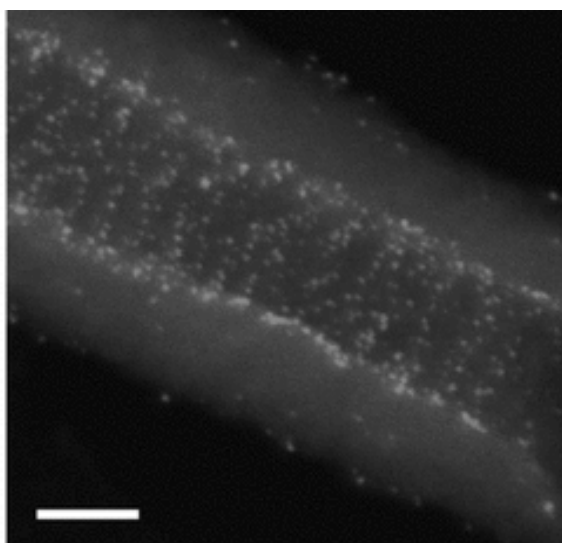


Figure 2.2. High angular dark field scanning transmission electron microscopy (STEM) of AuNP@GNF which demonstrates the maximised interactions at the internal anchoring sites promoting increased encapsulation of metal nanoparticles. Scale bar is 20nm. Reproduced from La Torre et al, copyright Wiley-VCH.⁴²

Moreover, the corrugated interior of the GNF facilitates the maximisation of host-guest interactions, often leading to the significant enhancement of

activity and selectivity, as well as improved stability and recyclability, of the confined nanocatalyst. This has been shown across a range of preparative catalytic reactions, including the Suzuki-Miyaura cross-coupling and hydrogenation reactions.^{40, 41}

It is clear that the nanofibre interior has the potential to act as a template promoting the formation of unique topologically complex nanostructures with larger surface areas that can be used to further drive improved catalytic performance. Dispersing group IV metal oxides uniformly within carbon nanotubes has been highlighted as a particular issue due to the rapid hydrolysis of their precursors, therefore, new filling and purification strategies are required to optimise encapsulation.⁴³ By exploiting nanoscale confinement effects to manipulate the physical and chemical properties of group IV metal oxides encapsulated within carbon nanotubes, new materials ideal for catalysis could be developed.

2.2. Aim and Objectives

The aim of this study is to encapsulate hydroxylated group IV metal oxide nanomaterials within hollow graphitised nanofibres to yield carbon nanoreactors, which may be suitable for catalysing reactions of environmental significance.

The filling of group IV metal chlorides into the internal cavity of graphitised nanofibres will be investigated. Appropriate filling and hydrolysis procedures must be identified for each of the corresponding metal chlorides in order to form hydroxylated metal oxide species encapsulated inside graphitised nanofibres ($\text{MO}_x(\text{OH})_y@ \text{GNF}$).

The resulting composite materials will be characterised using bulk and local probe techniques to confirm the loading, location, composition and morphology of the hydroxylated metal oxide component. The hybrid materials formed of hydroxylated Ti, Zr or Hf oxides on the inner surface of nanoreactors will be manipulated to change the physical and chemical properties of the encapsulated species by thermal treatment in air. The ability to tune the properties of confined group IV metal oxides species provides opportunities for the encapsulation of a wide range of chemically active species into nanoreactors which could be beneficial for environmental remediation reactions.

2.3. Results and discussion

2.3.1. Synthesis of $\text{MO}_x(\text{OH})_y@ \text{GNF}$

For the synthesis of low dimensional nanomaterials within carbon nanotubes, appropriate precursors and filling methods must be selected. Such group IV metal precursors must be stable in the liquid or gas phase to allow exploitation of common filling strategies. Several techniques have been previously employed for filling hollow carbon nanostructures with metal species, including the gas-phase deposition of metal carbonyl or metal acetylacetonate precursors (Figure 2.3).³²

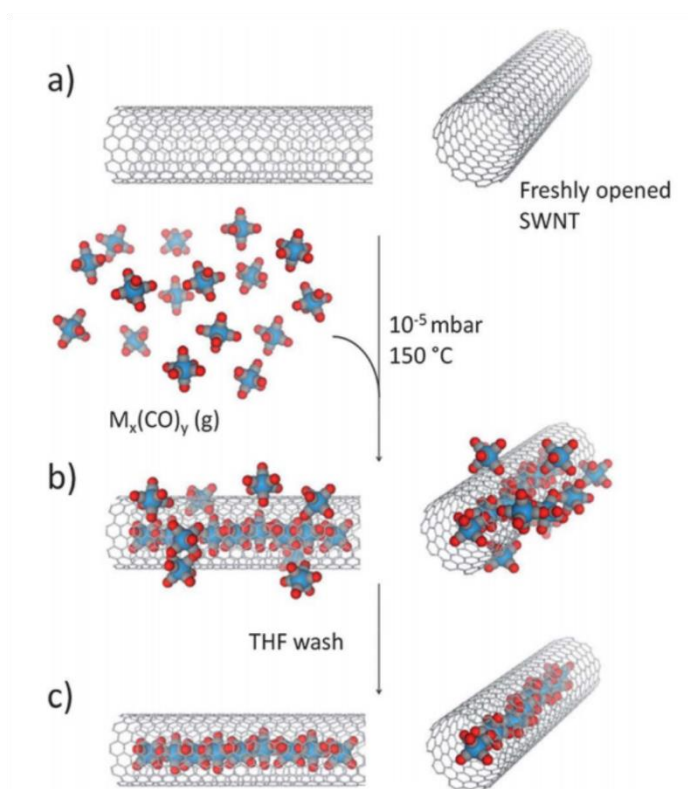


Figure 2.3. Gas phase deposition procedure for the encapsulation of metal precursors into SWNT by (a) metal precursor entering the nanotube from the vapour phase and (b) depositing onto the interior where they condense forming the encapsulated precursor composite material. (c) Externally absorbed precursor is removed using a solvent wash.³²

This procedure is followed by a decomposition step to afford transition metal nanoparticles within carbon nanotubes.^{44, 45 46} Nanostructured metal oxides can subsequently be formed by oxidising the metal nanoparticles at high temperature in air; however, this often leads to the development of larger and more crystalline particles with a consequently lower surface area and reduced catalytic activity.⁴⁷ Some metal halides, as potential precursors to metal oxides, have previously been inserted into nanotubes using capillary filling methods and used to probe the nature of host-guest interactions.⁴⁸ Yet, the confinement of group IV metal oxides inside carbon nanotubes remains largely unexplored, thus negating investigation of the catalytic properties of these promising materials in nanoreactors. Whilst many of the inorganic salts that have been encapsulated within the hollow channel of SWNTs are often unable to vaporise or sublime without decomposition.^{49, 50} Both the metal chlorides of hafnium and zirconium were shown to sublime at temperatures above 300 °C, making them suitable for a gas phase deposition strategy (Table 2.2).

Table 2.2. Group IV metal chlorides and their properties.

Precursor	Appearance at room temp	Sublimation temp (°C) ^a	Reactivity with water
TiCl ₄	Colourless liquid	- (136) ^b	Reacts violently with moisture in the air
ZrCl ₄	Hygroscopic white crystalline solid	310	Decomposes in water
HfCl ₄	Hygroscopic white crystalline solid	300	Decomposes in water

^a At a pressure of 3×10^{-5} mbar, ^b boiling point at atmospheric pressure.

Using this strategy offers several benefits compared to other filling methods, such as the direct molten filling of metal oxides, or the encapsulation of pre-formed metal oxide nanoparticles into nanotubes. It requires significantly lower temperatures than molten filling and gives better control over the composition and structure of the final product and is controllable by the conditions (such as pH) used in the hydrolysis step. This is not possible in the case of pre-formed nanoparticles, which additionally require a layer of stabilising ligand known to affect their surface chemistry.^{38, 51}

GNF were pre-treated at 500 °C for 45 min in air to remove any materials, such as adsorbed water or residual amorphous carbon, which could otherwise block the internal channel. A significantly large excess of precursor is used to maximise filling within the internal channel, therefore, zirconium and hafnium chlorides (ZrCl₄ and HfCl₄ respectively) (75mg) were sublimed at 400°C into the open cavities of the pre-treated GNF (75mg) in vacuum. The reactivity of these

precursors with water allows a facile route towards the formation of the oxide by employing a simple washing step. At this stage, washing with hydroxide solutions may result in maximal surface hydroxyl groups and would yield the metal oxyhydroxides of the general formula $\text{MO}_x(\text{OH})_y$.

Due to the reactivity of TiCl_4 with atmospheric moisture, a different filling strategy must be selected for this precursor. Fortuitously, with TiCl_4 being a liquid with relatively low surface tension, this precursor can be simply filled into GNF using capillary forces under atmospheric pressure. Pre-treated GNF (25mg) were, therefore, immediately placed into an inert atmosphere of argon and heated to 80 °C, where TiCl_4 (1 mL) was added. Due to the reactivity of this precursor, rapid hydrolysis with atmospheric moisture occurs. To ensure effective hydrolysis and to maximise the surface hydroxyl group post-washing with NH_4OH was used.

Traditional gas phase deposition reactions with SWNT implement a solvent washing step to dissolve and remove metal precursor not confined with the SWNT. An issue with this approach is that metal oxides are insoluble in many solvents and the large internal diameters of the GNF could result in total removal of the metal oxide if attempted. Therefore, a new strategy was developed to remove excess metal oxide that is not encapsulated within GNF. By harnessing the hydrophobic properties of the GNF, once the metal chloride is hydrolysed, an organic solvent can be added to the aqueous suspension, which draws the $\text{MO}_x(\text{OH})_y@$ GNF composite to the organic-aqueous interface

in order to reduce the surface tension. This leaves any free hydrophilic metal oxide particles remaining in the aqueous phase (Figure 2.4).

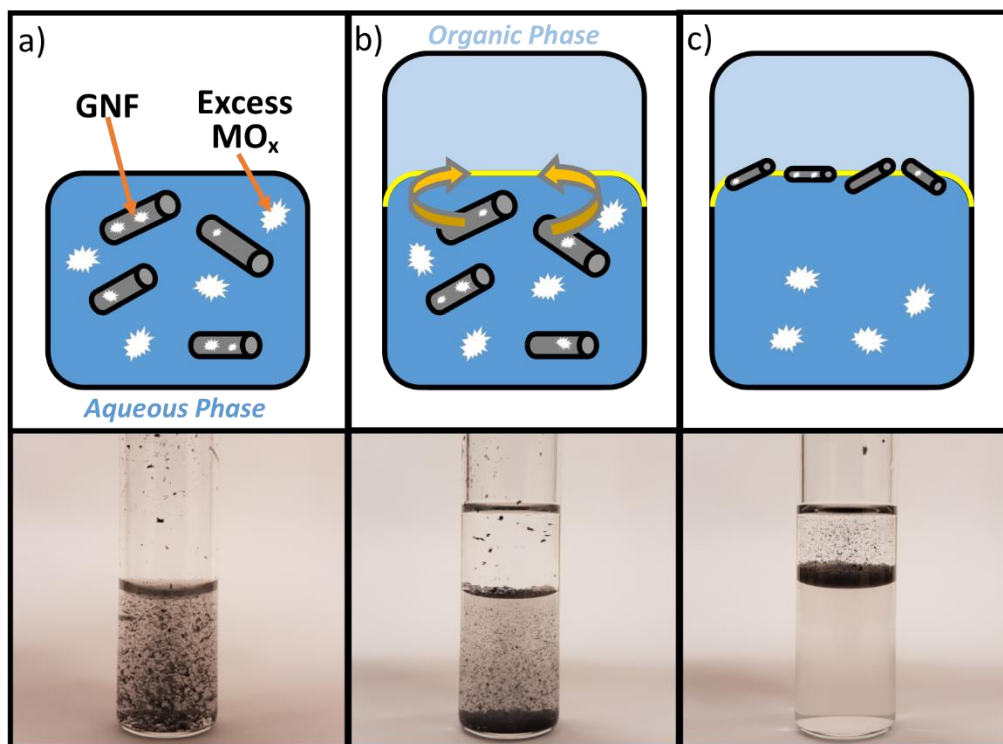
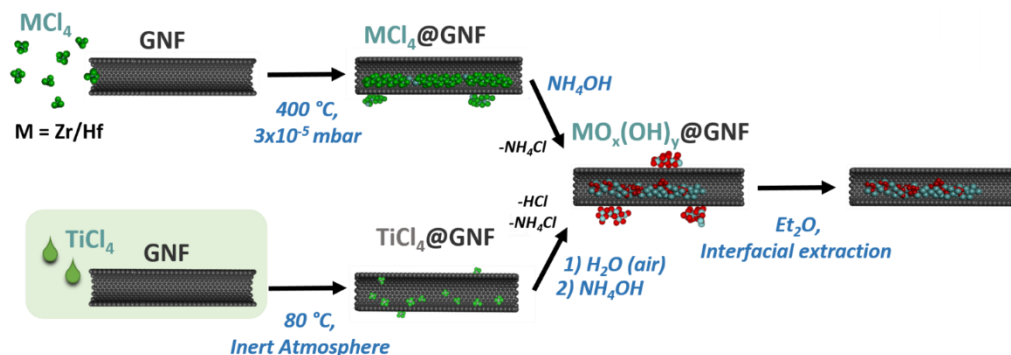


Figure 2.4. Schematic diagram and corresponding images of interfacial extraction technique. (a) After hydrolysis of metal chloride, excess metal oxide and nanoreactors reside in aqueous solution. (b) The addition of organic solvent generates an interface which the hydrophobic nanotubes are drawn to. Agitation of the solution results in (c) the separation of the nanoreactors in the diethyl ether organic phase and the excess metal oxide which remains in the aqueous phase.

This new and effective approach allows for the purification of the nanoreactors $\text{MO}_x(\text{OH})_y@ \text{GNF}$ from other poorly defined materials that might otherwise be present in the mixture following synthesis, whilst preserving the catalyst inside the GNF and was, therefore, implemented for all composites formed in this study.

A two-step synthetic strategy based on initial encapsulation of the respective metal chlorides in hollow GNF, followed by a hydrolysis step, converting the

precursor chloride into a hydroxylated metal oxide, was thus proposed (Scheme 2.1).



Scheme 2.1. The strategy for the liquid-phase filling of $TiCl_4$ and the gas-phase deposition of $ZrCl_4$ and $HfCl_4$ into GNF, followed by base-catalysed hydrolysis using atmospheric moisture and ammonium hydroxide to form the $MO_x(OH)_y$ nanomaterial encapsulated by GNF. The interfacial extraction procedure was used to remove externally adsorbed and excess hydrophilic metal oxides within the bulk sample.

Thermogravimetric analysis (TGA) was employed to confirm the uptake of the precursor molecules by the GNF, with the residual weight after GNF combustion diagnosing the loading (by weight) of the hydroxylated metal oxide in the final composite (Figure 2.5a,c,e). The differences in atomic number and solubility of the $MO_x(OH)_y$ species, critical during the purification step, accounts for the significant changes in loading down the period and result in a 3, 5 and 20% weight loading for the titanium, zirconium and hafnium species respectively.

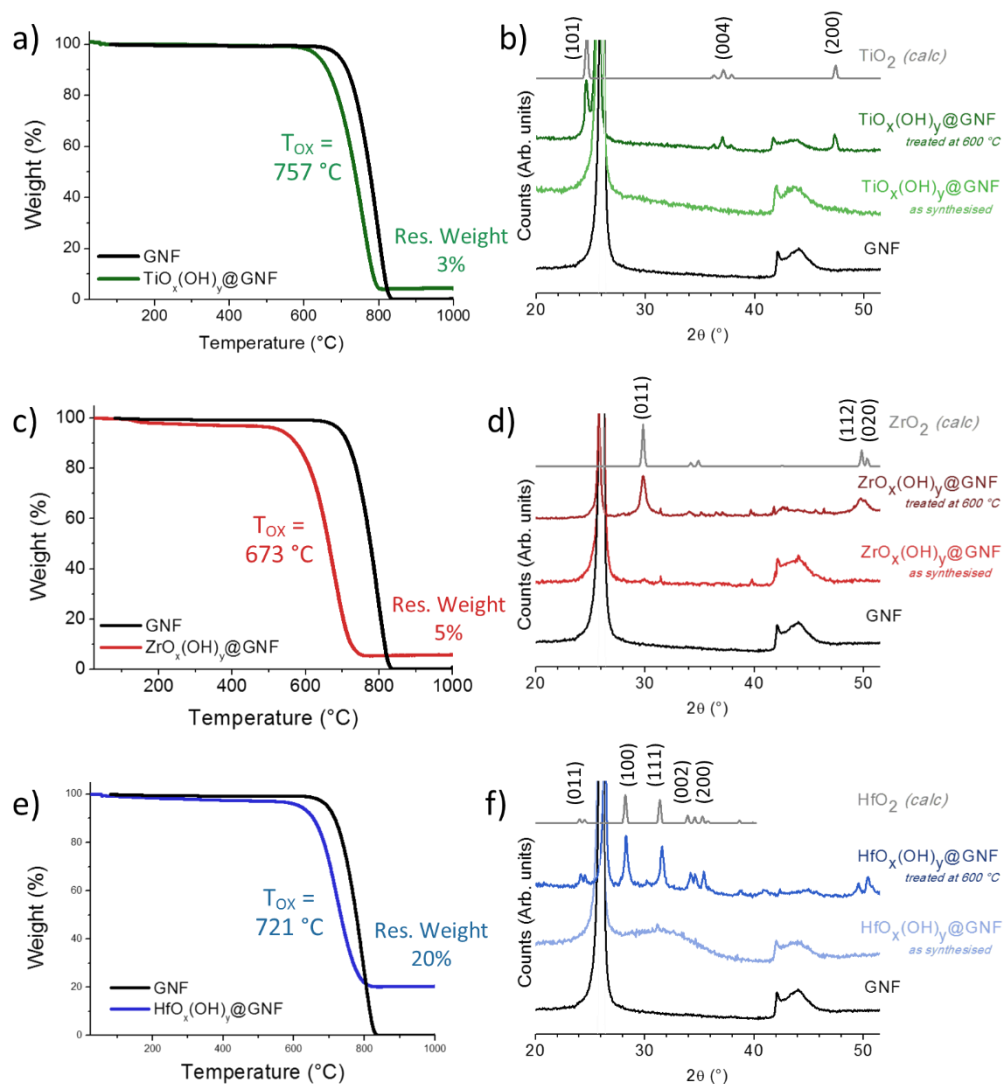


Figure 2.5. (a,c,e) TGA of $\text{TiO}_x(\text{OH})_y@\text{GNF}$ (green), $\text{ZrO}_x(\text{OH})_y@\text{GNF}$ (red) and $\text{HfO}_x(\text{OH})_y@\text{GNF}$ (blue) with empty GNF (black) for reference. (b,d,f) Corresponding PXRD analysis for empty GNF, as-synthesised, thermally treated $\text{MO}_x(\text{OH})_y@\text{GNF}$ and reference diffraction pattern for MO_2 species from a reference library. Temperature of combustion (T_{ox}) measured as peak maxima from the derivative of the TGA profile.

TGA also provides insight into the interactions of the guest ($\text{MO}_x(\text{OH})_y$) and host (GNF) components in the composite from the shift in the GNF combustion temperature (T_{ox}). Interestingly, the presence of an intercalant in the lumen of the GNF results in a clear decrease in the characteristic GNF oxidation temperature by 40, 124 and 76 °C for $\text{TiO}_x(\text{OH})_y@\text{GNF}$, $\text{ZrO}_x(\text{OH})_y@\text{GNF}$ and $\text{HfO}_x(\text{OH})_y@\text{GNF}$, respectively. This downshift in the combustion temperature

is related to the reducibility of the metal oxide and its ability to interact with the carbon surface. Metal oxides can be catalytic due to reactive oxygen atoms located at low coordination sites on the surface.⁵² As the metal oxide approaches the nanoscale the increased number of low-coordinated ions on the surface dramatically changes the redox behaviours, this results in substrates reacting with these sites to form oxygen vacancies and a reduced metal oxide.^{52, 53} ZrO_2 nanoparticles (2 nm) were shown to have significantly lower formation energy of oxygen vacancies when compared to the bulk which improved the catalytic abilities of the metal oxide.⁵⁴ At elevated temperatures in air, the vacancies can be refilled by molecular oxygen which regenerates the catalytic surface. The magnitude of the shifts in the TGA, therefore, could indicate the formation of nanoscale metal oxides with increased reactive sites, enhanced reducibility and more intimate contact with the GNF surface which is able to facilitate the catalysed combustion.

To identify the nature of the metal species responsible for the residual weight and shift in T_{OX} observed in the thermograms, powder X-ray diffraction (PXRD) analysis was performed. However, no peaks that would enable identification of the metal oxide species was observed (Figure 2.5b,d,f). This indicates a lack of crystallinity or small diameters of the intercalant as only the peaks at $2\theta = 25.9$ (002), 42.0 (100) and 44.1° (101) associated with GNF planes were significant. To further confirm the presence of the desired metal, post-synthetic thermal treatment of the composites was performed, which causes crystallisation of the metal oxyhydroxide into a MO_2 metal oxide phase at elevated

temperatures. Once heated to 600 °C, diffraction peaks at 24.5, 37.3 and 47.3° were observed for the $\text{TiO}_x(\text{OH})_y@\text{GNF}$ which correspond to the formation of anatase TiO_2 . A peak at $2\Theta = 29.7^\circ$ was also observed for the zirconia sample (indicative of tetragonal ZrO_2), and two distinctive peaks at $2\Theta = 28.2^\circ$ and 31.3° were observed for the hafnia sample (indicative of monoclinic HfO_2), confirming the presence of the metal and either an amorphous phase of hydroxylated metal oxide in GNF or extremely small crystalline domain size prior to heating for all the composite materials.

To investigate the effect of the hydrolysis reaction of $\text{MCl}_4@\text{GNF}$ on the metal loading, ZrCl_4 was hydrolysed with two hydrolysis reactants. A decrease in the residual weight loading from TGA is observed when the precursor is hydrolysed using water (Table 2.3).

Table 2.3. Comparative ZrCl_4 hydrolysis procedure with water or ammonium hydroxide.

Hydrolysis reactant ^a	Residual weight loading (%) ^b	T_{Ox} of GNF (°C) ^b
H_2O	3.1	673
NH_4OH	5.0	749

^a washed with 5mL of H_2O or NH_4OH (35%), ^b measured from TGA.

This precursor is known to form water-soluble species when hydrolysed using water as a result of incomplete hydrolysis, which leads to partial loss of material from the GNF cavity due to dissolution.⁵⁵ The reaction of $\text{MCl}_4@\text{GNF}$ (Zr/Hf) with ammonium hydroxide solution, due to the higher pH, results in a more complete hydrolysis, thus maximising the yield of the non-soluble surface-hydroxylated metal oxide species inside GNF, as shown for related bulk

materials previously.^{56,57} The T_{Ox} of the two components also reveal a significant shift for the sample hydrolysed using the hydroxide solution when compared to water. This indicates the chemical properties of this composite are controllable by washing with the hydroxide solution, as loading, reducibility and number of reactive oxygens present in the metal oxide appear to be manipulated. This results in the shift in T_{Ox} and will be important when considering these composites for catalytic decontamination. As a result of this, and with the abundance of hydroxyl surface groups being important for the catalytic applications of $MO_x(OH)_y@GNF$, utilising NH_4OH to aid hydrolysis was implemented as standard for all the synthesis procedures for the hydroxylated metal oxide species.

Although confirmation of the presence and loading of the metal oxide species can be achieved for the $MO_x(OH)_y@GNF$, by TGA and PXRD these techniques provide limited information about the local structure and composition of the as-synthesised hydroxylated metal oxide materials, therefore, local probe techniques such as electron microscopy can provide crucial information about these composite materials.

2.3.2. Transmission Electron Microscopy of $MO_x(OH)_y@GNF$

Transmission electron microscopy (TEM) is the only method which can unambiguously confirm the location, morphology and size of the nanomaterials within GNF.^{27, 58} Utilising electrons as an imaging tool allows for a resolution which can reach the atomic level, where optical microscopes are limited in resolution due to the wavelength of light. Bright field TEM utilises both direct

and elastically scattered electrons to generate an image which provides a 2D representation of the 3D structure. Bright field TEM imaging clearly shows the hydroxylated metal oxide encapsulated within the GNF structure with the image contrast (though sensitive to several parameters such as volume and density) clearly seen to increase from Ti to Zr to Hf consistent with the increasing atomic numbers of these elements (Figure 2.6).

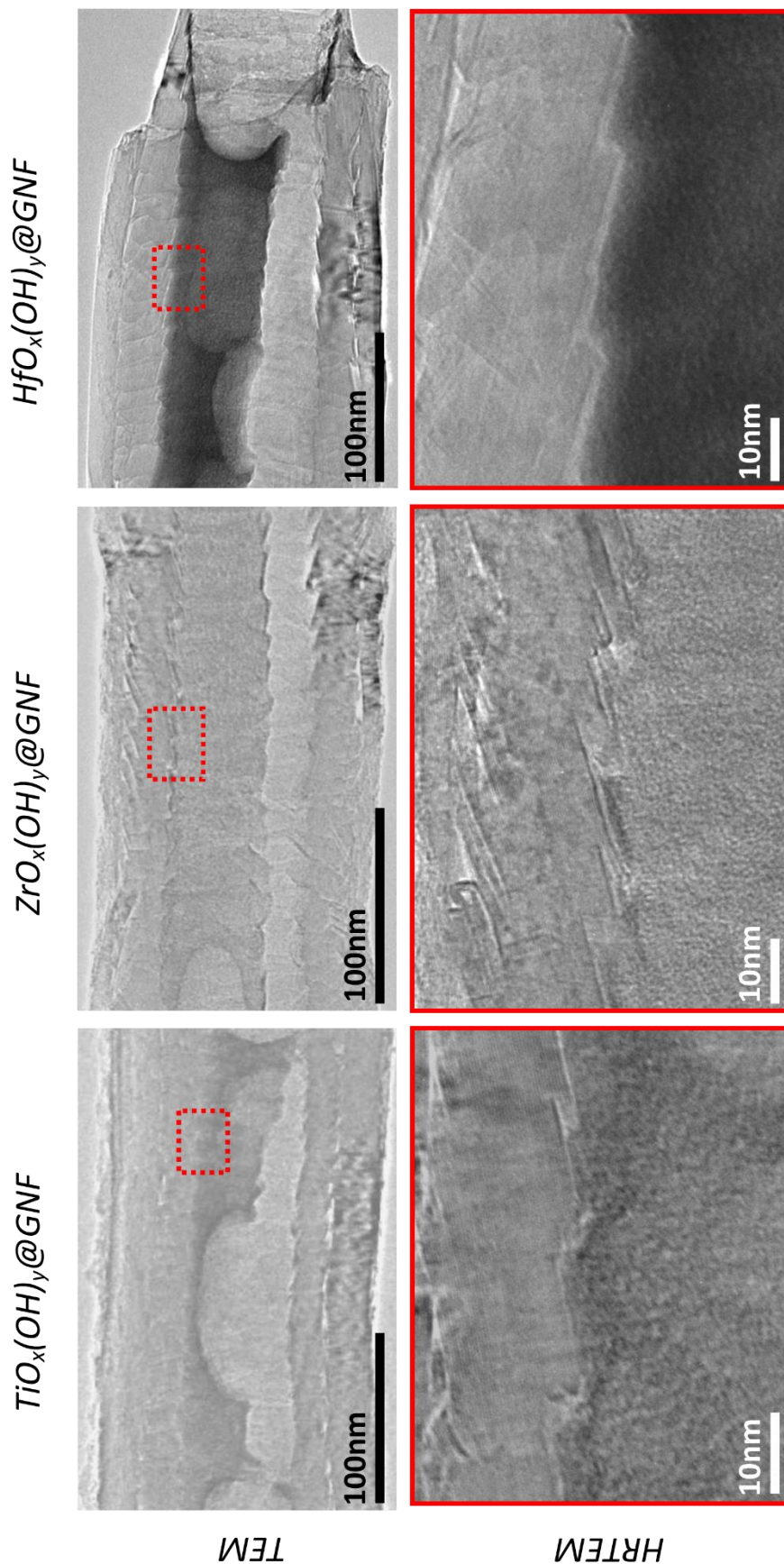


Figure 2.6. Electron microscopy analysis of $MO_x(OH)_y@GNF$ where $M = Ti, Zr$ and Hf (left to right). Bright field TEM provides evidence for the position of the hydroxylated metal oxide species within the internal channel of GNf in the composite material. High resolution TEM micrographs allow for crystalline layers in the GNf to be resolved and highlight the amorphous nature of the encapsulated material templated by the interior step-edges.

Surprisingly, instead of forming discrete metal oxyhydroxide nanoparticles, the $\text{MO}_x(\text{OH})_y$ appear to be coating the interior of the GNF as thin layers on average 6-10 nm in thickness, but with substantial variation from one GNF to another. High magnification images of the $\text{MO}_x(\text{OH})_y@$ GNF composites revealed no crystallinity in the metal hydroxides, consistent with the PXRD observations.

3D analysis of $\text{ZrO}_x(\text{OH})_y@$ GNF was achieved using TEM tomography. Both bright field TEM and dark field scanning transmission electron microscopy (STEM) tomography series were recorded by tilting the TEM grids around the GNF growth axis and revealed that the hydroxylated metal oxide layers did not cover the entire interior surface, but just under half of the interior side wall (Figure 2.7).

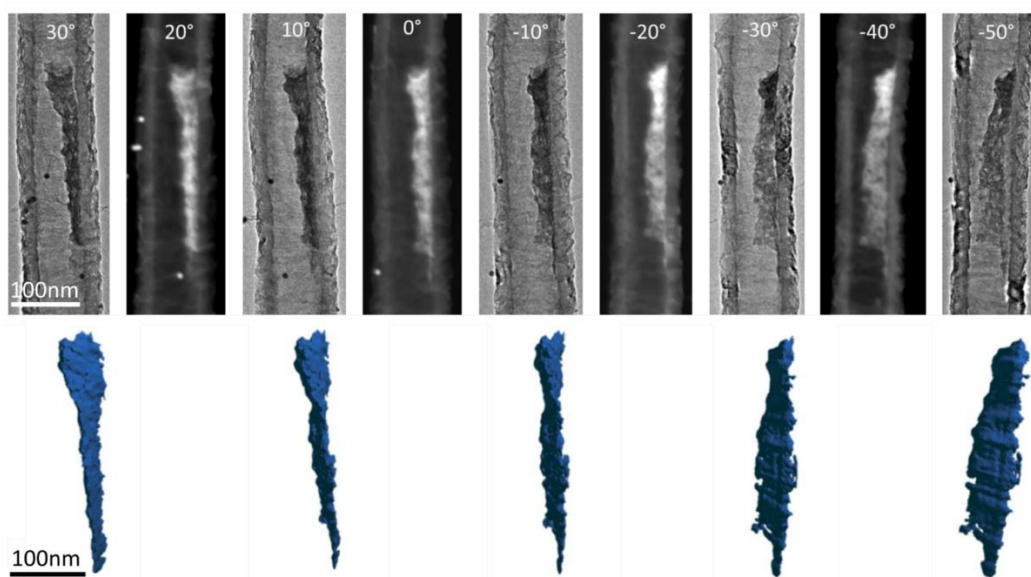


Figure 2.7. Bright field TEM and dark field STEM tilt series (top) of $\text{ZrO}_x(\text{OH})_y@$ GNF. The 3D model (bottom) of this species was reconstructed from bright field and dark field STEM images, which accentuate the contrast of the intercalant and highlight the thin layer coating on the interior surface, which has many topological defects and edges. Au fiducial markers were used to assist tomography and reconstruction.

Due to the improved contrast, TEM imaging and tomography of $\text{HfO}_x(\text{OH})_y@\text{GNF}$ further reveals the structures of the $\text{HfO}_x(\text{OH})_y$ layers to be uneven, exhibiting significant topological defects, which have potential as reactive sites for decontamination reactions (Figure 2.8).

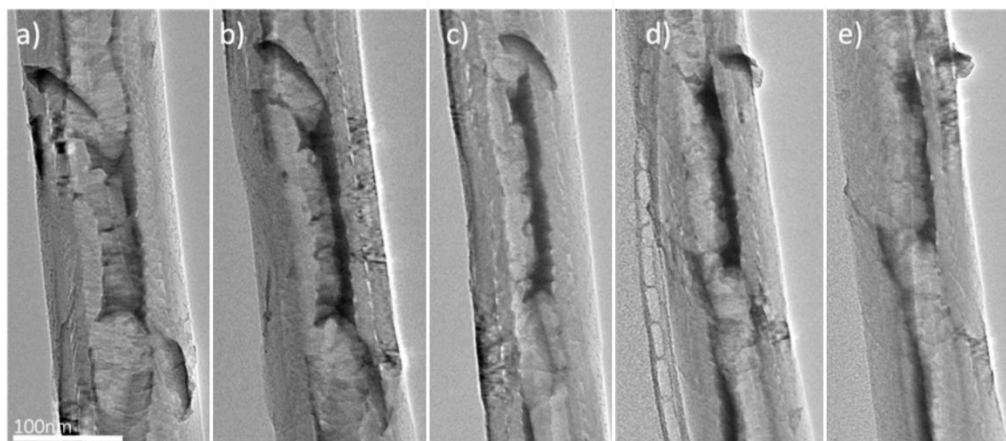


Figure 2.8. Bright field TEM images generated by rotating $\text{HfO}_x(\text{OH})_y@\text{GNF}$ species around GNF growth axis. a) 45° , b) 15° , c) -15° , d) -45° and e) -55° .

Low magnification microscopy indicates no significant variation to the GNF microstructure subsequent to filling with metal oxyhydroxides (Figure 2.9).

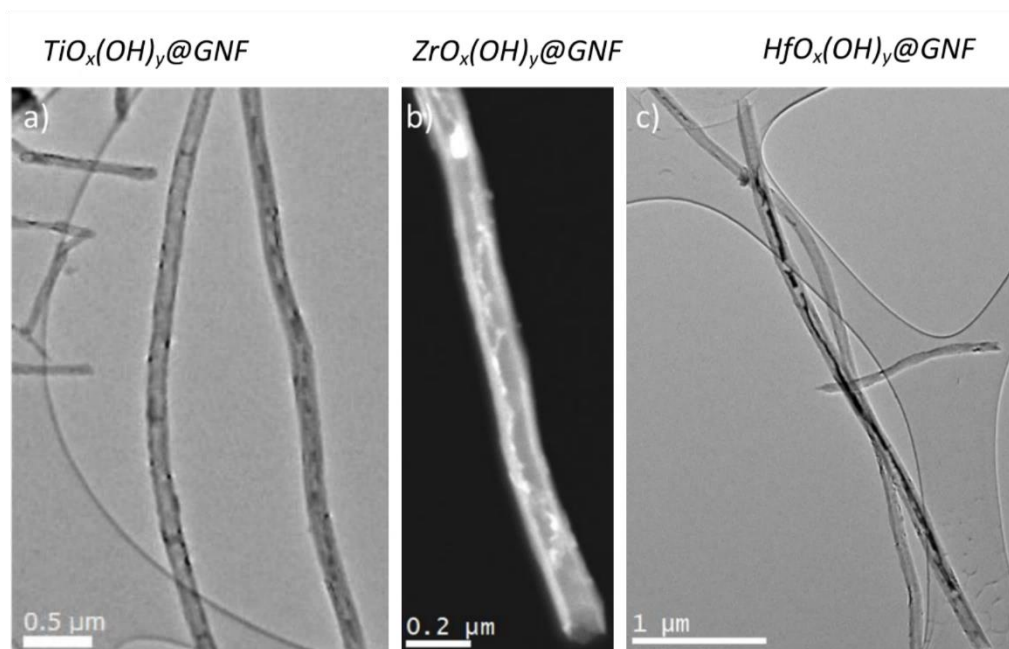


Figure 2.9. Microstructural analysis of the $MO_x(OH)_y$ composite materials. Low magnification TEM of a) $TiO_x(OH)_y@GNF$, c) $HfO_x(OH)_y@GNF$ and b) STEM of $ZrO_x(OH)_y@GNF$ composite materials.

This also confirms the effective removal of excess metal oxide as a result of the interfacial separation technique and can be further supported by scanning electron microscopy (SEM) imaging, which shows minimal exterior and excess metal oxide present (Figure 2.10).

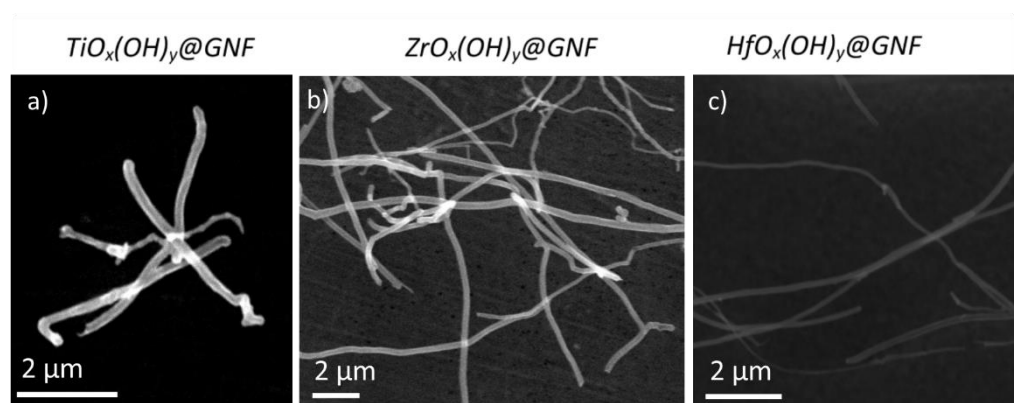


Figure 2.10. SEM of a) $TiO_x(OH)_y@GNF$, b) $ZrO_x(OH)_y@GNF$ and c) $HfO_x(OH)_y@GNF$.

Dark field STEM allows better differentiation of image contrast between carbon and the heavier elements as the contrast intensity is proportional to the $Z^{1.8}$ in dark field STEM as compared to $Z^{0.5}$ for bright field TEM (Figure 2.11).

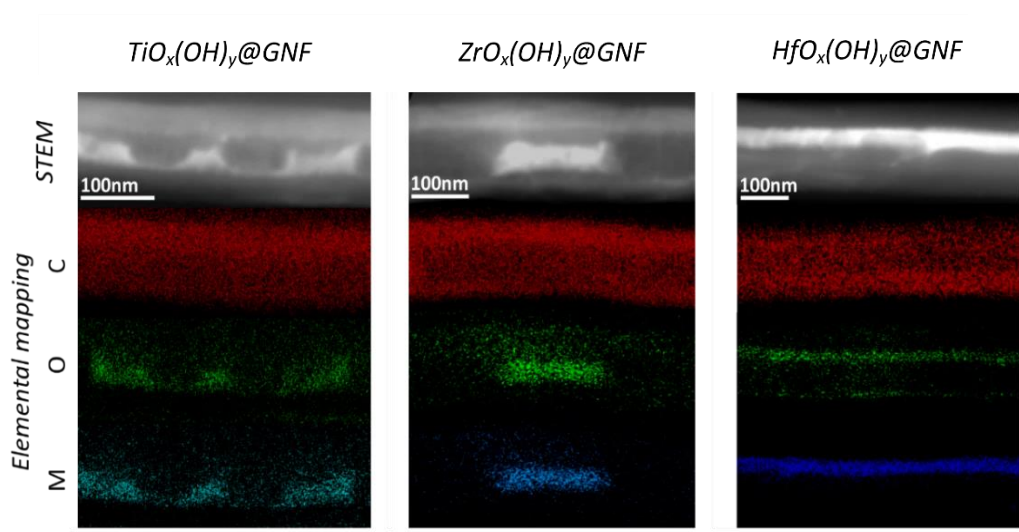


Figure 2.11. Dark field STEM of $MO_x(OH)_y@GNF$ of composite materials provides clearer contrast between the intercalant and the host, with the elemental mapping of the STEM micrograph identifying the respective positions of carbon (red), oxygen (green) and the metal (blue).

This technique can be used alongside energy dispersive X-ray spectroscopic (EDX) mapping in STEM mode which further supports the location of metal hydroxides inside GNF, and also links the high contrast in TEM images with the presence of Ti, Zr and Hf within $MO_x(OH)_y@GNF$. Furthermore, the distribution of oxygen correlates well with the distribution of metal atoms in GNF, indicating that the oxygen signals are predominantly associated with O atoms of metal hydroxides/oxides, rather than oxygen-containing surface groups of the GNF.

Microscopy has undoubtedly confirmed the morphology, size, crystallinity and location of the low dimensional nanomaterial. Further local probe techniques

such as STEM-EDX spectroscopy mapping has allowed for qualitative confirmation of the composition of the metal oxide, however, single point EDX spectroscopy can allow for quantitative analysis of the composition of the encapsulated hydroxylated metal oxide species.

2.3.3. Localised elemental analysis of $\text{MO}_x(\text{OH})_y@ \text{GNF}$

The significant number of carbon layers present in the GNF limits the application of many techniques which have been previously used to identify composition and oxidation state of materials. For example, X-ray photoelectron spectroscopy provides information on the identity and environment of the metal centre, but as the penetration depth is approximately 10 nm it cannot probe the interesting internal nanomaterials as they are more than 30 nm from the outer surface. Other techniques which could provide information about surface groups and oxides present, such as IR and Raman spectroscopies, are similarly unable to penetrate the large number of carbon atoms that comprise the outer walls.⁵⁹ Due to absorption of 2.3% of the photons per graphitic layer, any material possessing more than 20 layers will not allow the photons to pass through the sample to provide a signal. These techniques cannot, therefore, be employed to provide any information about the encapsulated metal species.

EDX spectroscopy uses a high-energy beam of electrons to stimulate the emission of distinctive X-rays to provide elemental information about the encapsulated species of interest. EDX spectroscopy as a local probe has already identified significant oxygen being associated with the metal species in the composite, and this technique has been used previously to quantitatively

confirm the presence of terminal iodine atoms within the structure of PtI_2 inside a SWNT.⁴⁶ This strategy was applied to these nanoreactors to help identify the composition of the confined hydroxylated metal oxide.

EDX spectroscopy indicates the presence of both M and O in $\text{MO}_x(\text{OH})_y@ \text{GNF}$, with small quantities of chloride detected indicative of a high conversion of chloride to hydroxide during hydrolysis (Figure 2.12).

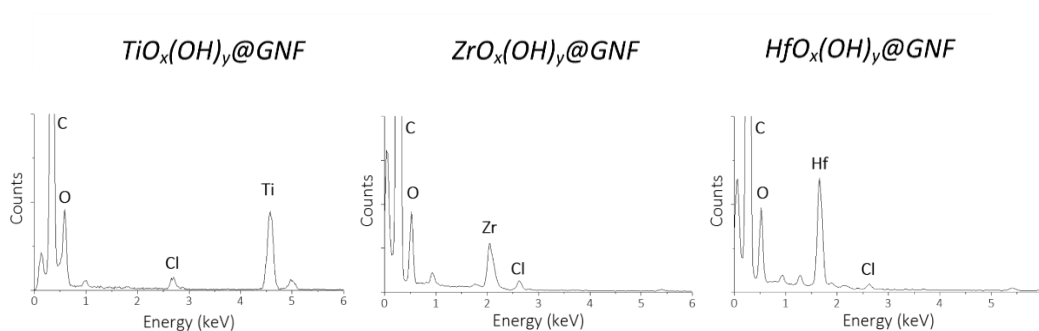


Figure 2.12. EDX spectra of $\text{MO}_x(\text{OH})_y@ \text{GNF}$ confirms the presence of the group IV metal in the confined nanomaterial.

Moreover, the extracted M:O ratios are 1:3.5, 1:3.4, and 1:2.5 for M = Ti, Zr and Hf, respectively, corresponding to an approximate formula of $\text{MO}(\text{OH})_2$ for Ti and Zr, supporting the abundant formation of hydroxyl groups during the hydrolysis of metal chlorides inside the GNF (Table 2.4). Due to the preferred formation of hafnium oxide, an approximate formula of HfO_2 is proposed from EDX spectroscopy.

Table 2.4. Extracted EDX spectroscopy data allowing calculation of composition of the metal oxyhydroxide species.

Material	Metal oxide weight (%) ^a	M : O atomic ratio (%) ^b	M : Cl atomic ratio (%) ^b
TiO _x (OH) _y @GNF	3.5	(1:) 3.5	(1:) 0.3
ZrO _x (OH) _y @GNF	5.3	3.4	0.1
HfO _x (OH) _y @GNF	20.1	2.5	0.2

^a Percentage weight loading of composite materials calculated from thermogravimetric analysis. ^b Atomic percentage ratio of oxygen and chlorine to the metal measured and calculated using EDX spectroscopy. 0.5% of the oxygen was found to be associated with the GNF and initially removed before calculating the atomic ratio. K α values used for carbon, oxygen, chlorine and titanium, L α value used for zirconium and M α values used for hafnium.

The non-stoichiometric composition of the hydrolysis products is likely to be responsible for the lack of crystalline order, which allows the metal hydroxides to spread over the inner surface of GNF (rather than to form compact crystalline particles), following the contours of the corrugated interior, thus maximising the surface area available for catalysis.

Quantification of the metal-oxygen ratio from the EDX spectra suggests the metal is in the +4 oxidation state, with hydroxyl groups produced during the hydrolysis of metal chlorides inside the GNF. The oxidation state of the metal can be further confirmed using electron energy loss spectroscopy (EELS) which measures the loss in energy of electrons as a result of inelastic scattering when the sample is exposed to a beam of electrons. For the TiO(OH)₂@GNF, the Ti L_{2,3} near edge structures at 459 and 465 eV match that expected for Ti⁴⁺, with lower oxidation states resulting in a shift towards lower energy loss. As for the ZrO(OH)₂@GNF composite the, Zr L_{2,3} edge positions at 2225 and 2309 eV respectively also match Zr⁴⁺. The Hf edge expected around 1800 eV proved too

difficult to resolve due to low signal and overlap with the Si edge from the TEM grid (Figure 2.13).⁶⁰

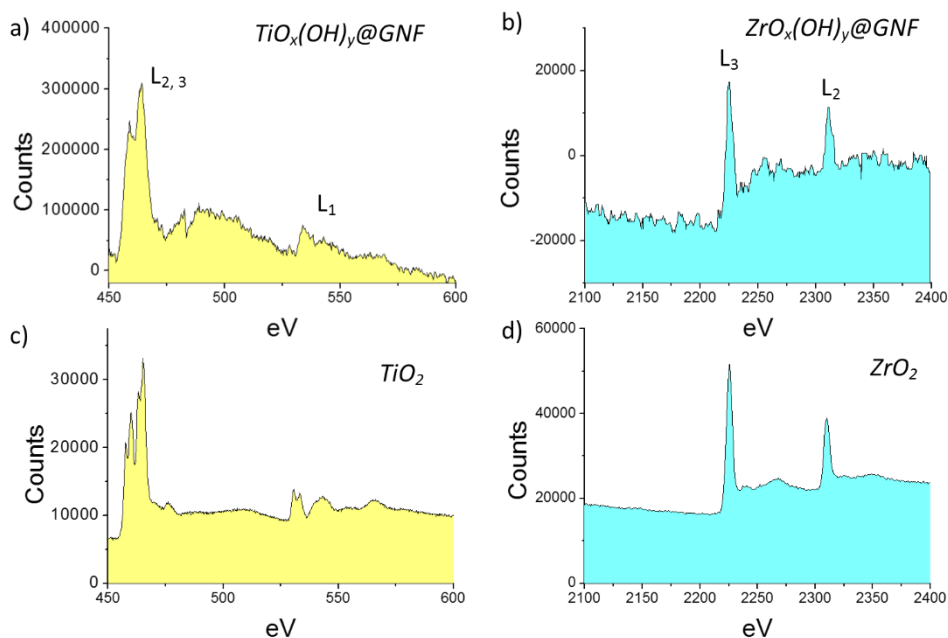


Figure 2.13. Electron energy loss spectroscopy (EELS) analysis for a) $TiO_x(OH)_y@GNF$ and b) $ZrO_x(OH)_y@GNF$. Reference EELS spectra of c) Ti and d) Zr as TiO_2 and ZrO_2 , respectively, in the +4 oxidation state.⁶⁰

Using several different characterisation techniques has provided evidence of the composition, structure, morphology, location, oxidation state and loading and of the $MO_x(OH)_y@GNF$ composite materials. These materials possess high surface areas, interesting surface groups and significant defect sites which could be useful as decontamination catalysts.

2.3.4. Thermally activated inorganic transformations of $MO_x(OH)_y@GNF$

As well as exploiting these materials as nanoreactors to catalyse organic reactions, carbon nanotubes can be applied to host inorganic transformations of encapsulated nanomaterials. Manipulating these materials leads to a

catalogue of spatially confined nanomaterials which can be applied to a variety of applications.

Thermal treatment in air has already been shown in this study to produce crystalline structures of the group IV metal oxides inside graphitised nanofibres from PXRD results however, further investigations were needed to understand the properties of the encapsulated species that could be controlled.

2.3.4.1. Thermal treatment of $\text{MO}_x(\text{OH})_y@ \text{GNF}$ in air

Demonstrating control over the crystallinity, size and shape of nanomaterials is a critical factor when designing devices with desired functions. This has been shown in metal oxide semiconductor field effect transistor where the physical properties can dramatically change the polarizability and corresponding bandgap of the materials.⁹ In section 2.3.1., distinctive peaks were observed in the PXRD diffractograms of samples thermally treated in air. As a consequence, a more detailed *in-situ* PXRD investigation was performed for all three of the group IV metal oxyhydroxide nanoreactors as to observe at which temperatures crystallisation and phase transitions occur (Figure 2.14). For the titania sample, the TiO_2 peaks are obscured by the alumina peaks of the background holder, therefore, this technique was not informative. However, crystallisation of the titania anatase phase appears at 600 °C as expected from previous work in the literature.⁶¹

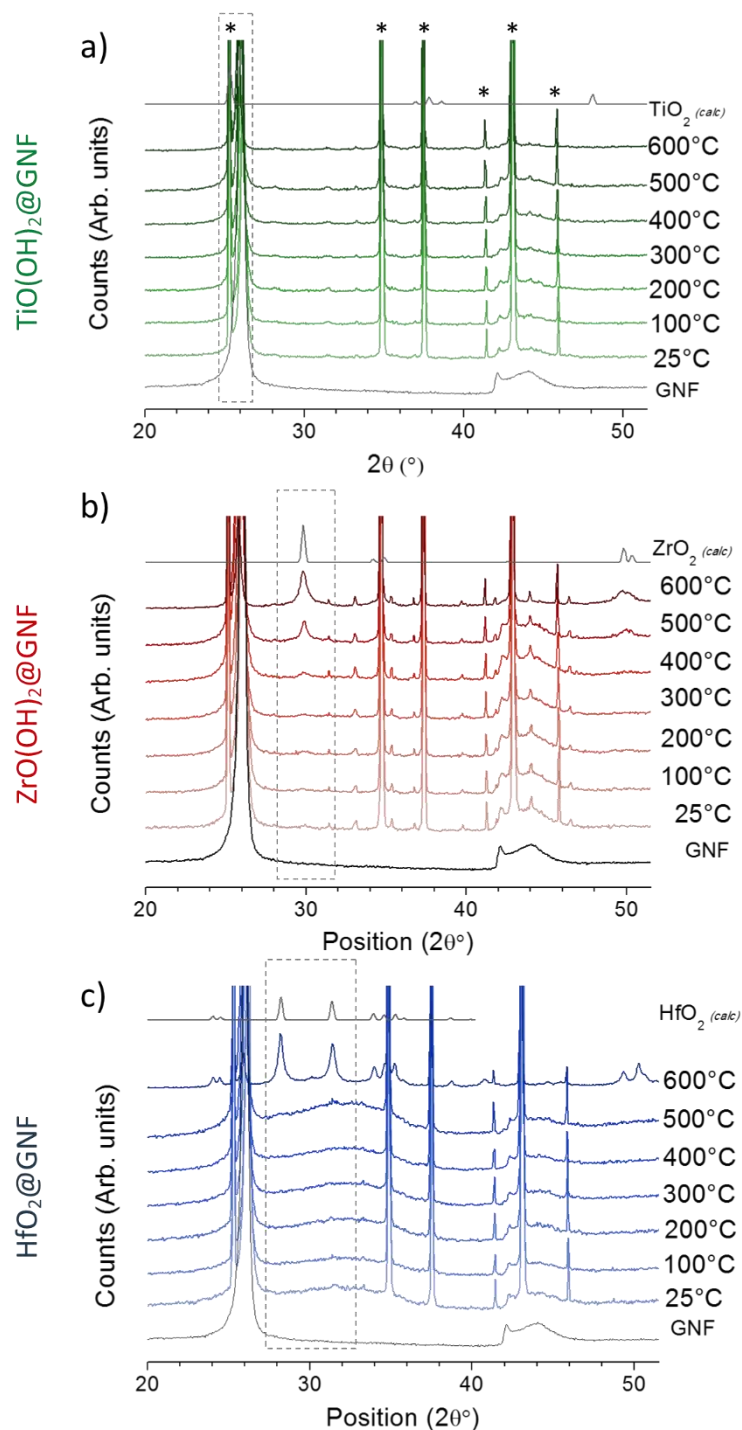


Figure 2.14. Variable temperature PXRD for (a) $\text{TiO(OH)}_2\text{@GNF}$, (b) $\text{ZrO(OH)}_2\text{@GNF}$, and (c) $\text{HfO}_2\text{@GNF}$ identifying the temperature at which crystallisation starts to occur. Persistent peaks at 25.1 , 34.8 , 37.3 , 41.1 , 43.1 and 45.9° are related to the alumina background support denoted by *.

Interestingly, the formation of new peaks in the diffractograms were observed for the Zr and Hf oxyhydroxide species when thermally treated in air. By

monitoring the peak at $2\theta = 29.7^\circ$ (consistent with the formation of the tetragonal phase of ZrO_2) the crystallisation process of the $ZrO(OH)_2@GNF$ material can be followed (Figure 2.14 - red). It was observed that the crystallisation starts between 300-400 °C. This broad peak becomes more distinctive at higher temperatures due to the growth in the crystalline domain size as a result of the thermal treatment. Similarly, for the hafnium sample peaks associated with monoclinic HfO_2 are clearly observed at 600 °C; however, up to 500 °C, a broad peak is present in the range of 30-35° (Figure 2.14 - blue). This broad peak could correspond to very small crystalline domains within the sample which cannot be properly resolved by the instrument. Above 500 °C, these small domains form more ordered and crystalline species. Previous work had indicated that 300 °C is the onset temperature for the crystallisation process of HfO_2 ; however, the small dimension of the encapsulated species and the effects of spatial confinement inside the nanotubes could explain the increase in temperature required to facilitate this process as observed by PXRD.⁶²

To investigate the morphology of the thermally treated samples at 600 °C, TEM was employed. The formation of nanoparticles is clearly noted in all cases; however, there is significant variation in the size and shape down the group (Figure 2.15). Discrete nanoparticles, approximately 12nm in diameter, which remain at the internal anchoring sites of the graphitised nanofibre were observed in the $TiO(OH)_2@GNF$ heated to 600 °C ($TiO_2@GNF-600$). Smaller nanoparticles (8 nm in diameter) clustered together analogous to the original

oxyhydroxide species were noted for thermally evolved $\text{ZrO}(\text{OH})_2@\text{GNF}$ ($\text{ZrO}_2@\text{GNF-600}$). Finally, the hafnium species ($\text{HfO}_2@\text{GNF-600}$), like the zirconia, seem to retain similar width and length to the amorphous species; however, larger crystalline elongated hafnia nanoparticles were now observed.

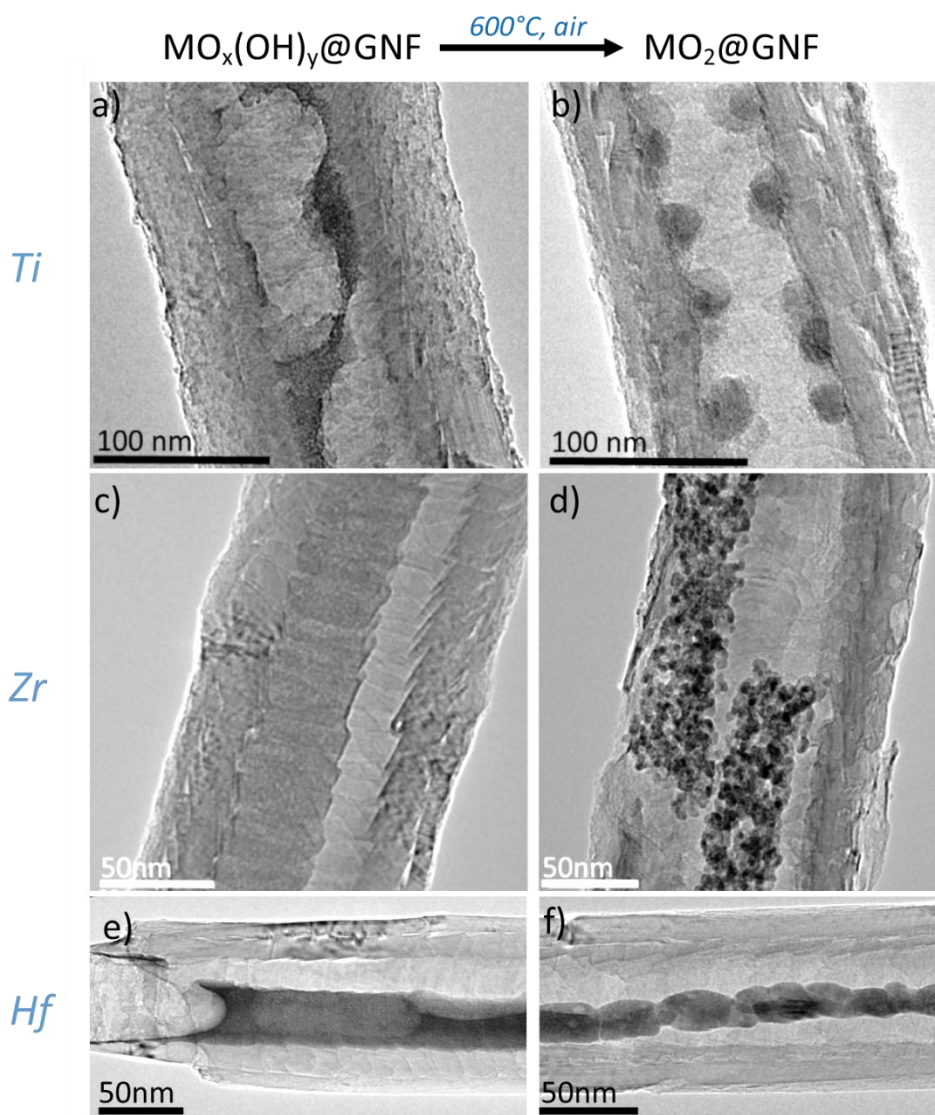


Figure 2.15. TEM analysis of $\text{MO}_x(\text{OH})_y@\text{GNF}$ before (a, c and e) and after treatment at 600 °C in air yielding (b) $\text{TiO}_2@\text{GNF-600}$, (d) $\text{ZrO}_2@\text{GNF-600}$ and (f) $\text{HfO}_2@\text{GNF-600}$ indicating the formation of metal dioxide nanoparticles after high temperature treatment.

Interestingly, when heating in air at 600 °C, the confined ZrO_2 sample has initiated the combustion of the GNF which can be seen by the damaged

external GNF sidewall (Figure 2.15d). In section 2.3.1., the zirconium composite possessed the largest shift in T_{Ox} (combustion temperature of the GNF), of 126 °C when compared with the Ti and Hf composites. This was attributed to the enhanced reducibility and increased contact between the metal oxide reactive sites and the carbon surface. This can now be confirmed by TEM as it was observed that at 600 °C, small nanoparticles of zirconium oxide are present which would allow for more intimate contact between the carbon atoms and the reactive oxygen atoms at low coordinated sites. As the carbon atoms around the metal oxide nanoparticles are affected the most, it appears the carbon surface may act as a reducing agent and results in localised oxidation of the carbon structure in the presence of oxygen. The increased defects in the GNF structure, therefore, result in a reduced T_{Ox} . The titanium and hafnium composites form larger nanoparticles with less contact and surface atoms which corresponds to the diminished ability to catalyse combustion.

From HRTEM analysis, thermal treatment is able to transform the amorphous oxyhydroxide species into encapsulated crystalline MO_2 nanoparticles (Figure 2.16). TiO_2 was shown to form nanoparticles with a d-spacing consistent with the anatase plane of titania (101). ZrO_2 and HfO_2 also possessed d-spacing of 0.29nm and 0.28nm, respectively, which has been previously reported as tetragonal zirconia (011) plane and the monoclinic hafnia plane (111) which supports the PXRD analysis.⁶³⁻⁶⁵

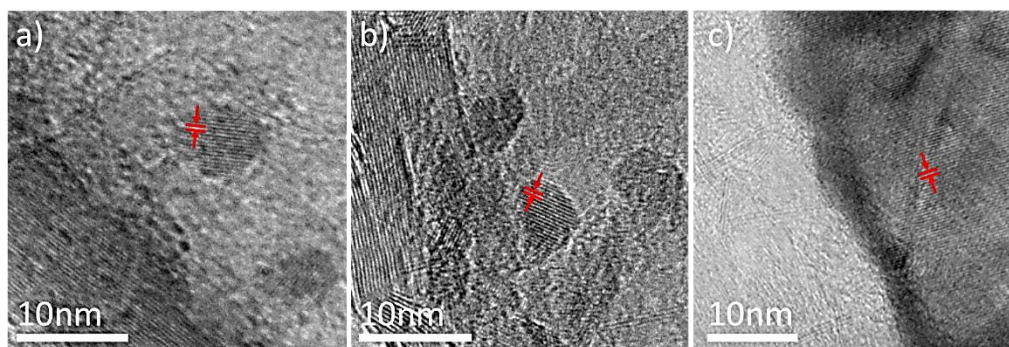


Figure 2.16. HRTEM after calcination at 600°C in air and the formation of discrete crystalline nanoparticles of a) anatase titanium dioxide (0.35nm) b) tetragonal zirconium dioxide (0.29nm) and c) monoclinic hafnium dioxide (0.28nm) compared to the lattice spacing of the sidewall of the GNF (0.34nm).⁶³

Thermal treatment clearly demonstrates an ability to control the morphology of nanoparticles in composite nanoscale materials; it is logical to assume that modulation of the size should also be possible under this framework. The *in-situ* PXRD heating experiment of $\text{ZrO}(\text{OH})_2@\text{GNF}$ indicates an increase in the width and height of the peak associated with the tetragonal ZrO_2 phase consistent with an increase in crystalline domain size (Figure 2.17). Calculating nanoparticle size from the PXRD is problematic due to overlapping domains and the broadening of the instrument being larger than the broadening of the metal oxide peak.⁶⁶ However, the PXRD shows a qualitative relationship between increasing temperature and growth in nanoparticle size indicated by the decreasing broadening of the diffraction peak.

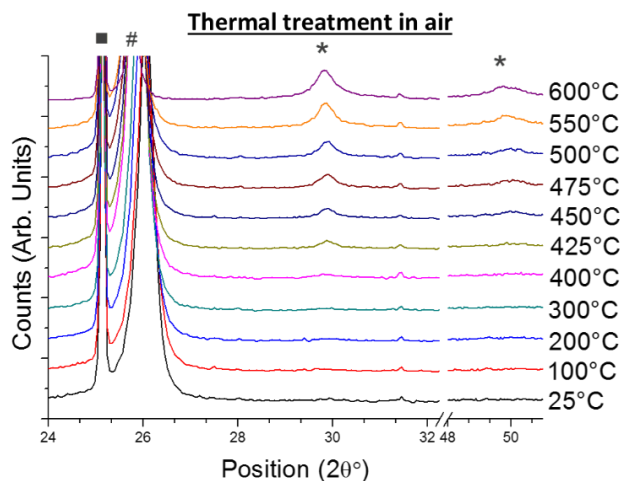


Figure 2.17. Variable temperature PXRD of $\text{ZrO}(\text{OH})_2@\text{GNF}$ thermally treated in air highlighting growth in ZrO_2 (011) peak at increasing temperatures. (* ZrO_2 , # GNF, ■ Alumina heated support).

TEM was collected for the materials heated to 400 °C and 600 °C with particle sizing analysis indicating the average particle size is 5.6 and 8.0 nm in diameter after thermal treatment in air at 400 and 600 °C, respectively (Figure 2.18).

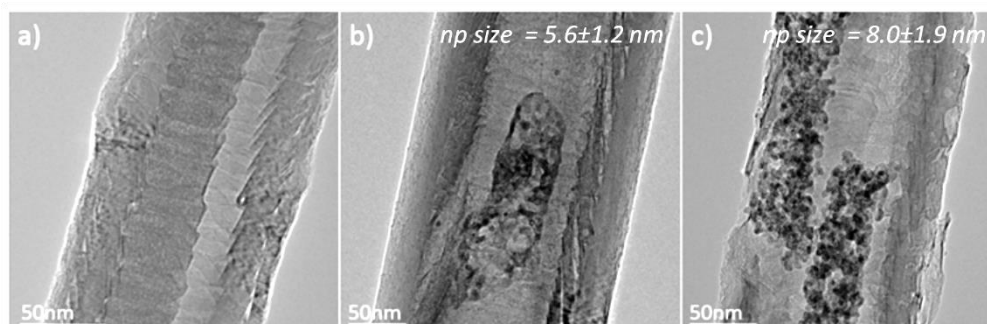


Figure 2.18. TEM of (a) as-synthesised $\text{ZrO}(\text{OH})_2@\text{GNF}$ and the composite thermally treated to (b) 400°C ($\text{ZrO}_2@\text{GNF-400}$) and (c) 600°C ($\text{ZrO}_2@\text{GNF-600}$) in air with corresponding nanoparticle sizing.

The TEM identifies the stages for nanoparticle growth, as at a 400 °C treatment there is still an amorphous nature about the encapsulated species which appears to possess smaller crystalline nanoparticles within the structure which produce the very broad peak in the diffraction pattern. When treated at 600 °C, the constant rearrangement of atoms leads to improved crystallinity and

most likely Oswald ripening of the nanoparticles which result in an increase in the nanoparticle size. The increased size from the TEM analysis supports the decrease in the broadening observed from PXRD which, therefore, confirms the control over the crystalline domain size and overall particle size which could allow for precise metal oxide nanoparticles to be synthesised within the internal channel of the GNF.

Although changing crystallinity, size and morphology of these group IV metal oxyhydroxide species are thought to reduce surface area and decrease the active defects sites present which would be essential for decontamination reactions. The ability to fine-tune the physical and chemical properties of the encapsulated materials could make them interesting for a range of applications beyond those explored here, particularly for electronics.^{9, 10}

2.3.4.2. Thermal treatment of MO_x(OH)_y@GNF in inert atmosphere

The crystal phase transitions of zirconia and hafnium oxides occur at very high temperatures (>1000 °C) not feasible in *in-situ* PXRD. However, it is well known in the literature that titania undergoes multiple phase transitions below 1000°C (Figure 2.19).⁶⁷

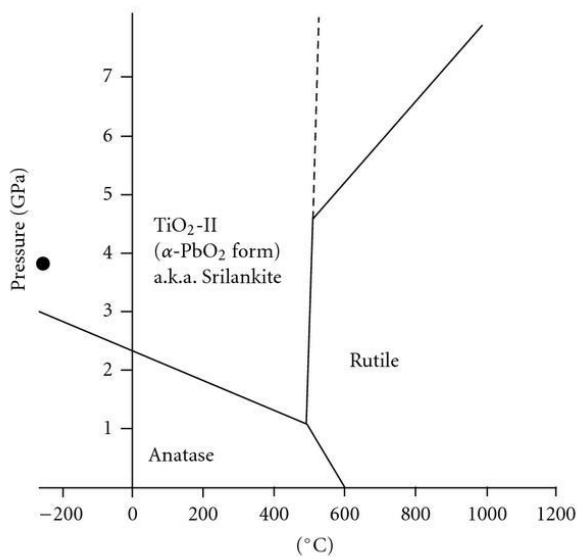


Figure 2.19. Phase diagram for TiO₂. Reproduced from Nie et al.⁶⁷

The thermal treatment of TiO(OH)₂@GNF in air at 600 °C results in peaks at $2\theta = 39^\circ$ and 49° in the PXRD diffractogram. This corresponds to the anatase TiO₂ which is expected to form according to previous literature.⁶⁸ With the combustion of the GNF also occurring at this temperature, the thermal treatment was performed under an argon atmosphere at higher temperatures to ensure retention of the nanofibre host (Figure 2.20).

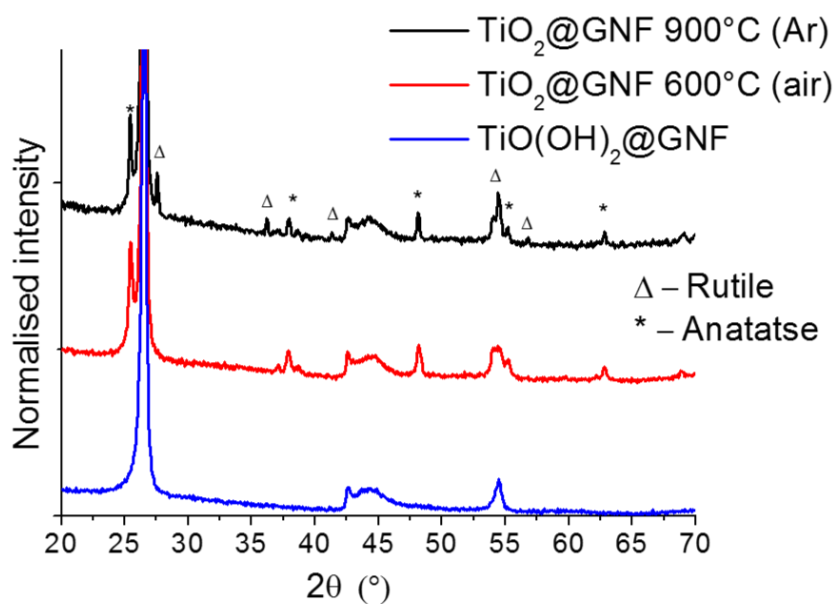


Figure 2.20. PXRD of $\text{TiO}(\text{OH})_2@GNF$ (blue) and the composite after thermal treatment at 600 $^{\circ}\text{C}$ (red) and at 900 $^{\circ}\text{C}$ under an inert atmosphere (black) which highlights the control of different crystal phases of TiO_2 .

The phase transition from anatase to rutile titania is previously shown by the phase diagram to be 600 $^{\circ}\text{C}$. However, with the thermal treatment being performed under an inert atmosphere 900 $^{\circ}\text{C}$ was chosen to probe any phase transitions. PXRD clearly indicates the formation of the rutile phase at this elevated temperature. Some peaks corresponding to the anatase phase remain, suggesting the confined space inside the GNF may stabilise this phase slightly or prevent rearrangement. TEM shows the formation of discrete nanoparticles encapsulated within the GNF structure (Figure 2.21).

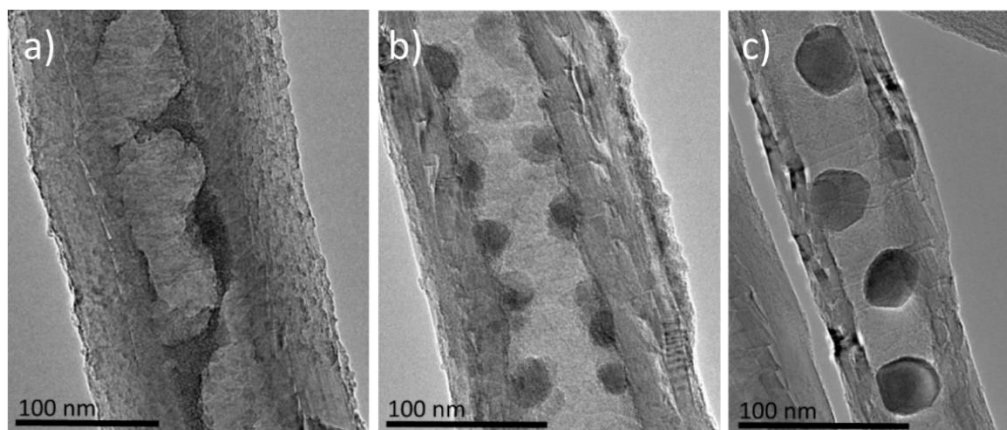


Figure 2.21. TEM analysis of (a) as-synthesised $\text{TiO(OH)}_2\text{@GNF}$, thermally treated $\text{TiO(OH)}_2\text{@GNF}$ at (b) 600 °C in air ($\text{TiO}_2\text{@GNF-600}$) and (c) 900 °C under an Ar atmosphere ($\text{TiO}_2\text{@GNF-900}$).

The formation of the crystal phases is complemented by an increase in nanoparticle size (Table 2.5). Interestingly, due to the thin internal coating originally produced the limited amount of material gives control of the nanoparticle size which prevents blocking of the nanotube making them very useful as nanoreactors.

Table 2.5. Summary of $\text{TiO(OH)}_2\text{@GNF}$ thermal treatment at different temperatures.

Material	TiO_2 particle size (nm) ^a	TiO_2 crystal structure ^b
$\text{TiO(OH)}_2\text{@GNF}$	N/A	Amorphous
$\text{TiO}_2\text{@GNF-600}$	12.4±4.0	Anatase
$\text{TiO}_2\text{@GNF-900}$	28.4±15.7	Anatase + Rutile

^a calculated from TEM ^b from PXRD.

The ability to control crystal phase is interesting as it can have dramatic effects of the chemical properties of the metal oxide as rutile titania nanoparticles were shown to have very high photocatalytic properties in the decomposition of phenol due to the presence of the (110) plane which provided an abundance

of reactive Ti^{3+} sites and hydroxyl groups.⁶⁹ This outperformed the anatase titania powder with the same specific surface area, highlighting the importance of being able to control crystal phase within our composite materials.

Simple thermal manipulation has identified some control over crystallinity, morphology, size and crystal phase of the metal oxides that are encapsulated within the graphitised nanofibres. Precise control of these features at the nanoscale offers the potential for the tailoring of materials for specific applications.

2.4. Conclusions

A versatile strategy for the confinement of hydroxylated group IV metal oxides inside GNF has been established using gas phase deposition or liquid filling approaches of the metal chlorides. Subsequent base-catalysed hydrolysis provides control over loading and chemical composition of the encapsulated metal oxyhydroxide nanomaterials. Excess metal oxide can be effectively removed by exploiting the hydrophobic nature of the GNF which allows for effective purification of the nanoreactors.

Using a holistic approach, several bulk and local probe techniques were combined to effectively characterise and rationalise the physical and chemical properties of the amorphous encapsulated material. The GNF was shown to template a unique thin layer amorphous coating which covers large portions of the nanofibre interior channel due to preferential interactions with the GNF corrugated folds. These metal oxyhydroxide structures have high surface areas, increased defects sites and surface groups but did not restrict mass transport through the internal cavity. This yields a new breed of nanoreactors which are very motivating for the use in catalytic reactions. Manipulation of the morphology, crystallinity, size and phase of the encapsulated materials could be achieved by thermal treatment and leads to a catalogue of spatially confined nanomaterials which could be applied to several fields of research.

2.5. Experimental

2.5.1. General

Standard reagents and solvents, titanium tetrachloride (>99%), zirconium tetrachloride (99%) and hafnium tetrachloride (98%) were purchased from Sigma-Aldrich Chemicals (Dorset, UK) and were stored under an inert environment and used as received.

Thermogravimetric analysis was performed using a TA Q500 thermogravimetric analyser. All samples were deposited onto platinum pans for analysis, heated in air (90 mL/min) from room temperature up to 1000 °C at a rate of 5 °C/min, followed by an isothermal hold at 1000 °C for 10 minutes.

All powder X-ray diffraction measurements were performed on a PANalytical X'Pert Pro diffractometer equipped with a Cu K(α) radiation source ($\lambda=1.5432\text{\AA}$, 40 kV, 40 mA) in Bragg-Brentano geometry. For ambient temperature measurements, the sample was mounted on a Si zero-background holder using isopropyl alcohol to aid adhesion. The parameters for a typical experiment were: 5 ° start angle, 80 ° stop angle, 0.0525 ° step size, 6080 s time per step and 0.00220 °/s scan speed. High temperature PXRD measurements were performed using an Anton Parr (HTK 1200N) high temperature oven chamber in air up to 600 °C on an alumina support.

Transmission electron microscopy (TEM) and dark field scanning transmission electron microscopy (STEM) were performed using a JEOL JEM-2100+ microscope operated at 200 keV. TEM samples were prepared *via* a drop

casting technique, where samples were dispersed in methanol, followed by deposition onto copper grid mounted “lacey” carbon films (Agar). All images were processed using Gatan Digital Micrograph software. Energy dispersive X-ray spectroscopy and mapping were acquired using an Oxford Instruments INCA X-ray microanalysis system. $K\alpha$ values were used for carbon, oxygen chlorine and titanium, $L\alpha$ value was used for zirconium and $M\alpha$ values were used for hafnium, and the beam was condensed to areas suspended over holes of the amorphous carbon film (to negate the contribution to the carbon signal from the support film). Electron energy loss spectroscopy (EELS) was performed using an Enfinium SE system. Tomography measurements were conducted using a JEOL FEGTEM microscope operating at 200 keV and using a Gatan 916 high tilt tomography holder, acquiring images at 1° tilt intervals over a range of -40 to $+40$ degrees with gold nanoparticles as fiducial markers. Annular dark-field images were acquired at 10 cm camera length. Tomographic reconstruction was performed via the IMOD v4.9.3 software, using 10 iterations of the SIRT algorithm and an approach proposed by DN Mastronarde (1997).⁷⁰ Scanning electron microscopy (SEM) was performed on a JEOL 6490LV SEM operating at 15kV.

2.5.2. Carbon nanomaterials sources and pre-treatment

Graphitised nanofibres (PR19-XT-HHT, Fe content <100 ppm) were obtained from Pyrograf Products Inc (Cedarville, Ohio) and were synthesised using a chemical vapour deposition technique. GNF pre-treatment consisted of thermal treatment at 500°C in air for 30 minutes to remove water or other

amorphous carbon. Pre-treated carbon nanomaterials were applied directly to reactions.

2.5.3. Preparation of hydroxylated metal oxides inside graphitised nanofibres

For the liquid-phase filling of TiCl_4 into graphitised nanofibres, GNF (25 mg) were pre-treated then immediately placed into a Schlenk tube under an inert atmosphere of argon and heated to 80 °C. TiCl_4 (1 mL) was added and the mixture stirred at 500 rpm for 1 hour. The obtained slurry was then exposed to air and, once the production of hydrochloric acid vapour had subsided, washed with ammonium hydroxide (5 mL, 35%) with gentle agitation.

For the gas-phase filling ZrCl_4 and HfCl_4 into graphitised nanofibres, GNF (75 mg) were pre-treated then immediately loaded into a Pyrex ampoule (d = 10 mm, L = 12 cm) with either ZrCl_4 or HfCl_4 (75 mg). The solids were then sealed under vacuum (3×10^{-5} mbar) and heated at 400 °C for 48 h. The ampoule was immediately cooled and opened, with the resultant black solid washed with ammonium hydroxide (5 mL, 35%) with gentle agitation.

For all materials, diethyl ether (5 mL) was then added and the biphasic mixture vigorously shaken. The aqueous layer was removed and discarded, with the remaining black solid collected from the organic layer by vacuum filtration (0.2 μm PTFE membrane) and dried under ambient conditions overnight.

2.5.4. Manipulation of hydroxylated metal oxides inside graphitised nanofibres

The composite materials (10mg) were heated to a specific temperature in air or an inert atmosphere for 1 hour at a ramp rate of 10 °C/min. The samples were held for 1 hour and then allowed to cool to room temperature over a specific length of time (Table 2.6).

Table 2.6. Thermal manipulation parameters.

Material	Corresponding section	Temperature (°C)	Procedure Atmosphere	Cooling time (hours)
TiO ₂ @GNF-600	2.3.4.1	600	Air	2
ZrO ₂ @GNF-600	2.3.4.1	600	Air	2
HfO ₂ @GNF-600	2.3.4.1	600	Air	2
ZrO ₂ @GNF-400	2.3.4.1	400	Air	2
TiO ₂ @GNF-900	2.3.4.2	900	Ar	5

2.6. References

1. Y. Bai, Y. B. Dou, L. H. Xie, W. Rutledge, J. R. Li and H. C. Zhou, *Chem. Soc. Rev.*, 2016, **45**, 2327-2367.
2. Y. M. Dai, L. L. Niu, J. Q. Zou, T. X. Chen, H. Liu and Y. Zhou, *Chin. Chem. Lett.*, 2018, **29**, 887-891.
3. X. Y. Xiao, L. L. Liu, J. H. Ma, Y. Ren, X. W. Cheng, Y. H. Zhu, D. Y. Zhao, A. A. Elzatahry, A. Alghamdi and Y. H. Deng, *ACS Appl. Mater. Interfaces*, 2018, **10**, 1871-1880.
4. M. N. Zhang, J. Jia, K. Huang, X. D. Hou and C. B. Zheng, *Chin. Chem. Lett.*, 2018, **29**, 456-460.
5. M. J. Katz, J. E. Mondloch, R. K. Totten, J. K. Park, S. T. Nguyen, O. K. Farha and J. T. Hupp, *Angew. Chem.-Int. Edit.*, 2014, **53**, 497-501.
6. N. E. Thornburg, A. B. Thompson and J. M. Notestein, *ACS Catal.*, 2015, **5**, 5077-5088.

7. J. E. Mondloch, M. J. Katz, W. C. Isley, 3rd, P. Ghosh, P. Liao, W. Bury, G. W. Wagner, M. G. Hall, J. B. DeCoste, G. W. Peterson, R. Q. Snurr, C. J. Cramer, J. T. Hupp and O. K. Farha, *Nat. Mater.*, 2015, **14**, 512-516.
8. N. Sharma and R. Kakkar, *Adv. Mat. Lett.*, 2013, **4**, 508-521.
9. J. H. Choi, Y. Mao and J. P. Chang, *Mater. Sci. Eng. R-Rep.*, 2011, **72**, 97-136.
10. I. Salem, *Catal. Rev.-Sci. Eng.*, 2003, **45**, 205-296.
11. I. Sulym, O. Goncharuk, D. Sternik, E. Skwarek, A. Derylo-Marczewska, W. Janusz and V. M. Gun'ko, *Nanoscale Res. Lett.*, 2016, **11**, 9.
12. A. Pucci and N. Pinna, *Z. Naturforsch., B: Chem. Sci.*, 2010, **65**, 1015-1023.
13. B. Ni and X. Wang, *Adv. Sci.*, 2015, **2**, 22.
14. T. J. Bandoz, M. Laskoski, J. Mahle, G. Mogilevsky, G. W. Peterson, J. A. Rossin and G. W. Wagner, *J Phys Chem C*, 2012, **116**, 11606-11614.
15. V. V. Singh, A. Martin, K. Kaufmann, S. D. S. de Oliveira and J. Wang, *Chem. Mater.*, 2015, **27**, 8162-8169.
16. T. Islamoglu, A. Atilgan, S. Y. Moon, G. W. Peterson, J. B. DeCoste, M. Hall, J. T. Hupp and O. K. Farha, *Chem. Mater.*, 2017, **29**, 2672-2675.
17. G. K. Prasad, T. H. Mahato, B. Singh, K. Ganesan, A. R. Srivastava, M. P. Kaushik and R. Vijayraghavan, *AIChE J.*, 2008, **54**, 2957-2963.
18. M. Drogenik, D. Lisjak and D. Makovec, in *Current Research in Advanced Materials and Processes*, eds. D. P. Uskokovic, S. K. Milonjic and D. I. Rakovic, Trans Tech Publications Ltd, Zurich-Uetikon, 2005, vol. 494, pp. 129-136.
19. C. C. Koch, *Rev. Adv. Mater. Sci.*, 2003, **5**, 91-99.
20. S. J. Smith, B. Y. Huang, S. F. Liu, Q. Y. Liu, R. E. Olsen, J. Boerio-Goates and B. F. Woodfield, *Nanoscale*, 2015, **7**, 144-156.
21. N. Pinna and M. Niederberger, *Angew. Chem.-Int. Edit.*, 2008, **47**, 5292-5304.
22. A. Ali, H. Zafar, M. Zia, I. U. Haq, A. R. Phull, J. S. Ali and A. Hussain, *Nanotechnol. Sci. Appl.*, 2016, **9**, 49-67.
23. Z. Q. Niu and Y. D. Li, *Chem. Mater.*, 2014, **26**, 72-83.
24. X. Xue, Z. Zhou, B. Peng, M. M. Zhu, Y. J. Zhang, W. Ren, Z. G. Ye, X. Chen and M. Liu, *Rsc Advances*, 2015, **5**, 79249-79263.
25. P. Serp and E. Castillejos, *ChemCatChem*, 2010, **2**, 41-47.
26. X. L. Pan and X. H. Bao, *Acc. Chem. Res.*, 2011, **44**, 553-562.
27. S. A. Miners, G. A. Rance and A. N. Khlobystov, *Chem. Soc. Rev.*, 2016, **45**, 4727-4746.
28. A. N. Khlobystov, *ACS nano*, 2011, **5**, 9306-9312.
29. R. S. Ruoff and D. C. Lorents, *Carbon*, 1995, **33**, 925-930.
30. K. Balasubramanian and M. Burghard, *Small*, 2005, **1**, 180-192.
31. D. Mattia and Y. Gogotsi, *Microfluid. Nanofluid.*, 2008, **5**, 289-305.
32. T. W. Chamberlain, T. Zoberbier, J. Biskupek, A. Botos, U. Kaiser and A. N. Khlobystov, *Chem. Sci.*, 2012, **3**, 1919-1924.

33. M. Chancolon, F. Archambault, S. Bonnamy, A. Traverse, L. Olivi and G. Vlaic, *J. Non-Cryst. Solids*, 2006, **352**, 99-108.
34. G. Lota, E. Frackowiak, J. Mittal and M. Monthieux, *Chem. Phys. Lett.*, 2007, **434**, 73-77.
35. R. Sagawa, W. Togashi, T. Akita and Y. Takai, *Microscopy*, 2013, **62**, 271-282.
36. P. Costa, J. Sloan, T. Rutherford and M. L. H. Green, *Chem. Mater.*, 2005, **17**, 6579-6582.
37. O. N. Metelkina, R. W. Lodge, P. G. Rudakovskaya, V. M. Gerasimov, C. H. Lucas, I. S. Grebennikov, I. V. Shchetinin, A. G. Savchenko, G. E. Pavlovskaya, G. A. Rance, M. D. Gimenez-Lopez, A. N. Khlobystov and A. G. Majouga, *J. Mater. Chem. C*, 2017, **5**, 2167-2174.
38. M. D. Gimenez-Lopez, A. La Torre, M. W. Fay, P. D. Brown and A. N. Khlobystov, *Angew. Chem., Int. Ed.*, 2013, **52**, 2051-2054.
39. M. A. Lebedeva, T. W. Chamberlain, M. Schroder and A. N. Khlobystov, *Chem. Mater.*, 2014, **26**, 6461-6466.
40. B. Cornelio, A. R. Saunders, W. A. Solomonsz, M. Laronze-Cochard, A. Fontana, J. Sapi, A. N. Khlobystov and G. A. Rance, *J. Mater. Chem.*, 2015, **3**, 3918-3927.
41. E. Castillejos, P. J. Debouttiere, L. Roiban, A. Solhy, V. Martinez, Y. Kihn, O. Ersen, K. Philippot, B. Chaudret and P. Serp, *Angew. Chem.-Int. Edit.*, 2009, **48**, 2529-2533.
42. A. La Torre, M. W. Fay, G. A. Rance, M. Del Carmen Gimenez-Lopez, W. A. Solomonsz, P. D. Brown and A. N. Khlobystov, *Small*, 2012, **8**, 1222-1228.
43. W. Chen, Z. Fan, B. Zhang, G. Ma, K. Takanahe, X. Zhang and Z. Lai, *J. Am. Chem. Soc.*, 2011, **133**, 14896-14899.
44. A. Botos, J. Biskupek, T. W. Chamberlain, G. A. Rance, C. T. Stoppiello, J. Sloan, Z. Liu, K. Suenaga, U. Kaiser and A. N. Khlobystov, *J. Am. Chem. Soc.*, 2016, **138**, 8175-8183.
45. T. W. Chamberlain, A. M. Popov, A. A. Knizhnik, G. E. Samoilov and A. N. Khlobystov, *ACS nano*, 2010, **4**, 5203-5210.
46. C. T. Stoppiello, J. Biskupek, Z. Y. Li, G. A. Rance, A. Botos, R. M. Fogarty, R. A. Bourne, J. Yuan, K. R. J. Lovelock, P. Thompson, M. W. Fay, U. Kaiser, T. W. Chamberlain and A. N. Khlobystov, *Nanoscale*, 2017, **9**, 14385-14394.
47. A. La Torre, M. D. Gimenez-Lopez, M. W. Fay, G. A. Rance, W. A. Solomonsz, T. W. Chamberlain, P. D. Brown and A. N. Khlobystov, *ACS nano*, 2012, **6**, 2000-2007.
48. M. V. Kharlamova, *Appl. Phys. A-Mater. Sci. Process.*, 2016, **122**, 8.
49. M. V. Kharlamova, M. M. Brzhezinskaya, A. S. Vinogradov, I. P. Suzdalev, Y. V. Maksimov, V. K. Imshennik, S. V. Novichikhin, A. V. Krestinin, L. V. Yashina, A. V. Lukashin, Y. D. Tret'yakov and A. A. Eliseev, *Nanotechnol. Russ.*, 2009, **4**, 634.
50. M. V. Kharlamova, L. V. Yashina, A. A. Eliseev, A. A. Volykhov, V. S. Neudachina, M. M. Brzhezinskaya, T. S. Zyubina, A. V. Lukashin and Y. D. Tret'yakov, *Physica Status Solidi B*, 2012, **249**, 2328-2332.

51. Y. K. Chen, A. Chu, J. Cook, M. L. H. Green, P. J. F. Harris, R. Heesom, M. Humphries, J. Sloan, S. C. Tsang and J. F. C. Turner, *J. Mater. Chem.*, 1997, **7**, 545-549.
52. A. R. Puigdollers, P. Schlexer, S. Tosoni and G. Pacchioni, *Acs Catalysis*, 2017, **7**, 6493-6513.
53. G. Pacchioni and P. Pescarmona, *Surf. Sci.*, 1998, **412-13**, 657-671.
54. A. R. Puigdollers, F. Illas and G. Pacchioni, *Rend. Lincei.-Sci. Fis. Nat.*, 2017, **28**, 19-27.
55. R. H. Nielsen and G. Wilfing, *Ullmann's Encyclopedia of Industrial Chemistry*, 2000.
56. D. A. Giannakoudakis, J. K. Mitchell and T. J. Bandosz, *J. Mater. Chem. A*, 2016, **4**, 1008-1019.
57. G. K. Chuah, S. Jaenicke, S. A. Cheong and K. S. Chan, *Appl. Catal. A-Gen.*, 1996, **145**, 267-284.
58. W. A. Solomonsz, G. A. Rance, B. J. Harris and A. N. Khlobystov, *Nanoscale*, 2013, **5**, 12200-12205.
59. R. Saito, M. Hofmann, G. Dresselhaus, A. Jorio and M. S. Dresselhaus, *Adv. Phys.*, 2011, **60**, 413-550.
60. C. Ahn and O. Krivanek, *EELS atlas*, Gatan, 1983.
61. Y. Q. Hou, D. M. Zhuang, G. Zhang, M. Zhao and M. S. Wu, *Appl. Surf. Sci.*, 2003, **218**, 97-105.
62. G. S. Chabey, Y. Yao, J. P. A. Makongo, P. Sahoo, D. Misra, P. F. P. Poudeu and J. B. Wiley, *RSC Adv.*, 2012, **2**, 9207-9213.
63. S. Dai, Y. Wu, T. Sakai, Z. Du, H. Sakai and M. Abe, *Nanoscale Res. Lett.*, 2010, **5**, 1829.
64. N. Chandra, D. K. Singh, M. Sharma, R. K. Upadhyay, S. S. Amritphale and S. K. Sanghi, *J. Colloid Interface Sci.*, 2010, **342**, 327-332.
65. P. S. Lysaght, P. J. Chen, R. Bergmann, T. Messina, R. W. Murto and H. R. Huff, *J. Non-Cryst. Solids*, 2002, **303**, 54-63.
66. D. Chiche, M. Digne, R. Revel, C. Chaneac and J. P. Jolivet, *J Phys Chem C*, 2008, **112**, 8524-8533.
67. X. L. Nie, S. P. Zhuo, G. Maeng and K. Sohlberg, *Int. J. Photoenergy*, 2009, 294042.
68. G. Kavei, A. Nakaruk and C. C. Sorrell, *Mater. Sci. Appl.*, 2011, **2**, 700.
69. J. Sun, L. Gao and Q. H. Zhang, *J. Am. Ceram. Soc.*, 2003, **86**, 1677-1682.
70. D. N. Mastronarde, *J. Struct. Biol.*, 1997, **120**, 343-352.

Nanoreactors and nanosponges for enhanced decontamination of organophosphates

3.1. Background

Organophosphorus (OP) species, containing phosphate and/or thiophosphate ester bonds, represent some of the most toxic chemicals in the world, posing a substantial threat to human health (Figure 3.1).¹⁻⁴

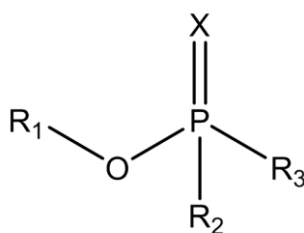
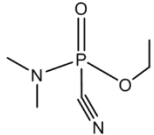
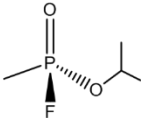
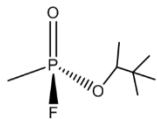
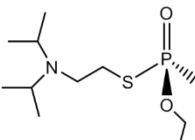
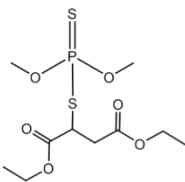


Figure 3.1. General structures of organophosphorus species, X = O/S.

Used in industry, agriculture and the military, they are considered deadly organic compounds because they are readily absorbed by skin contact, inhalation and ingestion (Table 3.1).^{5, 6} In warfare, they are commonly employed as a nerve agent acting to prevent the breakdown of the neurotransmitter acetylcholine at the neuromuscular junctions, resulting in the muscles and organs inability to relax. This leads to loss of muscle control, asphyxiation and subsequent death within minutes.⁷

Table 3.1. Physical and chemical properties of some common nerve agents.^{8,9}

OP agent	Application	Molecular structure	Molecular weight	LD ₅₀ in rat oral (mg/kg) ^a
Tabun (GA)	G agent in chemical warfare		162.12	3.6
Sarin (GB)	G agent in chemical warfare		140.10	0.67
Soman (GD)	G agent in chemical warfare		182.20	0.37
VX	V agent in chemical warfare		267.40	0.19
Malathion	Pesticide		330.36	>1000

^a LD₅₀ is the "Medium Lethal Dose" – Dosage required to kill half of a tested population

Although significant research has been performed targeting the decontamination of OP in the field, stockpiles of OP agents left over from conflicts and industry pose a new and important challenge.^{10, 11 12} Therefore, developing new strategies for decontaminating large amounts of OP species is essential.

Nanoscale metal oxides have been shown to readily adsorb and degrade OP agents into non-toxic products. The two-step mechanism involved significantly enhances the decontamination abilities of metal oxides as the toxic agent is first adsorbed onto the surface, followed by deactivation of the toxic compound. Owing to the inherent risk associated with the handling and use of

nerve agents with the laboratory environment, significant research has been performed using simulants such as dimethyl methyl phosphate (DMMP) and has critically identified that OP readily adsorbs through the phosphoryl oxygen onto the metal oxide at the Lewis acidic metal atom or Lewis basic hydroxyl sites (Figure 3.2). Once bound the decomposition of the simulant occurs via hydrolysis from the reactive groups on the surface.¹³

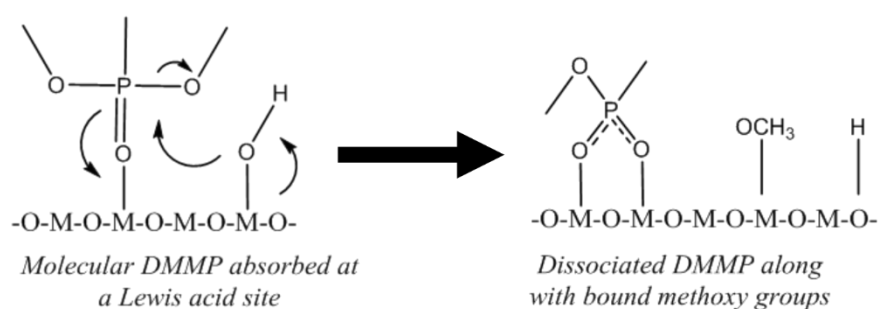


Figure 3.2. Accepted adsorption mechanism for OP agents (DMMP) onto metal oxide surfaces and the corresponding nucleophilic attack by surface groups resulting in decontamination. Reproduced from Gordon et al, copyright American Chemical Society.¹³

Zirconium hydroxide was shown to catalyse near instantaneous decontamination of VX, attributed to the basic metal oxide surface and the ability of acidic bridging hydroxyl groups to protonate and hydrolyse the VX agent.¹⁴ Other metal oxides such as MgO and CaO were found to be so basic that they irreversibly bind to OP agents, therefore, tuning the metal oxide surface is crucial.¹⁵ The combination of Lewis acidic metal cations and bridging and surface groups, such as hydroxide anions, has led to very short half-lives for OP agents when zirconium based metal-organic frameworks have been applied to hydrolysis reactions.¹⁶

Although metal oxides have shown promise towards the decontamination of OP, their reactivity can be further enhanced by using metal oxide species with nanosized dimensions.¹⁷ There are several features that make nanoscale metal oxides superior for OP destruction and these should be considered when developing new catalysts for this application (Table 3.2).

Table 3.2. Features of nanoscale metal oxides for decontaminating CWA.^{5, 18-20}

Feature	Comments
High surface area	This plays a significant role due to an increase of the available catalyst surface to interact with the OP
Increased reactive sites	Dislocations and defects in shape can lead to increased number of edges and corners with following reactive sites present which drives superior reactivity: There are more available metal cation (Lewis acidic) and oxide anion (Lewis basic) sites to interact with the agents Increase in number of Frenkel and Schottky defect sites leads to vacancies in the crystal structure which give new points of interaction
Morphology of nanocrystal	Unique morphologies can lead to a low coordination metal sites due to edges and kinks which gives increased reactivity
Increased surface bound hydroxyl species	These species allow for the adsorption on these sites but also provide reactive components necessary for hydrolysis

The unique morphology of nanotubular titania provided high surface area and increased reactive sites for adsorption which were able to assist in the hydrolysis of both sarin and VX as a solid catalyst.²¹ This catalyst was found to absorb the toxic species within the tube or between the titania sheets, which provided a spatially confined environment for hydrolysis which led to fast rates

of decontamination ($t^{1/2} < 30\text{mins}$) when compared to conventional anatase titania ($t^{1/2} > 250\text{mins}$).²² TiO_2 nanocrystals with increased surface hydroxyl concentration were found to perform even better than nanotubular titania at VX hydrolysis, which highlights the importance of these surface groups to drive enhanced hydrolysis.²² Cerium dioxide showed impressive abilities to destroy more than 90% of an OP simulant in less than 10 min.²³ This was attributed to its nanocrystalline nature which promoted the formation of crystal defects and resulted in increased adsorption. The presence of surface OH groups and Ce^{3+} cations were also found to be essential components to drive the adsorptive decontamination.

With the successes of nanoscale metal oxides improving OP decontamination, building composite materials to enhance their abilities is an emerging area of research.^{24, 25} Confining catalysts inside nanoscale vessels such as carbon nanotubes offers several benefits and has to date, not been explored. Carbon nanotubes can act as templates allowing the formation and stabilisation of unique nanoscale materials due to spatial confinement.²⁶ Previous work has shown that by encapsulating inorganic materials inside carbon nanotubes can lead to nanomaterials with high surface area and unique morphologies.^{27, 28} As well as a host for nanomaterials, carbon nanotubes can also act as nanoreactors, by promoting high concentrations of reagent to catalyst surfaces within the internal cavity of the nanotube which increases rates of reactions.²⁹ Previous work utilising carbon nanoreactors for catalysis has identified local

concentrations as key for confined reactions and was responsible for significant changes in the selectivity of the hydrosilylation reaction (Figure 3.3).³⁰

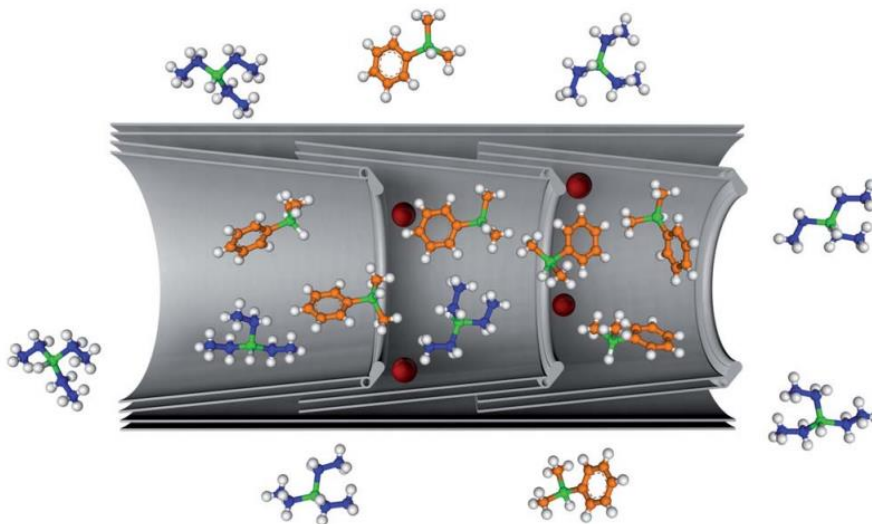


*Figure 3.3. Schematic representation of the selective enrichment of reactants by carbon nanoreactors. This leads to high local concentration effects within the internal channel and results in enhanced and selective confined reactions.*³⁰

The confinement of nanostructured group IV metal oxyhydroxides inside hollow carbon graphitised nanofibres was demonstrated in Chapter 2 and they were shown to possess high surface area, amplified defect sites and increased hydroxyl groups. Combining these features with the high local concentration effects observed inside carbon nanoreactors identifies an interesting research topic of applying these nanoreactors to investigate the decontamination of OP compounds.

3.2. Aim and Objectives

The aim of this study is to investigate carbon nanoreactors comprising group IV metal oxyhydroxide nanomaterials encapsulated inside hollow graphitised nanofibres (GNF) for the decontamination of toxic organophosphorus (OP) species (Figure 3.4).



Figure 3.4. Schematic diagram utilising carbon nanoreactors to promote hydrolysis of OP agents to facilitate decontamination.

With nanoscale group IV metal oxides known to promote the enhanced hydrolysis of organophosphorus agents, an appropriate standard hydrolysis procedure will be first developed which can be easily monitored by spectroscopic techniques.

The empty GNF and the hybrid group IV metal oxyhydroxide carbon nanoreactors developed in Chapter 2 will be evaluated for their abilities to enhance hydrolysis and decontamination of OP compounds from various aqueous solutions. The loading and composition of the catalyst will be manipulated to provide a further understanding of the structure-function relationship. These nanoreactors will be considered for the importance

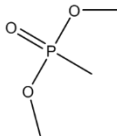
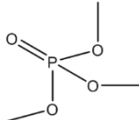
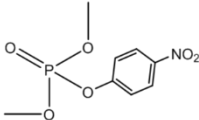
towards broader science and could provide significant knowledge for the development of future hydrolysis catalysts.

3.3. Results and discussion

3.3.1. Hydrolysis procedure of organophosphorus species

With organophosphorus agents representing a class of extremely toxic chemicals, experimentation involving OP species classed as chemical warfare agents (CWA) such as sarin, soman or VX are prohibited in university laboratories. Therefore, OP simulants are used to mimic the behaviour of the real agents. Such species contain similar functional groups and replicate the physical and chemical properties of the corresponding highly toxic compounds, but they have reduced toxicity making them suitable for a research laboratory.⁵ In the literature, many OP simulants have been utilised to investigate the decontamination of toxic organophosphorus agents (Table 3.3).

Table 3.3. Common nerve agent simulants used in the literature to simulate OP (sarin) hydrolysis.^{5,9}

Agent Simulant	Molecular structure	LD ₅₀ (mg/kg) ^a
Dimethyl methylphosphonate (DMMP)		8210
Trimethyl phosphate (TMP)		840
Dimethyl 4-nitrophenyl phosphate (DMNP)		2.5

^a LD₅₀ is the “Medium Lethal Dose” from oral route in mice – Dosage required to kill half of a tested population.

DMMP, TMP and DMNP are commonly used to simulate the decomposition reactions of G agents (such as sarin) on metal oxide surfaces.^{5, 31} These simulants share several similar features with sarin and other organophosphorus agents as the adsorption chemistry on metal oxides resembles that of the toxic species.⁵

For species such as DMMP and TMP, monitoring the rate of hydrolysis can be performed using NMR spectroscopy. ¹H and ³¹P NMR spectroscopy can provide quantitative data due to their distinctive spectra generated as a result of the loss of symmetry or aromatic group in the molecule after hydrolysis. DMMP was also shown to be stable in D₂O with minimal background hydrolysis observed after the agent was left in the solvent for 200 minutes (Figure 3.5).

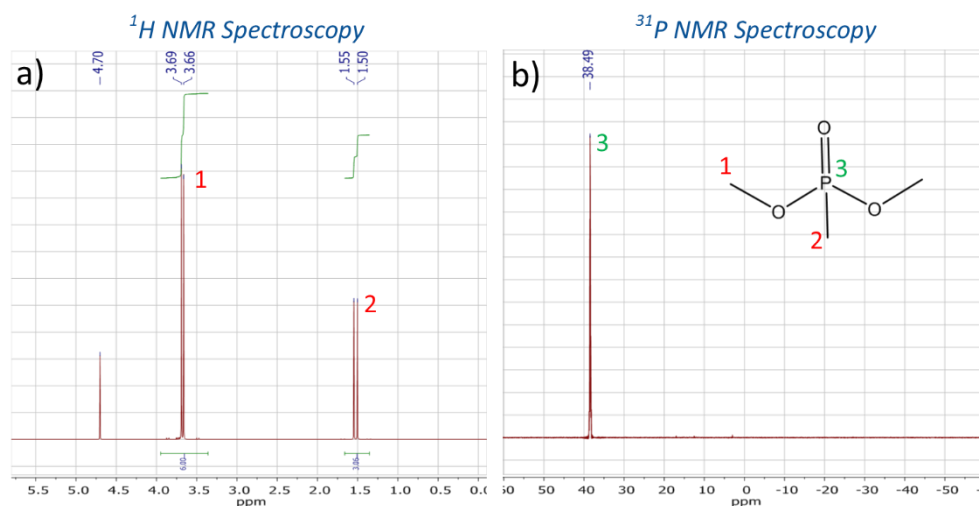


Figure 3.5. (a) ^1H and (b) ^{31}P NMR spectroscopy of DMMP in D_2O after 200 minutes highlighting no background hydrolysis occurred. The peak at 4.70 ppm identified as residual D_2O peak.

However, whilst informative, issues associated with sampling poses a key challenge when using ^1H NMR spectroscopy, especially for kinetic studies. For this reason, dimethyl 4-nitrophenyl phosphate (DMNP) is often used to study organophosphate decontamination as it has the added advantage of forming 4-nitrophenoxide during hydrolysis and thus allows the kinetics of this reaction to be readily monitored using UV-Vis spectroscopy (Figure 3.6).³²⁻³⁴ This method of analysis provides a quick and effective examination of the reaction progress and can be much more effectively sampled relative to NMR spectroscopy. UV-Vis spectroscopy analysis of DMNP hydrolysis is usually performed at pH 10 as the phenolate ion is exclusively produced resulting in a distinctive peak at 400 nm which simplifies analysis.³²

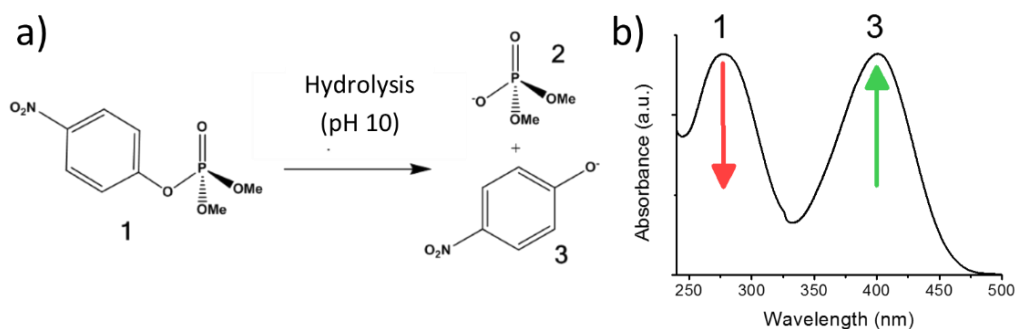


Figure 3.6. (a) Scheme for the hydrolysis of the simulant DMNP with the composite material which can be monitored by UV-Vis spectroscopy. (b) UV-Vis spectrum of DMNP and phenolate ion, with the diagnostic peaks at 273 and 400 nm for the starting material and product, respectively.

Previously, an organic buffer solution utilising *N*-ethylmorpholine was employed to regulate the pH of the reaction mixture. The benefit of using this organic buffer is that the reaction conditions are milder and so do not bring about decomposition of the catalyst (such as MOF based catalysts), a feature commonly observed when using hydroxide solutions. However, the organic buffers are flammable and highly toxic, and therefore, unsuitable for real-world applications; conversely, aqueous bases, such as KOH and NaOH, are already established in several industrial processes targeting hydrolysis reactions.²⁴ By increasing the number of hydroxides present in the solution, the ability to regenerate the surface hydroxide groups - which are crucial for adsorptive decontamination - may enhance hydrolysis further. Therefore, investigation of the hydroxide buffer was initially undertaken to probe the stability and effectiveness of the catalytic nanoreactors developed in Chapter 2.

In a typical OP decontamination experiment, 15-25 μmol of DMNP is employed with 1mL of a buffer solution.^{24, 32, 33} 10-30 μL aliquots extracted from the reaction mixture at specific time intervals are then diluted with the buffer

solution and a UV-Vis spectrum acquired immediately. Given the high toxicity and molar absorption coefficient of the DMNP and its products (9000 and 18000 $\text{m}^2 \text{mol}^{-1}$ respectively) only very small quantities of the OP simulant are required. In this study, an effective dispersion of the nanoreactors with sufficient active catalyst (23 mg of composite nanoreactors containing approximately 1 mg of $\text{MO}(\text{OH})_2$) required 2 mL the buffer solution. Although this uses more buffer than typical investigations, the concentration of nerve agent in the buffer will be kept consistent with previous work. Many hydrolysis reactions are generally performed at room temperature (RT) and although hydrolysis has been shown to be more effective at 60 °C, for applicability to on-field situations and safety reasons RT was employed for this work.²⁵

Based on this foundation, standard hydrolysis and measurement procedures for investigating the nanoreactors decontamination abilities were proposed (Figure 3.7).

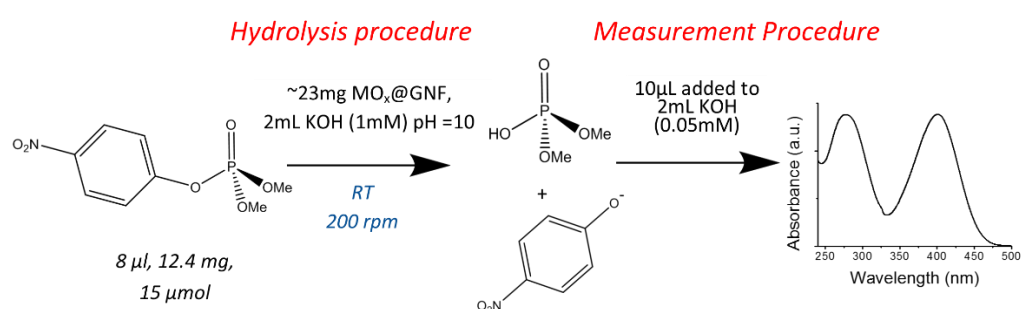


Figure 3.7. Proposed scheme for standard hydrolysis and measurement procedures for monitoring decontamination of DMNP with nanoreactors.

3.3.2. Hydrolysis of DMNP using nanoreactors

3.3.2.1. Hydrolysis of DMNP - Control reactions

To investigate the abilities of the nanoreactors to catalyse the hydrolysis of organophosphates, control experiments were first performed to understand the rate of DMNP hydrolysis with empty GNF and in the absence of any catalyst. Interestingly, when added to the aqueous buffer, DMNP appears to form an emulsion, which homogenises upon agitation. By measuring the absorbance at 273 and 400 nm, the concentration of the DMNP and the phenolate ion and thus the rate of hydrolysis conversion can be calculated. It was observed that 2.2% and 1.9% was hydrolysed after 200 minutes in the absence of a catalyst or when employing GNF respectively. Given the expected increase in hydrolysis rate in the presence of our catalytic nanoreactor this is a suitable time frame for our investigations (Figure 3.8).

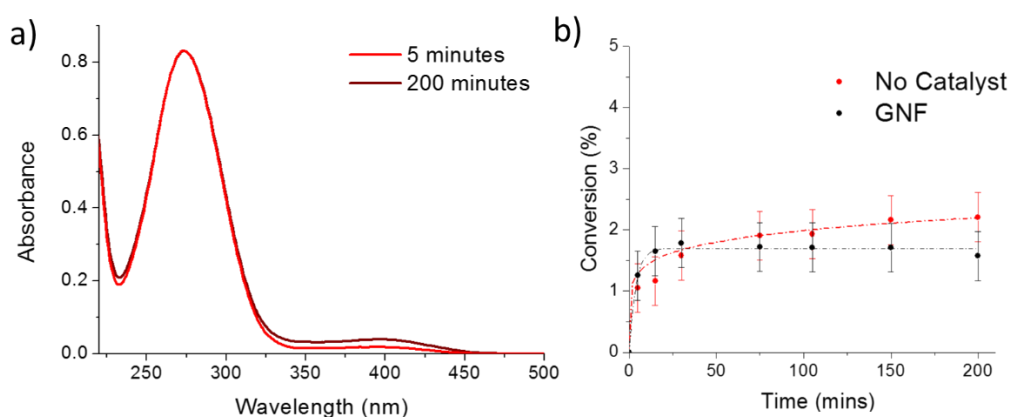


Figure 3.8. (a) UV-Vis spectra at the start (5 minutes - red) and end (200 minutes - brown) of the control hydrolysis reaction and (b) corresponding conversion calculated at different time intervals for no catalyst (red) and the empty GNF (black).

3.3.2.2. Effect of encapsulated metal oxide species on hydrolysis of DMNP

Based on previous literature and advice from an industrial collaborator, titanium and zirconium oxide species have shown reasonable successes in OP destruction *via* adsorptive decontamination.^{14, 22, 32, 35} Chapter 2 demonstrated the ability to synthesise confined Ti and Zr metal oxyhydroxides inside carbon nanoreactors (Figure 3.9).

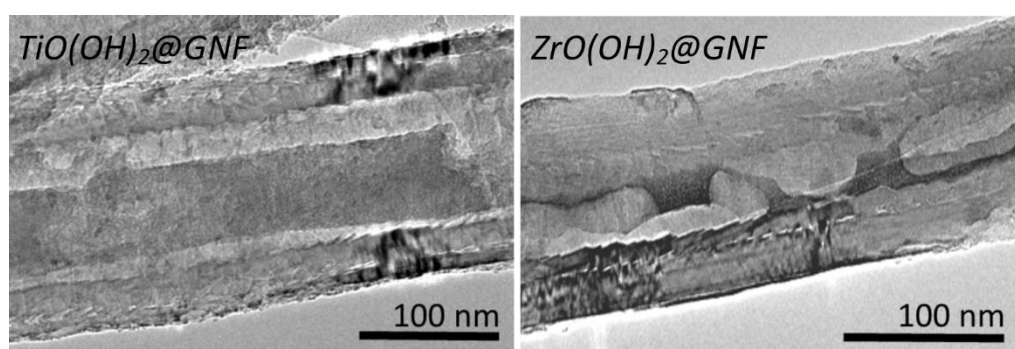


Figure 3.9. Transmission electron microscopy (TEM) of titanium and zirconium oxyhydroxide species encapsulated inside graphitised nanofibres. Metal oxyhydroxide species corresponds to the darker contrasting feature between the nanofibre sidewalls.

This material possessed several promising features such as high surface areas, increased defect sites and hydroxyl groups on the surface which are likely to promote the adsorptive decontamination. These catalytic nanoreactors were probed for their ability to enhance the hydrolysis of DMNP using the standard hydrolysis and measurement procedures (Table 3.4).

Table 3.4. Conversion of DMNP in KOH buffer solution investigating the hydrolysis abilities of composite nanoreactors.

Catalyst ^a	Conversion (%) ^b
None	2.1
GNF	1.8
TiO(OH) ₂ @GNF	2.5
ZrO(OH) ₂ @GNF	8.8

^a 2mL of KOH (1mM - pH 10), with GNF (22mg), ZrO(OH)₂@GNF (23.25mg – 1.25mg of ZrO(OH)₂), TiO(OH)₂@GNF (23.0mg – 1mg of TiO(OH)₂), 200 minutes, 200rpm, RT. ^b Conversion calculated using the concentration of phenolate measured by UV-Vis spectroscopy and the theoretical concentration of DMNP added.

After 200 minutes it was observed that the titanium oxyhydroxide was not able to enhance hydrolysis and the measurement was within the error of the control experiments. Poorer rates of hydrolysis have been attributed to the ineffective OH groups on less basic titania materials which are unable to destroy the toxic compounds.¹⁴ With such small amounts of metal oxide present, it is expected that even the adsorption effects are minimal in this case. For the ZrO(OH)₂@GNF, improved decontamination up to 200 minutes is observed showing that this catalytic surface is capable of adsorptive decontamination as it is not only able to adsorb but hydrolyse the DMNP.

A mechanism for the hydrolysis on the metal oxide can be proposed which involves (i) the coordination of the phosphate group with metal cations and (ii) nucleophilic attack of surface hydroxyl groups (Figure 3.10).

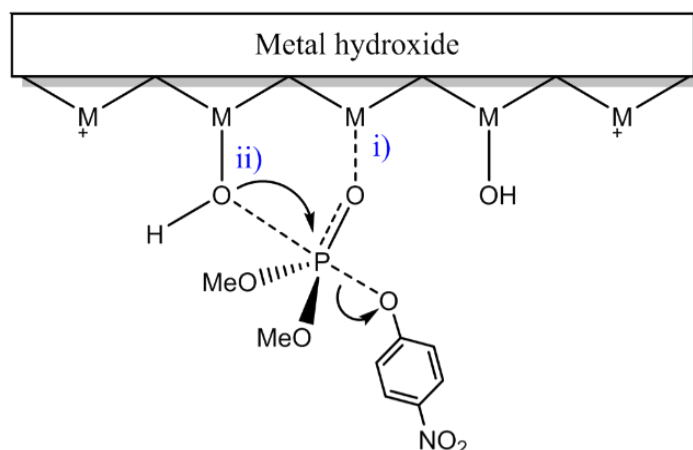


Figure 3.10. Mechanism for the hydrolysis of phosphate esters using $MO(OH)_2$ catalytic surface.

Hydrolysis conversion profiles for the $ZrO(OH)_2@GNF$ nanoreactor catalyst relative to control measurements were realised using the standard procedure (Figure 3.11).

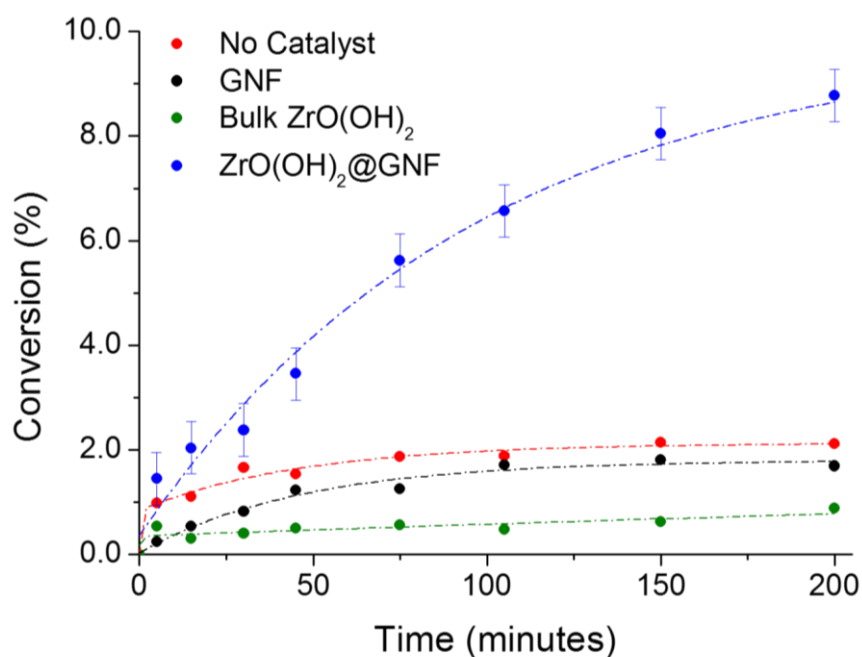


Figure 3.11. Conversions plots highlight the enhanced hydrolysis rate attained using the $ZrO(OH)_2@GNF$ (blue) relative to control reactions using no catalyst (red), GNF, (black) bulk $ZrO(OH)_2$ (green). Conversion calculated using the concentration of phenolate measured by UV-Vis spectroscopy and the theoretical concentration of DMNP added.

This identifies that after 200 minutes the catalyst can increase the rate of hydrolysis of the toxic species to the phenolate when compared to the empty GNF and background hydrolysis. To further understand the effect that confinement of the catalyst has on the hydrolysis reaction a bulk $\text{ZrO}(\text{OH})_2$ was synthesised in the same way as the catalyst in Chapter 2 without GNF being present. Due to its amorphous nature characterisation of this materials proved problematic but the broad peaks identified in powder X-ray diffraction (PXRD), supported literature diffraction patterns for bulk hydroxylated zirconia species (Figure 3.13).³⁶ The same quantity of the active bulk catalyst was applied to the standard hydrolysis procedure and minimal hydrolysis abilities were observed when compared to the significantly more active $\text{ZrO}(\text{OH})_2@GNF$.

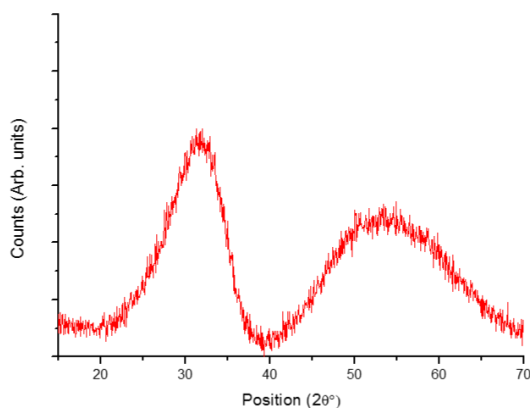


Figure 3.12. PXRD analysis of bulk hydroxylated zirconia. Broad peak at $2\theta = 30^\circ$ supports the formation of a $\text{ZrO}(\text{OH})_2$ species.³⁶

It is important to emphasise that individually GNF and bulk hydroxylated zirconia have little impact on the hydrolysis rate of DMNP; however, when combined in $\text{ZrO}(\text{OH})_2@GNF$, the synergistic effectiveness of the components is enhanced four-fold. Both the increased surface area of the metal species

coating smeared over the GNF internal surface, and the presence of structural defects in the non-stoichiometric hydroxide, can lead to increased Lewis acidity and accessibility of the active sites in $\text{ZrO}(\text{OH})_2@\text{GNF}$ which are important for the hydrolysis of OP agents.³⁷ To confirm the increased surface area for $\text{ZrO}(\text{OH})_2@\text{GNF}$, Brunauer-Emmett-Teller (BET) analysis showed a 13 m^2/g increase in the surface area in comparison to empty GNFs. Considering that the hydroxylated metal oxide comprises only 5 wt.% of $\text{ZrO}_x(\text{OH})_y@\text{GNF}$ this indicates the accessible surface area of encapsulated $\text{ZrO}_x(\text{OH})_y$ is 141 m^2/g ; four times higher than that of the metal hydroxide synthesised in the absence of GNF (Table 3.5).

Table 3.5. BET surface analysis.

Sample	Metal oxide weight in sample (mg)	Surface area (m^2/g) ^a	Pore Vol (cm^3/g)
GNF	0	22.30	0.0749
$\text{Zr}(\text{OH})_4$ bulk	30.5	31.82	0.0704
$\text{Zr}(\text{OH})_4@\text{GNF}$	2.90	36.09	0.0826
<i>Estimated surface area of encapsulated $\text{Zr}(\text{OH})_4 = 141.25 \text{ m}^2/\text{g}$</i>			

^a Surface area analysis was performed using the Brunauer-Emmett-Teller (BET) method.

BET measurements can also provide information about the pore volume in $\text{ZrO}_x(\text{OH})_y@\text{GNF}$, estimating the accessible volume to be $\sim 0.08 \text{ cm}^3/\text{g}$ in the nanoreactors, supporting no blockages and an effective space for confined reactions. Confinement of a catalyst in a nanoreactor is known to enhance local concentration of reactants around catalytic centres, and may also contribute to the increased rate of hydrolysis observed for $\text{ZrO}(\text{OH})_2@\text{GNF}$.²⁹

Considering the small percentage of the catalytically active material in $\text{ZrO}(\text{OH})_2@\text{GNF}$ to the high quantity of simulant present in solution (6.3 mol%) the catalytic nanoreactors have shown impressive initial decontamination abilities towards the organophosphate. A turn over frequency (TOF) for DMNP hydrolysis of $8.3 \times 10^{-3} \text{ min}^{-1}$ was calculated, which exceeds the TOF for sarin obtained using bulk zirconium hydroxide by a factor of 10.¹⁴

It appears from the UV-Vis spectra taken during the hydrolysis reaction that the relationship between the carbon nanoreactor is more complex than being just a hydrolysis catalyst (Figure 3.13). As the absorbance of the DMNP appears to increase during the reaction when the catalyst is present this may indicate that at the start of the reaction, the concentration of reactant changes not only due to the hydrolysis but also due to some additional, faster processes, such as physical absorption of DMNP into the GNF cavity at the start of the process.

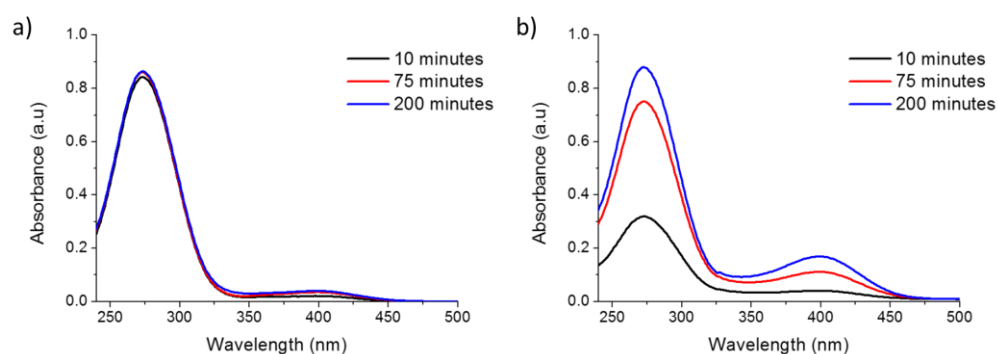


Figure 3.13. Absorption spectra of DMNP in KOH solution at different time intervals with a) no catalysts present and b) $\text{ZrO}(\text{OH})_2@\text{GNF}$ catalyst.

The hydrophobic interior channel is the driving force for the initial uptake, however, due to the weak physical interaction with the GNF and the rapidly stirred solution, homogenisation of the reagent within the solution is observed.

As a result, the concentration of the organophosphorus reagent increases during the hydrolysis reaction. The charged water-soluble phenolate product is expected to be released much faster from the GNF than the reagent, allowing conversion data to be calculated.

To investigate this uptake/release phenomenon, a control experiment monitoring the concentration of DMNP was performed with and without the GNF (Figure 3.14).

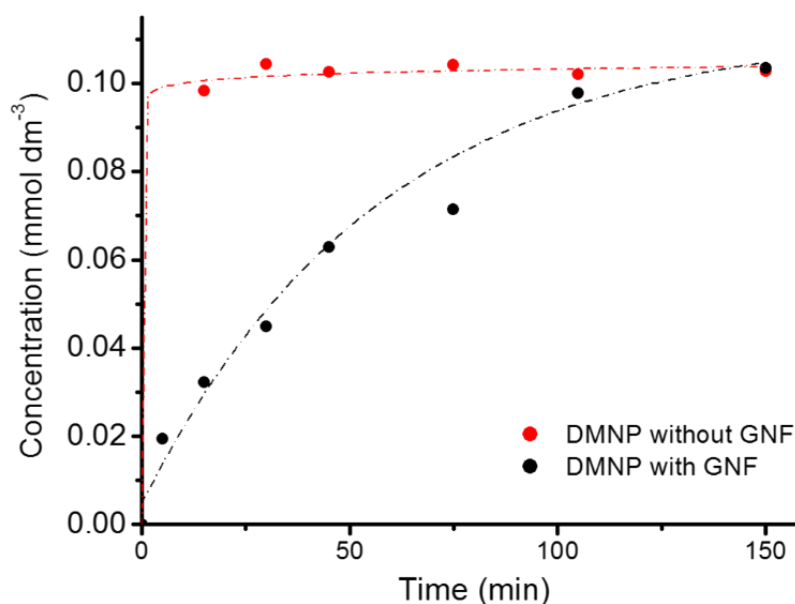


Figure 3.14. Concentration profile of DMNP with (black) and without (red) GNF in the KOH solution highlighting the rapid uptake and slow release of the toxic agent by the GNF shown during the hydrolysis procedure which resembles a 'Nanosponge' effect.

Interestingly, UV-Vis spectroscopy analysis appears to show a significant decrease in the concentration of DMNP, when compared to the control experiment without GNF at the start of the reaction. However, no corresponding phenolate peak is produced suggesting hydrolysis is not occurring. Measuring the concentration of the DMNP in the two control

experiments at different time intervals shows that GNF are able to physically remove the DMNP from the solution without facilitating hydrolysis, a process which results in the release of the OP compound back into the solution from the GNF over time due to homogenisation of the contaminant within the solvent. This rapid initial uptake provides evidence for reagent enrichment within the nanotube, resembling a “nanosponge” and induces a high local concentration effect within the nanoreactor (Figure 3.15).

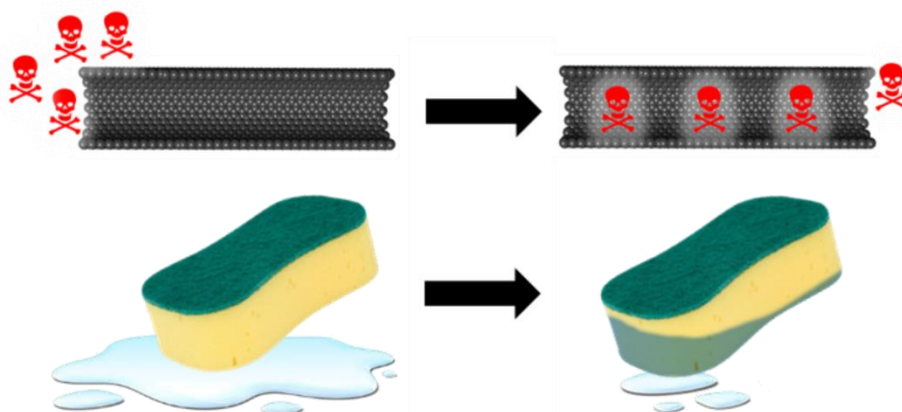


Figure 3.15. Schematic representation of the nanosponge effect where the toxic species are sequestered and retained into the interior of the nanotube.

This is particularly striking as GNF exhibit no change in volume and possess minimal flexibility – features typically associated with sponge-like absorbents – but this effect is responsible for the increased concentration of DMNP in the nanotubes, and is likely to be responsible for the enhanced conversion based on the rapid absorption and release of the starting material compared to the phenolate production when the catalyst is present. This idea could be responsible for the decreasing rate of hydrolysis over time as the enhancement of the reagent within the nanotube cavity is reduced as it becomes

homogenised within the solution. This leads to less effective catalyst to reagent concentrations and consequently reduced hydrolysis over the reaction.

From a decontamination perspective, the preference of this OP species to be selectively absorbed into the nanotube at a rapid rate offers a route for removal of these contaminants from aqueous solutions and provides a mechanism for decontamination within itself, i.e. through physical adsorption. These synergistic effects highlight the benefits of utilising a nanoreactor system for catalysis and offers new avenues that could be applied to many other reactions.

Another hypothesis for the hydrolysis retardation with $\text{ZrO}(\text{OH})_2@\text{GNF}$, could be due to catalyst poisoning and loss of the hydroxyl surface groups. Having the products irreversibly binding to the surface reduces the amount of active Lewis acidic sites present for hydrolysis.²¹ Thermogravimetric analysis (TGA) shows minimal catalyst loss after hydrolysis providing promising results regarding the stability of these materials within the nanoreactors. An increase in the combustion temperature of GNF could indicate less reactive oxygens at the catalyst surface due to the binding of the OP species or a change in the structure of the encapsulated material (Figure 3.16a). The weight loss below 150°C in the TGA (related to the loss of hydroxyl groups on the surface) is also not present after the decontamination reaction confirming their consumption during this process.

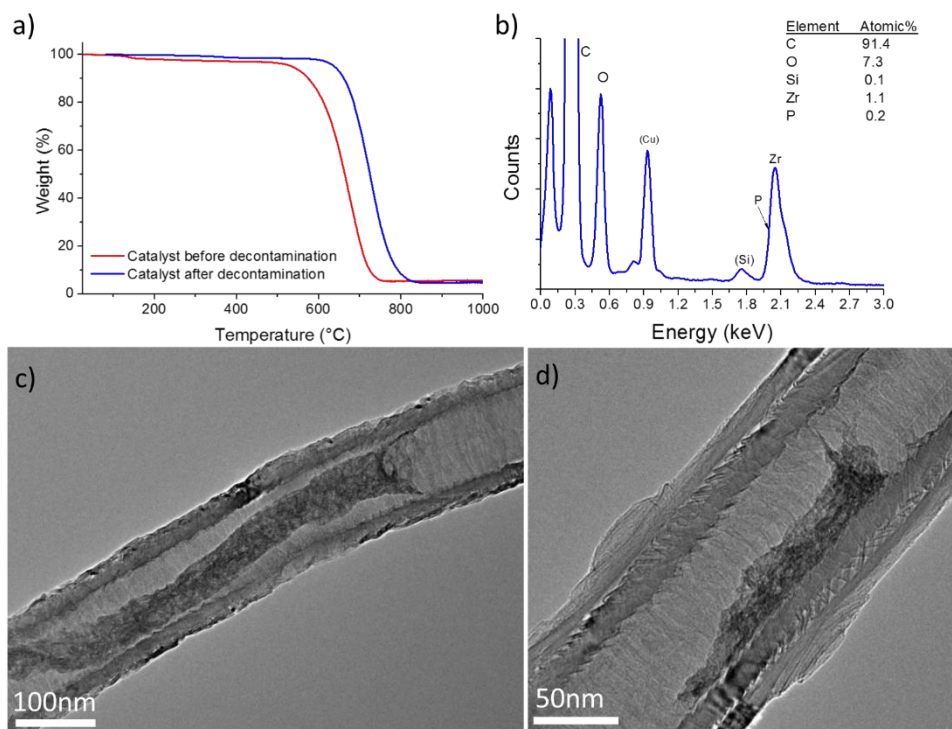


Figure 3.16. (a) TGA profile of $\text{ZrO}(\text{OH})_2@\text{GNF}$ catalyst pre (red) and post (blue) decontamination. (b) EDX analysis $\text{ZrO}(\text{OH})_2@\text{GNF}$, Aztec software for EDX does indicate the presence of phosphorus by calculating expected Zr peak at 2.1keV supporting the poisoning of the catalyst. (c, d) TEM of $\text{ZrO}(\text{OH})_2@\text{GNF}$ material after DMNP hydrolysis decontamination reaction supporting the presence of the material to remain within the internal channel of the carbon nanostructure.

TEM after the decontamination reaction indicates that the catalyst remains within the carbon nanostructure is still amorphous in structure (Figure 3.16c,d). Energy dispersive X-ray spectroscopy (EDX) also indicates the presence of phosphorus in this structure (Figure 3.16b). Therefore, removing the surface-adsorbed organophosphates from the catalyst is an important challenge, which has been previously addressed by applying a large excess of metal hydroxide.¹⁴ In our study, spatial confinement was employed to optimise and retain the catalytic performance of the metal hydroxides. Although enhanced hydrolysis was observed, regeneration of the catalytic activity in nanoreactors is a challenge which still needs to be addressed.

3.3.2.3. Effect of the catalyst composition on hydrolysis of DMNP

It was clear from the TGA in the previous section that thermal treatment of the $\text{ZrO}(\text{OH})_2@\text{GNF}$ results in the loss of the hydroxyl groups above 100 °C in air which gives control of the composition of the confined catalyst. Moreover, when thermally treating the catalyst to 600 °C in air, TEM confirms further control due to the formation of more structured and crystalline larger encapsulated nanoparticles of ZrO_2 (figure 3.17).

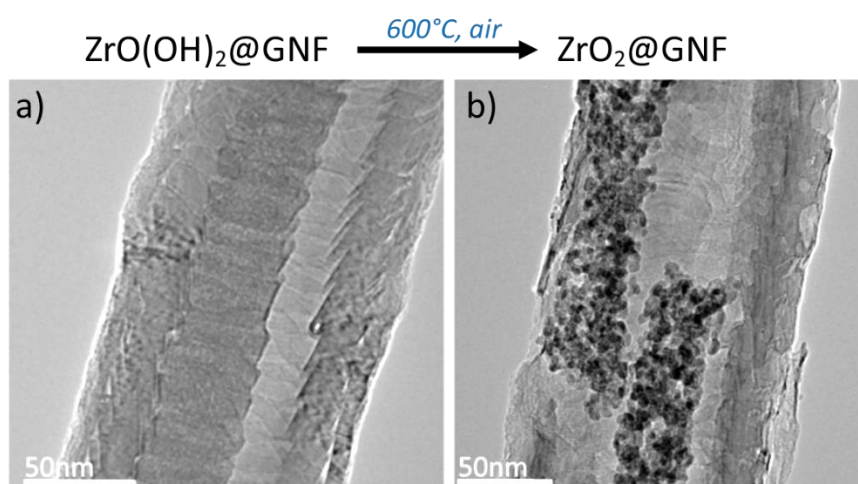


Figure 3.17. TEM analysis of (a) $\text{ZrO}(\text{OH})_2@\text{GNF}$ and (b) after treatment at 600 °C in air, indicating the formation of discrete metal dioxide nanoparticles. This simple process demonstrates that the composition, morphology and size of the encapsulated material can be readily changed (Chapter 2).

The impact of the change in morphology, composition, and loss of hydroxyl groups were investigated by applying the thermally treated nanoreactors towards the hydrolysis of DMNP (Figure 3.18). Interestingly, after the formation of the $\text{ZrO}_2@\text{GNF}$ nanoreactor at 600 °C in air, the catalytic effects on the hydrolysis pathway are lost and only the background hydrolysis is observed.

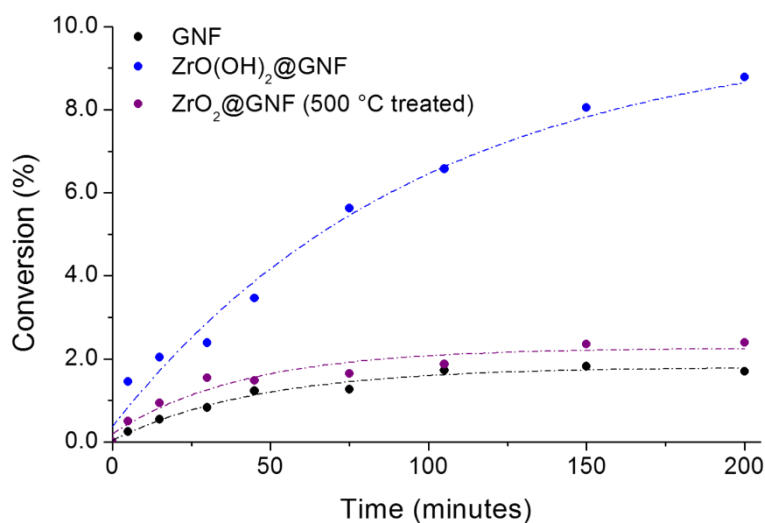


Figure 3.18. Comparison of the DMNP hydrolysis using thermally annealed ZrO₂@GNF (black), ZrO(OH)₂@GNF (blue) and empty GNF (red). Conversion calculated using the concentration of phenolate measured by UV-Vis spectroscopy and the theoretical concentration of DMNP added.

This result confirms the importance of a non-crystalline structured catalyst which possess increased defect and Lewis acidic sites which are crucial for adsorption. The surface OH-groups are expected to be lost during thermal treatment, which again would prevent the hydrolysis of OP species. Although this indicates that any thermal treatment may be detrimental to the performance of the catalyst it also highlights the importance of the unique structure of the ZrO(OH)₂@GNF species generated in Chapter 2 and identifies the potential that these catalysts could have towards many other catalytic reactions.

3.3.2.4. Effect of catalyst loading on hydrolysis of DMNP

To investigate the effects of catalyst loading on the hydrolysis system, double the quantity of the nanoreactors was added to the solution (46.6mg) resulting

in double the amount of active $\text{ZrO}(\text{OH})_2$ present (2.5mg). After 200 minutes it was observed that the additional catalyst present facilitates the higher conversion of DMNP by a factor of 1.8 (Figure 3.19).

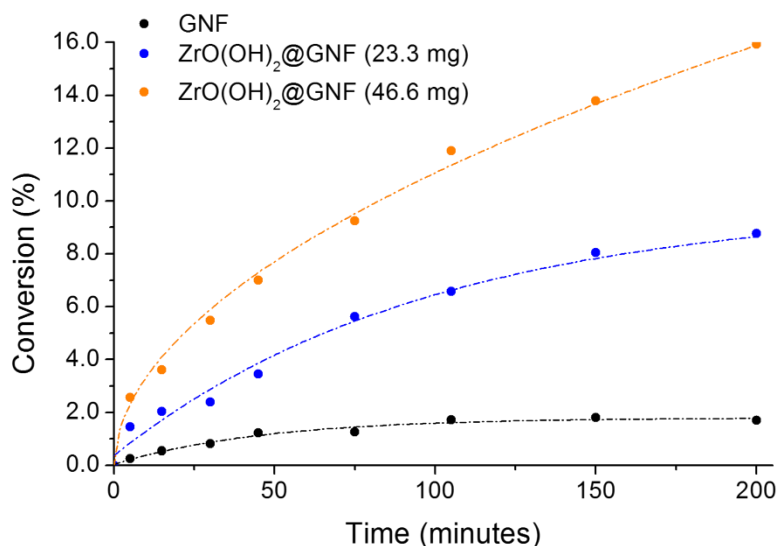


Figure 3.19. Comparison of the DMNP hydrolysis using higher loading of $\text{ZrO}(\text{OH})_2$ @GNF (red – 46.6mg, 2.5mg of $\text{ZrO}(\text{OH})_2$), previous loading of $\text{ZrO}(\text{OH})_2$ @GNF (blue – 23.3mg, 1.25mg of $\text{ZrO}(\text{OH})_2$), and empty GNF (black – 22mg). Conversion calculated using the concentration of phenolate measured by UV-Vis spectroscopy and the theoretical concentration of DMNP added.

As expected, the increased loading of the active catalyst by a factor of 2 within the hydrolysis reaction, therefore, led to the conversion to the phenolate product increasing by a similar quantity. The slightly lower conversion expected when double the active catalyst is used could be due to the saturation of the GNF in the aqueous solution, as when the quantity of nanoreactors is significantly increased, fewer GNF are able to disperse effectively within the solution, which results in less active catalyst being physically accessible. Over time, stirring promotes better homogenisation of the GNF within the solution

and hence leads to the maximised hydrolysis that appears to still be continuing even after 200 minutes.

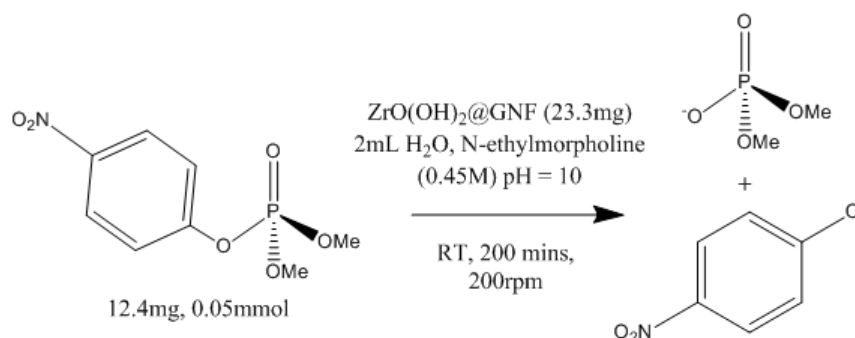
It appears that the reaction is dependant on the reactive surface groups on the catalyst, as when the loading of catalyst is increased the rate of the reaction increases similarly. Indeed, the initial reaction rate doubles from 0.067 to 0.112 $\mu\text{M}/\text{min}$ when twice the amount of catalyst is used. This suggests that the reaction possesses first order kinetics with respect to the reactive surface groups generated during the hydrolysis reaction.

If the quantity of GNF is increased further significant decreases in the conversion and rate of hydrolysis may be observed compared to increased active catalyst present. Increasing the loading of the metal oxide active component within the GNF could provide an optimised carbon nanoreactor with a maximised active catalyst which can be effectively dispersed. However, these results indicate that the dispersion of the GNF within the solution does not appear to be a significant issue at these loadings and highlight the effective decontamination abilities of these nanoreactors towards organophosphorus hydrolysis.

3.3.2.5. Effect of buffer system on hydrolysis of DMNP with $\text{ZrO}(\text{OH})_2@\text{GNF}$

Heretofore, an aqueous buffer solution employing KOH (1mM) has been utilised as a standard procedure however, previous literature found that an organic buffer system (*N*-ethylmorpholine (0.45M)) was effective for the hydrolysis of DMNP especially for catalysts sensitive to hydroxide solution.³² To

investigate the versatility of the $\text{ZrO}(\text{OH})_2@\text{GNF}$ catalyst towards different reaction conditions, the nanoreactor was applied to an organic buffer system (Scheme 3.1).



Scheme 3.1. Hydrolysis procedure in an organic buffer solution.

It was observed that when no catalyst was present the background hydrolysis is reduced by 0.5% in the organic buffer solution than when compared to the hydroxide solution. When the $\text{ZrO}(\text{OH})_2@\text{GNF}$ nanoreactor is applied it is clear that the catalyst is still able to promote hydrolysis of the OP agent in the organic solution, however, this ability is reduced by a factor of 1.2 (Table 3.6).

Table 3.6. Conversion of DMNP using $\text{ZrO}(\text{OH})_2@\text{GNF}$ nanoreactor investigating its hydrolysis abilities in different buffer systems.

Catalyst ^a	Buffer system ^b	Conversion (%) ^c
None	N-ethylmorpholine	1.6
$\text{ZrO}(\text{OH})_2@\text{GNF}$	N-ethylmorpholine	4.2
None	KOH	2.1
$\text{ZrO}(\text{OH})_2@\text{GNF}$	KOH	8.8

^a $\text{ZrO}(\text{OH})_2@\text{GNF}$ (23.25 mg – 1.25 mg of $\text{ZrO}(\text{OH})_2$), 200 minutes, 200 rpm, RT. ^b 2 mL of N-ethylmorpholine buffer (0.45 M – pH10) or 2 mL of KOH (1 mM - pH 10). ^c Conversion calculated using UV-Vis spectroscopy and absorbance's at 273 and 400 nm for DMNP and phenolate product respectively.

The decrease in the hydrolysis supports the fewer hydroxides present in the solution which regenerates the catalytic surface to provide effective catalytic adsorptive decontamination. The possibility for the organic base of N-ethylmorpholine to also interact with the catalytic surface is also an issue in this system as competition for Lewis acidic sites may reduce the effective ability to hydrolyse the OP agents. Therefore, it is not surprising that the hydrolysis abilities of the $\text{ZrO(OH)}_2\text{@GNF}$ are reduced in an organic buffer solution.

Although previous zirconium MOF based hydrolysis catalysts effectively decontaminate DMNP in organic buffers,³² this study indicates that the nanoreactors seem to be more effective at hydrolysis in the KOH aqueous system when compared to the organic buffer solution, which is important as the toxic organic buffers are unsuitable for industrial applications. This also highlights that the nanoreactor catalyst is significantly more stable and can withstand harsher conditions that the benchmarked catalysts fall short due to catalyst decomposition.

With the nanoreactor still enhancing the hydrolysis of DMNP in the organic buffer, this catalyst is, therefore, significantly more versatile and can be effective in different buffer solutions. This crucial feature could be a key step in generating catalysts suitable for real-world applications.

3.4. Conclusions

This chapter has identified the benefits of utilising carbon nanoreactors and nanosponges for the enhanced decontamination of organophosphorus agents

(OP). The zirconium oxyhydroxide hybrid nanoreactor has shown rapid initial decontamination abilities when applied to chemical warfare nerve agent simulant hydrolysis, with a 4-fold enhancement relative to its constituent components observed. It has also been clearly demonstrated that GNF act not only as a nano-container but are also instrumental in effective sequestration of the DMNP simulant from aqueous solutions and have been identified as promising candidates for toxic OP 'nanosponges.' This effective absorption in the presence of the nanoscale hydroxylated zirconia is thought to be one of the key driving forces behind the increased activity of the catalyst and, although surface deactivation and poisoning remain a challenge, the ability of the catalyst to remain within the nanoreactor after decontamination is advantageous. The encapsulated zirconium oxyhydroxide nanomaterial has both a high surface area and a large number of reactive topological edges which proves crucial for decontamination catalysis even in harsher hydrolysis conditions. Thermal treatment in air results in a reduction of surface area, reactive sites and hydroxyl groups which proved detrimental to the hydrolysis. This work highlights the potential of confining unique active catalysts within carbon nanostructures to form nanoreactors with remarkable hydrophobic 'nanosponge' properties that can absorb and decontaminate reagents of interest.

3.5. Experimental

3.5.1. General

Standard reagents and solvents, including the simulant dimethyl nitrophenyl phosphate (97 % purity) and Dimethyl methylphosphonate (97 % purity), were purchased from Sigma-Aldrich Chemicals (Dorset, UK) and were used as-received. Graphitised nanofibers (PR19-XT-HHT, Fe content <100 ppm) were obtained from Pyrograf Products Inc (Cedarville, Ohio).

Thermogravimetric analysis was performed using a TA Q500 thermogravimetric analyser. All samples were deposited onto platinum pans for analysis, heated in air (90 mL/min) from room temperature up to 1000 °C at a rate of 5 °C/min, followed by an isothermal hold at 1000 °C for 10 min.

Transmission electron microscopy (TEM) was performed using a JEOL JEM-2100+ microscope operated at 200 keV. TEM samples were prepared *via* a drop casting technique, where samples were dispersed in methanol, followed by deposition onto copper grid mounted “lacey” carbon films (Agar). All images were processed using Gatan Digital Micrograph software. Energy dispersive X-ray spectroscopy and mapping were acquired using an Oxford Instruments INCA X-ray microanalysis system, the beam was condensed to areas suspended over holes of the amorphous carbon film (to negate the contribution to the carbon signal from the support film).

Powder X-ray diffraction measurement was performed on a PANalytical X'Pert Pro diffractometer equipped with a Cu K(α) radiation source ($\lambda=1.5432\text{\AA}$, 40 kV,

40 mA) in Bragg-Brentano geometry. The sample was mounted on a Si zero-background holder using isopropyl alcohol to aid adhesion. The parameters for a typical experiment were: 15 ° start angle, 70 ° stop angle, 0.0525 ° step size, 6080 s time per step and 0.00220 °/s scan speed.

¹H NMR spectroscopy spectra were recorded at room temperature using a Bruker AVANCE-DPX-400 spectrometer (TopSpin 1.3 PL4) unless otherwise stated. Proton 16 scan experiments were run with D₂O as the solvent unless otherwise stated. Spectra were analysed using MestReNova software.

UV-Vis absorption spectra were recorded at room temperature using 1 cm quartz cuvettes. The samples were analysed using a Perkin-Elmer Lambda 25 UV/Vis spectrometer at a scan rate of 240 nm/min over a wavelength range of 200-500 nm. Spectra were analysed using UV WinLab ES software.

Surface area analysis was performed using the Brunauer–Emmett–Teller (BET) method based on adsorption data in the relative pressure (P/P₀) range from 0.02 to 0.22 by measuring nitrogen sorption isotherms of the samples at -196 °C on a Micromeritics ASAP 2020 sorptometer. Samples were degassed for 16 hours at 100 °C.

3.5.2. Preparation of bulk hydroxylated zirconia

ZrCl₄ (75mg) was washed with ammonium hydroxide solution (10ml, 35%) during a vacuum filtration procedure (0.2µm PTFE membrane) and dried under ambient conditions overnight to yield a white solid.

3.5.3. Hydrolysis procedure of DMNP in KOH buffer

Hydrolysis experiments were performed at room temperature. In a typical experiment, the composite material (Table 3.7) was suspended in potassium hydroxide solution (2 mL, 1 mM, pH10) with gentle agitation. DMNP (8.0 μ L, 0.05mmol) was added to this suspension and homogenised with orbital shaking at 200 rpm for 200 minutes. The progress of the hydrolysis reaction was monitored by removing a 10 μ L aliquot from the reaction mixture, diluting with potassium hydroxide solution (2 mL, 0.5mM, pH 10), filtering and then recording the UV-Vis spectrum. At each time point, the absorbance at 273 nm (DMNP reactant) and 400 nm (*p*-nitrophenoxide product) were noted. Turn over frequencies were calculated using the half-lives of literature value of GD, and conversion after 15 minutes of DMNP from this work (1.25mg used as ZrO_x(OH)_y loading).

Table 3.7. Catalyst parameters for hydrolysis reactions.

Material	Quantity of material in reaction (mg)	Active catalyst present in reaction (mg)
GNF	22.0	-
TiO(OH) ₂ @GNF	23.0	1.00
ZrO(OH) ₂ @GNF	23.3	1.25
ZrO(OH) ₂ @GNF	46.6	2.50
Bulk ZrO(OH) ₂	1.25	1.25
ZrO ₂ @GNF	23.3	1.25

3.5.4. Hydrolysis procedure of DMNP in organic buffer

Hydrolysis experiments were performed at room temperature. In a typical experiment, the composite material (23.25 mg, containing 1.25 mg of ZrO_x(OH)_y) was suspended in N-ethylmorpholine buffer solution (2 mL, 0.45M, pH10) with gentle agitation. DMNP (8.0 μL, 0.05 mmol) was added to this suspension and homogenised with orbital shaking at 200 rpm for 200 minutes. The progress of the hydrolysis reaction was monitored by removing a 10 μL aliquot from the reaction mixture, diluting with N-ethylmorpholine buffer solution (2 mL, 0.15M, pH 10), filtering and then recording the UV-Vis spectrum. At each time point, the absorbance at 273 nm (DMNP reactant) and 400 nm (*p*-nitrophenoxide product) were noted.

3.6. References

1. P. W. Elsinghorst, F. Worek and M. Koller, *Toxicol. Lett.*, 2015, **233**, 207-213.
2. Q. F. Yang, J. Wang, W. T. Zhang, F. B. Liu, X. Y. Yue, Y. N. Liu, M. Yang, Z. H. Li and J. L. Wang, *Chem. Eng. J.*, 2017, **313**, 19-26.
3. F. M. Raushel, *Nature*, 2011, **469**, 310-311.
4. G. M. Kazankov, V. S. Sergeeva, E. N. Efremenko, L. Alexandrova, S. D. Varfolomeev and A. D. Ryabov, *Angew. Chem.-Int. Edit.*, 2000, **39**, 3117-3119.
5. N. Sharma and R. Kakkar, *Adv. Mat. Lett*, 2013, **4**, 508-521.
6. S. Chauhan, S. Chauhan, R. D'Cruz, S. Faruqi, K. K. Singh, S. Varma, M. Singh and V. Karthik, *Environ. Toxicol. Pharmacol.*, 2008, **26**, 113-122.
7. K. Cannard, *J. Neurol. Sci.*, 2006, **249**, 86-94.
8. N. Umetsu, F. H. Grose, R. Allahyari, S. Abu-El-Haj and T. R. Fukuto, *J. Agric. Food Chem*, 1977, **25**, 946-953.
9. J. Misik, R. Pavlikova, J. Cabal and K. Kuca, *Drug Chem. Toxicol.*, 2015, **38**, 32-36.
10. P. W. Elsinghorst, F. Worek, H. Thiermann and T. Wille, *Exp. Op. Drug Disc.*, 2013, **8**, 1467-1477.
11. F. Gonzaga, E. Perez, I. Rico-Lattes and A. Lattes, *New J. Chem.*, 2001, **25**, 151-155.
12. Y. C. Yang, *Acc. Chem. Res.*, 1999, **32**, 109-115.
13. W. O. Gordon, B. M. Tissue and J. R. Morris, *J Phys Chem C*, 2007, **111**, 3233-3240.
14. T. J. Badosz, M. Laskoski, J. Mahle, G. Mogilevsky, G. W. Peterson, J. A. Rossin and G. W. Wagner, *J Phys Chem C*, 2012, **116**, 11606-11614.
15. Y. C. Yang, L. L. Szafraniec, W. T. Beaudry, D. K. Rohrbaugh, L. R. Procell and J. B. Samuel, *J. Org. Chem.*, 1996, **61**, 8407-8413.
16. M. J. Katz, J. E. Mondloch, R. K. Totten, J. K. Park, S. T. Nguyen, O. K. Farha and J. T. Hupp, *Angew. Chem.-Int. Edit.*, 2014, **53**, 497-501.
17. G. W. Wagner, P. W. Bartram, O. Koper and K. J. Klabunde, *J. Phys. Chem. B*, 1999, **103**, 3225-3228.
18. K. J. K. J. G. Ekerdt, J. R. Shapley, J. M. White, and J. T. Yates Jr., *J Phys Chem C*, 1988, **92**, 6182-6188.
19. T. H. Mahato, G. K. Prasad, B. Singh, J. Acharya, A. R. Srivastava and R. Vijayaraghavan, *J. Hazard. Mater.*, 2009, **165**, 928-932.
20. D. B. Mawhinney, J. A. Rossin, K. Gerhart and J. T. Yates, *Langmuir*, 1999, **15**, 4789-4795.
21. G. W. Wagner, Q. Chen and Y. Wu, *J Phys Chem C*, 2008, **112**, 11901-11906.
22. G. W. Wagner, G. W. Peterson and J. J. Mahle, *Ind. Eng. Chem. Res*, 2012, **51**, 3598-3603.

23. P. Janos, J. Henych, O. Pelant, V. Pilarova, L. Vrtoch, M. Kormunda, K. Mazanec and V. Stengl, *J. Hazard. Mater.*, 2016, **304**, 259-268.
24. V. V. Singh, A. Martin, K. Kaufmann, S. D. S. de Oliveira and J. Wang, *Chem. Mater.*, 2015, **27**, 8162-8169.
25. T. Wang, J. N. Wang, Y. Yang, P. Su and Y. Yang, *Ind. Eng. Chem. Res.*, 2017, **56**, 9762-9769.
26. X. L. Pan and X. H. Bao, *Chem. Commun.*, 2008, 6271-6281.
27. M. D. Gimenez-Lopez, A. La Torre, M. W. Fay, P. D. Brown and A. N. Khlobystov, *Angew. Chem., Int. Ed.*, 2013, **52**, 2051-2054.
28. M. Aygun, C. T. Stoppiello, M. A. Lebedeva, E. F. Smith, M. D. Gimenez-Lopez, A. N. Khlobystov and T. W. Chamberlain, *J. Mater. Chem. A*, 2017, **5**, 21467-21477.
29. A. N. Khlobystov, *ACS nano*, 2011, **5**, 9306-9312.
30. W. A. Solomonsz, G. A. Rance, B. J. Harris and A. N. Khlobystov, *Nanoscale*, 2013, **5**, 12200-12205.
31. S. L. Bartelt-Hunt, D. R. U. Knappe and M. A. Barlaz, *Crit. Rev. Environ. Sci. Technol.*, 2008, **38**, 112-136.
32. J. E. Mondloch, M. J. Katz, W. C. Isley, 3rd, P. Ghosh, P. Liao, W. Bury, G. W. Wagner, M. G. Hall, J. B. DeCoste, G. W. Peterson, R. Q. Snurr, C. J. Cramer, J. T. Hupp and O. K. Farha, *Nat. Mater.*, 2015, **14**, 512-516.
33. D. T. Lee, J. J. Zhao, C. J. Oldham, G. W. Peterson and G. N. Parsons, *ACS Appl. Mater. Interfaces*, 2017, **9**, 44847-44855.
34. G. E. Fryxell and G. Cao, *Environmental applications of nanomaterials: synthesis, sorbents and sensors*, World Scientific, 2012.
35. I. V. Schweigert and D. Gunlycke, *J. Phys. Chem. A*, 2017, **121**, 7690-7696.
36. A. A. M. Ali and M. I. Zaki, *Thermochim. Acta*, 2002, **387**, 29-38.
37. Y. J. Jang, K. Kim, O. G. Tsay, D. A. Atwood and D. G. Churchill, *Chem. Rev.*, 2015, **115**, PR1-76.

Synthesis of group VI metal oxides in hollow graphitised nanofibres

4.1. Background

There is undoubtable evidence that carbon nanotubes (CNT) represent an excellent class of nanoscale containers for preparative chemical reactions; however, the role of the nanotube in these reactions is more diverse than simply hosting the reaction.¹⁻⁵ Spatial confinement effects observed inside carbon nanotubes that enhance catalysis can be divided into three categories, and these effects govern the abilities of nanoreactors. Firstly, the space restriction that CNT impose on confined molecules controls dimensions and allows for the preparation of unique nanomaterials, which can provide high surface areas and enhance catalytic reactions.^{6,7} Secondly, the increased local concentration of reactants inside CNT, facilitated by non-covalent interactions, drives improved catalytic rates and modulates selectivity.^{8,9} Finally, electronic interactions of confined materials and CNT can be tuned to modify the electronic or redox properties of the guest or host species and promote more active catalytic surfaces.^{10,11} Chapter 2 and 3 focused on preparing unique nanomaterials inside carbon nanoreactors and exploiting a nanosponge effect to promote contaminant absorption in the internal cavity.⁵ However, the implications of the guest-host interactions of nanoreactors has yet to be fully investigated.

Due to the curved nature of carbon nanotubes, their interactions with metal catalyst species are more complex compared to graphene. In particular, both the location of the metal species (inside vs outside) and the diameter of the nanotube play important roles in defining the magnitude of the metal to nanotube interactions. Narrower CNT have an increased curvature and a greater differentiation between the environment at the interior and exterior surfaces.³ In this case, the convex outer surface of CNT is more reactive than the concave inner surface due to increasing pyramidalisation angle (θ_p) promoting increased electron density in the carbon p_z -orbital pointing radially outwards from the CNT surface (Figure 4.1).¹² As the nanotube diameter increases, this effect becomes reduced as the p_z -orbitals become symmetric and electron density is more evenly distributed.⁴ Despite minimised carbon p_z -orbital overlap expected in the interior of the nanotube, a driving force for encapsulating materials is the result of the high electron density per volume in the internal channel of the nanotube. The possibility for multiple overlapping orbitals also maximises the electronic interactions of encapsulated species dramatically when compared to the exterior surface.

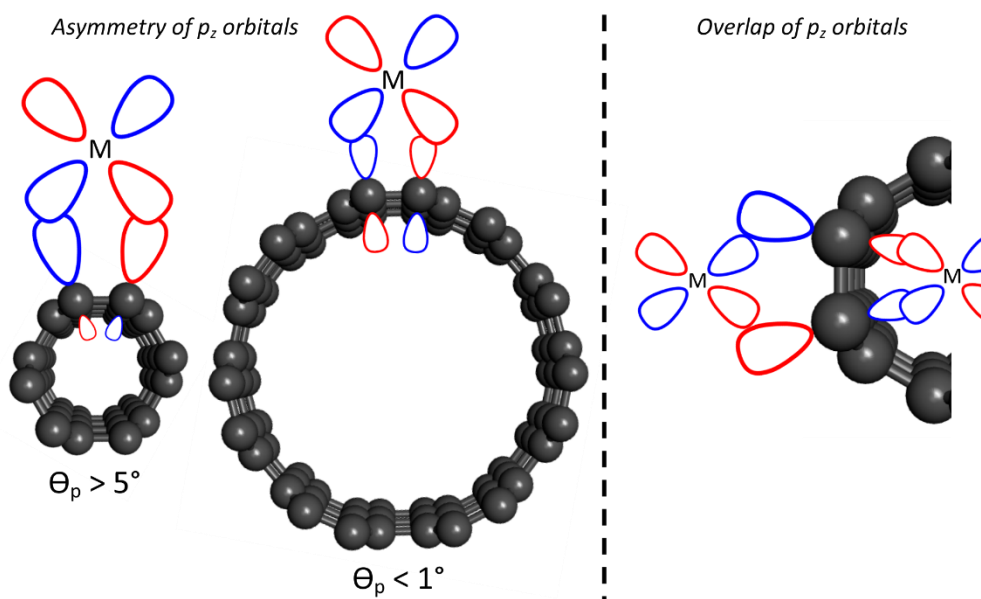


Figure 4.1. Schematic diagrams representing the features of metal and CNT orbital interactions that control the magnitude of the electronic interactions. Decreasing diameters of the CNT increases the curvature of the CNT leading to the asymmetry of the p_z -orbitals on the C atoms. As a metal approaches the exterior side wall of the CNT the smaller diameter nanotube has increased orbital overlap and enhanced electronic interactions. However, the possibility for multiple overlapping p_z -orbitals for metals approaching from the interior results in increased electronic interactions when compared to the exterior surface.

Indeed, the electronic interactions between iron and iron oxide centres and multi-walled carbon nanotubes (MWNT) interior surfaces have been previously shown to have modified redox behaviours. The ease of reduction of iron oxide was shown to be dependent on the decreasing diameter of the CNTs, due to the increased curvature on the interior of the nanotube and corresponding increased orbital overlap with the iron oxide, leading to modified electronic properties.¹³ This study also highlighted that electron transfer between iron nanoparticles and CNT stabilised the metal in its zero oxidation state, decreasing reactivity towards oxidation. Confined TiO_2 NP within double-walled carbon nanotubes (DWNT) with internal diameters less than 1.5nm also

showed an impressive 14-fold increase of the formation of propylene oxide when compared to the same TiO₂NP confined inside a multi-walled nanotube with internal diameters between 4-8nm.⁷

Small diameter nanotubes, such as SWNT, therefore, facilitate increased electron transfer between guest and host species; however, the restricted interior space results in increased transport resistance towards reactants making these less suitable as nanoreactors. Conversely, although larger diameter nanotubes allow for effective encapsulation of catalysts with sufficient room for reactants, their lower curvature results in reduced electronic interactions between the guest and host. A CNT host which harnesses the increased electronic interactions with metal species but possesses a larger diameter is a desirable concept for nanoreactors.

Hollow graphitised carbon nanofibres (GNF) are large internal diameter (30-60 nm) multiwall nanotubes with interesting internal corrugated folds which can assist in maximising guest-host interactions due to the increased non-covalent interactions at these anchoring sites (Figure 4.2).

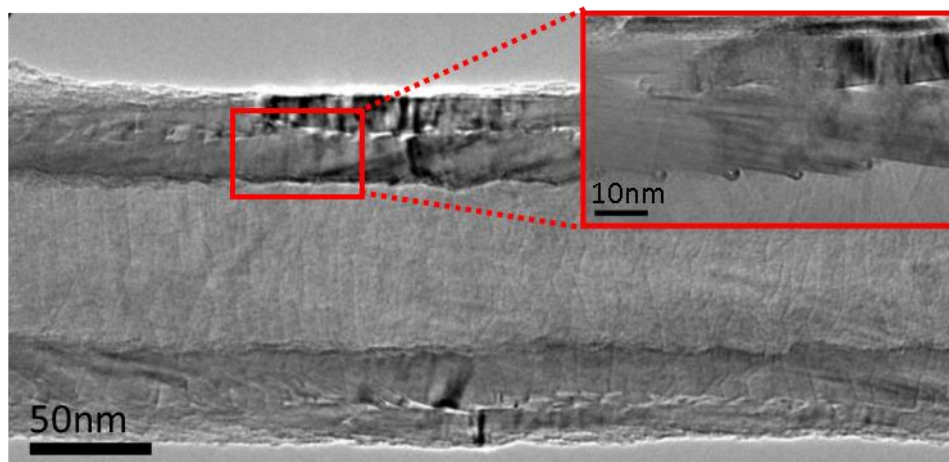


Figure 4.2. Transmission electron microscopy image of a hollow graphitised nanofibre with a large internal diameter and internal corrugated structures (inset).

The high pyramidalisation angle at the folds of the corrugated interior of the GNF, which maximises van der Waals interactions and thus enhances overlap between the guest and host interactions, represents a perfect environment for a catalytic nanoparticle. Moreover, as shown in Chapter 2 these sites provide additional synergistic effects, such as permitting control of unique morphologies and sizes of nanoparticles. They have been employed previously as nanoreactors as they reduce transport resistance of reactants due to their large diameter and enhance local concentrations around the encapsulated catalysts; however, limited work has been performed to investigate the influence of guest-host interactions on the electronic or redox properties of the metal oxide.^{9, 14}

Group VI metals and their oxides have shown impressive abilities as catalysts particularly in environmental remediation. Moreover, when a support is utilised enhanced catalytic properties have been observed.¹⁵ Their d-electrons and multiple oxidation states provide interesting electronic and redox

properties, which makes them a suitable candidate for investigations in a nanoreactor composite as they may possess the ability to donate or accept electrons depending on their initial oxidation state (Figure 4.3).

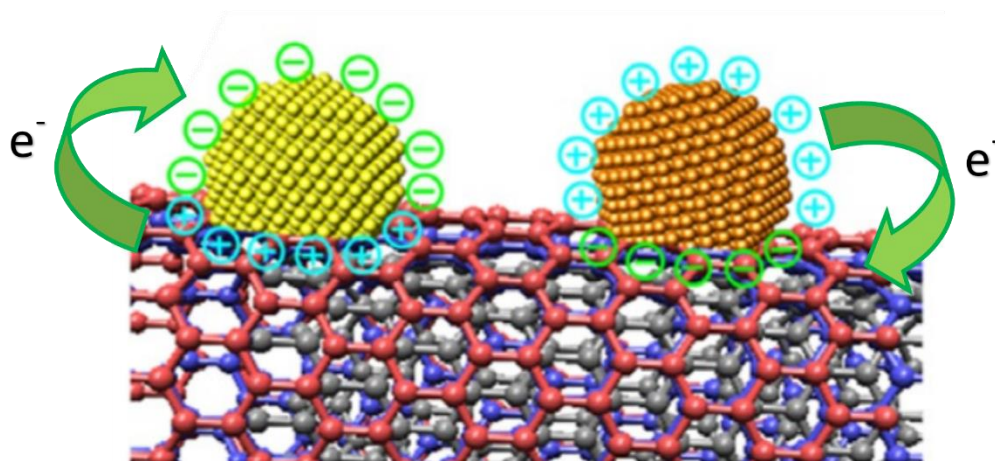


Figure 4.3. Schematic diagram of electron transfer between metal nanoparticles and carbon support indicating the activation of the catalytic surface. These activated surfaces possess new electronic properties which can change the reduction and oxidation behaviour of the catalytic nanoparticles and catalyse chemical reactions. Adapted from Chen et al, copyright American Chemical Society. ^{16,17}

The interactions of several group VI metal species with carbon nanotubes have been previously reported in the literature to create materials with diverse and interesting electrochemical, photochemical and catalytic properties (Table 4.1).¹⁸⁻²³ MWNT were found to facilitate the reduction and sulfidation of molybdenum oxide and enhance the activity and hydrogenolysis/hydrogenation of the catalysts.¹⁹ Other supports such as Al₂O₃ were found to interfere with the active species and resulted in the poisoning of the catalytic surface, highlighting further motivation for utilising CNT. MWNT were also shown to prevent the complete reduction of WO₃ which limited deactivation and enhanced catalysis of monofunctional acidic skeletal

isomerisation reactions.²⁴ Clearly, the tuneable electronic interactions that group VI metal oxides possess can enhance several catalytic reactions.

Table 4.1. Group VI compounds with carbon nanotube supports and their observed electronic interactions.

Group VI metal species	Carbon nanotube host and internal diameter (nm)	Electronic interactions observed	Ref
CrO ₃	SWNT (1.5)	Metal species accepts electron density from the SWNT	18
MoO ₃	MWNT (10-30)	Electron transfer assisted reduction of molybdenum oxide	19
MoC ₂ , MoS ₂ and MoN ₂	MWNT (10-20)	Charge transfer between metal and support enhanced hydrogen evolution catalysis	20
MoS ₂ and WS ₂	SWNT (1.3-1.5)	SWNT was able to act as reservoir of electrons during chemical transformations	21
Py-SiW ₁₁ O ₃₉	SWNT (1.0-1.5)	Electron transfer between polyoxometalates and SWNT quenches emission spectrum	22
WO ₃	MWNT (10-20)	MWNT transport electrons from WO ₃	23

Polyoxometalates (POMs) represent one highly studied, specific form of group VI metal oxides which have extremely small diameters of less than 2nm leading to increased surface areas and impressive electrochemical and photoactive properties.^{25,26} Carbon nanotube and W or Mo based POM hybrids also showed electron transfer between the two species which resulted in surface activation, improved accessibility of active sites and quenching of emissive properties due to the impressive electronic interactions.^{22, 27, 28} Although polyoxometalates possess many desirable features for catalysis, they are often highly charged, unstable and limited to specific elements, sizes and reactions. Therefore, group VI metal oxides may provide more effective facile encapsulation of metal oxide

species which can be manipulated and probed for their electronic interactions within a confined environment.

Controllable electronic interactions have been shown to be effective at regulating the transformation of a molybdenum precursor as the SWNT was able to host anionic nanoclusters.²¹ It was revealed that the nanotube host acted as a reservoir of electrons which stabilised the anionic metal iodide which proved crucial for subsequent transformations to metal sulphide nanoribbons (Figure 4.4).

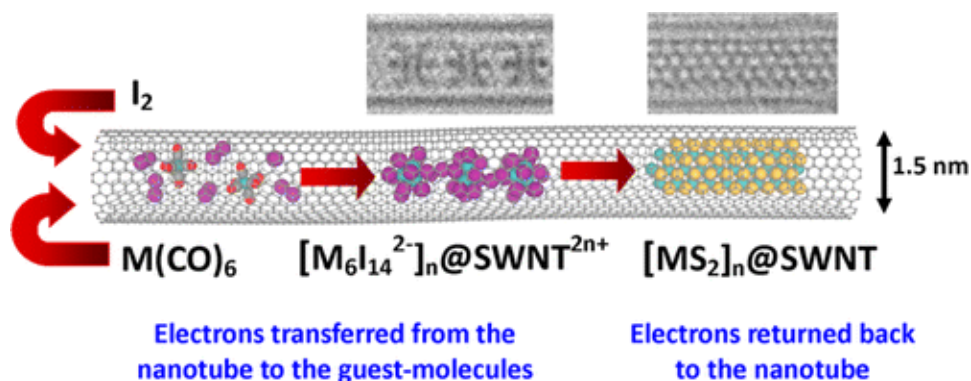


Figure 4.4. Schematic diagram of electron donation towards and from the nanotube stabilising the internal species. Adapted from Botos et al, copyright American Chemical Society.²¹

Other molybdenum based hybrid compounds (MoC_2 , MoS_2 and MoN_2) within MWNT showed electron transfer from the molybdenum species to the support providing enhanced hydrogen evolution.²⁰ By controlling the electronic and redox properties of the metal species, the hydrogen binding energy was reduced and hydrogen evolution maximised. The ability to use nanotubes to modify these properties, therefore, makes them very applicable to catalytic reactions.

With group VI metal species and carbon nanotube supports showing significant and controllable electronic interactions further investigation of these species in GNF carbon nanoreactors - which can promote modified interactions at the internal anchoring sites without restricting catalyst reactants - represents an interesting and motivating research challenge.

4.2. Aim and objectives

The aim of this study is to confine group VI metal oxide nanoparticles within hollow carbon nanotubes and investigate any interactions between the guest and host species.

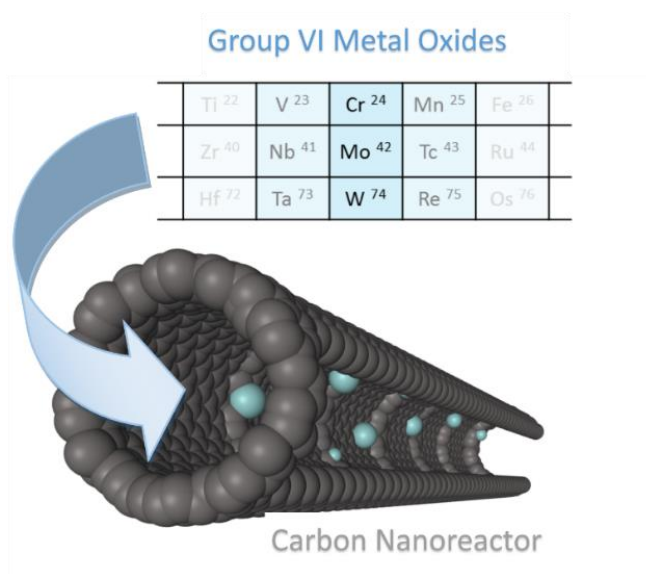


Figure 4.5. Schematic representation of a carbon nanoreactor filled with selected group VI metal oxides.

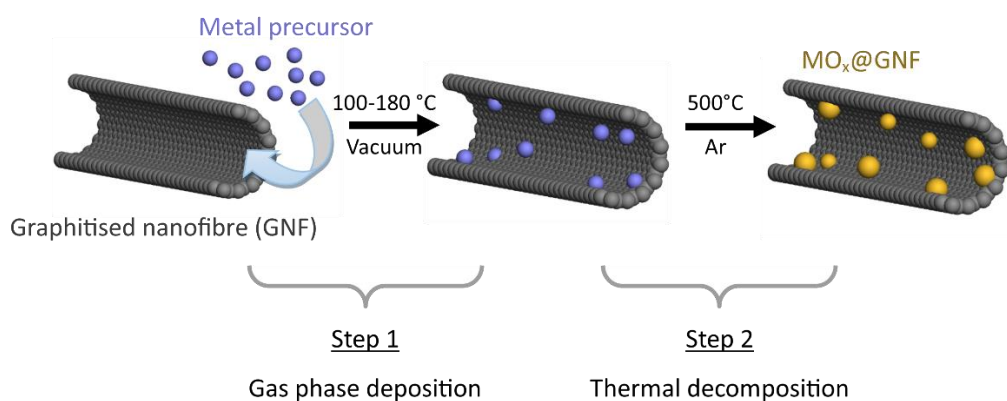
With Group VI metal species showing interesting electronic and redox properties, they represent a guest component which can be modified by encapsulation and exploitation of the confinement effects of carbon nanotubes. For this to be achieved, appropriate precursors, such as the group VI hexacarbonyl and acetylacetonate for a gas phase deposition inside nanotubes will be investigated. Suitable characterisation techniques to examine the loading, size, morphology, oxidation state and composition of the confined metal oxide will be additionally probed. Any distinctive guest-host interactions will be examined to understand the role of the carbon nanotube during these processes.

4.3. Results and discussion

In order to probe guest-host interactions between confined group VI nanomaterials and CNT, a suitable method for encapsulation must be developed. Recent approaches for filling W and Mo metal oxides into carbon nanotubes include impregnation using aqueous solutions of metal-ammonia complexes. This is an attractive approach as it can allow for multiple precursors to be added simultaneously,²⁹ but provides minimal control of particle size and is restricted by nanotube diameter and capillary forces which can lead to poor internal filling.^{30, 31} Effective molten filling of MoO₃ has been used to synthesise MoO₃@SWNT but this technique also relies on capillary forces and requires very high temperatures (>850 °C).³² Gas phase deposition of group VI metal-organic species has also been utilised, permitting deep penetration of the metal precursor into carbon nanotubes as the gaseous molecules diffuse without restriction into the empty nanotube cavity and can then be decomposed into clean uncapped surfaces.^{21, 33, 34}

The ability to encapsulate species within larger nanocarbon structures, such as hollow graphitised carbon nanofibres (GNF), has been established using the gas phase deposition reaction of group IV metal chloride species (Chapter 2) but has also been tested using several other late transition metal species, such as metal carbonyls or acetylacetonates.^{35, 36} The filling of GNFs can be achieved by exposure to a metallic vapour during gas phase deposition. A suitable precursor must contain the desired elements, sublime readily at relatively low temperatures, be stable in the gas-phase and decompose into the desired

species using external stimuli. Importantly, the synthesis of metal oxides inside graphitised nanofibres requires two steps: i) Gas phase deposition and ii) thermal decomposition. In the first step, GNF and the precursor are sealed under a high vacuum and heated, thus allowing sublimed guest-molecules to diffuse into the empty GNF. This is then rapidly cooled to trap precursor molecules inside the GNF cavity. In the second step, the sample is sealed under an inert atmosphere and heated to decompose the precursor (Scheme 4.1).



Scheme 4.1. Gas phase deposition and thermal decomposition technique proposed for filling group VI metal oxides inside GNF.

The oxygen present on the GNF surface as functional groups or adsorbed molecular O₂ and from the decomposed metal ligands has been previously shown to produce metal oxide species encapsulated within the graphitised nanofibre (MO_x@GNF). Using an argon atmosphere provides an overall deficiency of oxygen in the entire system and may produce significant oxygen defects in the metal oxide structure which will be important for the catalytic properties of these composite materials. This procedure has been adopted as a general strategy for all gas phase deposition reactions.

4.3.1. Synthesis of tungsten oxide inside graphitised nanofibres

4.3.1.1. Tungsten hexacarbonyl as a precursor

Tungsten hexacarbonyl satisfies the requirements as a suitable precursor and has been previously used to fill single-walled carbon nanotubes with tungsten species.³³ The gas phase deposition (Step 1) for this precursor was performed using a ratio of 0.02mol of W metal ($W(CO)_6$ -13.6mg) to 60mg of GNF based on previous successes with this precursor, i.e. a loading of 0.33 mol/g of the group VI metal to GNF. The sublimation temperature was found to be 120 °C under high vacuum (3×10^{-5} mbar) and the sealed system was left for 3 days to allow for sufficient migration of the precursor into the nanofibres. For the thermal decomposition of the hexacarbonyl precursor (Step 2), this intermediate material was sealed in an argon environment and was rapidly heated to 500 °C for 1 hour. Oxygen from the GNF and the decomposed ligand is thought to promote oxide formation and the material was allowed to cool for 9 hours to structurally equilibrate any oxides formed. This composite will be referenced as $WO_x@GNF-1$ onwards.

To confirm the presence of any metal species, thermogravimetric analysis (TGA) can be used to assess the loading of metal oxide in the composite material. Heating to elevated temperatures in air results in the oxidation of the GNF leaving a residual weight as the loading of the metal oxide species (Scheme 4.2).



Scheme 4.2. Combustion of carbon nanotube in air results in the production of CO₂.

For the WO_x@GNF-1 composite material, a 5.8% weight loading was achieved (Figure 4.6). Based on the mass ratio of reactants, the maximum possible residual weight loading would yield 11.8%, indicating that 49% of the precursor employed is involved in the composite formation.

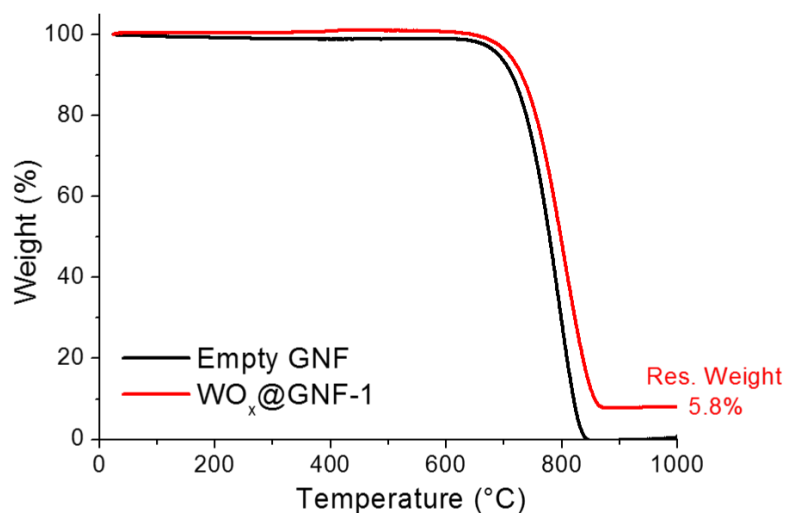


Figure 4.6. TGA profiles of WO_x@GNF-1 (0.33 mol/g) composite material (red) and empty GNF (black).

Powder X-ray diffraction (PXRD) can be used to identify any crystalline species present within the composite materials and can provide information on the oxidation state of the tungsten species formed after the thermal deposition. After the synthesis procedure, no sharp distinctive peaks in the diffractogram were observed; however, there does appear to be a large broad peak in the region of 35-40°. Comparisons to reference diffraction patterns indicate the possible formation of very small nanoparticles of monoclinic WO₂ with the peak broadening consistent with the inverse relationship between peak width and

nanoparticle grain size (Figure 4.7).³⁷ Due to the limits of the diffractometer, it would be expected that the grain size is close to 10nm as the instrument is unable to identify peaks below this threshold.

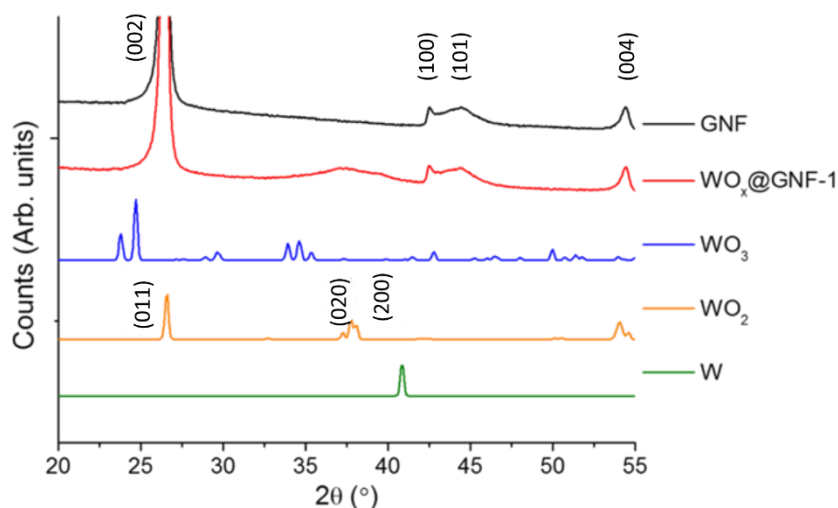


Figure 4.7. PXRD patterns of empty GNF (black) and $WO_x@GNF$ composite material (red). Corresponding diffraction patterns from a reference library for WO_3 (blue) and WO_2 (orange) and W (green) indicating the formation and crystal phases present.

When using the $W(CO)_6$ precursor, oxygen present during the thermal decomposition from the GNF and decomposed ligands is available for the transformation of metal into an oxide species at high temperatures. Due to the limited oxygen present oxidation to the WO_3 is not observed with semi-crystalline nanoparticles afforded containing oxygen deficiencies and a chemical composition close to WO_2 . The small size and poor crystallinity rationalise the difficulty in their observation using PXRD.

The techniques so far have provided evidence for the formation of a hybrid of WO_2 and GNF structures; however, transmission electron microscopy (TEM) is the only method which can confirm the location, morphology and size of the metal oxide species. TEM of the composite material reveals the presence of

darker contrasting nanoparticles which corresponds to the heavier atomic number of tungsten relative to the carbon. It appears from this procedure that the encapsulated species comprise very irregular shaped nanoparticles, deposited on both the internal and external surfaces of the GNF (Figure 4.8). Quantification of the internal and external loading of this material is challenging due to the irregular structure and morphology of the metal oxide. High resolution TEM indicates that the deposited material does lack crystallinity supporting the PXRD analysis.

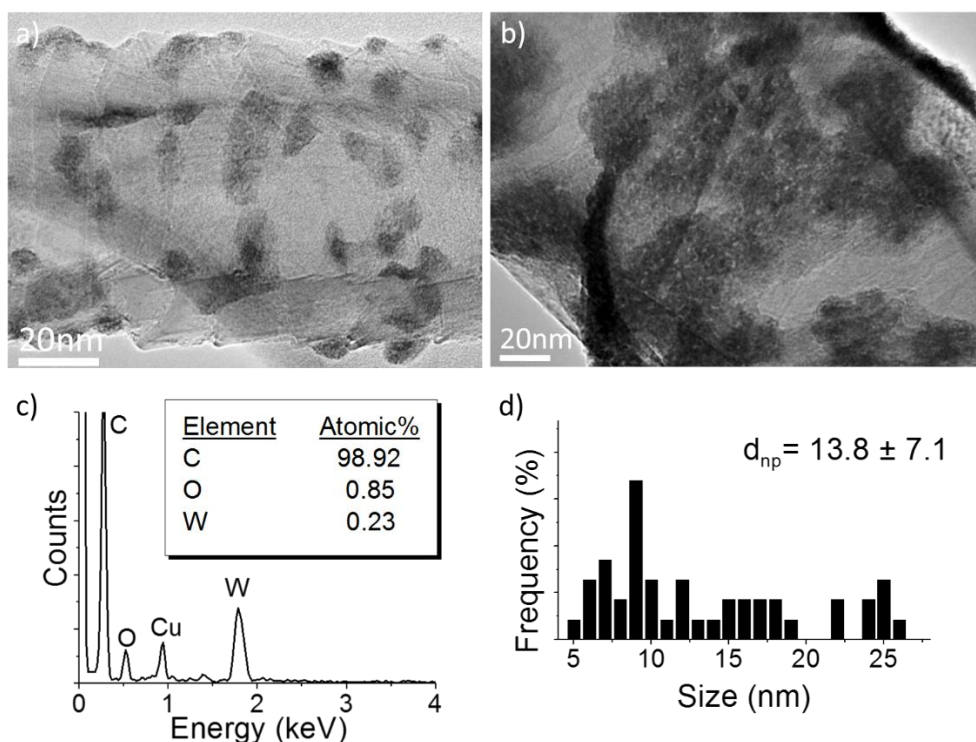


Figure 4.8. (a, b) TEM OF $WO_x@GNF-1$ composite material with (d) nanoparticle size distribution profile. (c) Corresponding EDX spectrum for the composite material and with 0.49% of the oxygen associated with carbon nanofibre a $WO_{1.6}$ stoichiometry can be estimated.

Energy dispersive X-ray spectroscopy (EDX) of this sample highlights an excess of oxygen present relative to tungsten, consistent with the formation of a tungsten oxide species. EDX can be used semi-quantitatively (Chapter 2) where

the oxygen associated with the GNF is calculated as 0.5% of the carbon atomic percentage. The remaining oxygen is related to the oxide which predicts an atomic stoichiometry close to WO_2 for the $\text{WO}_x@GNF-1$ (0.33 mol/g) composite which supports the PXRD analysis.

4.3.1.2. The effect of thermal treatment on $\text{WO}_x@GNF$

Thermal treatment in air is expected to allow for manipulation of oxidation state, size and crystallinity of the nanoparticle.^{5, 38} Heating the hybrid material to over 400 °C in air is expected to lead to the formation of WO_3 . Indeed, such treatment results in peaks at 23.3, 24.1, 29.0 and 33.8° in the diffraction pattern which match those expected for the trioxide (Figure 4.9).³⁹ These peaks are still relatively broad indicating small WO_3 nanoparticles are present, estimated at 8-10nm by employing the Scherrer equation. The thermally treated $\text{WO}_x@GNF-1$ will be referenced as $\text{WO}_3@GNF-1$ onwards.

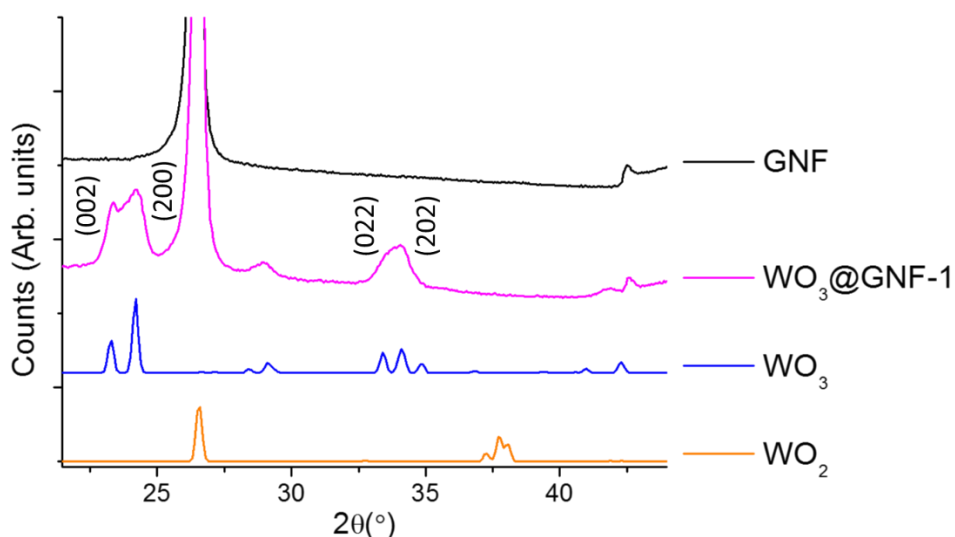


Figure 4.9. PXRD patterns of empty GNF (black) and $\text{WO}_3@GNF-1$ composite material thermally treated at 440°C in air (pink). Corresponding diffraction patterns from a reference library for WO_3 (blue) and WO_2 (orange) allow for the confirmation of the crystal phase present in the composite material.

TEM suggests that when heating in air the abundance of oxygen leads to the formation of more discrete spherical nanoparticles with an increased diameter and improved crystallinity that also support the formation of the WO_3 peaks from the PXRD analysis (Figure 4.10b). From TEM, however, the nanoparticle sizing after thermal treatment is 19.5 ± 4.9 nm which is almost double that predicted from the Scherrer equation. As the Scherrer equation is a measure of grain-size it could be suggested that these larger nanoparticles are made up of small multiple grains that have combined and grown.

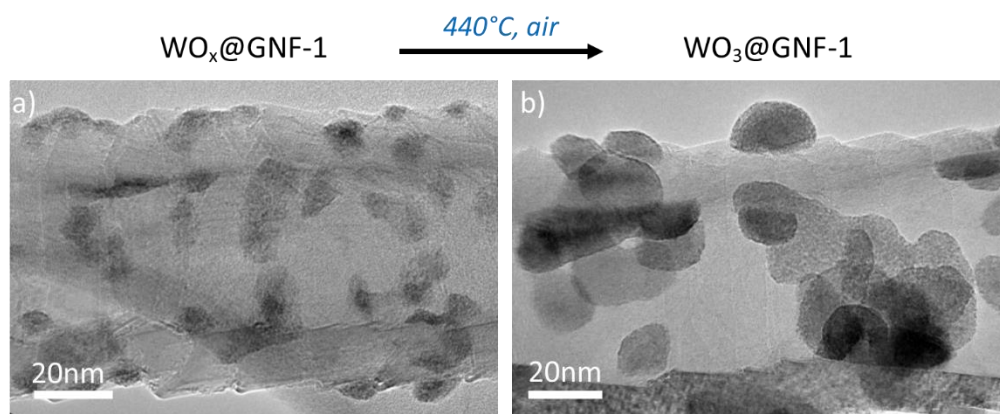


Figure 4.10. TEM of (a) $WO_x@GNF-1$ after synthesis and (b) $WO_3@GNF-1$ after thermal treatment at elevated temperatures in air.

High resolution TEM (HRTEM) provides evidence of a d-spacing of 0.34 nm which corresponds to the expected (200) interplanar spacing of monoclinic WO_3 (Figure 4.11).⁴⁰ This technique can also confirm the preferred depositing position at the internal anchoring sites of the GNF even for larger nanoparticles and supports that growth starts preferentially from these sites.

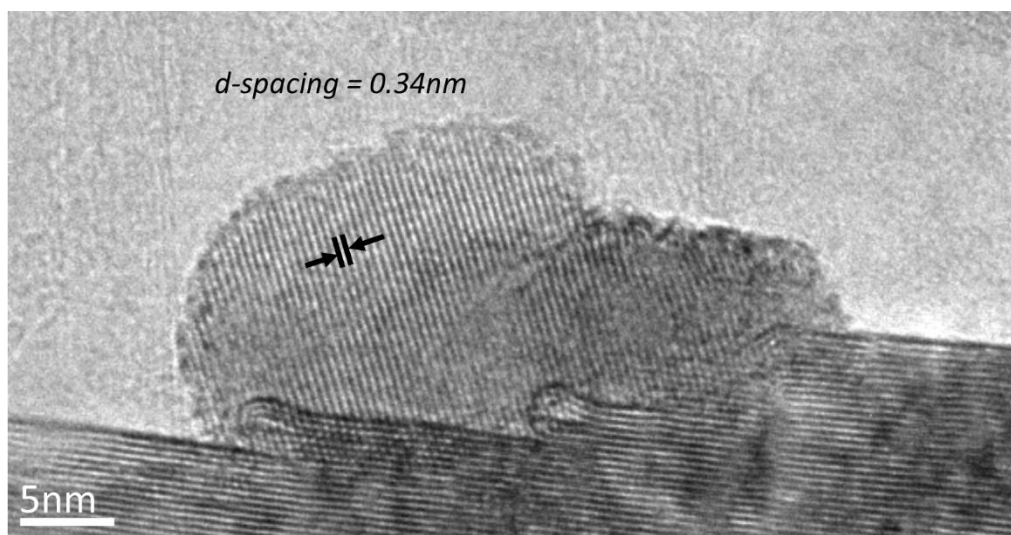


Figure 4.11. HRTEM of $\text{WO}_3@\text{GNF-1}$ nanoparticle formed after thermal treatment which resides at the internal folds of the graphitised nanofibre. Measured d -spacing is shown as 0.34nm.

4.3.1.3. The effect of precursor loading on the $\text{WO}_x@\text{GNF}$ formation

The large excess of precursor to GNF appears to allow for encapsulation, however, saturation of the metal species on the interior leads to significant external loading. For effective nanoreactors, exclusive internal filling is crucial, therefore, to maximise internal filling and minimise external filling, the quantity of metal precursor used in Step 1 was reduced by half. This material will be referenced as $\text{WO}_x@\text{GNF-2}$ onwards. TGA was able to confirm a 3.2% weight loading when half the metal precursor was employed (0.17 mol/g metal to GNF), which equates to 62% of the metal added being involved in the final composite. This is a 13% increase when compared to the higher loading and indicates that lower quantities of precursor relative to GNF increases the effective yield of the composite. With the same amount of oxygen provided by the GNF, this may additionally result in increased oxidation of the metal oxide nanoparticles; however, no peaks were observed in the diffractograms for the

metal oxide species (Figure 4.12a,b). From TEM, the reduced loading of $\text{WO}_x@$ GNF-2 not only ensured maximisation of filling when compared with the higher concentration used previously, but also the formation of very small nanoparticles (~ 3 nm) at the internal folds of the GNF (Figure 4.12d,e,f). EDX confirms the presence of tungsten, however, due to the small particles, semi-quantitative analysis proved problematic (Figure 4.12c).

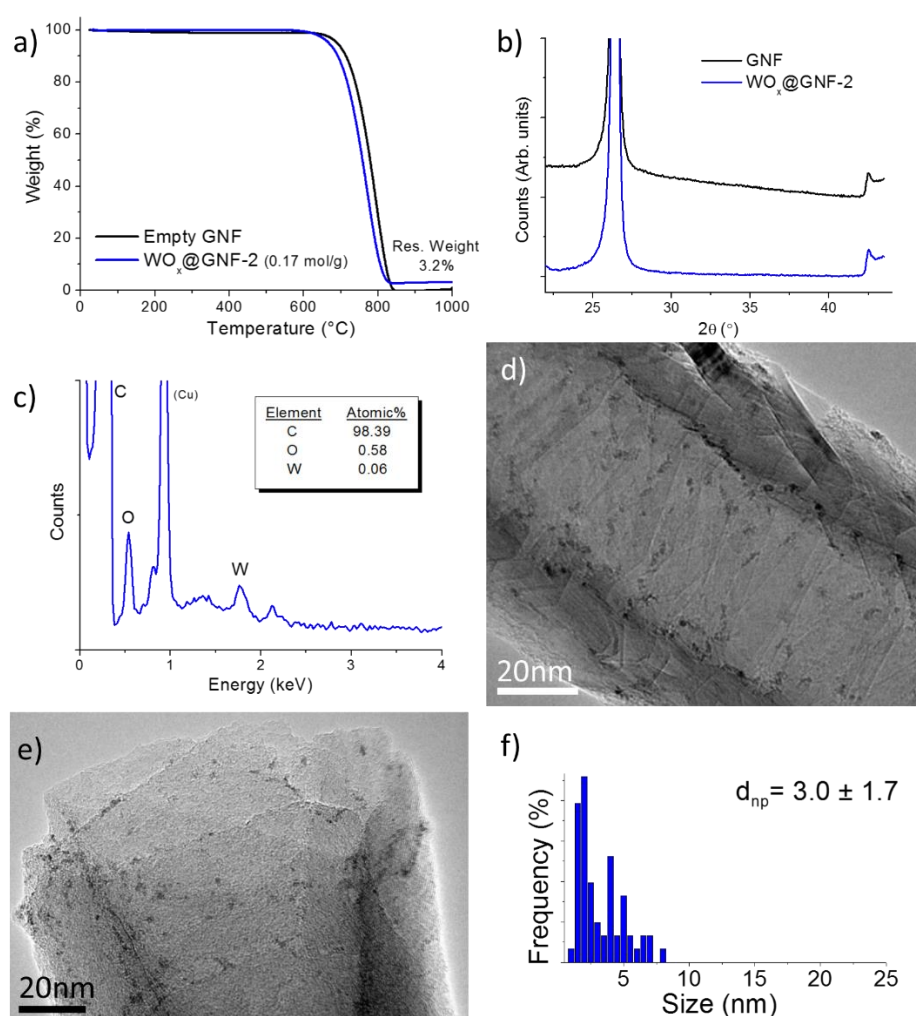


Figure 4.12. (a) TGA profile and (b) PXRD pattern of empty GNF (black) and $\text{WO}_x@$ GNF-2 (blue) with 0.17 mol/g of metal to GNF loading. Corresponding (c) EDX spectrum and (d,e) TEM analysis for the composite material with the (f) size distribution profile of WO_x nanoparticles.

The internal folds can be clearly shown to act as anchoring points for precursor deposition and growth due to increased van der Waals interactions compared to the smooth external carbon layers and allows for maximised internal filling. The 4.6-fold reduction in the nanoparticle size associated with the 2-fold reduction in the precursor is particularly striking. Although this results in a 21-fold difference in the surface area of the individual nanoparticles this will lead to an overall increase in the total surface area of the catalyst. This significant difference was unexpected and permits examination of the guest host interactions. As it is proposed that all nanoparticles nucleate at the internal folds, when the concentration is low the nanoparticle growth is restricted due to a reduced concentration of precursor. As a result, the nanoparticles remain at these anchoring sites and small in diameter. However, when more precursor is available the nanoparticles become larger resulting in their growth and consequent reduction in their van der Waals interactions which hold them at the fold. Once they become big enough they are able to migrate away from the fold and coalesce to become even larger as seen in 4.3.1.1.⁴¹ Evidently, manipulating the loading of the precursor in Step 1 of the synthesis can dramatically change the size, shape and position of the tungsten species.

4.3.1.4. The effect of the decomposition rate of the precursor on WO_x@GNF formation

To further investigate the properties of these smaller tungsten oxide nanoparticles, the ramp rate of the thermal decomposition (Step 2) was varied to evaluate if nanoparticle size or morphology could be changed to

demonstrate further control and provide additional information on the oxidation states of these species. Heretofore, Step 2 involved a rapid thermal decomposition rate (500 °C/min) of the precursor in an inert atmosphere; however, the use of a lower thermal ramp rate was investigated to probe whether nanoparticle growth could be controlled further. This material will be referenced as WO_x@GNF-3 onwards. When thermally decomposing at 10 °C/min there was no significant change to the residual loading from TGA supporting the reproducibility in the loading of this filling technique; however, a distinctive peak at 23.9° was observed by PXRD analysis (Figure 4.13). Previously reported monoclinic W₁₈O₄₉ nanowires show an identical peak in the PXRD, corresponding to the (010) plane, and could suggest this approach has resulted in the formation of a similar tungsten sub-oxide.⁴² For the sub-oxide species, the lowest energy surface is likely to be the (010) surface, therefore the formation of high aspect ratio nanowires is the result of preferential growth in this direction due to binding to this facet. This growth in one specific direction would result in the sharp peak in the PXRD and indicates that a slower decomposition temperature rate allows controlled mobility of the metal species.

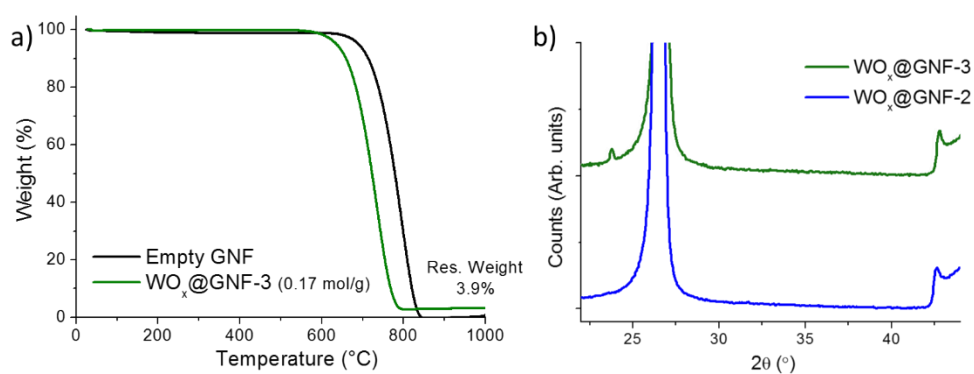


Figure 4.13. (a) TGA profiles of empty GNF (black) and $WO_x@GNF-3$ with 0.17 mol/g of metal to GNF with slow thermal decomposition step (10 °C/min – green) and its corresponding (b) PXRD pattern (green) compared against $WO_x@GNF-2$ with 0.17 mol/g of metal to GNF with a fast thermal decomposition step (500 °C/min – red).

TEM and EDX were employed to investigate the changes during the thermal decomposition process and clearly shows that using a slower thermal decomposition process allows for the formation of $W_{18}O_{49}$ nanorods encapsulated within the internal cavity of the GNF which would support the PXRD of a sub-oxide formation. (Figure 4.14).

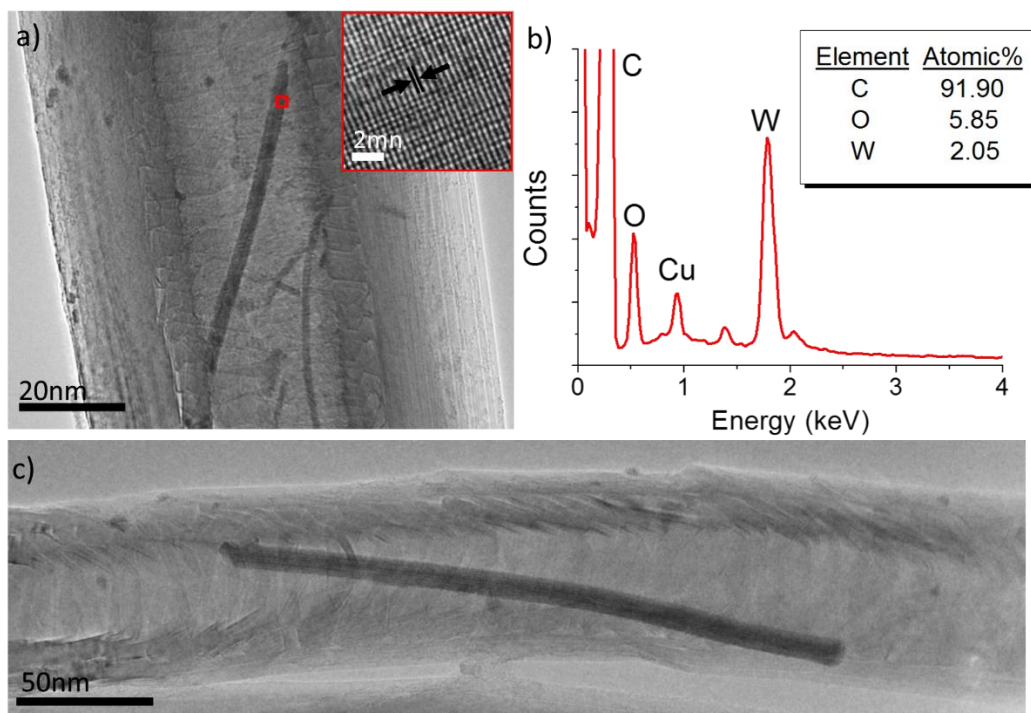


Figure 4.14. (a,c) TEM of $WO_x@GNF-3$ nanomaterial at slower thermal decomposition rate with HRTEM of WO_x nanorod identifying the lattice planes (red square - inset) and corresponding EDX spectra for the $WO_x@GNF-3$ nanorod species. With 0.46% of the oxygen associated with the carbon nanofibre, a stoichiometry of $WO_{2.6}$ for the nanorod can be estimated.

The lattice spacing of the nanorods was found to be 0.37nm by HRTEM which again corresponds to the (010) plane of the tungsten sub-oxide $W_{18}O_{49}$ species. Discrete nanoparticles are still present due to stabilisation at the GNF corrugated interior; however, a slower rate of decomposition results in the mobility of the metal species being slow enough that growth along a minimum energy crystallographic face is allowed resulting in anisotropic particles. When a faster thermal process is used, increased mobility results in the growth of the nanoparticles in all directions leading to small isotropic nanoparticles.

Interestingly, this result indicates that when a 0.17 mol/g of the precursor is used the composite composition resembles a more WO_3 species encapsulated

whereas when the higher 0.33 mol/g precursor loading a species closer to WO_2 was observed. This suggests that by decreasing the precursor to nanofibre ratio the gas phase thermal deposition reaction not only allows for control over size and morphology of the metal oxide but also control of the composition and the oxidation state. Although providing interesting morphologies of encapsulated materials, for a catalytic nanoreactor, having smaller nanoparticles encapsulated, as developed in 4.3.1.3, provides many benefits; therefore, the lower concentrations of precursors in Step 1 and rapid thermal rates for thermal decomposition in Step 2 will be implemented as standard hereafter.

4.3.2. Synthesis of molybdenum oxide inside graphitised nanofibres

4.3.2.1. Molybdenum hexacarbonyl as a precursor

One significant difference between the group VI hexacarbonyl series is their relative vapour pressures, which decreases down the group. For the gas phase deposition (Step 1) this poses problems as when sealing the precursor and GNF together under vacuum significant amounts of the precursor are often lost.

Using the understanding attained from experiments using tungsten hexacarbonyl, an identical strategy was utilised involving lower loadings and a rapid thermal decomposition for $\text{Mo}(\text{CO})_6$. The precursor (0.17 mol/g, metal to GNF) and GNF were sealed under a high vacuum (3×10^{-5} mbar) and heated to 110 °C to allow the sublimed guest-molecules to diffuse into the empty nanofibres. This was then thermally decomposed at a ramp rate of 500 °C/min

up to 500 °C in a sealed Ar environment to form the composite material and will be referenced as MoO_x@GNF-1 onwards.

TGA indicated that by employing the molybdenum hexacarbonyl precursor a residual weight loading of 0.3% was achieved. This is significantly lower than the corresponding tungsten species and suggests around only 5% of the precursor is involved in the composite formation. Arguably, the recorded 0.3 wt.% loading is within the error of the instrument; however, the formation of the hybrid materials with this precursor is confirmed from the significant shift in the oxidation temperature of the GNF once the composite is formed (Figure 4.15a). This decrease of over 100 °C is thought to originate from interactions between the guest molecules and the GNF which weakens the carbon structure leading to lower temperatures of combustion and will be discussed in detail later.

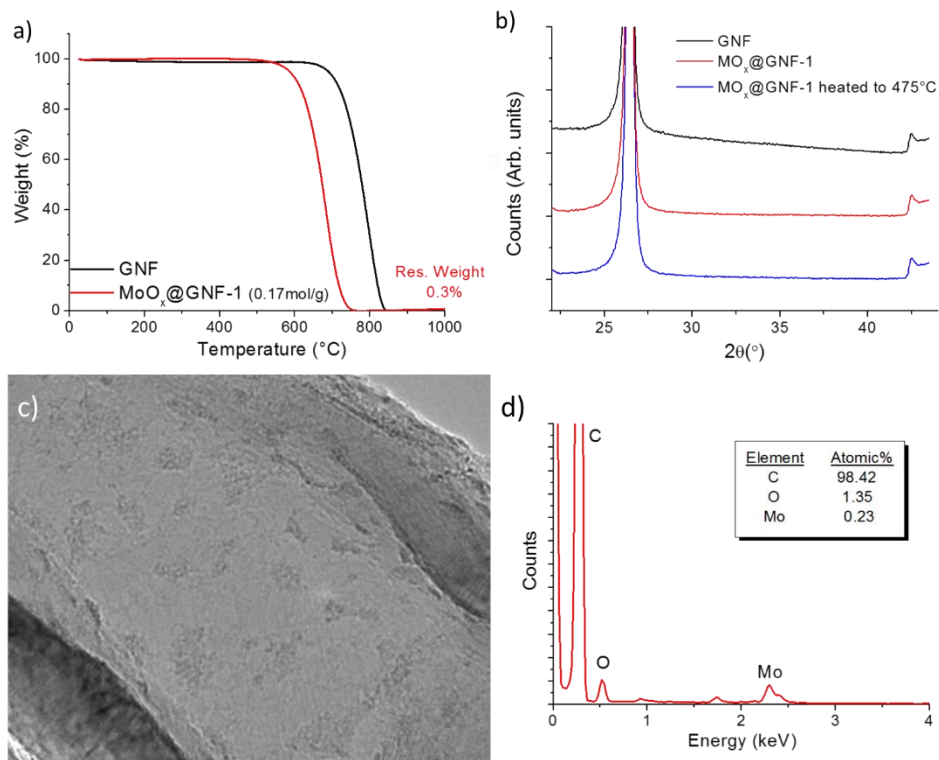


Figure 4.15. (a) TGA profiles of MoO_x@GNF-1 composite material (red) and empty GNF (black). (b) PXRD patterns of empty GNF (black), MoO_x@GNF-1 (red) and thermally treated MoO_x@GNF (blue). (c) Representative TEM and (d) EDX spectra of MoO_x@GNF-1 from the hexacarbonyl precursor.

PXRD of the sample after synthesis shows no distinctive crystalline features and thermal treatment in air also results in no crystalline peaks formed most likely due to the small amount of catalyst present in the system (Figure 4.15b). TEM allows for the identification of very small nanoparticles but confirming location proved problematic (Figure 4.15c). EDX confirms the presence of the molybdenum and oxygen, but the low signal precludes estimation of the molybdenum oxidation state (Figure 4.15d). Although the particles are small and therefore attractive for catalysis, the efficiency of this procedure and small quantities of encapsulated metal oxide formed inside the GNF make this composite problematic and unsuitable for applications as a catalytic

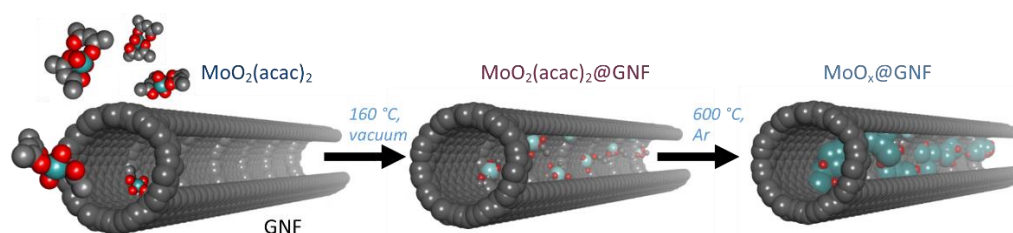
nanoreactor. The poor loading is thought to be the result of the volatile precursor being lost from the ampoule during the vacuum filling step, resulting in minimal quantities of the precursor being present during the sublimation stage. With molybdenum oxide showing some promising guest-host interactions further investigation into the synthesis of a MoO_x@GNF nanoreactor was explored. As the yield of MoO_x@GNF-1 using the molybdenum hexacarbonyl precursor was so low, further experiments into other precursors were necessary.

4.3.2.2. Molybdenum dioxide bisacetylacetonate as a precursor

One class of metal precursors that have shown consistent successes in the gas phase deposition over the transition metals are the acetylacetonate complexes.³⁶ The large organic groups allow effective sublimation of the precursor to sublime without decomposition at relatively low temperatures. Molybdenum dioxide bisacetylacetonate (MoO₂(acac)₂) has been previously sublimed and decomposed to form the oxide and therefore, was adopted for the gas-phase thermal deposition reaction in an attempt to develop an effective encapsulation strategy for confining other group VI metal oxides within graphitised nanofibres.^{43, 44}

Based on the gas phase deposition reactions with the hexacarbonyls performed so far, a similar strategy was developed for MoO₂(acac)₂ gas phase deposition (Scheme 4.3). The sublimation temperature for this precursor was observed to be higher (160 °C), therefore, the precursor (containing 0.01 mol of the metal) and GNF were sealed under a high vacuum (3x10⁻⁵ mbar) and heated to 160 °C

to allow the sublimed guest-molecules to diffuse into the empty nanofibres. Once trapped within the nanofibre cavity the material was heated in an inert atmosphere to 600 °C to facilitate rapid decomposition of the precursor molecules into molybdenum oxide nanoparticles entrapped in GNF.



Scheme 4.3. Gas-phase encapsulation procedure of $\text{MoO}_2(\text{acac})_2$ and molybdenum oxide nanoparticles within the GNF.

TGA showed the loading (by weight) of the metal oxides in the final composite as 4.0% (Figure 4,16b). In addition, TGA again also indicates a significant reduction in the combustion temperature of the GNFs by more than 150 °C, indicating intimate contact between the nanoparticles and the nanofibre and promising guest-host interactions present.⁴⁵ To confirm the oxidation state and crystallinity of the molybdenum oxide species within the composite material, PXRD analysis was employed. Peaks at $2\theta = 37.1^\circ$ and 53.6° can be clearly observed in the diffractogram, consistent with the crystal phase of molybdenum(IV) dioxide (Figure 4.16a).⁴⁶ Grain size was estimated to be 20 nm based on the analysis of the peak at $2\theta = 37.1^\circ$ (FWHM = 0.51°) and application of the Scherrer equation. EDX spectroscopy reveals the elemental composition of the $\text{MoO}_2@GNF$, with a near 2:1 atomic ratio of oxygen to molybdenum, further supporting the formation of the dioxide species (Figure 4.16c). This material will be referenced as $\text{MoO}_2@GNF-2$ onwards.

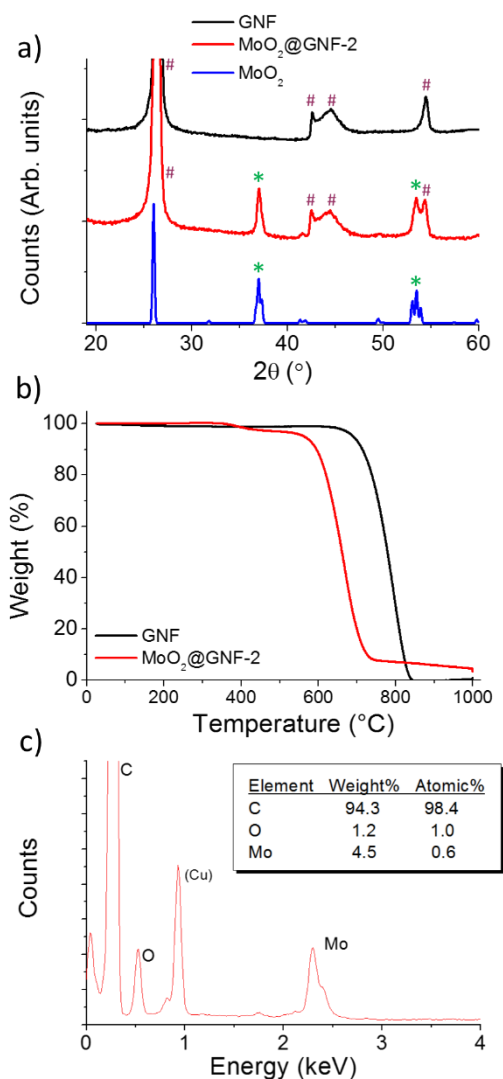


Figure 4.16. (a) PXRD patterns of MoO₂@GNF-2 (red), empty GNFs (black) and bulk MoO₂ (blue) show the composite is the combination of the two components. (b) TGA profiles of MoO₂@GNF-2 (red) and empty GNF (black). (c) EDX spectroscopy of MoO₂@GNF-2 confirms the presence of Mo and O inside GNF in a ratio close to the stoichiometry in MoO₂.

To evaluate the size, morphology and position of the molybdenum dioxide nanoparticles within GNFs, TEM was employed. Statistical analysis of images taken from multiple parts of the specimen grid indicates nanoparticles with an average diameter of 29 ± 10 nm are found predominantly within the internal cavity of the GNFs. The distinctive contrast relative to the carbon of the GNFs strongly supports the formation of metal oxide (Figure 4.17b). This

nanoparticle size distribution information does better support the Scherrer equation estimation compared to the tungsten composite. This suggests that the application of the Scherrer equation is only suitable for larger nanoparticles but could also confirm that larger nanoparticles are most likely made up of multiple grain sizes. The interior surfaces appear to be the favoured site for the growth of nanoparticles relative to the external walls, confirming the importance of internal folds which provide anchoring points for the nucleation of the metal oxide, which are absent on the smooth graphitic layers of the exterior. High resolution TEM of the nanoparticles reveals a d-spacing of 0.37 nm which corresponds to the (110) lattice planes of MoO₂ (Figure 4.17c). To extract information on the 3D structure of the nanoparticles, images were captured at different extents of angular tilt (Figure 4.17d). As the GNF is rotated around its growth axis it can be observed that the MoO₂ nanoparticles remain within the interior channel confirming their confinement within the internal volume and exhibit faceted morphologies.

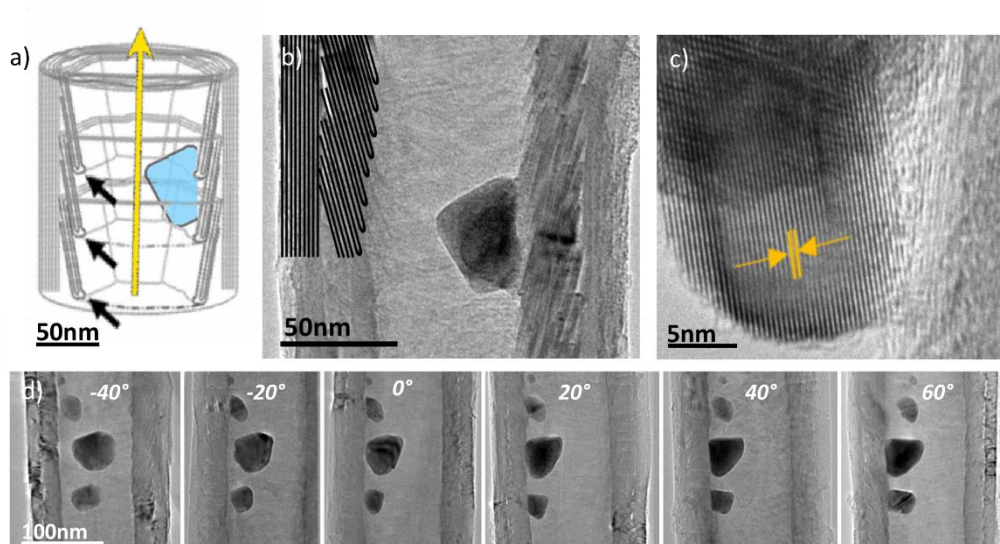


Figure 4.17. (a) Schematic representation of the structure of GNF (corrugated interior are denoted by black arrows; the yellow arrow signifies the direction of the nanofibre axis). (b) Bright field transmission electron microscopy (TEM) image $\text{MoO}_2@\text{GNF-2}$. The internal anchoring points have been highlighted for clarity, with the MoO_2 nanoparticle clearly shown residing at the interior fold. (c) High resolution TEM of the MoO_2 nanoparticle providing a lattice spacing of 0.37nm, consistent with the (110) planes in MoO_2 . (d) TEM tilt series of $\text{MoO}_2@\text{GNF-2}$, rotating around the GNF growth axis, which allows for a better understanding of the morphology of the nanoparticles and confirms their encapsulation within the internal cavity of the GNF.

Scanning transmission electron microscopy (STEM) in combination with EDX elemental mapping additionally confirms the composition of the nanoparticles as molybdenum and oxygen and co-location of oxygen and molybdenum in the nanoparticles which is consistent with the formation of metal oxide. (Figure 4.18).

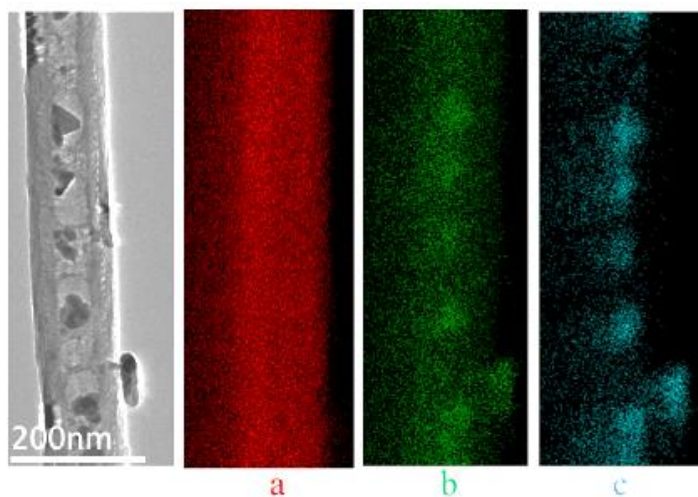


Figure 4.18. Bright field TEM image and EDX elemental mapping of (a) carbon, (b) oxygen and (c) molybdenum in $\text{MoO}_2\text{@GNF-2}$.

4.3.2.2.1. The effect of precursor loading on $\text{MoO}_x\text{@GNF}$ formation

By varying the quantity of precursor during synthesis it has been shown that loading, size, location and oxidation of the nanomaterials could be controlled (4.3.1.3), therefore, changing the loading of $\text{MoO}_2(\text{acac})_2$ to GNF in the gas phase deposition reaction was additionally investigated (Table 4.2).

Table 4.2. Different loadings of $\text{MoO}_2(\text{acac})_2$ precursor for the formation of MoO_2 nanoparticles inside graphitised nanofibres.

Composite	Quantity of $\text{MoO}_2(\text{acac})_2$ (mg)	Quantity of metal to GNF mol/g	Loading of MoO_2 (%)	T_{ox} ($^{\circ}\text{C}$) ^a
$\text{MoO}_2\text{@GNF-3}$	7.8	0.12	3.5	629
$\text{MoO}_2\text{@GNF-2}$	11.1	0.17	4.0	634
$\text{MoO}_2\text{@GNF-4}$	14.4	0.22	6.8	632

^a Temperature of oxidation of the GNF due to combustion measured from TGA.

To investigate how the precursor to GNF ratio would impact the mean loading of MoO_2 , the amount of $\text{MoO}_2(\text{acac})_2$ added to the GNFs was altered. This series of experiments showed that there does appear to be a strong

relationship between the increase in precursor added and the observed loading. Interestingly, all the composite materials synthesised showed a diffraction pattern characteristic of MoO_2 and the same features as previously identified with a decrease in the GNF oxidation temperature observed by TGA (T_{Ox}). This feature appears to have no dependency on the loading suggesting this process may be catalytic. TEM analysis of the three materials confirms the presence of more molybdenum oxide with higher initial loadings; however, it also shows that decreasing the loading enables better control of the nanoparticles location, with more nanoparticles observed on the inside of the GNF (Figure 4.19). This is consistent with the behaviour observed using tungsten precursors (section 4.3.1.3), where the internal anchoring sites were preferred. This demonstrates the ability to not only have control over the loading but also the position of the molybdenum dioxide species within the composite materials, with the observed structures representing an interplay of these two effects. The MoO_2 @GNF-2, where loading is moderately high, but nanoparticles are largely retained inside the GNF represents the most suitable and would be a material to investigate in catalytic reactions (Chapter 5).

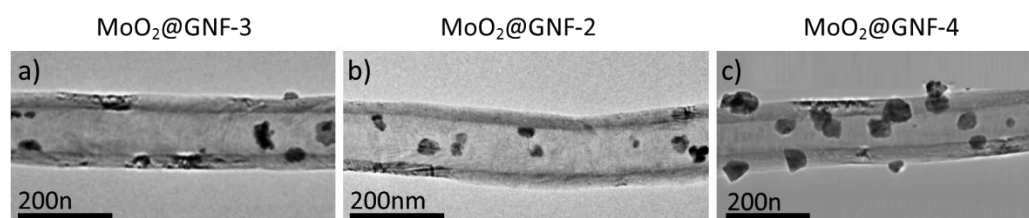


Figure 4.19. TEM images of different loadings of MoO_2 inside graphitised nanofibres with (a) 0.12 mol/g, (b) 0.17 mol/g and (c) 0.22 mol/g of metal quantity to GNF during the gas phase thermal deposition.

4.3.2.2.2. The effect of thermal treatment on MoO_x@GNF

To probe the ability to control the structure and composition of the metal oxide nanoparticles by post-synthesis treatment, small quantities of the sample were heated to elevated temperatures in air. *In-situ* PXRD indicates peaks at $2\theta = 27.4, 33.9$ and 39.3° emerge in the diffractogram above 250°C which are consistent with the formation of MoO₃ (Figure 4.20a). This material will be referenced as MoO₃@GNF-2 onwards.

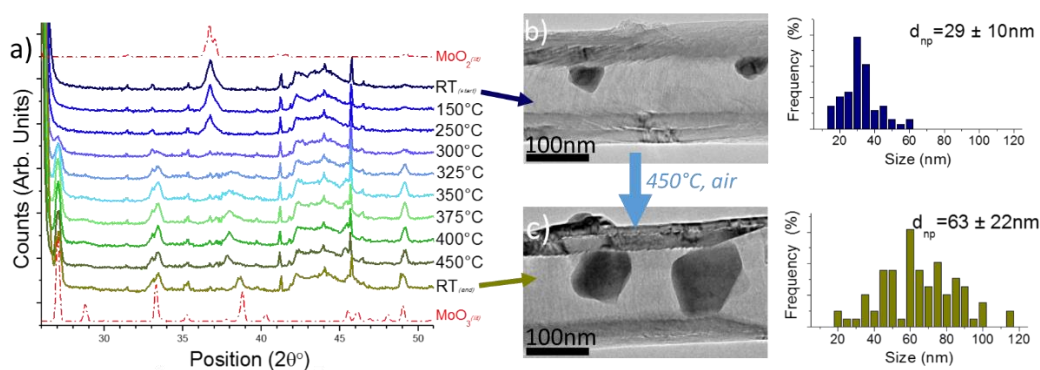


Figure 4.20. (a) PXRD analysis of thermal annealing MoO₂@GNF-2 in air clearly shows the change from MoO₂ to MoO₃ between 250 and 300 °C and formation of MoO₃@GNF-2. (b, c) TEM images and corresponding nanoparticle size distributions before and after post-synthesis thermal treatment at 450°C, respectively. This highlights the increase in nanoparticle size and blocking of the GNF interior channel for materials treated at elevated temperatures.

This transformation from MoO₂ to MoO₃ means that the oxidation state of the encapsulated molybdenum species can be readily tuned. This thermal treatment resulted in an increase of the MoO₃ particle size to 63 ± 22 nm which appears to block the GNF interior channel for materials treated at elevated temperatures which may cause issues in transport resistance of reactants for chemical reactions (Figure 4.20c). This strategy offers an effective mechanism for controlling both the size and composition of the metal oxide nanoparticles,

opening a door for a broad range of different catalytic nanoreactors that can be readily afforded and manipulated using this simple versatile strategy of nanoparticles growth in GNF.

During the thermal treatment, an accompanying thermal process is observed in the TGA as a weight loss (3%) at 359 °C, which cannot be accounted for by the addition of oxygen during the change in the oxidation state of the metal oxide, therefore, further investigation is required (Figure 4.21).

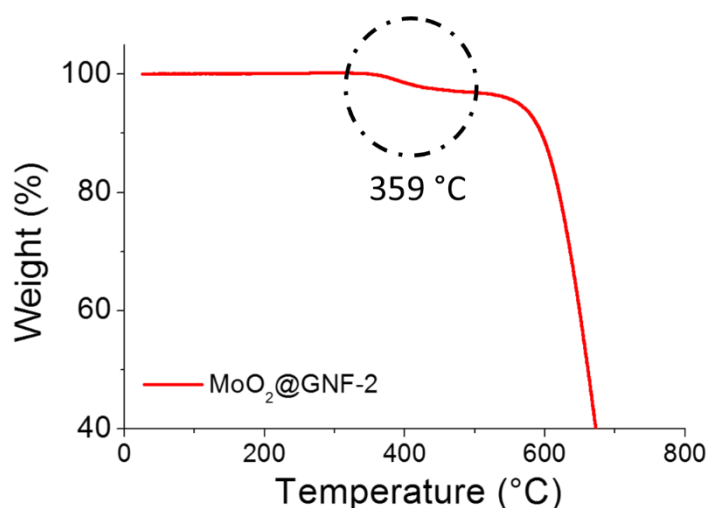


Figure 4.21. Zoomed in TGA profile of MoO₂@GNF-2 highlighting the distinctive weight loss at 359°C.

TGA of the MoO₂(acac)₂ in isolation shows that acetylacetonate groups are lost below 270 °C and as Step 2 involves decomposing under an argon atmosphere at 500 °C, it is very unlikely that any acetylacetonate species remain. At temperatures of 350 °C, it is not expected that the nanofibre will oxidise by a direct reaction with O₂; however, TEM was employed after a thermal treatment to 450 °C (after the initial weight loss but before T_{ox}) to investigate the carbon surface. Interestingly, it was observed that many nanofibres had cavities and

It appears the carbon is acting as a catalyst and facilitates the reduction of metal oxide at its surface at elevated temperature. A scheme can be proposed for the site-selective oxidation of the C atoms of the GNF, involving the metal oxide acting as an oxidant resulting in the formation of CO₂. It has been previously suggested that changing morphology and dimensionality of the oxide particles to the nanoscale leads to control over the reducibility of the oxide.⁴⁷ This is due to the much higher reactivity of the low-coordinated oxygen sites at the steps and corners. The regeneration of the oxidising species by molecular oxygen at the metal oxide surface results in the site-selective oxidation and thus the defects in the GNF structure. At temperatures above 400 °C, this localised combustion subsides shown by a plateau in the TGA weight loss. This is likely due to the corresponding growth in the nanoparticle and homogenisation of the metal oxide surface which causes decreased contact between the oxygen atoms and the carbon surface and loss of the highly reactive sites at the metal oxides facets.

This unique feature of the metal oxide species enables the generation of defects in the carbon surfaces and side walls, with site-specific precision. This has many benefits, such as allowing new favourable sites for catalyst deposition which may have increased interactions and stability. Nanotube sidewalls with increased defects and oxygen groups improves the dispersibility of the GNF in aqueous media as identified by the functionalisation of multi-walled carbon nanotubes previously.⁴⁸⁻⁵⁰ The larger openings in the sidewalls of the nanotube not only allows for deeper penetration of precursor molecules during the gas

phase deposition but could improve the transport resistance of reagents when the composite is applied as a nanoreactor.

4.3.3. Synthesis of chromium oxide inside graphitised nanofibres

4.3.3.1. Chromium hexacarbonyl as a precursor

For the synthesis of chromium oxide nanomaterials inside graphitised nanofibres, an identical strategy was implemented utilising the gas phase deposition with the chromium hexacarbonyl precursor. With the significantly high vapour pressure of chromium hexacarbonyl, it was unsurprising that the TGA indicated a 0% residual loading and the PXRD pattern resembled the parent GNF. Therefore, volatile chromium hexacarbonyl resulted in no composite formation and was not investigated any further (Figure 4.23).

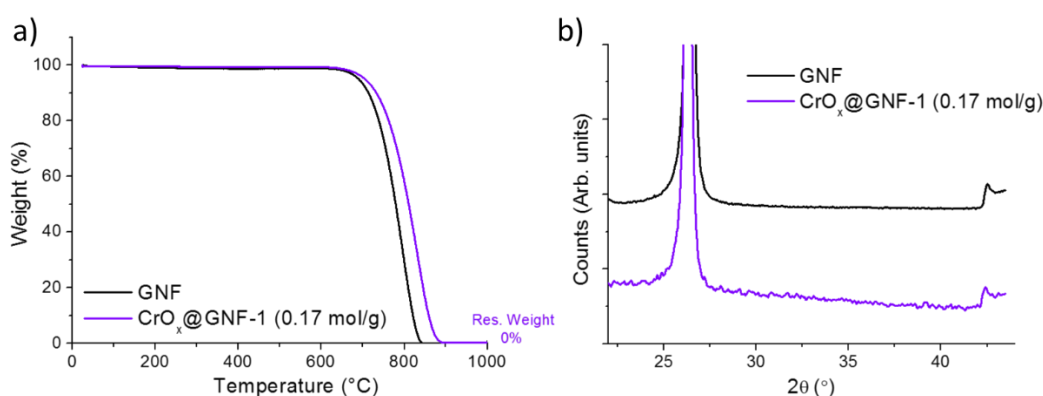


Figure 4.23. (a) TGA profiles and PXRD patterns of CrO_x@GNF-1 composite material (purple) and empty GNF (black) showing no composite formation.

4.3.3.2. Chromium acetylacetonate as a precursor

Following the success of the molybdenum oxide formation, using the acetylacetonate precursor (Cr(acac)₃) with a lower vapour pressure than the previous chromium hexacarbonyl precursor was used. The addition of Cr(acac)₃

and GNF (0.17 mol/g) follows the same procedure as described previously, but only required heating to 110°C for 3 days to allow the sublimed precursor sufficient time to diffuse into the GNF. The procedure was analogous to the MoO_x@GNF synthesis and involved the formation of a Cr(acac)₃@GNF as an intermediate, which is then decomposed in an argon atmosphere at 600 °C to synthesise CrO_x@GNF. This material will be referenced as CrO_x@GNF-2 onwards. TGA confirms a residual weight of 6.5% for this composite with a weight loss at 340 °C similar to the molybdenum oxide composite material; however, the PXRD does not possess any distinctive peaks which would match the expected oxides of chromium that could be formed (Figure 4.24).⁵¹⁻⁵³

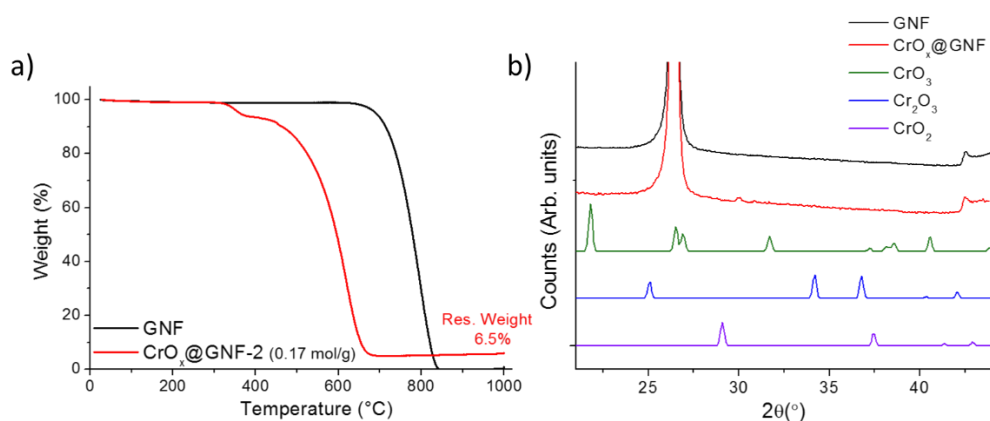


Figure 4.24. (a) TGA profiles of CrO_x@GNF-2 composite material (red) and empty GNF (black). (b) PXRD patterns of empty GNF (black), CrO_x@GNF composite material (red). Reference patterns for CrO₃ (green) Cr₂O₃ (blue) and CrO₂ (purple) from a reference library indicating the formation of no crystalline oxide phases.⁵¹⁻⁵³

TEM and EDX of the composite confirm that small non-crystalline nanoparticles with an average diameter of 5 nm are formed on the interior and exterior of the nanofibre which are composed of chromium and oxygen and have sufficient excess of oxygen supporting the formation of an oxide species.

Removal of oxygen associated with the GNF functional groups, estimates an approximate stoichiometry of $\text{CrO}_{1.5}$, supporting the formation of Cr_2O_3 (Figure 4.25).

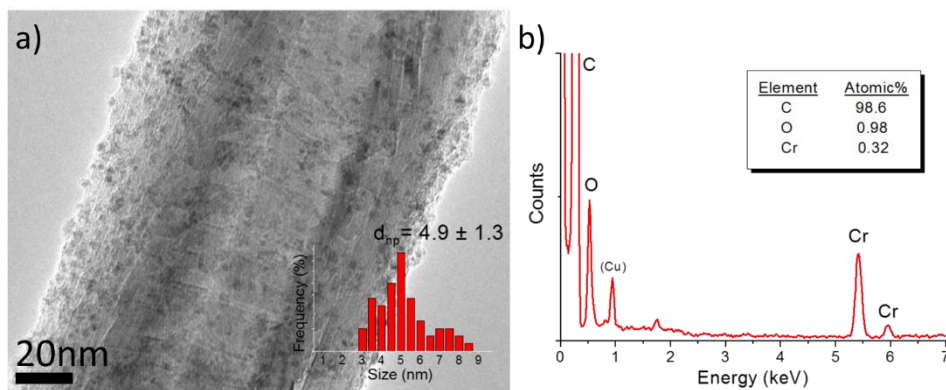


Figure 4.25. (a) TEM with corresponding nanoparticle sizing distribution profile (inset) and (b) EDX spectra of CrO_x @GNF-2, showing composite formation with the presence of chromium oxide nanoparticles, where 0.49% of the oxygen is associated with the GNF.

To support the EDX, electron energy loss spectroscopy (EELS) can be employed to chromium oxides as it has defined peaks unlike the tungsten analogue, and provides information regarding the oxidation state of the metal and the state of the oxygen groups present. The EELS analysis confirms the chromium species is in the +3 oxidation state when compared to a Cr_2O_3 reference due to minimal shifts in the Cr L edges (Figure 4.26).^{54, 55}

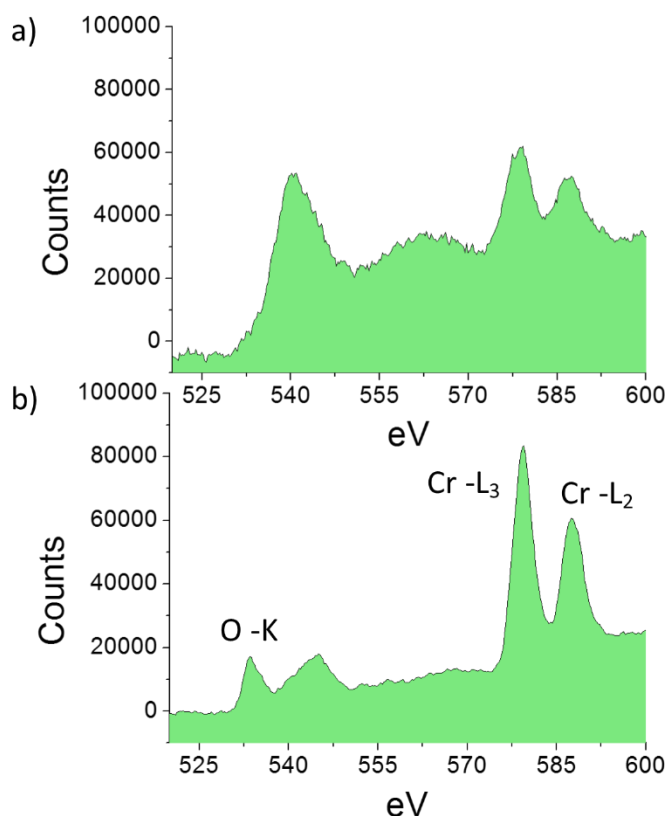


Figure 4.26. EEL spectra of (a) as synthesised $\text{CrO}_x@GNF-2$ and (b) Cr_2O_3 reference showing oxygen K edge (532 eV), oxygen near edge fine structure (544 eV) and chromium L edges (579 and 587 eV). This supports no change in chromium oxidation state, but the broadness of the oxygen peak suggests increased oxygen vacancies in the metal oxide structure.

The unusual oxygen edge in the as synthesised sample is a broad single peak rather than the expected oxygen edge and its near edge fine structure as seen in the thermally treated sample. This broadening could be the result of low signal to noise but also could suggest significant oxygen deficiencies and vacant sites in the metal oxide lattice.⁵⁶ This indicates that the small chromium nanoparticles are similar in structure to the Cr_2O_3 but may possess increased oxygen vacancies which would be very interesting for catalysis. According to previous literature reports, chromium oxide species possess the least impressive catalytic abilities out of the group VI metal oxides and, therefore,

further procedural manipulation to control loading or location of the nanoparticle was not investigated. However, the interesting thermally activated processes observed in the TGA of this composite material required further attention.

4.3.3.2.1. The effect of thermal treatment on CrO_x@GNF

Due to the interesting results observed during thermal treatment of the other group VI composites in air, CrO_x@GNF-2 was performed to investigate the influence of temperature on particle size, morphology and composition of the metal oxide nanoparticles. To probe the changes in oxidation state and structure of the metal oxide the *in-situ* method of variable temperature PXRD was employed. The chromium species appears to form crystalline Cr₂O₃ nanoparticles at temperatures above 375 °C within the composite material with peaks at $2\theta = 24^\circ, 33^\circ$ and 36° that are characteristic of Cr₂O₃ in PXRD. This material will be referenced as Cr₂O₃@GNF-2 onwards and interestingly, the formation of the crystalline oxide isn't the only feature observed (Figure 4.27).

57, 58

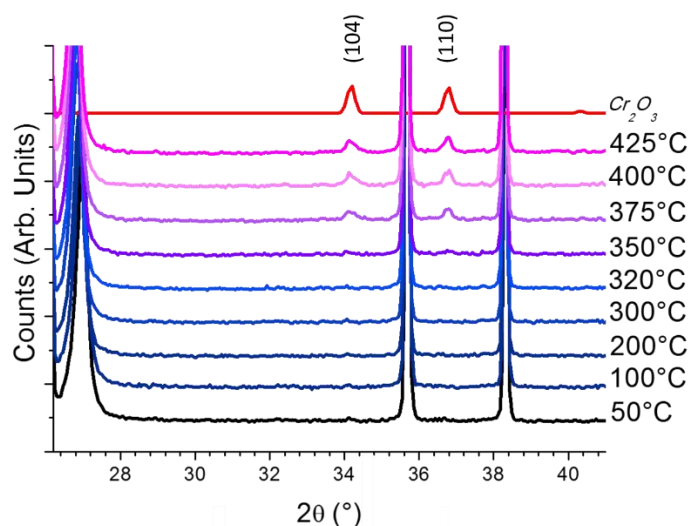


Figure 4.27. PXRD patterns of thermally treated $\text{CrO}_x\text{@GNF-2}$ composite material in air resulting in the formation of the crystalline Cr_2O_3 within the composite as confirmed by the Cr_2O_3 reference pattern (grey).⁵²

The thermal processes shown by the TGA of $\text{CrO}_x\text{@GNF-2}$ share similarities with the molybdenum composite species, as a more pronounced distinctive weight loss (6%) is observed at 336 °C. With this weight loss being better defined, analysis by TGA-MS was performed to probe the nature of the gaseous products formed at this weight. From this, it was shown that CO_2 (typified by a fragment at 44 m/e) is lost significantly at both major weight losses (336 and 581 °C) confirming the first weight loss is the result of site-selective oxidation as observed in the molybdenum composite (Figure 4.28).

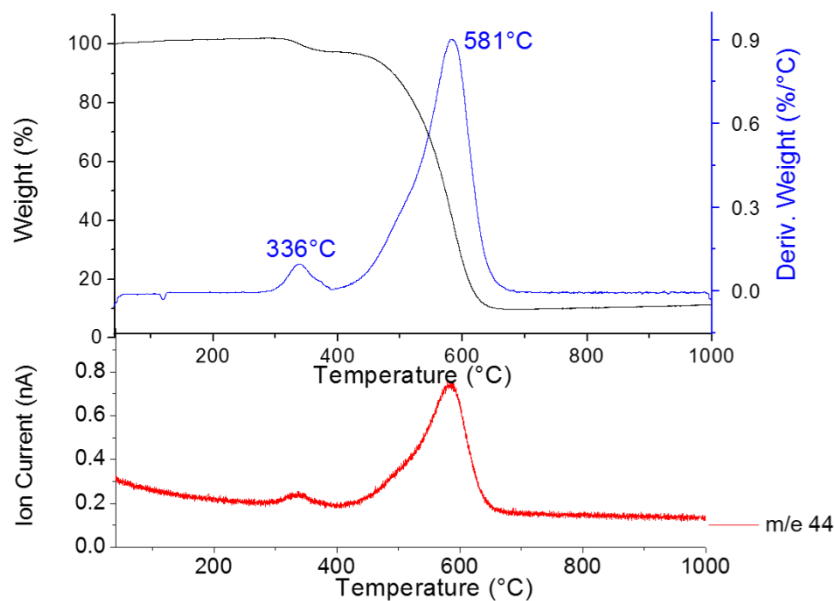


Figure 4.28. TGA profile (black) and derivative weight function (blue) of $\text{CrO}_x\text{@GNF-2}$ with corresponding mass spectroscopy gas analysis (red) for CO_2 (44 m/z).

To investigate this further an *ex-situ* approach to probe changes in the structure of the carbon nanofibre employing TEM was performed of the sample before and after heating to 385°C (Figure 4.29). These striking results show that there is a change in the morphology and increase in nanoparticle size (32.6nm) which happens in conjunction with site-selective oxidation of the GNF around the chromium oxide nanoparticles.

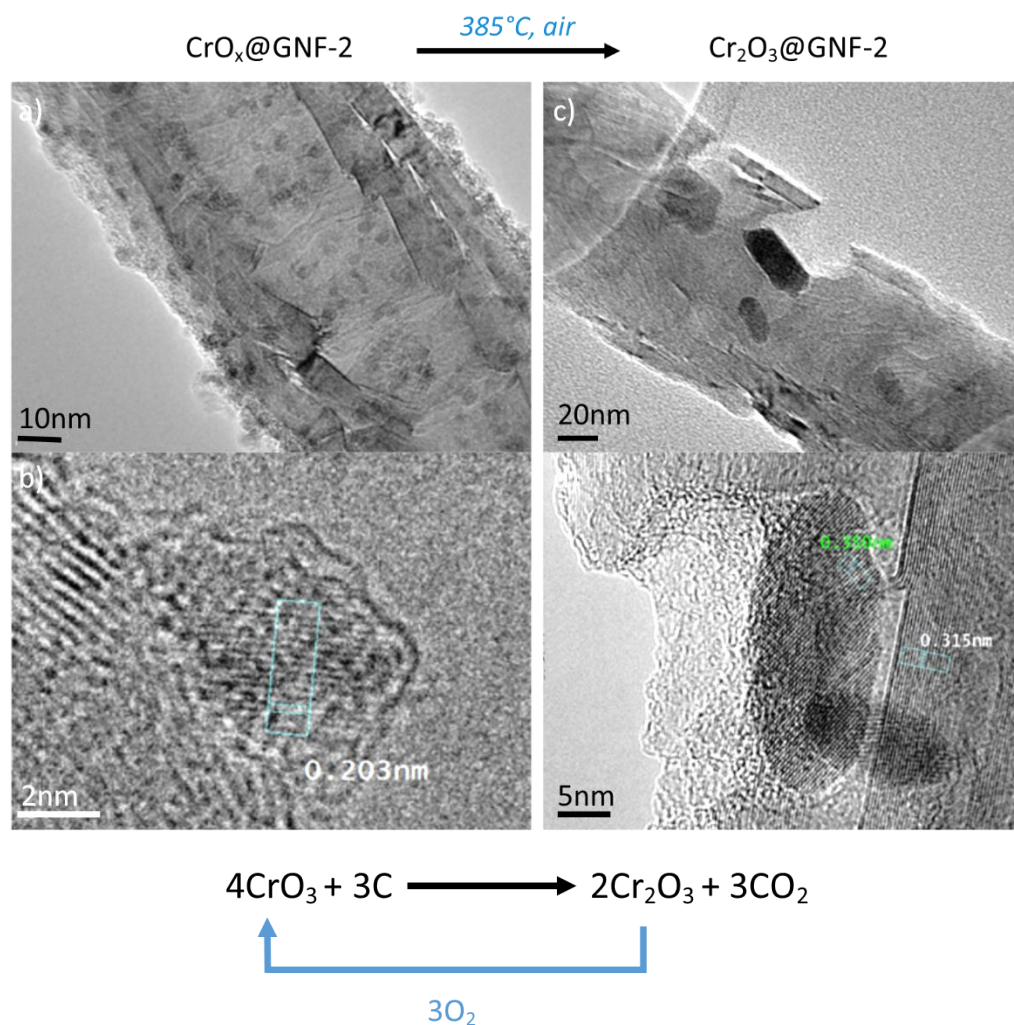


Figure 4.29. TEM images of (a, b) as synthesised $\text{CrO}_x\text{@GNF-2}$ and (c, d) $\text{Cr}_2\text{O}_3\text{@GNF-2}$ after thermal treatment and weight loss at 385°C showing localised combustion of the carbon structure. Proposed scheme for the decomposition of Cr_2O_3 in air at temperatures between $300\text{-}500^\circ\text{C}$.

A similar scheme can be produced involving the carbon once again facilitating the reduction of the chromium species which is able to be re-oxidised to form its reactive species. In this composite material, the ability for selective site oxidation is even more pronounced and can indeed form useful openings and cavities in the sidewalls of the carbon nanotubes which could be very interesting for not only nanoreactors systems but also for the preparation of novel modified holey carbon supports in the future.

4.3.4. Nanoreactor guest-host interactions

Strong evidence for prominent guest-host interactions between the metal oxide nanoparticles and the carbon support arises from the TGA thermographs, where both the chromium oxide and the molybdenum oxide species induce a significant shift in the combustion temperature of the GNF (T_{ox}) by 161 and 200 °C respectively (Figure 4.30).

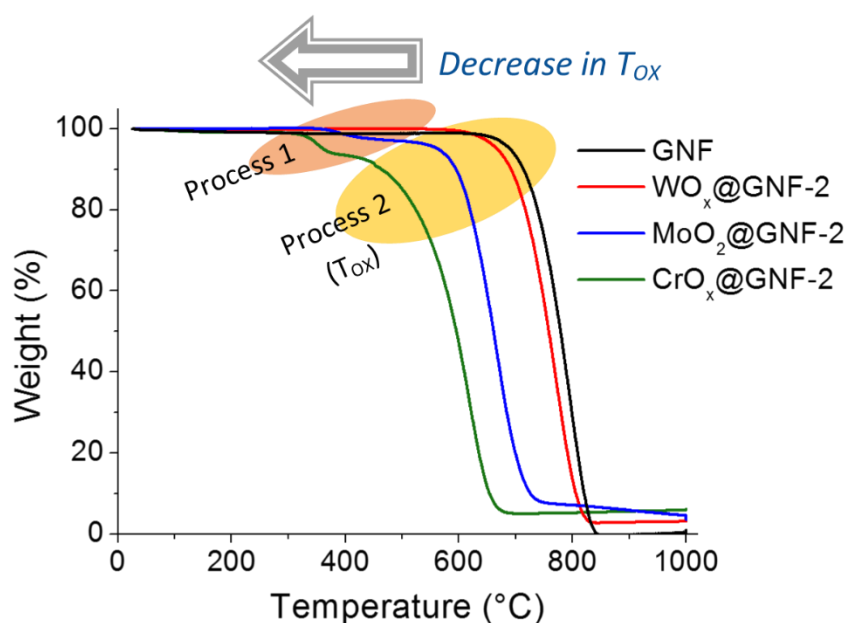


Figure 4.30. TGA profiles for GNF (black), WO_x@GNF-2 (W(CO)₆ precursor, 0.17mol/g - red), MoO₂@GNF-2 (MoO₂(acac)₂ precursor, 0.17mol/g - blue), CrO_x@GNF-2 (Cr(acac)₃ precursor, 0.17mol/g - green) all synthesised using the similar gas phase thermal deposition reactions, highlighting the large shift in combustion temperature of the composite materials.

For both metal oxide species, there appear to be two distinctive thermal processes. The first process is a weight decrease at the lower temperature which has been attributed to the site-selective oxidation of the GNF. The second process is the combustion temperature of the GNF and both these processes appear to be affected by the metal oxide species present.

The origins and magnitude of these thermal processes are related to the reduction potential of the metal oxides in their highest oxidation state, which results from oxidation of the metal oxide surface in air at elevated temperatures. More positive reduction potential is related to the ease of reduction of the metal species, therefore, it is to be expected from the standard reduction potentials that the order of reactivity should be $\text{Cr} > \text{Mo} > \text{W}$ (Table 4.3).

Table 4.3. TGA data and standard reduction potentials for the metal oxides in their highest oxidation state.

As-synthesised composite	NP size (nm)	Redox process	Corresponding reduction potential (V) ^b	Onset temp for process 1 (°C) ^a	ΔT_{ox} (°C) ^a
$\text{CrO}_x\text{@GNF-1}$	5	$\text{Cr}^{6+} \rightarrow \text{Cr}^{3+}$	1.38	304	200
$\text{MoO}_2\text{@GNF-2}$	29	$\text{Mo}^{6+} \rightarrow \text{Mo}^{4+}$	0.64	375	161
$\text{WO}_x\text{@GNF-2}$	3	$\text{W}^{6+} \rightarrow \text{W}^{4+}$	-0.06	-	22

^a Measured from TGA compared to empty GNF. ^b Measured from standard potentials.⁵⁹

This correlates with the TGA supporting that the chromium oxide is the most easily reduced by the carbon of the GNF. As a result, the chromium requires the lowest onset temperature of process 1 and results in the biggest weight decrease due to this being the strongest oxidising agent. Molybdenum requires a higher temperature due to a less positive reduction potential and the weight decrease is approximately half that achieved by the chromium oxide. With the reduction potential being even smaller and negative for the tungsten composite, combustion of the GNF (process 2) occurs before the onset temperature for process 1 for this material could be reached.

Confinement of the metal oxides within the GNF is, therefore, able to promote two features; firstly, intimate contact between the reactive metal oxide surface and the carbon atoms. Secondly, nanoscale catalysts with increased reactive oxygens located at low coordinated surfaces. The synergistic effect of these features results in catalysed oxidation of the GNF surface.

For the second process (T_{ox}), the extent of the shift in T_{ox} is most likely attributed to the increased defects in the GNF walls which weakens the structure and results in the catalysed combustion (Figure 4.31).

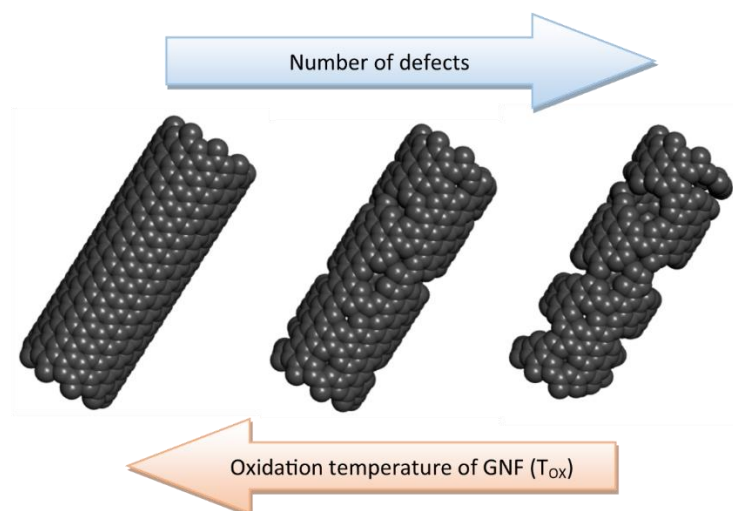


Figure 4.31. Schematic diagram correlating the number of defects generated by the metal oxide and the oxidation temperature of the GNF.

Although other non-covalent interactions may play a role in decreasing the T_{ox} , their effect cannot be distinguished from the effect of the weakening of the carbon surface by localised oxidation. These results do identify that the presence of low coordinated reactive oxygen groups on the surface and ease in reducibility of the metal oxide due to its small dimensions may allow enhanced catalytic abilities towards other substrates. As a result, these

nanoreactors may be very effective in the oxidation reactions of other compounds and could show potential in several applications such as environmental remediation.

4.4. Conclusions

Confined group VI metal oxides inside GNF which exhibit prominent host-guest interactions have been explored. Effective control of the physical and chemical properties were demonstrated by manipulating a gas phase deposition strategy with a tungsten hexacarbonyl precursor. As a result, tungsten oxide nanomaterials could be preferentially loaded onto the interior channel due to the corrugated interior of the GNF providing anchoring points for the nucleation of the metal oxide. The metal acetylacetonate precursors of molybdenum and chromium were employed using a similar gas phase deposition procedure for the encapsulation of their oxides within the nanofibre internal channel. Well-defined nanoparticles of MoO₂ with diameters of 29nm could be encapsulated, with loading and location readily tuned by modifying precursor loading to afford promising nanoreactor candidates. Thermal treatment of the MoO₂@GNF composite provided control of oxidation state, composition and size of these nanoparticles. Smaller (5 nm) non-crystalline oxygen deficient chromium oxide nanoparticles were also encapsulated within the GNF and showed enhanced guest-host interactions. The intimate contact between the metal oxide and interior of the nanotube due to confinement, redox properties and low coordinated reactive oxygen species at the surface were able to promote site-selective oxidation of the GNF which resulted in

catalysed combustion of the nanotube host. The magnitude of this effect decreased down the group but highlighted promising surface reactivity of the metal oxides that could be important in catalytic reactions.

4.5. Experimental

4.5.1. General

Standard reagents and solvents were purchased from Sigma-Aldrich Chemicals and were used as purchased. Tungsten hexacarbonyl (98%), molybdenum hexacarbonyl (98%), chromium hexacarbonyl (99%) and Chromium acetylacetonate (97%) were purchased from Arcos chemicals and was used as purchased. Bis(acetylacetonate)dioxymolybdenum(VI) (99 %) was purchased from Alfa Aesar and was used as purchased. Graphitised nanofibres were PR19-XT-HHT carbon nanofibers purchased from Pyrograf products inc (iron content <100ppm).

Transmission electron microscopy (TEM) and dark field scanning transmission electron microscopy (STEM) were performed using a JEOL JEM-2100Plus microscope operated at 200keV. TEM samples were prepared *via* a drop casting technique, where samples were first dispersed in methanol and deposited on a copper grid mounted “lacey” carbon films. All images were processed using Gatan Digital Micrograph. Energy dispersive X-ray spectroscopy and mapping were acquired for samples mounted on the TEM grid using an Oxford Instruments INCA X-ray microanalysis system. The beam was condensed on to areas suspended over holes of the amorphous carbon

film to eliminate contributions from the support film itself. The copper and silicon peak signals, associated with the grid mesh and an artefact of grid fabricated, were removed. Electron energy loss spectroscopy (EELS) was performed using an Enfinium SE system. Tomography measurements were conducted using Gatan 916 high tilt tomography holder, acquiring images at 20° tilt intervals over a range of -40 to +60 degrees with gold nanoparticles as fiducial markers.

Thermogravimetric analysis was performed using a TA Q500 Thermogravimetric Analyser. All samples were analysed using a platinum pan and in the presence of air. The parameters for all experiments were: Ramp 5 °C/minute from 20-1000 °C with an isotherm for 10 minutes at 1000 °C, air flow: 60 mL/minute. Thermogravimetric analysis mass spectrometry was performed using the same parameters as before but TA Q500 was equipped with an EGA furnace with a 90 mL/minute flow rate. A Hiden analytical QGA mass spectrometry was used in Bar Scan mode using the SEM detector between 10-80 m/e with electron energy 70eV and an emission current of 20µA. The analysis was performed using EGA soft from Hiden Analytical.

The powder X-ray measurements were performed using a PANalytical X'Pert Pro diffractometer equipped with a Cu K(α) radiation Source ($\lambda=1.5432$, 40kV 40mA) in Bragg-Brentano geometry using a Si zero background holder. All samples were wetted with isopropyl alcohol to aid GNF adhesion. The parameters for a typical experiment were: Start angle: 5°, Stop angle: 80°, Step size: 0.0525°, Time/step: 6080s, Scan speed: 0.00220°/s. High temperature

PXRD measurements were performed using an Anton Parr (HTK 1200N) high temperature oven chamber in air up to 450°C.

4.5.2. Preparation of metal oxides inside graphitised nanofibres using gas phase deposition procedure

To remove any moisture, PR19 graphitised nanofibres were pre-treated by heating below their oxidation temperature (500°C) in air for 1 hour. The pre-treated graphitised nanofibres (60mg) were then loaded into a Pyrex glass tube (d=100mm, L=6 cm) with metal precursor (Table 4.4) and sealed under vacuum ($\sim 5 \times 10^{-5}$ mbar) unless otherwise stated. The sealed vessel was then heated for 3 days at a specific temperature. Following sublimation and prior to opening, the Pyrex glass tube was immediately cooled for 5 minutes. The resulting composite was placed into a new Pyrex glass tube (d=100 mm, L=6 cm) and evacuated and backfilled with argon (repeated 3 times) to remove any oxygen or moisture present. Before sealing, the Pyrex glass tube was filled with argon gas (~ 0.5 bar). For the decomposition step, the sealed vessels were heated at 1 hour at a specific temperature and thermal rate ramp (Table 4.4) The composite material was then cooled down slowly for 9 hours in the furnace.

Table 4.4. Parameters for composite formation using gas phase thermal deposition reactions.

Composite material	Corresponding section	Precursor	Precursor loading (mg)	Sublimation temperature (°C) ^a	Thermal decomposition (Step 2) temperature (°C)	Thermal decomposition (Step 2) ramp rate (°C/min)	Post-synthesis thermal treatment temperature (°C) ^b
WO _x @GNF-1	4.3.1.1	W(CO) ₆	13.6	120	500	500	-
WO ₃ @GNF-1	4.3.1.2	W(CO) ₆	13.6	120	500	500	440
WO _x @GNF-2	4.3.1.3	W(CO) ₆	6.8	120	500	500	-
WO _x @GNF-3	4.3.1.4	W(CO) ₆	6.8	120	500	10	-
MoO _x @GNF-1	4.3.2.1	Mo(CO) ₆	8.8	120	500	500	-
MoO ₂ @GNF-2	4.3.2.2	MoO ₂ (acac) ₂	11.1	160	600	500	-
MoO ₂ @GNF-3	4.3.2.2.1	MoO ₂ (acac) ₂	14.4	160	600	500	-
MoO ₂ @GNF-4	4.3.2.2.1	MoO ₂ (acac) ₂	7.8	160	600	500	-
MoO ₃ @GNF-2	4.3.2.2.2	MoO ₂ (acac) ₂	11.1	160	600	500	450
CrO _x @GNF-1	4.3.3.1	Cr(CO) ₆	12.0	120	500	500	-
CrO _x @GNF-2	4.3.3.2	Cr(acac) ₃	23.5	110	600	500	-
Cr ₂ O ₃ @GNF-2	4.3.2.2.2	Cr(acac) ₃	23.5	110	600	500	385

^a at 5x10⁻⁵ mbar, ^b in air

Post synthesis thermal manipulation of the composite involved heating the composite material in an open vessel at a specific temperature (Table 4.4) for 30 minutes in air. This was then cooled slowly over 2 hours to form the corresponding thermal treated composite material.

4.6. References

1. A. N. Khlobystov, *ACS nano*, 2011, **5**, 9306-9312.
2. Y. H. Cao, H. Yu, J. Tan, F. Peng, H. J. Wang, J. Li, W. X. Zheng and N. B. Wong, *Carbon*, 2013, **57**, 433-442.
3. S. A. Miners, G. A. Rance and A. N. Khlobystov, *Chem. Soc. Rev.*, 2016, **45**, 4727-4746.
4. X. L. Pan and X. H. Bao, *Acc. Chem. Res.*, 2011, **44**, 553-562.
5. M. A. Astle, G. A. Rance, M. W. Fay, S. Notman, M. R. Sambrook and A. N. Khlobystov, *J. Mater. Chem. A*, 2018, **6**, 20444-20453.
6. R. M. M. Abbaslou, A. Tavassoli, J. Soltan and A. K. Dalai, *Appl. Catal., A*, 2009, **367**, 47-52.
7. H. B. Zhang, X. L. Pan, J. Y. Liu, W. Z. Qian, F. Wei, Y. Y. Huang and X. H. Bao, *ChemSusChem*, 2011, **4**, 975-980.
8. J. Guan, X. L. Pan, X. Liu and X. H. Bao, *J Phys Chem C*, 2009, **113**, 21687-21692.
9. W. A. Solomonsz, G. A. Rance, B. J. Harris and A. N. Khlobystov, *Nanoscale*, 2013, **5**, 12200-12205.
10. S. J. Guo, X. L. Pan, H. L. Gao, Z. Q. Yang, J. J. Zhao and X. H. Bao, *Chem.-Eur. J.*, 2010, **16**, 5379-5384.
11. J. P. Xiao, X. L. Pan, S. J. Guo, P. J. Ren and X. H. Bao, *J. Am. Chem. Soc.*, 2015, **137**, 477-482.
12. Z. F. Chen, W. Thiel and A. Hirsch, *Chemphyschem*, 2003, **4**, 93-97.
13. W. Chen, X. L. Pan and X. H. Bao, *J. Am. Chem. Soc.*, 2007, **129**, 7421-7426.
14. B. Cornelio, A. R. Saunders, W. A. Solomonsz, M. Laronze-Cochard, A. Fontana, J. Sapi, A. N. Khlobystov and G. A. Rance, *J. Mater. Chem. A*, 2015, **3**, 3918-3927.
15. H. J. Zhai, B. Kiran, L. F. Cui, X. Li, D. A. Dixon and L. S. Wang, *J. Am. Chem. Soc.*, 2004, **126**, 16134-16141.
16. W. Chen, Z. Fan, X. Pan and X. Bao, *J. Am. Chem. Soc.*, 2008, **130**, 9414-9419.
17. W. Chen, X. Pan, M.-G. Willinger, D. S. Su and X. Bao, *J. Am. Chem. Soc.*, 2006, **128**, 3136-3137.
18. G. Lota, E. Frackowiak, J. Mittal and M. Monthieux, *Chem. Phys. Lett.*, 2007, **434**, 73-77.

19. H. Y. Shang, C. U. Liu, Y. Q. Xu, J. S. Qiu and F. Wei, *Fuel Process. Technol.*, 2007, **88**, 117-123.
20. D. H. Youn, S. Han, J. Y. Kim, J. Y. Kim, H. Park, S. H. Choi and J. S. Lee, *ACS nano*, 2014, **8**, 5164-5173.
21. A. Botos, J. Biskupek, T. W. Chamberlain, G. A. Rance, C. T. Stoppiello, J. Sloan, Z. Liu, K. Suenaga, U. Kaiser and A. N. Khlobystov, *J. Am. Chem. Soc.*, 2016, **138**, 8175-8183.
22. D. Ma, L. Y. Liang, W. Chen, H. M. Liu and Y. F. Song, *Adv. Funct. Mater.*, 2013, **23**, 6100-6105.
23. S. Wang, X. Shi, G. Shao, X. Duan, H. Yang and T. Wang, *J. Phys. Chem. Solids*, 2008, **69**, 2396-2400.
24. B. Pietruszka, F. Di Gregorio, N. Keller and V. Keller, *Catal. Today*, 2005, **102**, 94-100.
25. N. I. Gumerova and A. Rompel, *Nat. Rev. Chem.*, 2018, **2**, 20.
26. D. L. Long, R. Tsunashima and L. Cronin, *Angew. Chem., Int. Ed.*, 2010, **49**, 1736-1758.
27. J. P. Tessonier, S. Goubert-Renaudin, S. Alia, Y. S. Yan and M. A. Barteau, *Langmuir*, 2013, **29**, 393-402.
28. S. Wang, H. L. Li, S. Li, F. Liu, D. Q. Wu, X. L. Feng and L. X. Wu, *Chem.-Eur. J.*, 2013, **19**, 10895-10902.
29. S. A. Al-Hammadi, A. M. Al-Amer and T. A. Saleh, *Chem. Eng. J.*, 2018, **345**, 242-251.
30. Y. N. Prajapati and N. Verma, *Energy & Fuels*, 2018, **32**, 2183-2196.
31. D. M. Nejad, N. Rahemi and S. Allahyari, *React. Kinet. Mech. Catal.*, 2017, **120**, 279-294.
32. R. Sagawa, W. Togashi, T. Akita and Y. Takai, *Surf. Interface Anal.*, 2012, **44**, 797-800.
33. T. W. Chamberlain, T. Zoberbier, J. Biskupek, A. Botos, U. Kaiser and A. N. Khlobystov, *Chem. Sci.*, 2012, **3**, 1919-1924.
34. R. Sagawa, W. Togashi, T. Akita and Y. Takai, *Microscopy*, 2013, **62**, 271-282.
35. M. Aygun, C. T. Stoppiello, M. A. Lebedev, E. F. Smith, M. D. Gimenez-Lopez, A. N. Khlobystov and T. W. Chamberlain, *J. Mater. Chem. A*, 2017, **5**, 21467-21477.
36. M. Aygun, T. W. Chamberlain, M. D. Gimenez-Lopez and A. N. Khlobystov, *Adv. Funct. Mater.*, 2018, **28**, 15.
37. D. J. Palmer and P. G. Dickens, *Acta Crystallogr. Sect. B-Struct. Commun.*, 1979, **35**, 2199-2201.
38. Y. M. Sun, X. L. Hu, W. Luo and Y. H. Huang, *ACS nano*, 2011, **5**, 7100-7107.
39. P. M. Woodward, A. W. Sleight and T. Vogt, *J. Phys. Chem. Solids*, 1995, **56**, 1305-1315.
40. R. Ganesan and J. S. Lee, *J. Power Sources*, 2006, **157**, 217-221.

41. R. W. Lodge, G. A. Rance, M. W. Fay and A. N. Khlobystov, *Nanoscale*, 2018, **10**, 19046-19051.
42. K. Huang, Q. Pan, F. Yang, S. Ni and D. He, *Mater. Res. Bull.*, 2008, **43**, 919-925.
43. M. Baltes, O. Collart, P. Van der Voort and E. F. Vansant, *Langmuir*, 1999, **15**, 5841-5845.
44. T. L. Drake and P. C. Stair, *J. Vac. Sci. Technol. A*, 2016, **34**, 7.
45. A. La Torre, M. D. Gimenez-Lopez, M. W. Fay, G. A. Rance, W. A. Solomonsz, T. W. Chamberlain, P. D. Brown and A. N. Khlobystov, *ACS nano*, 2012, **6**, 2000-2007.
46. P. X. Han, W. Ma, S. P. Pang, Q. S. Kong, J. H. Yao, C. F. Bi and G. L. Cui, *J. Mater. Chem. A*, 2013, **1**, 5949-5954.
47. A. R. Puigdollers, P. Schlexer, S. Tosoni and G. Pacchioni, *Acs Catalysis*, 2017, **7**, 6493-6513.
48. X. P. Wang, Z. L. Zhou and F. F. Chen, *Materials*, 2017, **10**, 11.
49. S. Kang, M. S. Mauter and M. Elimelech, *Environ. Sci. Technol.*, 2009, **43**, 2648-2653.
50. Y. B. Wang, Z. Iqbal and S. Mitra, *J. Am. Chem. Soc.*, 2006, **128**, 95-99.
51. T. J. Swoboda, N. L. Cox, M. S. Sadler, A. L. Oppegard, J. N. Ingraham and P. Arthur, *J. Appl. Phys.*, 1961, **32**, S374-&.
52. A. Bystrom and K. A. Wilhelmi, *Acta Chem. Scand.*, 1950, **4**, 1131-1141.
53. N. O. Golosova, D. P. Kozlenko, S. E. Kichanov, E. V. Lukin, H. P. Liermann, K. V. Glazyrin and B. N. Savenko, *J. Alloys Compd.*, 2017, **722**, 593-598.
54. H. Kurata, K. Ishizuka and T. Kobayashi, *Bull. Inst. Chem. Res*, 1989, **66**, 572-579.
55. L. A. Grunes, R. D. Leapman, C. N. Wilker, R. Hoffmann and A. B. Kunz, *Physical Review B*, 1982, **25**, 7157-7173.
56. D. A. Muller, N. Nakagawa, A. Ohtomo, J. L. Grazul and H. Y. Hwang, *Nature*, 2004, **430**, 657-661.
57. H. Ma, Y. M. Xu, Z. M. Rong, X. L. Cheng, S. Gao, X. F. Zhang, H. Zhao and L. H. Huo, *Sens. Actuators, B*, 2012, **174**, 325-331.
58. M. M. Abdullah, F. M. Rajab and S. M. Al-Abbas, *AIP Adv.*, 2014, **4**, 11.
59. P. W. Atkins, Overton, T., Rourke, Jonathan P., Weller, M. and Armstrong, F. A., *Inorganic Chemistry*, Oxford University, Oxford, 2010.

*Carbon nanoreactors as a catalytic nanosponge for the
efficient desulphurisation of liquid fuels*

5.1. Background

Despite the advancement of environment-friendly technologies, the transportation and energy industries still depend heavily on diesel fuel. However, recent trends of increased diesel consumption and the dwindling reserves of crude oil have triggered questions about satisfying demand for the future.^{1, 2} Moreover, the available sources of crude oil contain a high content of refractory sulphur compounds, which can have adverse industrial and environmental effects, including the formation of acid rain.^{3, 4} Therefore, a key current research challenge concerns the development of an efficient and economically viable process to remove sulphur-containing contaminants from fuels, in order to satisfy the ultra-low sulphur diesel (ULSD) regulations of less than 10 ppm imposed by international policies.⁵⁻⁷

For industrial applications, the removal of sulphur compounds using the hydrodesulphurisation (HDS) reaction is currently the most widely utilised process; yet, it has several disadvantages, including harsh reaction conditions, high costs and limited applicability to the aromatic sulphur compounds.⁸ As a result, the development of other desulphurisation processes has been more

recently explored with reasonable levels of sulphur removal being achieved under milder conditions (Figure 5.1).⁹⁻¹⁶

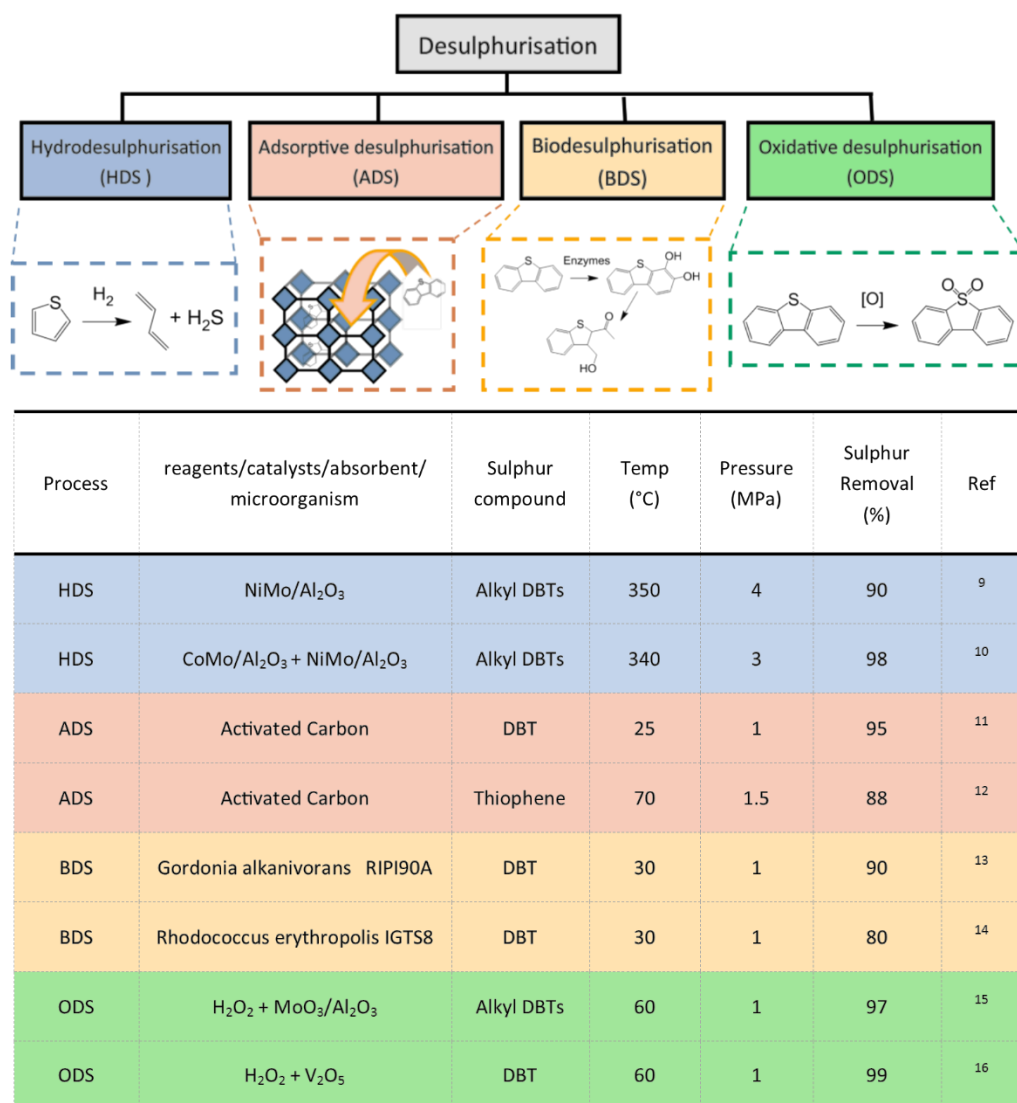


Figure 5.1. Current strategies for the desulphurisation of fuel. The application of hydrodesulphurisation (HDS) for aromatic sulphur compounds, such as thiophene uses hydrogen and produces H₂S. Adsorptive desulphurisation (ADS) using porous media and biodesulphurisation via the Kodama pathway in the presence of enzymes have both shown promise for the selective removal of dibenzothiophene (DBT). Oxidative desulphurisation (ODS) has the greatest potential for oxidation of DBT, yielding ultra-low sulphur fuels.

With biodesulphurisation currently hindered by low enzyme activity and stability, oxidative desulphurisation (ODS) and adsorptive desulphurisation

(ADS) technologies offer more realistic promise.¹⁷⁻²⁰ Specifically, the use of ODS to remove the refractory sulphur compounds from fuels exploits key changes in the polarity of the oxidised products relative to the parent organosulfur contaminant during extraction and has already been established for the production of ULSD.²¹ However, limiting the quantity of extractant needed to avoid fuel loss during extraction and the development of cheap, efficient and readily recoverable catalysts represent major stumbling blocks for this pathway.⁶ ADS has also shown reasonable success, utilising the physical adsorption of organosulphur compounds within the internal volumes of porous materials, such as zeolites, aluminosilicates and activated carbon.²²⁻²⁴ However, a new strategy for active materials with high and specific adsorption capacity for sulphur compounds is needed urgently. Therefore, significant further research is required to improve these individual strategies for ULSD production which could be based on more than one desulphurisation mechanism simultaneously.

Molybdenum oxide has recently emerged as a class of promising materials for the ODS of fuel. MoO₃ catalysts on alumina were shown to be the most catalytically active when compared to other transition metal oxide species (MoO₃ > WO₃ > V₂O₅ > ZrO₂ > CrO₃) and have been shown to oxidise several dibenzothiophene species under various conditions resulting in over 95% conversion.²⁵⁻²⁷ The ease of formation of the electrophilic molybdenum peroxo intermediate species has been identified as the driving force for the effective oxidation of the sulphur contaminants (Figure 5.2).¹⁵ It is produced when an

oxidant, such as a peroxide, reacts with the Lewis acidic sites of the metal oxide and leads to the formation of electrophilic species, essential to promote efficient ODS.

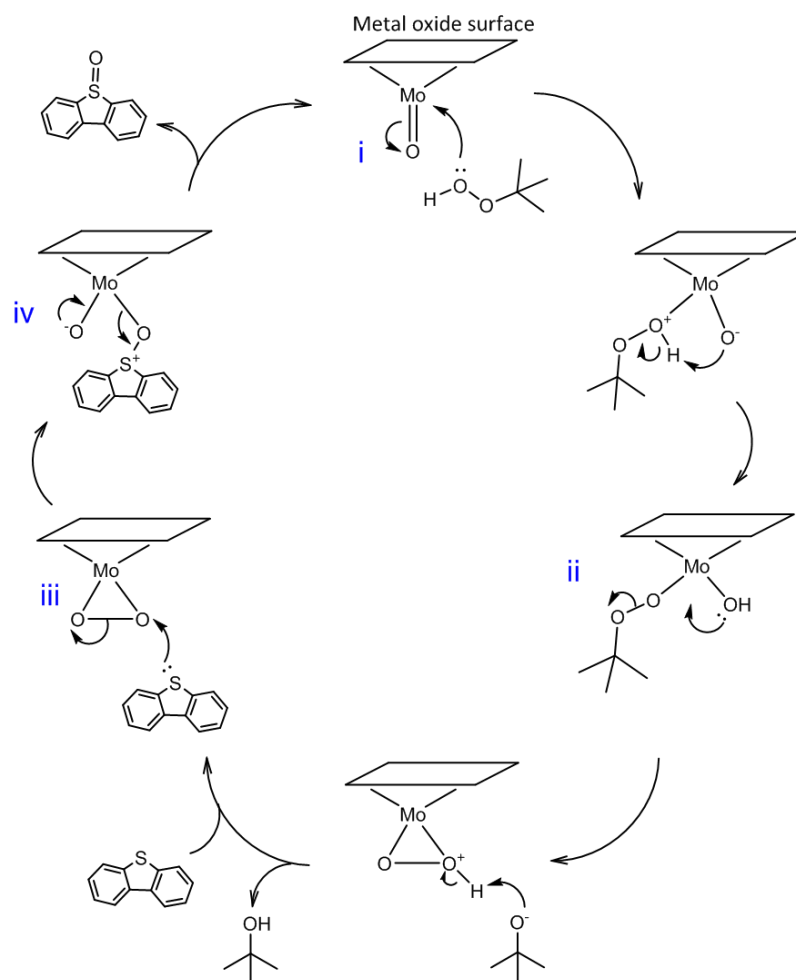


Figure 5.2. Proposed mechanism for the oxidation of sulphur contaminants using molybdenum oxide catalysts with peroxide species.^{15, 28-31}

It is believed that the electrophilicity of the peroxide oxygen is increased by the formation of the peroxy group and leads to thioethers being oxidised to sulfoxides by electrophilic oxidants.³¹ Firstly, a nucleophilic attack of the peroxide forms the hydroperoxymolybdate species (i) followed by a migration to the electrophilic oxygen and reversible loss of alcohol to produce the monoperoxo species (ii). The peroxy group is activated electrophilically *via*

coordination to molybdenum and results in a nucleophilic attack from the sulphur atom in the organosulphur species (iii). The regeneration of the catalyst surface results in the loss of the oxidised product (iv).

In addition, the performance of molybdenum-based nanomaterials can be optimised using catalyst supports, which are known to both stabilise nanoparticles against sintering and promote further activity by facilitating electron transfer between the catalysts and the support material. Al₂O₃, TiO₂ and SiO₂ supports have been recently shown to improve the catalyst performance, therefore, selection of an appropriate support is key for refining the ODS of sulphur contaminants in fuel.³²⁻³⁵ Among catalyst supports, hollow carbon nanostructures, such as carbon nanotubes, may offer several potential benefits for ODS catalysts.^{36,37} Hollow graphitised nanofibres (GNF) with an internal diameter of 60 nm – structural analogues to carbon nanotubes, but comprising of a herringbone-like internal structure – are particularly attractive as their corrugated interior surfaces promote the formation and enhance the stability of catalytic centres³⁸⁻⁴⁰ while increasing concentration of reactants around the catalyst (Figure 5.3).^{41, 42}

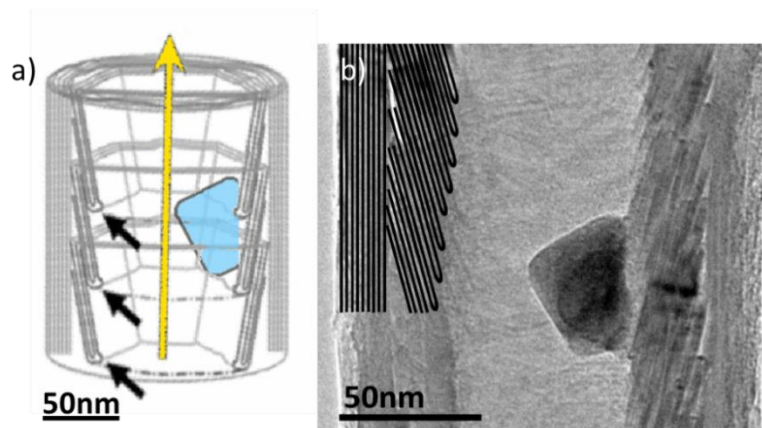


Figure 5.3. (a) Schematic representation of the structure of GNF (corrugated interior is denoted by black arrows; the yellow arrow signifies the nanofibre axis; the blue shape represents a metal oxide nanoparticle). (b) Bright field transmission electron microscopy image of $MO_x@GNF$. The internal anchoring sites have been highlighted for clarity, with the contrasting metal oxide nanoparticle clearly shown residing at the interior folds.

Based on the fact that activated carbons have shown promise in the desulphurisation of fuels,^{43, 44} the high internal surface area of nanotubes and maximal π - π stacking interactions between guest and host species may offer enhanced extraction of aromatic organosulphur contaminants, promoting desulphurisation *via* the ADS mechanism in addition to the ODS.⁴⁵ Having the potential of dual functionality in one composite material would be extremely applicable to the desulphurisation process and therefore, this offers an interesting research opportunity.

5.2. Aim and objectives

The aim of this study is to investigate carbon nanoreactors of group VI metal oxide nanoparticles encapsulated inside hollow graphitised carbon nanofibres (GNF) for the desulphurisation of liquid fuels (Figure 5.4).

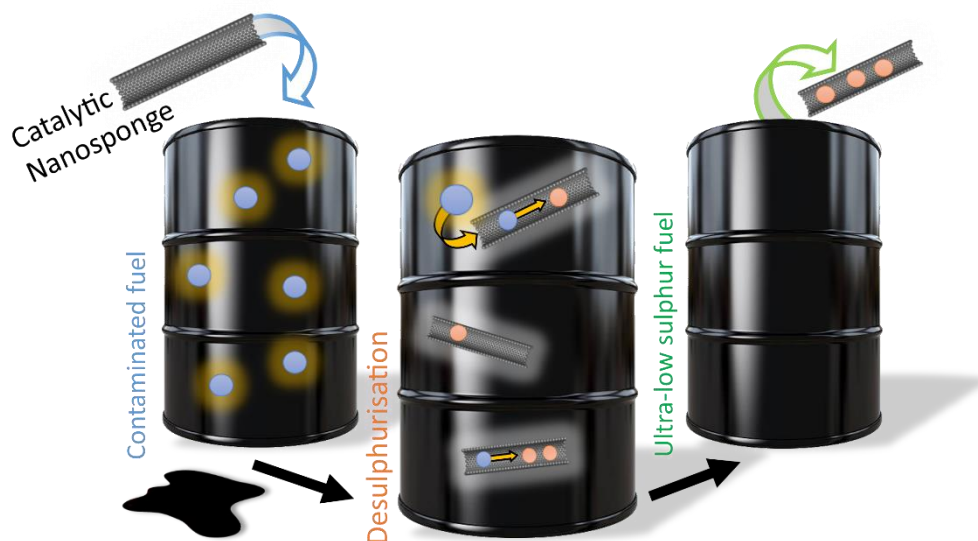


Figure 5.4. Schematic diagram of the desulphurisation process using catalytic nanosponges to desulphurise liquid fuel.

An appropriate oxidative desulphurisation procedure will first be investigated employing dibenzothiophene in hexane as a simple model contaminated fuel. Hybrid group VI metal oxide-carbon nanoreactors will then be applied as desulphurisation catalysts, and their abilities to oxidise the organosulphur species (using an ODS approach) and remove them from the system (using an ADS approach) evaluated. By altering experimental variables such as time, peroxide type or concentration, and temperature, an understanding of the potential of the catalyst can be realised. Manipulating the catalysts loading, location and oxidation state allows for a critical evaluation of these catalytic

nanoreactors towards desulphurisation. Successful candidates will be extended to several model fuel systems containing more realistic OS contaminant conditions (benzothiophene and dimethyl dibenzothiophene in octane) and assessed for their ability to oxidise and remove the sulphur-containing compounds using multiple desulphurisation pathways to produce ULSD.

5.3. Results and discussion

5.3.1. Investigation of oxidative desulphurisation reactions

Due to the complexity of real fuel systems, ODS procedures are often tested in research laboratories by dissolving refractory organosulphur compounds known to be present in crude oil, in a suitable hydrocarbon solvent, thus simulating the properties of crude oil.

There is significant variation in the model fuel systems and ODS procedures applied to evaluate the effectiveness of modern catalysts. Systems containing only one organosulphur contaminant (one-component systems) offer simplicity in analysis and rapid evaluation of the catalyst's performance whereas, systems with several more complex organosulphur species (multi-component systems) offer a more representative model fuel (Table 5.1).^{33, 46-50}

Table 5.1. Model fuel systems typically used for ODS experiments, the catalysts employed, and their associated ODS efficiencies.

Catalyst	Sulphur contaminant	Solvent	Concentration (ppm)	ODS procedure time (mins)	O : S ratio	Temp (°C)	Sulphur removal (%)	Ref.
(HPW)/SiO ₂	DBT	Petroleum ether	500	120	3 (H ₂ O ₂)	60	100	41
	BT						83	
	4,6-DMDBT						91	
MoO ₂ /g-C ₃ N ₄	DBT	<i>n</i> -octane	500	180	24 (H ₂ O ₂)	60	96	42
	T						38	
	4,6-DMDBT						62	
Fe ₃ O ₄ @SiO ₂ -ionic liquid	DBT	<i>n</i> -hexane	100	60	100 (H ₂ O ₂)	40	98	43
WO ₃ /MoO ₃ /Al ₂ O ₃	DBT	<i>n</i> -octane	200	30	3 (^t BuOOH)	60	100	28
	T		200				93	
	4,6-DMDBT		200				100	
Cs ₂ Mo ₈ W ₄ /SBA	DBT	<i>n</i> -hexane	500	80	5 (^t BuOOH)	60	100	44
TiO ₂ anatase supported V ₂ O ₅	DBT	hexadecane	445	60	21.3 (^t BuOOH)	52	100	45
	BT		612				97	
	4-MDBT		414				97	
	2-MT		847				86	
	2,5-DMT		720				85	
	4,6-DMDBT		387				75	

HPW = hierarchically mesoporous phosphotungstic acid, SBA = mesoporous silica platelets. DBT = dibenzothiophene, BT = benzothiophene, 4,6-DMDBT= 4,6-dimethyldibenzothiophene, T = thiophene, 4-MDBT = 4-methyldibenzothiophene, 2-MT = 2-methylthiophene, 2,5-DMT = 2,5-dimethylthiophene.

In this study, initial experiments using a model system comprising 500 ppm dibenzothiophene (DBT) in *n*-hexane was explored.^{47, 48} DBT was selected as it is commonly found in oil, thus presenting a real and important environmental

issue in its own right, and has distinctive absorption features in the UV-Vis spectrum. Indeed, facile measurement of the intensity of the peak at 326 nm, corresponding to the π - π^* transition in the aromatic ring, can be used to quantify the removal of DBT from the model fuel as it obeys the Beer-Lambert Law with a linear relationship between absorbance and contaminant concentration (Figure 5.5). The aliphatic hydrocarbon *n*-hexane is a common constituent of fuel and represents a valuable model fuel simulant used in previous research.⁴⁹

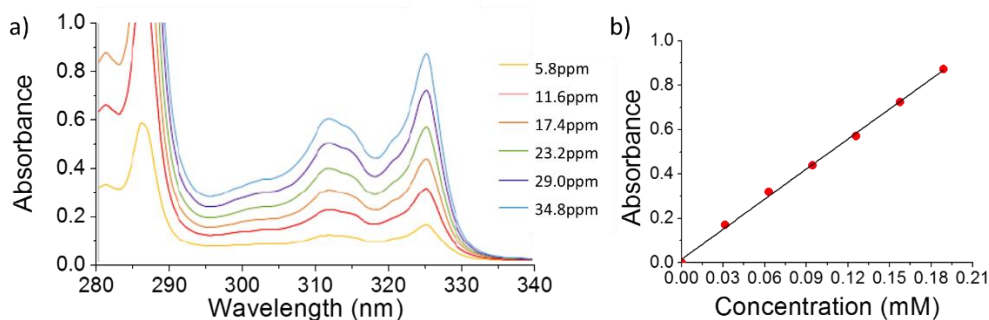


Figure 5.5. (a) UV-Vis spectroscopy calibration traces produced by diluting specific volume aliquots of the DBT model fuel (500 ppm) into 2.5 mL of *n*-hexane. (b) Calibration absorption measurements at 326 nm.

In the ODS procedure, a peroxide is required to generate the reactive molybdenum peroxy species during the reaction. Commonly used peroxides include hydrogen peroxide (HP) and tert-butyl hydroperoxide (TBHP) which have been previously successfully applied; however, there is no consistency in the literature between the ratio of peroxide to sulphur (O : S ratio) and an excess is usually implemented. H_2O_2 provides several benefits such as low cost, environmental compatibility and availability and has shown significant successes towards ODS reactions.⁵¹ However, some studies report that thermal

decomposition of H₂O₂ during the ODS procedure inhibits the oxidation mechanism.⁵⁰ This can be overcome by increasing the oxygen to sulphur ratio and by choosing organic peroxides, as unlike H₂O₂ they are oil soluble and do not produce water as a by-product, thereby making them attractive in industrial processes. Tert-Butyl hydroperoxide (TBHP) is commonly selected as an organic peroxide to avoid potential phase transfer limitations and has been utilised with several transition metal oxides to produce successful catalytic systems.^{25, 32, 33, 52} The temperature of the ODS reaction has been generally standardised at 60 °C allowing improved rates of reactions under comparatively mild conditions, with no significant energy cost imposed by the use of higher temperatures. Based on previous studies, the typical ODS procedure investigated in this study involved, an organic peroxide of TBHP, in a ratio of 1:20 (S:O) to ensure sufficient peroxide present. This was added to the model fuel with the catalyst and stirred at 60 °C for 120 minutes.^{6, 33, 47, 49} Consistent with prior literature, a subsequent extraction procedure was completed in which the model fuel was vigorously stirred with acetonitrile (in a 1 to 5 ratio of extractant to fuel) for 30 minutes.^{33, 48} Deuterated acetonitrile was selected as the extraction solvent due to its known effectiveness towards the products of DBT oxidation, enables facile analysis of extracted products by NMR spectroscopy, and has reduced toxicity relative to other commonly utilised extraction solvents, such as dimethylformamide.⁵³ A pertinent desulphurisation procedure can now be proposed to evaluate any potential composite materials (Figure 5.6).

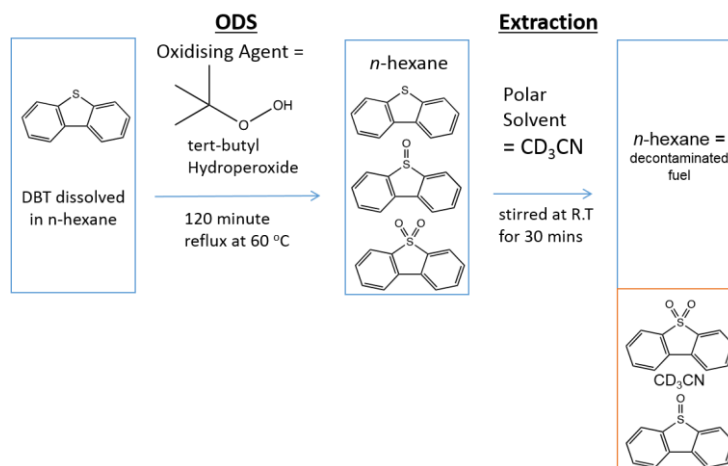


Figure 5.6. Schematic diagram illustrating the oxidative desulphurisation of a contaminated model fuel.

To monitor the removal of the sulphur containing species both UV-Vis spectroscopy and gas chromatography-mass spectrometry (GC-MS) can be used to confirm any final sulphur removal percentages (Figure 5.7a,b). Using a deuterated acetonitrile solvent to act as our solvent extractant provides removal of the polarised products and delivers a method of monitoring which products are removed during the extraction process by NMR spectroscopy (using minimal procedural steps and avoiding reduced pressures). ¹H NMR spectroscopy of the combined sulphur contaminants in the solvent extraction phase and a washed solid catalyst, allows quantitative confirmation of the efficiency of DBT oxidation in the ODS procedure and will provide information about the selectivity of oxidised products (Figure 5.7c).

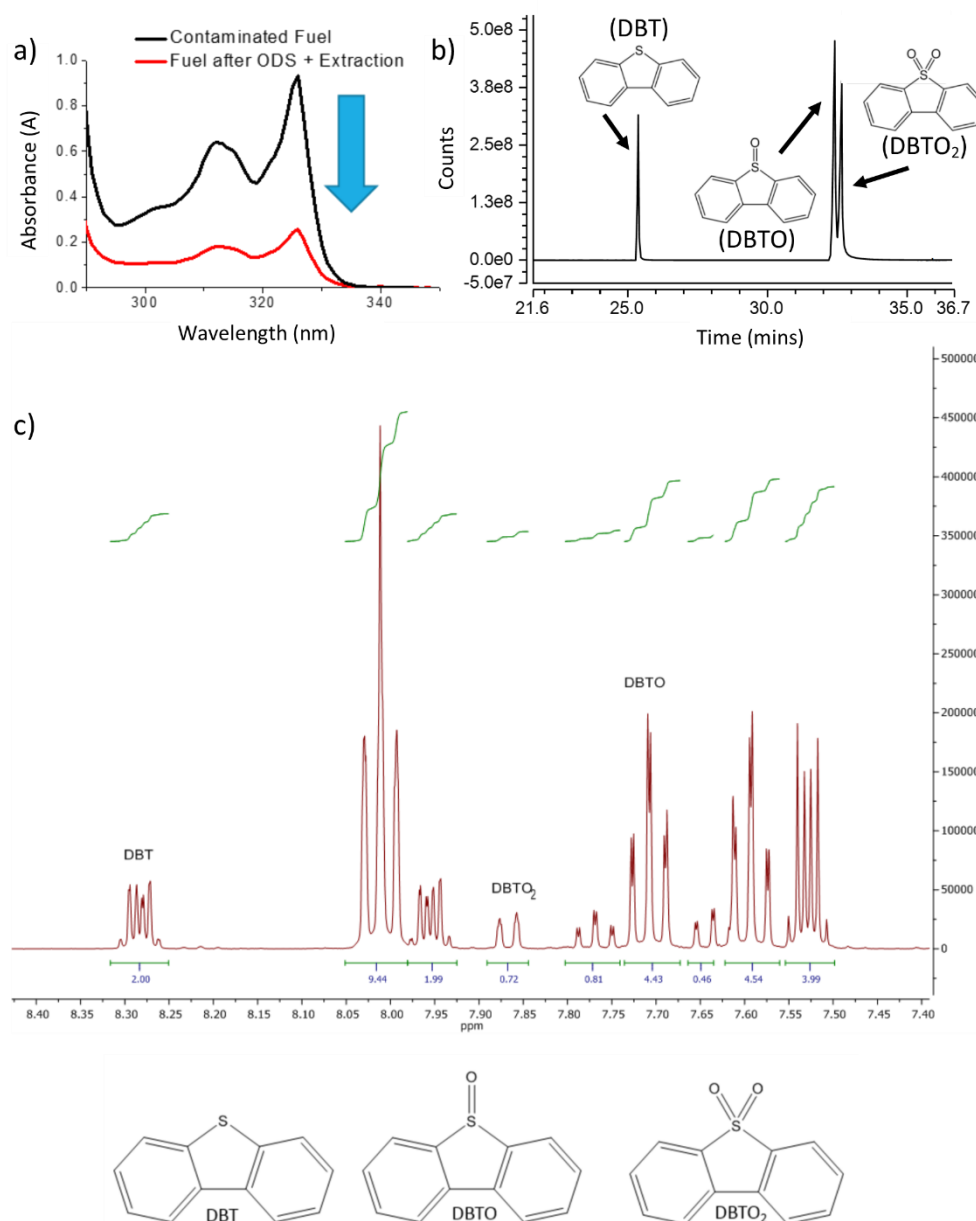


Figure 5.7. (a) UV-Vis spectra of DBT model fuel system before and after the ODS procedure. (b) Representative GC-MS analysis of the fuel phase after ODS reaction without solvent extraction. (c) Representative ¹H NMR spectrum obtained from the reaction mixture after a typical ODS reaction of DBT. Asterisk (*) corresponds to the environments used for calculation of the DBT conversion and selectivity for the two oxidised products.

Using all these techniques collectively provides for a powerful and comprehensive method for probing contaminant oxidation, product selectivity and sulphur removal. They will provide information about the procedure,

reagents and catalysts in the ODS nanoreactor system which will result in the expansion of knowledge and development of this field.

Interestingly, in the initial experiments, it was noted that up to 30% of DBT can be removed from the fuel simply through extraction alone, reflecting the moderate solubility of DBT in *n*-hexane.

To understand the GNF adsorptive properties the extraction procedure was performed after GNF alone were stirred and removed from the model fuel. It was observed that the GNF had no affinity for DBT and was therefore unable to facilitate sulphur removal using the adsorptive desulphurisation pathway. These control tests clearly demonstrate that neither the extractant solvent nor empty GNF can desulphurise model fuel to satisfactory levels (Table 5.2).

Table 5.2. Standard extraction procedures monitored by different techniques.

Entry	Adsorptive nanocarbon ^a	Sulphur removal using solvent extraction only UV-Vis (%) ^b	Sulphur removal using solvent extraction only GC-MS (%) ^c
1	None	28.8	29.4
2	GNF	28.6	30.1

^a No catalyst or 5 mg of empty GNF, 5 mL of *n*-hexane containing 500 ppm DBT ^b Percentage of sulphur-containing contaminants removed via solvent extraction (1 mL CD₃CN, 30 mins) was determined using UV-Vis spectroscopy by diluting a 40 μL aliquot into 2.5 mL of *n*-hexane before measurement. ^c Percentage of sulphur-containing contaminants removed via solvent extraction (1 mL CD₃CN, 30 mins) was determined using GC-MS.

5.3.2. Evaluation of group VI metal oxide-carbon nanoreactors for the ODS of a model fuel

Firstly, both no catalyst and empty GNF were applied to the model fuel with the combined ODS and extraction procedure (Table 5.3, entries 1-2). Both resulted in no DBT oxidation and yielded DBT removal of 29 and 25% from the model fuel, respectively, which is consistent with that observed from solvent extraction alone. When employing $\text{MO}_x\text{@GNF}$ to evaluate their catalytic abilities towards desulphurisation, a 5 mg quantity of the group VI metal oxide nanoreactor catalysts ($\text{WO}_x\text{@GNF-2}$, $\text{MoO}_2\text{@GNF-2}$, and $\text{CrO}_x\text{@GNF-2}$ as discussed in Chapter 4 unless otherwise stated) was added to the model fuel. Both the chromium and tungsten oxide containing $\text{MO}_x\text{@GNF}$ nanoreactors were unable to oxidise DBT (Table 5.3, entry 3 and 5). In contrast, after 120 minutes, an ODS reaction and subsequent solvent extraction using the $\text{MoO}_2\text{@GNF-2}$ catalyst enabled 99% removal of the DBT from the model fuel, yielding the doubly oxidised sulfone species at a low 5.9 mol% catalyst loading (Table 5.3, entry 4).

Table 5.3. Carbon nanoreactors of group VI metal oxides encapsulated inside GNF for the ODS of fuel.

Entry	Catalyst	Sulphur removal with ODS and solvent extraction (%) ^a	Conversion (%) ^b	Selectivity RO : RO ₂ (%) ^c
1	None	29	0	- :-
2	Empty GNF	25	0	- :-
3	WO _x @GNF-2	28	0	- :-
4	MoO ₂ @GNF-2	99	97	14 : 86
5	CrO _x @GNF-2	30	0	- :-

^a 5 mL of *n*-hexane containing 500 ppm DBT, sulphur:oxidant molar ratio is 1:20, *tert*-butyl hydroperoxide oxidant, 60 ° C, 120 mins. Extraction; 1mL CD₃CN, 30 mins. Removal calculated using UV-Vis spectroscopy.

^b Conversion and ^c selectivity calculated using UV-Vis spectroscopy of fuel phase, ¹H NMR spectroscopy of extraction phase and washed solid catalyst.

Molybdenum oxide has been previously shown to outperform the other group VI metal oxides for this application. This is thought to be due to a balance between the stability of the hydroperoxymolybdate species and the reactivity towards electrophilically promoting the peroxo oxygen.²⁵ Despite the larger nanoparticles present compared to the other composites, the molybdenum dioxide carbon nanoreactor seems to possess optimal properties that can facilitate oxidation of the sulphur species (Figure 5.8).

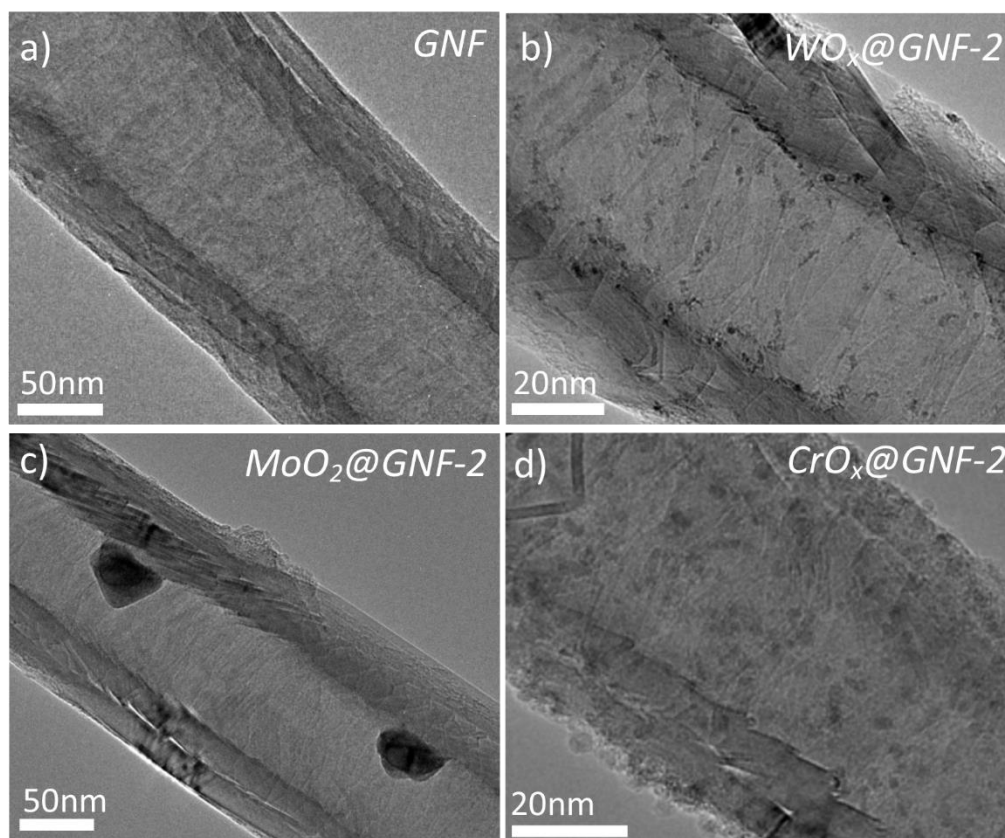


Figure 5.8. Transmission electron microscopy (TEM) of candidate nanoreactor materials for the ODS procedure composed of a) empty GNF, b) $\text{WO}_x\text{@GNF-2}$, c) $\text{MoO}_2\text{@GNF-2}$ and d) $\text{CrO}_x\text{@GNF-2}$.

With the $\text{MoO}_2\text{@GNF}$ catalyst providing effective sulphur removal from the model fuel which supports molybdenum oxide catalysts outperforming other group VI metal oxides throughout the literature, the $\text{MoO}_2\text{@GNF}$ nanoreactor was selected as a candidate to investigate comprehensively with the desulphurisation procedure.²⁵

5.3.3. Investigating $\text{MoO}_2\text{@GNF}$ towards the ODS of fuel

Due to the success of the $\text{MoO}_2\text{@GNF-2}$ effectively oxidising DBT, the conditions of the reaction were systematically varied to investigate the versatility of this catalyst (Table 5.4).

Table 5.4. Procedural modification for MoO₂@GNF-2 catalyst during the ODS of fuel.

Entry	Experimental variable ^a	ODS procedure Time (mins)	Oxidant	Oxidant ratio O : S	Temp (°C)	Sulphur removal with ODS and solvent extraction (%) ^b
1	Standard	120	TBHP	20 : 1	60	99
2	Time	30	TBHP	20 : 1	60	77
3	Peroxide concentration	120	TBHP	5 : 1	60	89
4		30	TBHP	5 : 1	60	59
5	Peroxide used	120	HP	20 : 1	60	61
6	Temperature	30	TBHP	5 : 1	25	51

^a Standard conditions: 5 mg MoO₂@GNF-2 (containing 4 wt.% MoO₂), 5 mL of n-hexane containing 500 ppm DBT, tert-butyl hydroperoxide (TBHP) oxidant (S:O is 1:20), 60 °C, 120 mins. ^b Percentage of sulphur-containing contaminants removed via combined ODS and solvent extraction (1 mL CD₃CN, 30 mins) was determined using UV-Vis spectroscopy.

By decreasing the reaction time, it was found that an impressive 77% removal could still be achieved after only 30 minutes (Table 5.4, entry 2). It is clear that the MoO₂@GNF is highly catalytically active, and this result suggests that the catalyst is most effective at the start of the ODS procedure, and decreases in efficiency over time.

The ratio of oxidant to sulphur contaminant is highly varied throughout literature studies due to increased oxidant quantities employed to overcome the peroxide decomposition. The above data indicates that a 20:1 O:S ratio is highly successful at oxidising the sulphur species and thus promoting removal during the extraction. However, the catalytic nanoreactor provided effective

removal using a four-fold decrease in the O:S ratio enabling the removal of 59% and 89% of DBT from the model fuel after 30 or 120 minutes, respectively (Table 5.4, entry 2 and 4). At lower oxidant concentration, the benefits of the catalytic nanoreactor materials of high local concentration of the peroxide to catalyst, enables the facile formation of the reactive species at increased rates yielding higher sulphur removal. Using minimal amounts of oxidant is beneficial for industrial-scale applications and this result indicates the plausibility of the use of these catalysts in such settings.

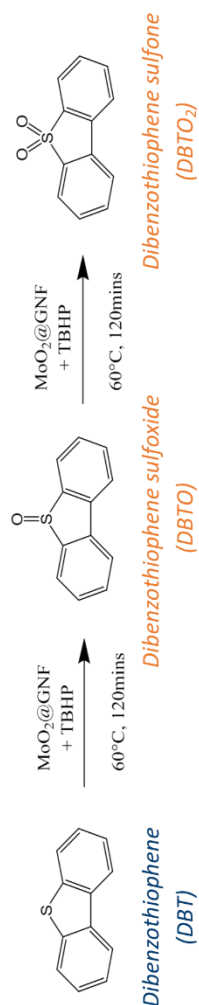
H₂O₂ is a more cost-effective peroxide for the ODS reaction; however, its use with the MoO₂@GNF catalyst results in a 37% decrease in the sulphur removal when compared with the organic peroxide (Table 5.4, entry 5). This is thought to be due to phase transfer limitations which result in minimal peroxide being in the organic phase and being available during the ODS reactions. Yet, the catalyst still enables desulphurisation by 61% which suggests that the hydrophobic internal channel may promote the absorption of minimal amounts of the aqueous peroxide into the nanoreactor. This result indicates that the organic peroxide does result in enhanced catalytic performance when utilising a nanoreactor system and can achieve effective desulphurisation far beyond what hydrogen peroxide can offer.

Another feature of this procedure of industrial relevancy is the reaction temperature. This study and many others cited in the literature have utilised a reaction temperature of 60 °C as standard. Comparison of equivalent reactions at room temperature and 60 °C indicated it there was only an 8% decrease in

the sulphur removal (Table 5.4, entry 6). Despite the decrease in removal, the fact the composite material oxidises the contaminants at room temperature indicates that confining the nanoparticles appears to result in a catalytic surface which doesn't require thermal energy to drive the reaction. Instead, the nanoreactor offers a mechanism which can promote absorption of the reagents and enhance local concentration at the reactive catalytic surface, thus promoting faster rates of oxidation. This result is significant as it shows that applying these nanoreactors with small amounts of oxidants (5:1) at ambient temperatures (25 °C) for short periods of time (30 minutes) can still promote almost double what a solvent extraction procedure alone could achieve.

By varying the conditions of the ODS procedure the importance that the time, temperature, peroxide type and concentration have on the catalyst system can be better understood, enabling the development of an optimum industrially applicable procedure. However, to understand the properties of the ODS catalyst, variation in the structural properties of the nanoreactor was investigated.

To further explore the catalyst activity, experiments were conducted using shorter reaction times, but with variable quantities of catalyst. This highlighted that even more effective sulphur removal could be realised by increasing the loading of MoO₂@GNF present in the reaction mixture (Table 5.5, entry 1-2).

Table 5.5. Manipulation of MoO₂@GNF catalyst and their associated ODS efficiencies.

Entry	Catalyst	Catalyst loading (mg) ^a	ODS reaction time (mins)	Sulphur removal with ODS and solvent extraction (%) ^b	DBT conversion (%) ^c	Selectivity (%) ^c DBTO : DBTO ₂	Turnover frequency (mol mol ⁻¹ min ⁻¹) ^d
1	MoO ₂ @GNF	1.0	30	57.3	44	83 : 17	1.22
2	MoO ₂ @GNF	5.0	30	76.7	68	69 : 31	0.43
3	MoO ₂ @GNF	5.0	120	98.8	97	14 : 86	0.14
4	MoO ₂ @Graphite	5.0	120	71.5	61	75 : 25	0.09
5	MoO ₃ @GNF	5.0	120	72.7	57	76 : 24	0.08

^a 5 mg catalyst (containing 4 wt.% MoO₂), 5 ml of n-hexane containing 500 ppm DBT, tert-butyl hydroperoxide (TBHP) oxidant (S:O is 1:20), 60 °C, 120 mins. ^b Percentage of sulphur-containing contaminants removed via either (i) ODS or (ii) combined ODS and solvent extraction (1 ml CD₃CN, 30 mins) was determined using GC-MS. ^c The conversion of DBT and selectivity of products was calculated using GC-MS of fuel phase and ¹H NMR spectroscopy of solvent extraction phase and a solvent washing of post-reaction solid catalysts. ^d Turnover frequency calculated from conversion of 4% weight loaded MoOx nanomaterials at 120 mins.

It is clear that having a greater number of catalytically active sites present promotes faster conversion of DBT and leads to increased sulphur removal.

From the turnover frequency values, even smaller quantities of catalysts present in the reaction still promote effective reaction turnover and result in higher turn-over frequencies (TOF) when compared to the standard procedure. The driving force for effective oxidation of the sulphur contaminants using our catalytic nanoreactors strongly relates to the environment at which the catalyst resides. By confining within the internal channel both the modulated surface reactivity and heightened local concentrations of the contaminant to catalyst provide enhance catalytic ability, as previously demonstrated for reactions of hydrosilylation.³⁹ To further explore the importance of internal anchoring folds, a sample of MoO₂ on graphite was produced using an identical procedure described in Chapter 4. Graphite flakes provide anchoring sites for the catalyst, similarly to GNF, but no spatial confinement as observed inside the GNF (Figure 5.9).

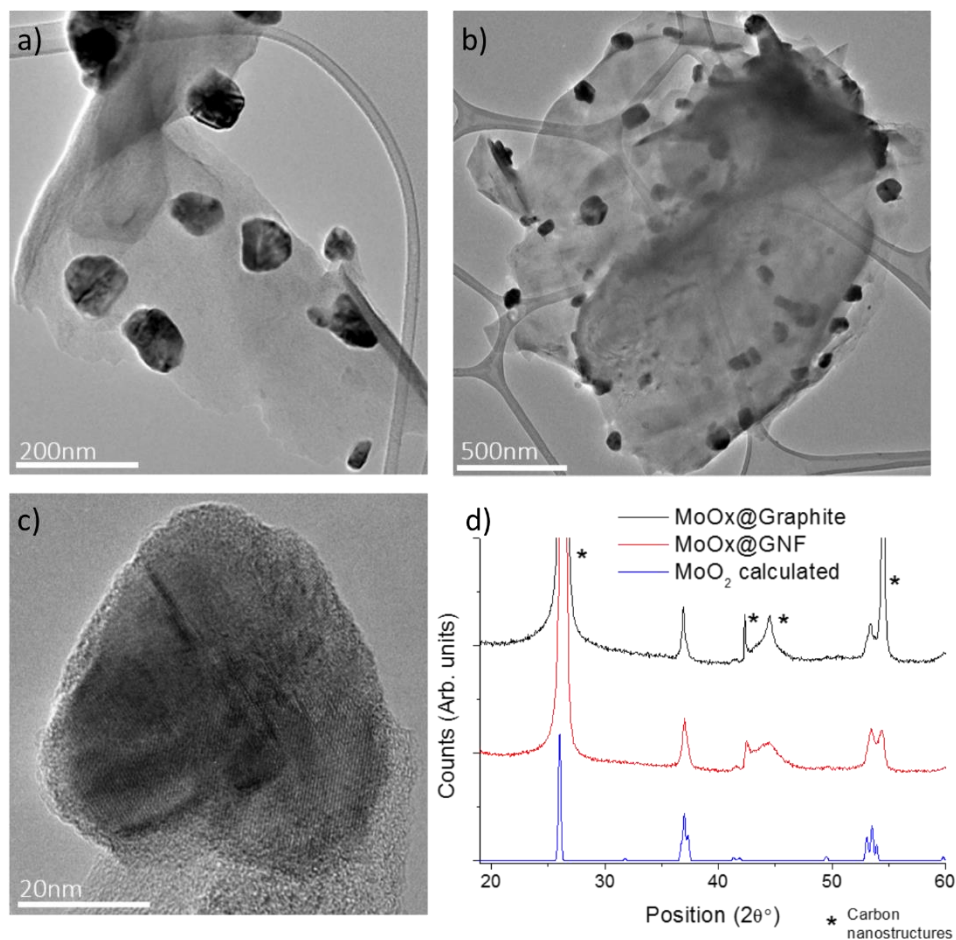


Figure 5.9. (a), (b) and (c) TEM of MoO_2 @graphite confirming the formation of composite materials with no confinement present. Powder X-ray diffraction (PXRD) analysis (d) confirms the presence of larger MoO_2 nanoparticles formed by peaks formed at $2\theta = 37.1^\circ$ and 53.6° consistent with the crystal phase of molybdenum (IV) dioxide.

The results of the catalyst performance showed that DBT oxidation still occurred, yet to a lower extent than observed using MoO_2 @GNF, with a reduction of 27% in organosulphur removal noted (Table 5.5, entry 4), supporting the importance of confinement of the catalyst within GNF nanoreactors. In all ODS reactions, the selectivity of the oxidised products was shown to be mostly dependant on the conversion of the DBT as expected in consecutive reactions such as this. The nanoreactor, therefore, did not promote the selective formation of the doubly oxidised product but simply

increased the rate of oxidation of first DBT, then DBTO due to the effects of high local concentration in the GNF cavity. (Figure 5.10).

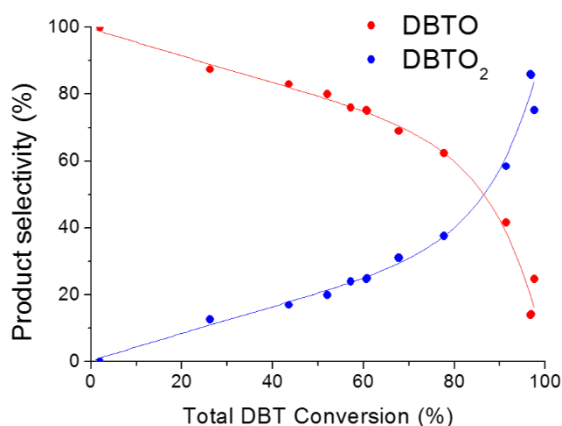


Figure 5.10. Product selectivity for DBTO and DBTO₂ when compared with total DBT conversion using several ODS procedures achieving different oxidation conversions.

Another benefit of encapsulating metal catalysts within carbon nanoreactors is the improved stability of catalytic nanoparticles. TEM indicates that after the ODS reaction MoO₂ nanoparticles remain practically unchanged inside GNF, thus the interior of GNF provides an ideal protective environment, inhibiting nanoparticle desorption and leaching, ensuring the re-use of the catalyst in subsequent ODS reactions. The residual weight from TGA is shown to be 3.6 % indicating a small loss in weight of the metal loading (0.4%) in comparison to the parent catalyst. However, there remains a notable reduction in the GNF combustion temperature indicative of the retention of MoO_x species (Figure 5.11a). TEM additionally confirms the retention of the encapsulated species after catalysis (Figure 5.11b).

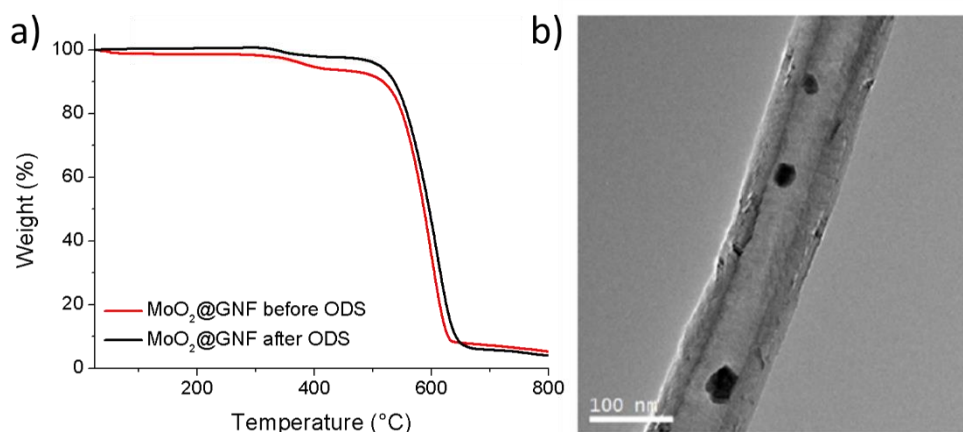


Figure 5.11. TGA and TEM of the catalyst recycled after 3 cycles of the ODS procedure with a CD_3CN wash between cycles.

Previously, MoO_3 has been shown to be an effective ODS catalyst; however, the $MoO_3@GNF-2$ nanocatalyst generated by thermal treatment post-synthesis in Chapter 4 (4.3.2.2.2) removed comparatively lower amounts of the sulphur contaminant relative to $MoO_2@GNF$ (Table 5.5, entry 5).^{54, 55} Although the difference in oxidation state is likely to impact catalyst performance, TEM analysis revealed an increase in nanoparticle size and therefore, the observed decrease in ODS activity could be a result of surface area loss of the catalyst (Figure 5.12). However, in $MoO_2@graphite$ the nanoparticles are even larger but yield similar turnover frequencies, thus suggesting that surface area may not be a major contributor here.

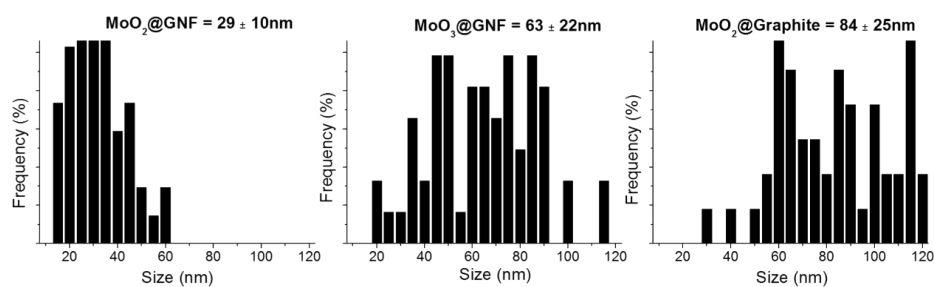


Figure 5.12. Nanoparticle sizing distribution profiles for composite materials.

A more likely explanation for the unexpected decrease in the activity of the $\text{MoO}_3@\text{GNF}$ is a consequence of the confined catalysts growing to the diameter of the nanofibre, which results in blocking of the internal cavity and subsequently restricting access of reactants to the confined catalyst (Figure 5.13).

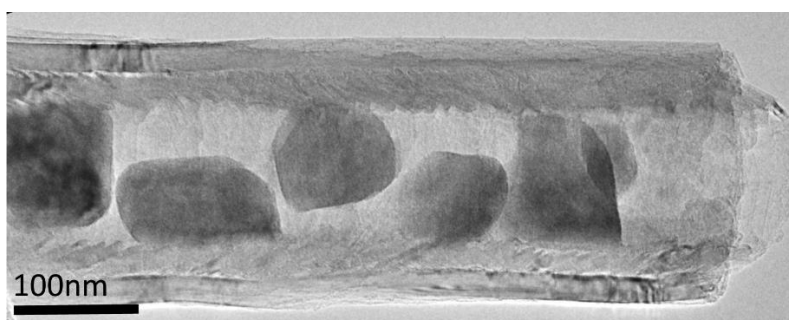


Figure 5.13. TEM of $\text{MoO}_3@\text{GNF}$ indicating the blocking of the interior nanotube channel which prevents efficient reactant transport.

With evidence supporting the successful application of the $\text{MoO}_2@\text{GNF}$ nanoreactors for oxidative desulphurisation, a kinetic profile was realised. This result shows that there is moderate sulphur removal from the model fuel using solvent extraction alone; however, when combined with the ODS reaction, near complete removal can be achieved on a relatively short timescale (Figure 5.14).

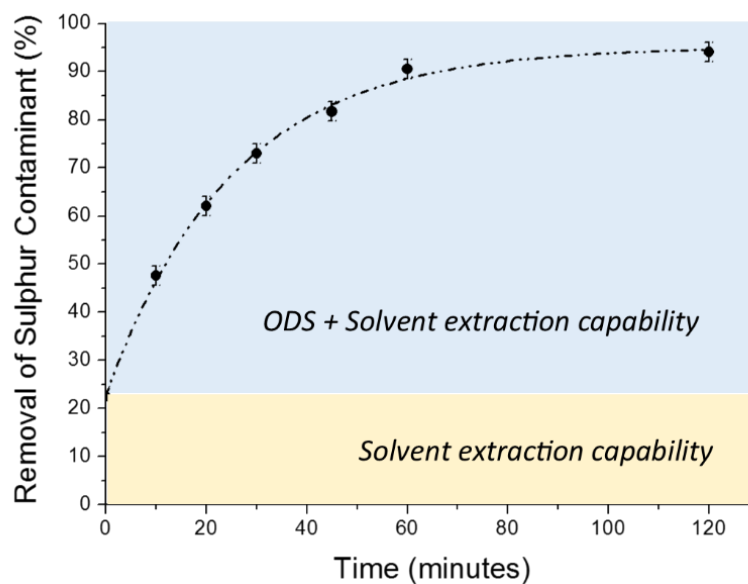


Figure 5.14. (a) Kinetic profile for the removal of DBT from *n*-hexane using the ODS (5 mg MoO₂@GNF, 5ml fuel, 1:20 S:O ratio, 60 °C) and solvent extraction (5:1 hexane:acetonitrile, 30 minutes) procedures.

Up to 30 minutes there appears to be a linear relationship between time and removal, yielding 70% total sulphur removal; however, there is a retardation in the removal after 45 minutes. This suggests that after the initial oxidation process the nanoreactor system does not facilitate effective transport of the contaminant molecules. TEM of the MoO₂@GNF post ODS procedure showed no growth or blocking of the internal diameter by the catalysts, therefore, there must be a different source to the resulting decrease in activity.

5.3.3.1. Catalytic nanosponge for ODS

Interestingly, initial attempts to recycle the catalyst were only moderately successful when a solvent wash was not used between cycles, with an approximate 40% drop in sulphur removal capacity noted after the first cycle (red bars, Figure 5.15a). Analysis of the catalyst after the first ODS run with no solvent wash by TGA indicated there was a significant mass loss at 242 °C, which

is consistent with the boiling point of the doubly oxidised sulfone product (Figure 5.15, b and c). These adsorbed products block the channel to further DBT reactant molecules, lowering the sulphur removal capacity. The introduction of either a 250 °C thermal treatment or washing step with a polar solvent between consecutive ODS reactions effectively removed the products from the channel, ensuring high catalytic activity even after 5 uses (green bars, Figure 5.15a). A very small drop in catalyst performance is still noted between uses 1 to 5 and this has been attributed to subtle changes in nanoparticle morphology and loading induced during successive reactions.

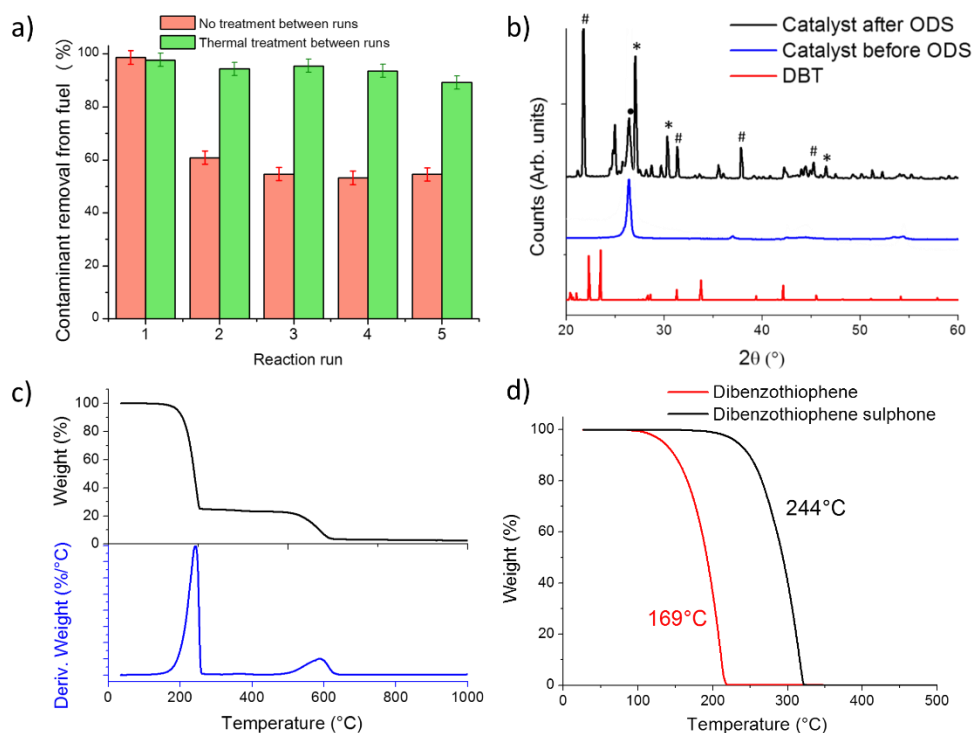


Figure 5.15. (a) Recycling experiments using $\text{MoO}_2@\text{GNF}$ for the ODS of DBT indicated that some organosulphur species remain within the nanoreactor cavity after the initial use, identified by (b) as the products of ODS (* sulfoxide, # sulfone), (c) TGA of the used catalyst $\text{MoO}_2@\text{GNF}$ indicating the presence of a species lost at 243 °C, consistent with the formation of the doubly oxidised product as confirmed by (d) TGA of sulphur containing species in isolation.

Complementary analysis by powder X-ray diffraction (PXRD) (Figure 5.15b) revealed the presence of a mixture of organic molecules adsorbed on GNF nanoreactors, comprising predominately DBTO_2 , a small amount of DBTO, but importantly no DBT. This indicates that solely the products of the ODS reaction become trapped within the GNF. From a practical point of view, accumulation of ODS products necessitates an additional thermal treatment between uses, which maintains the high sulphur removal capacity use-to-use. However, this nanosponge effect ensures efficient removal of the sulphur contaminants

through adsorptive desulphurisation (ADS), negating the requirement for a separate and potentially costly additional extraction step (Figure 5.16a).

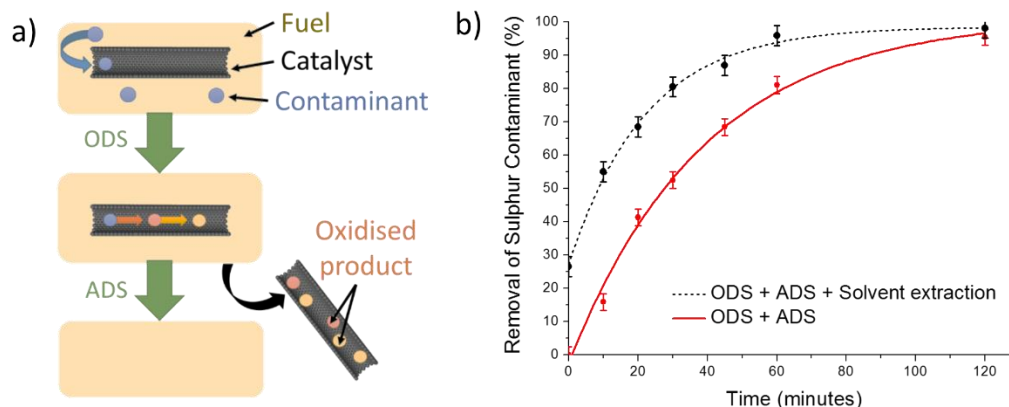


Figure 5.16. (a) Schematic diagram demonstrating the process of oxidation and extraction using the nanoreactor and nanosponge composite material to achieve an effective removal of sulphur contaminants. (b) Kinetic profile for the removal of DBT from an *n*-hexane model fuel using the ODS procedure alone (red - 5mg MoO₂@GNF, 5ml fuel, 1:20 S:O ratio, 60 °C) and with the solvent extraction (black - 5mg MoO₂@GNF, 5ml fuel, 1:20 S:O ratio, 60 °C, 1mL CD₃CN extraction for 30mins).

In light of this, the efficiency of sulphur contaminant removal using only ODS, i.e. without a solvent extraction was considered, with over 90% removal of the DBT observed. The kinetic profile based on just the nanosponge extraction shows that there is a near linear removal of DBT up to 60 minutes, with retardation due to absorption effects of the oxidised products (Figure 5.16b). After 120 minutes, near complete removal can be achieved without the need for a separate solvent extraction, and after 60 minutes the level of sulphur contaminants within the fuel approaches that which is required to meet current ULSD regulations. When comparing active catalyst loading, time and sulphur removal, the catalytic nanosponges MoO₂@GNF in this work

significantly outperform other catalysts in their ability to desulphurise fuel by more than an order of magnitude (Table 5.6).^{33, 49, 56, 57}

Table 5.6. Comparison of various catalysts for oxidative desulphurisation of DBT in model fuels.

Catalyst	Weight of Contaminant : catalyst (mol g ⁻¹) ^a	Reaction time (mins)	DBT removal (%)	O : S ratio	Temperature (°C)	Desulphurisation factor (mol g ⁻¹ min ⁻¹) ^b	Ref
HPMo/BN-IL	0.0016	100	94.3	4	40	1.48x10 ⁻⁵	56
Ce ₂ Mo ₁₀ W ₂ /SBA	0.0040	80	100.0	5	60	4.92x10 ⁻⁵	49
MoO ₃ /Al ₂ O ₃	0.00056	30	90.5	3	60	1.70x10 ⁻⁵	33
Cs ₂ H[PW ₄ Mo ₉ O ₄₀] on Iron Oxide @ Mesoporous Silica	0.023	60	94.0	17	60	3.54x10 ⁻⁴	57
MoO ₂ @GNF	0.39	120	98.8	20	60	3.13x10 ⁻³	This work
MoO ₂ @GNF	0.20	120	89.0	5	60	1.46x10 ⁻³	This Work

^a The contaminant weight (mol) per active catalyst weight (g) in each oxidative desulphurisation reaction.

^b Calculated using the percentage of contaminant removal per weight percent of contaminant to catalysts loading per unit time. Example calculation for desulphurisation factor: moles of sulphur contaminant in each ODS reaction divided by the active catalyst loading without support in grams. This value is multiplied by percentage removal/100 and divided by the reaction time to give a term similar to turn over frequency called "desulphurisation factor" which allows normalisation of all literature data and effective comparisons of the catalyst.

Although desulphurisation efficiency is often used to quantify the effectiveness of ODS catalysts a new desulphurisation factor was introduced to normalise sulphur removal with active catalyst loading and reaction time. This factor allows standardisation in ODS procedures and identifies that the nanoreactors studies here can desulphurise model fuels to similar levels as those reported previously, but with significantly lower catalyst loadings. The application of catalysts with higher specific surface areas and good dispersion often in porous structures have accelerated ODS catalysts forward in the literature; however, using carbon nanoreactors appears to represent a superior catalyst system, by

also increasing local concentrations around enhanced catalyst surfaces and promoting the ADS pathway leading to significant desulphurisation factors. The ability to selectively remove the absorbed oxidised products results in impressive recyclability of these carbon nanoreactors with only a small drop in desulphurisation after five cycles observed (green bars, Figure 5.15a). This makes the composite material a very promising candidate for this application and could further revolutionise this field of research.

5.3.4. ODS of more representative model fuel systems with MoO₂@GNF

5.3.4.1. Individual component model fuels

To assess the effectiveness of the MoO₂@GNF catalysts towards more realistic fuel systems, a more sterically demanding contaminant (dimethyl dibenzothiophene - DMDBT) and electron-poor contaminants (benzothiophene – BT, and thiophene – T) were investigated alongside DBT in *n*-octane as a more representative fuel. No effect of solvent, i.e. *n*-hexane vs. *n*-octane, was noted in the sole oxidation of DBT (Table 5.7). For the analysis of thiophene, GC-MS must be utilised as the UV-Vis spectrum possesses no uniquely identifiable electronic transitions for thiophene. With *n*-hexane and thiophene possessing very similar retention times, employing *n*-octane as a suitable fuel solvent is further justified.

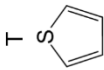
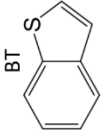
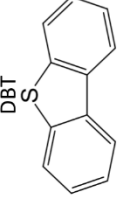
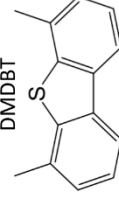
Table 5.7. The effect of solvent on the ODS of DBT. These results show minimal difference when *n*-hexane or *n*-octane are employed as the solvent in the model fuel.

	Sulphur removal with ODS and solvent extraction procedures (%) ^{a,b}		Oxidation conversion (%) ^c
	GNF	MoO ₂ @GNF	
DBT in Hexane	25.3	93.9	85
DBT in Octane	25.7	93.5	87

^a 5mg catalyst (containing 3.5wt% MoO₂), 5 mL of *n*-hexane or *n*-octane containing 500 ppm DBT, sulphur:oxidant molar ratio is 1:20, tert-butyl hydroperoxide oxidant, 60 ° C, 120 mins. ^b Percentage of sulphur-containing contaminants removed via combined ODS and solvent extraction (1ml CD₃CN, 30minutes) was determined using GC-MS ^c The conversion of DBT and selectivity of products was calculated using GC-MS of the fuel phase and ¹H NMR spectroscopy of solvent extraction phase and a solvent washing of the post-reaction solid catalysts.

To investigate the additional contaminants for any initial desulphurisation using an adsorptive or solvent extraction, ODS procedures and solvent extractions were performed with the individual species in *n*-octane and empty GNF (Table 5.8).

Table 5.8. Effect of GNF and MoO₂@GNF as catalysts in the ODS procedure on four individual sulphur contaminants.

Sulphur Contaminant	Electron density ^a	GNF		MoO ₂ @GNF		
		Sulphur removal with ODS procedure (%) ^b	Conversion (%) ^c	Sulphur removal with ODS procedure (%) ^d	Conversion (%) ^c	Selectivity (%) ^e RO : RO ₂
T 	5.696	33.8	0.0	38.4	0.0	0 : 0
BT 	5.739	26.8	0.0	43.4	18.7	33 : 67
DBT 	5.758	25.7	0.0	97.5	95.6	14 : 86
DMDBT 	5.760	10.2	0.0	89.0	70.7	79 : 21

^a Electron density is the probability of electrons being present on the sulphur atom as calculated by Otsuki et al using a modified neglect of diatomic overlap (Parametric Method 3) semiempirical Hamiltonian.^{54, b} GNF ODS procedures contaminant 500ppm in octane, O:S = 20:1, 60 °C, 5 mg empty GNF, 5 mL model fuel, 1 mL extractant, measured using GC-MS.^c Calculated using GC-MS of fuel phase for conversion.^d ODS procedures contaminant 500ppm in octane, O:S = 20:1, 60 °C, 5 mg MoO₂@GNF (2.3% loading), 5 mL model fuel, 1 mL extractant).^e Calculated using GC-MS of fuel phase and ¹H NMR spectroscopy of the extraction phase for the selectivity of products.

Similar to the DBT measurements previously, the use of empty GNF did not result in any oxidation of the sulphur containing species. Interestingly, if we consider the ability of the solvent extraction to remove the contaminants from the fuel, we observed that the more electron poor species are removed with higher efficiency. For thiophene the lack of benzene rings and decreased electron density of the sulphur results in an increased polarity of this molecule thus, it becomes more easily removed by acetonitrile during the extraction. Conversely, with BT and DBT possessing large aromatic groups and higher electron density on the sulphur, their polarity is reduced. The sterically hindered species of DMDBT is harder to extract relative to the other contaminants. This is thought to be due to the methyl groups shielding the electron density on the sulphur resulting in the most non-polar species. A simple solvent extraction remains unable to remove any of the other investigated sulphur contaminants to effective levels and thus the application of the combined ODS and ADS is essential.

The MoO₂@GNF catalyst material was then applied to the individual component systems in *n*-octane (Table 5.8). It was observed that in the cases of the electron poorer contaminants oxidation was less effective resulting in only 19% conversion for BT and no oxidation for the thiophene. The lack of electron density on the sulphur atoms makes these species less nucleophilic so they are unable to attack the peroxy species which would be generated by the molybdenum catalyst. This issue has been reported previously for analogues

with electron deficient sulphur species and thus remains a significant challenge for this catalyst and the field.^{25, 26}

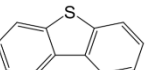
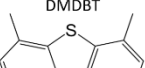
Although possessing similar electron density on the sulphur, 70% of the more sterically hindered DMDBT is converted when compared with 96% for DBT after 120 minutes at the same concentration and conditions. This indicates that the methyl groups hinder the adsorption of the sulphur containing species. Blocking of the activated oxygen from the approaching sulphur species may also contribute. As the DMDBT becomes singly oxidised these steric effects become even more pronounced as shown by the preferred selectivity towards the sulfoxide species which could account for the reduction of desulphurisation observed. Almost 90% of this sterically hindered species is still able to be removed with solvent extraction and although thiophene still remains a challenge and limitation for this catalyst, this study has clearly demonstrated that MoO₂@GNF can be successfully applied to the oxidation of a diverse range of individual organosulphur contaminant systems. A multi-component sulphur contaminant system will allow for understanding desulphurisation effects towards a more representative model fuel.

5.3.5.2. Multi-component model fuels

The three previous sulphur contaminants which could be oxidised by the catalysts were combined into one system each with a 125ppm concentration in *n*-octane to simulate a more representative fuel. By comparing the sulphur removal efficiency of GNF and MoO₂@GNF (including and without the solvent extraction) after 18 hours, it is clear that MoO₂@GNF is effective towards

oxidation of organosulphur species, with the nanosponge able to remove the oxidised contaminants from the mixed fuel system (Table 5.9).

Table 5.9. Oxidative desulphurisation procedure of the mixed component system.

Contaminant	GNF ^a		MoO ₂ @GNF ^a	
	Sulphur removal with ODS procedure (%) ^b	Sulphur removal with ODS and solvent extraction procedures (%) ^b	Sulphur removal with ODS procedure (%) ^b	Sulphur removal with ODS and solvent extraction procedures (%) ^b
BT 	1.6	30.8	94.8 (2.6)	98.3 (44.7)
DBT 	4.1	26.3	100.0 (84.3)	100.0 (94.3)
DMDBT 	10.9	16.9	100.0 (99.3)	100.0 (99.4)
Sulphur contaminants remaining in fuel (ppm)^c	354.2	282.5	6.5* (142.2)	2.1* (58.9)

^a 5mg of heterogeneous catalyst (empty GNF or MoO₂@GNF containing 4wt% MoO_x), 5ml of octane containing 3 contaminants (125ppm of benzothiophene – BT, dibenzothiophene – DBT and dimethyldibenzothiophene – DMDBT), sulphur:oxidant molar ratio is 1:20, tert-butyl hydroperoxide (TBHP) oxidant, 60 °C, 18 hr. Values in parentheses correspond to data collected after 2 hr. ^b Percentage of sulphur-containing contaminants removed via either (i) ODS or (ii) combined ODS and solvent extraction (1ml CD₃CN, 30 minutes) was determined using GC-MS. ^c Sum of contaminants removed from the fuel in ppm. * Represents values below those required by current regulations.

The order of reactivity of these contaminants was shown to be DMDBT > DBT > BT and after 2 hours it was found that there was almost 100% removal of DMDBT. The reason for this is thought to be the higher affinity of DMDBT to GNF which encourages absorption into the internal channel of the nanoreactors and leads to high concentrations of DMDBT at the location of the catalyst. This is supported by the increased removal of DMDBT with just the empty GNF and no solvent extraction. The observation of a small decrease in the removal of DBT in the mixed system from what would be expected after 2

hours in isolation, indicates competition within the nanoreactor of DMDBT and DBT for access to the catalyst (Table 5.9, values in parentheses).

For a molecule to be preferentially encapsulated inside the nanoreactor the solvent-nanoreactor and solvent-reagent molecule interaction must be weak, therefore, making the reagent molecules-nanoreactor interaction strong (Figure 5.17). When oxidised, the OS species become more polar making them less favourable to remain in the solvent and hence makes the nanotube-OS interaction stronger. As DMDBT and its oxidised products are the most insoluble in *n*-octane they are preferentially absorbed, oxidised and retained by the nanoreactor resulting in the increased removal of this species.

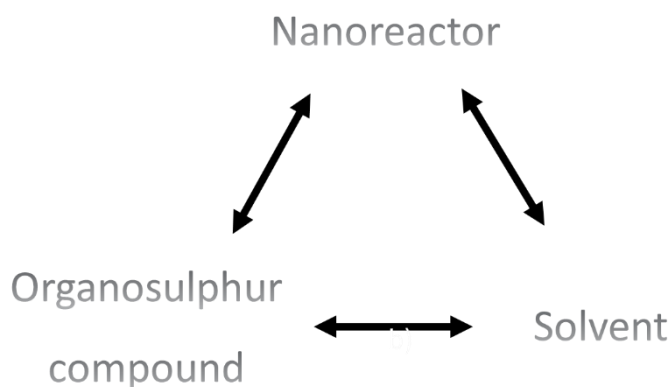


Figure 5.17. Diagrammatic representation of the interaction between nanoreactor, reagent molecules and the solvent.

Similarly, with limited access to the catalyst surface and possessing the highest solubility in *n*-octane only 45% of BT removal was observed in the mixed system after 2 hours. Only 9.1% of BT could be converted after 2 hours which is significantly lower than the previous conversion for the higher concentration individual system of BT, which achieved 19% removal after 2 hours. This further supports the competitive effects for the catalyst surface against the other

contaminants and due to the expected decreased reactivity of BT, results in reduced oxidation and desulphurisation (Table 5.10).

Table 5.10. Oxidation conversion values for mixed fuel system with MoO₂@GNF.

	Contaminant conversion using GNF (%) ^a	Contaminant conversion using MoO ₂ @GNF (%) ^{a, b}
BT	0	95 (9)
DBT	0	96 (87)
DMDBT	0	95 (92)

^a 5 mL of n-octane containing 3 contaminants (125 ppm of benzothiophene - BT, dibenzothiophene - DBT and dimethyldibenzothiophene - DMDBT), sulphur:oxidant molar ratio is 1:20, tert-butyl hydroperoxide (TBHP) oxidant, 60 ° C, 18 hr (2 hr values in parentheses). The conversion of contaminants was calculated using GC-MS analysis of the fuel phase and ¹H NMR spectroscopy of the solvent extraction phase and a solvent washing of post-reaction solid catalysts. ^b 5 mg catalyst (containing 4wt% MoO_x).

After an 18 hour ODS procedure, significant amounts of the DMDBT and DBT can be effectively oxidised and nearly all contaminants are effectively removed by the solid nanosponge extraction process (Table 5.10). Although BT can be oxidised by the catalyst, it requires 18 hours for the near total (95%) removal, which for this mixed contaminant fuel system achieves a sulphur concentration of 6.5ppm when relying on the adsorptive nanosponge effects, but can be further maximised to 2.1 ppm with a solvent extraction. Both of these values satisfy the ultra-low sulphur diesel (ULSD) regulations of less than 10 ppm imposed by international policies and this work highlights the promise of catalytic nanosponges towards the effective ODS but selective ADS of sulphur contaminants in liquid fuels.⁷

5.4. Conclusions

This study has demonstrated the principle of a 'catalytic nanosponge' that combines catalysis of organosulphur oxidation and sequestration of the products from the reaction mixture. Group VI (chromium, molybdenum and tungsten) metal oxide nanoparticles encapsulated in carbon graphitised nanofibres were evaluated as nanoreactors for the desulphurisation of fuel. When immersed in a model liquid alkane fuel contaminated with organosulphur compounds (benzothiophene, dibenzothiophene, dimethyldibenzothiophene), MoO₂@GNF nanoreactors with an organic peroxide showed superior abilities towards oxidative desulphurisation (ODS). The MoO₂@GNF outperformed both the other catalysts investigated in this study and related catalytic materials of this type, affording over 98 % fuel desulphurisation of dibenzothiophene within 2 hours at only 5.9 mol% catalyst loading. Desulphurisation abilities of the nanoreactor were found to be affected by manipulating reaction time, temperature and peroxide concentration, but still possessed enhanced decontamination abilities. Altering the location, oxidation state and size of the metal oxide catalyst highlighted the importance and limitations of the confined environment where the catalyst resides. The roles of the carbon nanoreactor in MoO₂@GNF are to enhance the activity of catalytic centres during the reaction and enable effective catalyst stability without any significant loss of activity over at least five cycles. Surprisingly, the nanoscale cavity of the GNF selectively absorbs the ODS oxidation products, thus effectively removing them from several model fuel

systems. This nanosponge effect is related to the adsorptive desulphurisation (ADS) mechanism, which in combination with ODS within the same material, yields a 'catalytic nanosponge' MoO₂@GNF. This material negates the need for a solvent extraction step in fuel desulphurisation by ODS and leads to the ultra-low sulphur fuel required by current international regulations. The MoO₂@GNF nanoreactors were applied to more sterically and electronically demanding contaminants which provided a more representative model fuel system. Despite showing inferior oxidation capability when compared to DBT, this system could still be decontaminated to levels below what is required for ULSD using both the ODS and ADS pathways. This study introduces catalytic nanoreactors with dual functionality and highlights the significant success and importance of the MoO₂@GNF nanoreactors towards desulphurisation.

5.5. Experimental

5.5.1. General

Standard reagents and solvents were purchased from Sigma-Aldrich Chemicals and were used as purchased. 4,6-dimethyldibenzothiophene (97 %), benzothiophene (98 %), thiophene (>99 %) and hydrogen peroxide (30% w/w) was purchased from Sigma Aldrich. Dibenzothiophene (98 %) was purchased from Acros Chemicals. *N*-octane (95 %) and *n*-hexane were purchased from VWR Chemicals and Fischer Scientific respectively. Tert-butyl hydroperoxide (70 % aqueous solution) and bis(acetylacetonato)dioxymolybdenum(VI) (99 %) was purchased from Alfa Aesar and was used as purchased. Graphitised nanofibres were PR19-XT-HHT carbon nanofibers purchased from Pyrograf

products inc (iron content <100ppm), graphite flakes (Code G/0900/60, Batch 043775) were purchased from Fisher Scientific.

Transmission electron microscopy (TEM) was performed using a JEOL JEM-2100Plus microscope operated at 200 keV. TEM samples were prepared *via* a drop casting technique, where samples were first dispersed in methanol and deposited on a copper grid mounted “lacey” carbon films. All images were processed using Gatan Digital Micrograph. Nanoparticle sizing distribution information was measured by recording over 50 separate units from the samples in multiple images.

Thermogravimetric analysis was performed using a TA Q500 Thermogravimetric Analyser. All samples were analysed using a platinum pan and in the presence of air. The parameters for all experiments were: Ramp 5 °C/minute from 20-1000 °C with an isotherm for 10 minutes at 1000 °C, air flow: 60 mL/minute.

The powder X-ray measurements were performed using a PANalytical X'Pert Pro diffractometer equipped with a Cu K(α) radiation Source ($\lambda=1.5432 \text{ \AA}$, 40kV 40mA) in Bragg-Brentano geometry using a Si zero background holder. All samples were wetted with isopropyl alcohol to aid GNF adhesion. The parameters for a typical experiment were: Start angle: 5°, Stop angle: 80°, Step size: 0.0525°, Time/step: 6080s, Scan speed: 0.00220°/s.

UV-Vis absorption spectra were recorded at room temperature using 1 cm quartz cuvettes. The samples were run using a Perkin-Elmer Lambda 25 UV-Vis

spectrometer at a scan rate of 240 nm/min⁻¹ over a wavelength range of 200-500 nm. Spectra were analysed using UV WinLab ES software. For all analysis, 30 µL of the treated model fuel was diluted using 2.5 mL of the same solvent.

¹H NMR spectroscopy spectra were recorded in CD₃CN at room temperature using a Bruker AVANCE- DPX-400 spectrometer (TopSpin 1.3 PL4) in Wilmad NMR tubes (5 mm diameter). Spectra were analysed using MestReNova software.

Samples were analysed by GC-MS using a Thermo Scientific ISQ-LT single quadrupole mass spectrometer, attached to a Thermo Scientific Trace 1300 GC. Samples were injected through a Thermo Scientific TriPlusRSH liquid autosampler onto a Thermo Scientific TG5MS GC column (15 m x 0.25 mm x 0.25 µm)(Thermo Fisher Scientific Inc., Massachusetts, USA). Instrument conditions were as follows: GC injector temperature 200 °C; injections were performed in split mode, employing a 50:1 split ratio. The GC oven temperature programme was 40 °C (3 min) to 320 °C (10 min) at 5 °C min⁻¹. The GC carrier gas was helium, with a column flow of 1mL min⁻¹. The mass spectrometer was programmed to acquire data after a 3 minute delay, over the mass range 50-600Da, with a 0.2 s scan time. Mass spectra were acquired in EI mode (70eV ionisation energy). The ion source temperature was 200 °C and the MS transfer line was maintained at 250 °C. Total Ion Current chromatograms and associated mass spectra were processed with Chromeleon software (Version 7.2; Thermo Fisher Scientific Inc., Massachusetts, USA).

5.5.2. Oxidative desulphurisation procedure with extraction procedure

The first model fuel (500 mg/L of sulphur) was prepared by dissolving DBT (0.870 g, 4.72 mmol) in *n*-hexane (300 mL). The second mixed component model fuel contains benzothiophene (125ppm), dibenzothiophene (125ppm) and dimethyl dibenzothiophene (125ppm) in octane. The desulphurisation experiments were conducted at 60 °C (unless stated otherwise). In general, 5mg of the catalyst was added to 5 mL of the model fuel and sonicated for 2 minutes. 0.14mL of 70 wt. % TBHP aqueous solution was added and the solution was heated for 120 minutes unless otherwise stated and stirred at 500 rpm. Once complete, the solid was removed and the reaction was extracted using 1 mL CD₃CN. The extraction process was vigorously stirred at a constant speed (1000 rpm) for 30 minutes at ambient temperature. The removed catalyst was washed with deuterated solvent and the washings were combined with the extraction layer. The extraction phase and organic fuel layer were analysed by UV-Vis spectroscopy, GC-MS and ¹NMR spectroscopy. The extraction layer was analysed using GC-MS and ¹H NMR spectroscopy for oxidation products. The oxidation of DBT was monitored by the disappearance of the characteristic chemical shifts between 8.28 and 8.21 ppm (m, 2H). Confirmation of the sulfoxide and sulfone products was afforded by monitoring by the integrals between 7.71–7.64 (t, 2H) and 7.86–7.81 (d, 2H), respectively. The treated diesel was stored in a sealed vial and kept refrigerated at 2 °C. UV-Vis peak maxima for DMDBT and DBT taken at 326 nm and at 297 nm for BT. GC-MS retention times for organosulphur compounds were DBT=25.27mins,

DBTO=32.23mins, DBTO₂=32.51mins; DMDBT=29.27, DMDBTO=34.67mins,
DMDBTO₂=34.48mins; BT=11.94, BTO=21.54mins, BTO₂=22.18mins,
T=0.84mins.

5.5.3. Oxidative desulphurisation procedure without extraction procedure

The desulphurisation experiments without the solvent extraction were conducted as previously mentioned at 60 °C (unless stated otherwise). In general, 5mg of the catalyst was added to 5 mL of the model fuel and sonicated for 2 minutes. 0.14 mL of 70 wt. % TBHP aqueous solution was added and the solution was heated for 120 minutes unless otherwise stated and stirred at 500 rpm. Once complete, the solid was removed and the organic phase analysed by UV-Vis spectroscopy, GC-MS and ¹NMR spectroscopy. The solid catalyst removed was washed with deuterated solvent and the products removed and analysed by UV-Vis spectroscopy.

5.5.4. Preparation of MoO₂@Graphite

Graphite flakes (30mg) were then loaded into a Pyrex glass tube (d=100mm, L=6 cm) with molybdenum dioxide bisacetylacetonate (5.6mg) and sealed under vacuum ($\sim 3 \times 10^{-5}$ mbar). The sealed vessel was then heated to 160 °C for 3 days. Following sublimation and prior to opening, the Pyrex glass tube was immediately cooled for 5 minutes. MoO₂(acac)₂@Graphite were placed into a new Pyrex glass tube (d=100 mm, L=6 cm) and evacuated and backfilled with argon (repeated 3 times) to remove any oxygen or moisture present. Before

sealing, the Pyrex glass tube was filled with argon gas (~0.5 bar). For the decomposition step, the sealed vessels were heated at 500 °C for 1 hour in a pre-heated furnace to obtain the MoO₂@Graphite composite material which was then cooled down slowly for 9 hours.

5.6. References

1. S. Mohankumar and P. Senthilkumar, *Renew. Sust. Energ. Rev.*, 2017, **80**, 1227-1238.
2. A. K. Agarwal, *Prog. Energy Combust. Sci.*, 2007, **33**, 233-271.
3. G. Mohebbali and A. S. Ball, *Int. Biodeterior. Biodegrad.*, 2016, **110**, 163-180.
4. V. C. Srivastava, *RSC Adv.*, 2012, **2**, 759-783.
5. H. A. El Sayed, A. M. A. El Naggar, B. H. Heakal, N. E. Ahmed, S. Said and A. A. H. Abdel-Rahman, *Fuel*, 2017, **209**, 127-131.
6. E. Ito and J. A. R. van Veen, *Catal. Today*, 2006, **116**, 446-460.
7. P. S. Kulkarni and C. A. M. Afonso, *Green Chem.*, 2010, **12**, 1139-1149.
8. J. Bu, G. Loh, C. G. Gwie, S. Dewiyanti, M. Tasrif and A. Borgna, *Chem. Eng. J.*, 2011, **166**, 207-217.
9. E. Pedernera, R. Reimert, N. L. Nguyen and V. van Buren, *Catal. Today*, 2003, **79-80**, 371-381.
10. K.-H. Choi, N. Kunisada, Y. Korai, I. Mochida and K. Nakano, *Catal. Today*, 2003, **86**, 277-286.
11. C. Ania, J. Parra, A. Arenillas, F. Rubiera, T. J. Bandoz and J. Pis, *Appl. Surf. Sci.*, 2007, **253**, 5899-5903.
12. Y. Sano, K. Sugahara, K.-H. Choi, Y. Korai and I. Mochida, *Fuel*, 2005, **84**, 903-910.
13. H. Chen, W.-J. Zhang, Y.-B. Cai, Y. Zhang and W. Li, *Bioresour. Technol.*, 2008, **99**, 6928-6933.
14. A. Caro, P. Letón, E. García-Calvo and L. Setti, *Fuel*, 2007, **86**, 2632-2636.
15. J. L. Garcia-Gutierrez, G. A. Fuentes, M. E. Hernandez-Teran, P. Garcia, F. Murrieta-Guevara and F. Jimenez-Cruz, *Appl. Catal., A*, 2008, **334**, 366-373.
16. L. Cedeño-Caero, H. Gomez-Bernal, A. Fraustro-Cuevas, H. D. Guerra-Gomez and R. Cuevas-Garcia, *Catal. Today*, 2008, **133**, 244-254.
17. M. Armaghan, M. M. Amini, H. R. Khavasi, W. H. Zhang and S. W. Ng, *RSC Adv.*, 2016, **6**, 85381-85389.
18. L. H. Zhang, J. Y. Wang, Y. L. Sun, B. Jiang and H. W. Yang, *Chem. Eng. J.*, 2017, **328**, 445-453.

19. J. Wang, R. R. Butler, F. Wu, J. F. Pombert, J. J. Kilbane and B. C. Stark, *PLoS One*, 2017, **12**, 20.
20. R. Menzel, D. Iruretagoyena, Y. F. Wang, S. M. Bawaked, M. Mokhtar, S. A. Al-Thabaiti, S. N. Basahel and M. S. P. Shaffer, *Fuel*, 2016, **181**, 531-536.
21. M. F. Ali, A. Al-Malki, B. El-Ali, G. Martinie and M. N. Siddiqui, *Fuel*, 2006, **85**, 1354-1363.
22. R. T. Yang, A. J. Hernandez-Maldonado and F. H. Yang, *Science*, 2003, **301**, 79-81.
23. A. R. Lopes, A. D. Scheer, G. V. Silva and C. I. Yamamoto, *Materia*, 2016, **21**, 407-415.
24. E. Deliyanni, M. Seredych and T. J. Bandosz, *Langmuir*, 2009, **25**, 9302-9312.
25. D. H. Wang, E. W. H. Qian, H. Amano, K. Okata, A. Ishihara and T. Kabe, *Appl. Catal., A*, 2003, **253**, 91-99.
26. M. A. Safa and X. L. Ma, *Fuel*, 2016, **171**, 238-246.
27. L. Qiu, Y. Cheng, C. P. Yang, G. M. Zeng, Z. Y. Long, S. N. Wei, K. Zhao and L. Luo, *RSC Adv.*, 2016, **6**, 17036-17045.
28. T. J. Donohoe, *OXFORD CHEMISTRY PRIMERS*, 2000, **6**, 37-44.
29. D. V. Deubel, J. Sundermeyer and G. Frenking, *J. Am. Chem. Soc.*, 2000, **122**, 10101-10108.
30. G. Wahl, D. Kleinhenz, A. Schorm, J. Sundermeyer, R. Stowasser, C. Rummey, G. Bringmann, C. Fickert and W. Kiefer, *Chemistry-a European Journal*, 1999, **5**, 3237-3251.
31. M. Munoz, M. A. Gallo, A. Gutierrez-Alejandre, D. Gazzoli and C. I. Cabello, *Appl. Catal. B-Environ.*, 2017, **219**, 683-692.
32. A. Bazyari, A. A. Khodadadi, A. H. Mamaghani, J. Beheshtian, L. T. Thompson and Y. Mortazavi, *Appl. Catal. B-Environ.*, 2016, **180**, 65-77.
33. W. A. W. Abu Bakar, R. Ali, A. A. A. Kadir and W. Mokhtar, *Fuel Process. Technol.*, 2012, **101**, 78-84.
34. M. Zhang, W. S. Zhu, S. H. Xun, J. Xiong, W. J. Ding, M. Li, Q. Wang and H. M. Li, *Chem. Eng. Technol.*, 2015, **38**, 117-124.
35. Y. Q. Xu, W. M. Xuan, M. M. Zhang, H. N. Miras and Y. F. Song, *Dalton Trans.*, 2016, **45**, 19511-19518.
36. A. La Torre, M. W. Fay, G. A. Rance, M. Del Carmen Gimenez-Lopez, W. A. Solomonsz, P. D. Brown and A. N. Khlobystov, *Small*, 2012, **8**, 1222-1228.
37. X. L. Pan and X. H. Bao, *Acc. Chem. Res.*, 2011, **44**, 553-562.
38. T. H. Noh and O. S. Jung, *Acc. Chem. Res.*, 2016, **49**, 1835-1843.
39. W. A. Solomonsz, G. A. Rance, B. J. Harris and A. N. Khlobystov, *Nanoscale*, 2013, **5**, 12200-12205.
40. A. La Torre, M. D. Gimenez-Lopez, M. W. Fay, G. A. Rance, W. A. Solomonsz, T. W. Chamberlain, P. D. Brown and A. N. Khlobystov, *ACS nano*, 2012, **6**, 2000-2007.

41. A. N. Khlobystov, *ACS nano*, 2011, **5**, 9306-9312.
42. S. Gupta and N. H. Tai, *J. Mater. Chem. A*, 2016, **4**, 1550-1565.
43. T. A. Saleh, S. A. Al-Hammadi, A. Tanimu and K. Alhooshani, *J. Colloid Interface Sci.*, 2018, **513**, 779-787.
44. T. A. Saleh, *J. Clean Prod.*, 2018, **172**, 2123-2132.
45. J. A. Arcibar-Orozco, J. R. Range-Mendez and T. J. Bandoz, *Energy & Fuels*, 2013, **27**, 5380-5387.
46. D. Yue, J. Lei, Z. Lina, G. Zhenran, X. Du and J. Li, *Catal. Lett.*, 2018, **148**, 1100-1109.
47. L. P. Hou, R. X. Zhao, X. P. Li and X. H. Gao, *Appl. Surf. Sci.*, 2018, **434**, 1200-1209.
48. A. Alizadeh, M. Fakhari, M. M. Khodeai, G. Abdi and J. Amirian, *RSC Adv.*, 2017, **7**, 34972-34983.
49. M. Chamack, A. R. Mahjoub and H. Aghayan, *Chem. Eng. J.*, 2014, **255**, 686-694.
50. L. C. Caero, E. Hernandez, F. Pedraza and F. Murrieta, *Catal. Today*, 2005, **107-08**, 564-569.
51. F. Al-Shahrani, T. C. Xiao, S. A. Llewellyn, S. Barri, Z. Jiang, H. H. Shi, G. Martinie and M. L. H. Green, *Appl. Catal. B-Environ.*, 2007, **73**, 311-316.
52. W. Mokhtar, W. A. W. Abu Bakar, R. Ali and A. A. A. Kadir, *Clean Technol. Environ. Policy*, 2015, **17**, 1487-1497.
53. I. Martinez, M. E. S. Mohamed, D. Rozas, J. L. Garcia and E. Diaz, *Metab. Eng.*, 2016, **35**, 46-54.
54. L. Z. Zhuang, Q. H. Li, S. X. Chen, X. N. Hou and J. T. Lin, *J. Mater. Sci.*, 2014, **49**, 5606-5616.
55. C. P. Yang, K. Zhao, Y. Cheng, G. M. Zeng, M. M. Zhang, J. J. Shao and L. Lu, *Sep. Purif. Technol.*, 2016, **163**, 153-161.
56. H. Y. Ji, H. T. Ju, R. Lan, P. W. Wu, J. Sun, Y. H. Chao, S. H. Xun, W. S. Zhu and H. M. Li, *RSC Adv.*, 2017, **7**, 54266-54276.
57. M. Chamack and A. R. Mahjoub, *Catal. Lett.*, 2016, **146**, 1050-1058.
58. S. Otsuki, T. Nonaka, N. Takashima, W. H. Qian, A. Ishihara, T. Imai and T. Kabe, *Energy & Fuels*, 2000, **14**, 1232-1239.

Concluding remarks

The destruction of environmental contaminants represents an important and constantly evolving field of scientific research. In this thesis, the preparation and application of metal oxide nanostructures incarcerated within hollow carbon nanotubes, thereby harnessing the unique effects of spatial confinement at the nanoscale, was explored across a range of environmental remediation challenges.

Carbon nanotubes represent an exemplary class of nanoscale reaction vessels, requiring only ubiquitous van der Waals interactions to drive the encapsulation of the broadest spectrum of molecules and nanoscale materials. Owing to the complementarity between the size of the confined guest-species and the internal dimensions of the host-nanotube, carbon nanotubes are often termed the world's smallest test tubes, critically permitting control of the properties of the guest that can be harnessed to template the formation of unique one-dimensional materials inaccessible by other means. As nanoreactors for preparative chemical transformations, the synergy of interactions between the nanotube, confined catalysts and reactants increases the local concentration of reactants and modulates the activity, selectivity and stability of the catalyst, all features of which underpin the potential of carbon nanotubes for synthetic chemistry.¹ However, their narrow dimensions impact restrictions on the transport of reactants to and products from the internal channel and represents a major obstacle for further research. Conversely, hollow

graphitised carbon nanofibres (GNF) – a special class of carbon nanotubes – possess (i) large internal diameters (30-60 nm), allowing for the effective transport of molecules into, through and out of the nanoreactor, and (ii) corrugated internal structure, which provide ideal sites for molecular adhesion due to maximised van der Waals interactions, replicating the spatial confinement effects observed inside narrower carbon nanotubes. Thus, GNF represents an optimal nanoscale reactor for the promotion of catalytic decontamination reactions.

The confinement and enhanced catalytic properties of hydroxylated group IV metal oxide nanostructures inside GNF has been demonstrated. GNF were effectively filled with suitable precursor molecules of metal chlorides from the gas and liquid phases. Subsequent base-catalysed hydrolysis afforded amorphous, nanostructured hydroxylated metal oxide ($\text{MO}_x(\text{OH})_y$ where M = Zr, Ti and Hf) thin films, which coat the internal surfaces of GNF, thus affording $\text{MO}_x(\text{OH})_y@GNF$. *This versatile and general strategy allows the chemical composition and morphology of the encapsulated material to be readily tuned by varying the conditions used for hydrolysis and post-synthesis thermal treatment.* By utilising local probe techniques, including electron microscopy and elemental spectroscopy, the physical and chemical properties of the amorphous encapsulated material were effectively characterised and rationalised.

The unique morphology, increased reactive sites and surface area of the zirconium composite that promoted the catalysed hydrolysis of dimethyl

nitrophenyl phosphate (DMNP) – a simulant for toxic organophosphorus compounds. *A four-fold enhancement in the rate of DMNP hydrolysis relative to its separate constituent components was observed, highlighting the surprising synergistic abilities of this composite material, acting as both a ‘nano-sponge’, absorbing the harmful compounds inside the GNF, and a nanoreactor, enhancing the local concentration of organophosphates around the hydroxylated metal oxide species, leading to improved catalytic performance.*

Discrete group VI metal oxide nanoparticles were preferentially confined within the internal channel of the GNF using a gas-phase deposition strategy, affording $\text{MO}_x@\text{GNF}$ where $\text{M} = \text{Cr}, \text{Mo}$ and W . *Control over the morphology, size, location and loading of the metal oxide species could be manipulated by simply modifying the type, loading or rate of thermal decomposition of specific group VI hexacarbonyl or acetylacetonate precursors.* Post-synthesis thermal treatment allowed further control over the size, composition and oxidation state of the metal oxide nanoparticles. Due to the intimate contact and redox properties of the guest materials, site-selective oxidation of the GNF was observed, the magnitude of which varied down the group, indicating that surface reactivity of the metal oxide could be important in catalytic reactions.

When immersed in a model liquid alkane fuel contaminated with organosulphur compounds (benzothiophene, dibenzothiophene, dimethyldibenzothiophene), *the $\text{MoO}_2@\text{GNF}$ nanoreactors showed superior abilities towards oxidative desulphurisation (ODS), affording over 98 % fuel desulphurisation at only 5.9 mol% catalyst loading.* The roles of the carbon

nanoreactor in MoO₂@GNF are to enhance the activity and stability of catalytic centres over at least five cycles. The importance and limitations of encapsulating catalysts in confined spaces were highlighted by investigating the location, oxidation state and size of the catalytic nanoparticles towards its ODS abilities. Surprisingly, the nanoscale cavity of the GNF can selectively absorb and remove the ODS products from several model fuel systems. This nanosponge effect is related to the adsorptive desulphurisation (ADS) mechanism. The dual functionality of this material to promote a combination of ODS and ADS within the same material, yields a 'catalytic nanosponge' MoO₂@GNF, negating the need for a solvent extraction step in fuel desulphurisation and resulting in ultra-low sulphur fuel.

In summary, the work presented in this thesis demonstrates the enhanced catalytic properties of metal oxides as a consequence of spatial confinement inside carbon nanotubes across a range of decontamination reactions. This includes: (i) promotion of the unique morphologies, sizes and increased reactive sites by synthesising metal oxides in confined nanocavities; (ii) improving the stability, surface reactivity and electronic properties of metal oxide nanocatalysts due to preferential non-covalent interactions between the guest and host species; (iii) enrichment of reagents into the internal cavity due to hydrophobic effects which results in high local concentration effects around the confined catalytic centres; (iv) selective retention of the reagent or products within the nanoreactor resulting in improved removal of undesirable species from the reaction medium. Moreover, this work has successfully

applied these carbon nanoreactor confinement effects towards the important environmental remediation challenges of the destruction of organophosphorus compounds and fuel desulphurisation.

One property of carbon nanotubes which has not been exploited in this study is their documented high electrical conductivity. It is known that carbon nanotubes can be simultaneously used as nanoscale electrodes as well as the reaction vessels, such that the electrons are delivered directly to the molecules confined within the nanoreactor.² By building on the fundamental discoveries made during this work, development and application of electrocatalytic active carbon nanoreactors for targeted decontamination could be achieved. A nanoscale electrochemical platform is expected to be universally applicable for the dual-use (absorption and decontamination) by sequestering contaminants from the solution (nanosponge) and harnessing electrocatalytic reactions to drive the decontamination process (nanoreactor). This two-in-one process, where the electrochemically active nanoreactors absorb and transform harmful species to benign compounds within the single platform, allows for the fabrication of an extremely portable device which would be applicable for onsite decontamination or sensing applications (Figure 6.1).

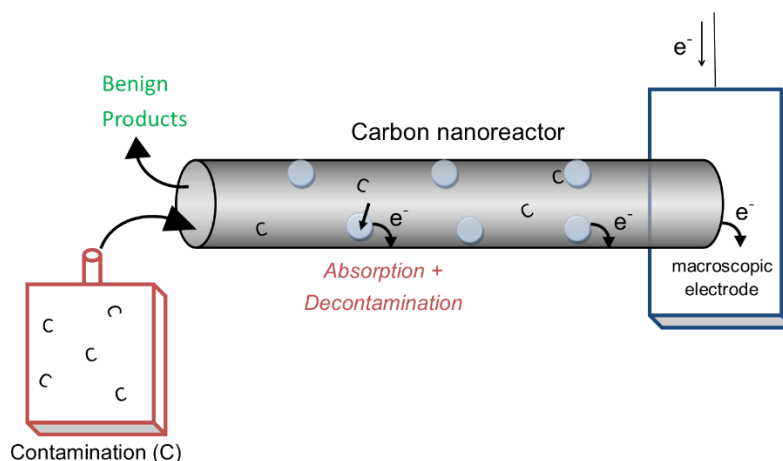


Figure 6.1. Schematic diagrams of electrocatalysis setup for absorption and decontamination of contaminants employing an electrocatalytic nanoreactor.

Further advancement of these materials towards current environmental remediation situations is an important next step and could include investigating their abilities to desulphurise real fuel and the decontamination of actual chemical warfare agents. As shown in Chapter 5, the destruction of multiple organosulphur compounds simultaneously is not trivial as the competition of reactant for the catalyst may influence the abilities of the composite in practice, therefore, interferants from the environment should be considered. However, this study has taken the first steps in developing hybrid materials with synergistic effects that can enhance the decontamination of organophosphorus and organosulphur compounds.

Although this work has clearly demonstrated the confinement, transformations and catalytic abilities of group IV and VI metal oxides inside GNF, the broader applicability of this catalytic nanoreactor approach has yet to be fully explored. Complimentary work performed alongside this study highlighted that discrete small CeO_2 nanoparticles (3-8 nm) encapsulated inside GNF showed good selectivity towards the allylic oxidation of cyclohexene (Figure 6.2). This

6. Concluding remarks

nanoreactor system showed similar trends to this work as the stability and activity of the catalyst could be enhanced due to confinement effects.

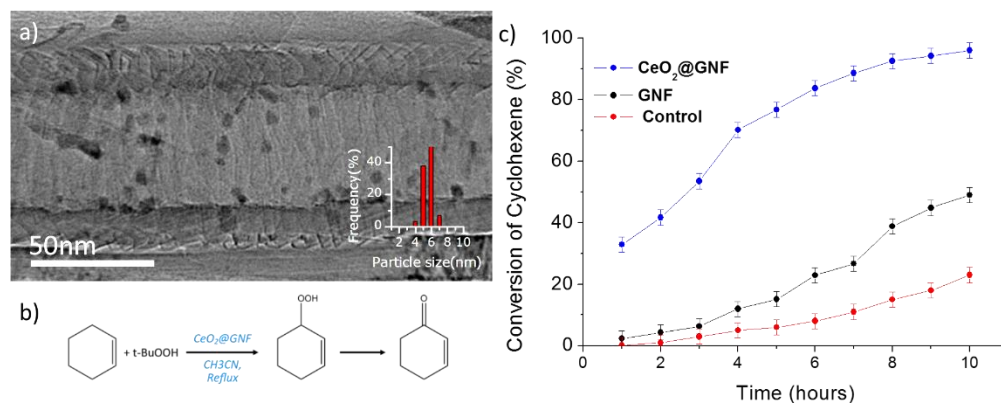


Figure 6.2. (a) Transmission electron microscopy and particle size distribution profile (inset) of CeO₂@GNF nanoreactor which was applied for the (b) oxidation of cyclohexene which showed (c) improved conversion when compared to empty GNF or control reactions. This demonstrated the potential that other metal oxide nanoreactors possess towards enhancing catalytic reactions and the wide scope for future work.

As well as a wide range of confined metal oxides to examine, environmental pollution and adapting remediation challenges will remain an issue for the foreseeable future, therefore, considering nanoreactors towards other contaminants is imperative. Additional investigations regarding the oxidation abilities of the MoO₂@GNF nanoreactor were performed and resulted in enhanced oxidation of a chemical warfare agent simulant of Mustard Gas. Preliminary results regarding the decontamination of this toxic organosulphur species highlighted that this system showed a similar catalytic nanosponge effect to this work, however, in this case, the doubly oxidised sulfone product (which is undesirable and considered very toxic), was selectively removed from the solution by the nanoreactor. Further work is, therefore, needed to

understand the full potential and limits of these catalytic nanoreactors within the field.

This study has presented significant evidence for the versatility and capability that nanoreactors possess towards targeting a diverse range of environmental pollutants. A foundation for the synthesis and application of metal oxide-carbon nanotube composites has now been established, with further research expected to make a significant contribution to the field of environmental nanoremediation.

6.1. References

1. S. A. Miners, G. A. Rance and A. N. Khlobystov, *Chem. Soc. Rev.*, 2016, **45**, 4727-4746.
2. R. L. McSweeney, T. W. Chamberlain, E. S. Davies and A. N. Khlobystov, *Chem. Commun.*, 2014, **50**, 14338-14340.